UNIVERSITY OF SOUTHAMPTON

FACULTY OF ENGINEERING, SCIENCE & MATHEMATICS

School of Engineering Sciences

Materials Research Group

Materials Assessment and Optimisation of Aluminium Alloys for Fatigue Resistance

by

Kern Hauw Khor

Thesis for the degree of Doctor of Philosophy

June 2005

UNIVERSITY OF SOUTHAMPTON

ABSTRACT

FACULTY OF ENGINEERING, SCIENCE & MATHEMATICS
SCHOOL OF ENGINEERING SCIENCES
MATERIALS RESEARCH GROUP

Doctor of Philosophy

MATERIALS ASSESSMENT AND OPTIMISATION OF ALUMINIUM ALLOYS FOR FATIGUE RESISTANCE

by Kern Hauw Khor

In quantifying the fatigue crack growth behaviour of a material, it is possible to identify intrinsic and extrinsic contributions to failure resistance, with intrinsic resistance representing the inherent mechanical and environmental material response to cyclic loading at the crack tip. The incidence of crack closure has been widely recognised as a major factor extrinsic factor affecting fatigue crack growth rates (via the shielding of cyclic load conditions in the crack-tip region), for many engineering alloys (include Al-alloys). Significant origins of crack closure may be identified as the essentially mechanical process of plasticity-induced crack closure (PICC), and the more microstructurally dependent roughness-induced crack closure (RICC). However, significant problems exist in both the experimental determination and micromechanical modelling of closure behaviour.

In the present work, several advanced variants of the established aerospace alloy 2024-T351 (with different dispersoid contents and degrees of recrystallisation) are studied for micromechanistic influences on fatigue crack growth behaviour under constant amplitude (CA) and variable amplitude (VA) loading conditions. Degrees of recrystallisation level have been seen to have limited influence on CA crack growth resistance and closure levels in the advanced 2024 alloy variants. Dispersoids are found to be a key factor controlling fracture surface faceting levels and hence, closure processes in these materials. Physical interpretation of RICC effects in terms of residual shear displacements at 3D crack wake asperities has been compared to a variety of experimental results. 3D surface profilometry techniques are applied to obtain crack deflection parameters (deflection angles and length-scales) from fatigue fracture surfaces. For CA loading conditions, where the model is most readily applied, predictions of plane strain crack closure levels from real fracture surface features has been shown to be in reasonable functional accord with experimental data.

Crack behaviour has been further investigated via synchrotron X-ray tomography at an enhanced resolution level of 0.7μm per isotropic voxel. Microstructural displacement gauging and ray casting analysis technique have been successfully developed as novel methods to measure 2D and 3D crack opening displacements. A liquid Gallium (Ga) grain boundary wetting technique has been investigated in conjunction with the microtomography to visualise and analyse simultaneously the correlation between the 3D grain structure and fatigue crack paths. Subsequent electron backscattering diffraction (EBSD) assessment of grain orientation in the computed tomography samples provides detailed crystallographic information on crack propagation mechanisms, where large crack deflections were found to be generated mostly by {111} and {100} plane oriented fracture.

In terms of VA loading (simple peak load transients), closure measurements close to the crack tip appear to describe growth rate transients well. Reasonable correlation between transient crack growth and measured closure variations has been observed when used in conjunction with '*intrinsic*' CA crack growth data. Fractographic observations and previous FE modelling results suggest that PICC may be the predominant closure mechanism over RICC in controlling post-overload retardation effects in these materials at intermediate to high baseline stress intensity loading, consistent with a limited effect of microstructure on transient crack growth.

CONTENTS

Page No.

ABSTRACT

In quantifying the fatigue crack growth behaviour of a material, it is possible to identify intrinsic and extrinsic contributions to failure resistance, with intrinsic resistance representing the inherent mechanical and environmental material response to cyclic loading at the crack tip. The incidence of crack closure has been widely recognised as a major factor extrinsic factor affecting fatigue crack growth rates (via the shielding of cyclic load conditions in the crack-tip region), for many engineering alloys (include Al-alloys). Significant origins of crack closure may be identified as the essentially mechanical process of plasticity-induced crack closure (PICC), and the more microstructurally dependent roughness-induced crack closure (RICC). However, significant problems exist in both the experimental determination and micromechanical modelling of closure behaviour.

In the present work, several advanced variants of the established aerospace alloy 2024-T351 (with different dispersoid contents and degrees of recrystallisation) are studied for micromechanistic influences on fatigue crack growth behaviour under constant amplitude (CA) and variable amplitude (VA) loading conditions. Degrees of recrystallisation level have been seen to have limited influence on CA crack growth resistance and closure levels in the advanced 2024 alloy variants. Dispersoids are found to be a key factor controlling fracture surface faceting levels and hence, closure processes in these materials. Physical interpretation of RICC effects in terms of residual shear displacements at 3D crack wake asperities has been compared to a variety of experimental results. 3D surface profilometry techniques are applied to obtain crack deflection parameters (deflection angles and length-scales) from fatigue fracture surfaces. For CA loading conditions, where the model is most readily applied, predictions of plane strain crack closure levels from real fracture surface features has been shown to be in reasonable functional accord with experimental data.

Crack behaviour has been further investigated via synchrotron X-ray tomography at an enhanced resolution level of 0.7μm per isotropic voxel. Microstructural displacement gauging and ray casting analysis technique have been successfully developed as novel methods to measure 2D and 3D crack opening displacements. A liquid Gallium (Ga) grain boundary wetting technique has been investigated in conjunction with the microtomography to visualise and analyse simultaneously the correlation between the 3D grain structure and fatigue crack paths. Subsequent electron backscattering diffraction (EBSD) assessment of grain orientation in the computed tomography samples provides detailed crystallographic information on crack propagation mechanisms, where large crack deflections were found to be generated mostly by {111} and {100} plane oriented fracture.

In terms of VA loading (simple peak load transients), closure measurements close to the crack tip appear to describe growth rate transients well. Reasonable correlation between transient crack growth and measured closure variations has been observed when used in conjunction with '*intrinsic*' CA crack growth data. Fractographic observations and previous FE modelling results suggest that PICC may be the predominant closure mechanism over RICC in controlling post-overload retardation effects in these materials at intermediate to high baseline stress intensity loading, consistent with a limited effect of microstructure on transient crack growth.

PREFACE

This thesis is an account of work which has been carried out by the author in the Materials Research Group, School of Engineering Sciences, University of Southampton (UK), under the supervision of Dr. Ian Sinclair in the periods of October 2001 – October 2004.

No part of this thesis has been submitted for a degree at any other university. The research work described in this thesis is original, with work of others has been drawn upon freely with due acknowledgements and references in the text.

ACKNOWLEDGEMENTS

The first person I would like to give my special thanks is Dr. Ian Sinclair, who has given me a golden opportunity in doing this PhD under his active, dedicated and tirelessness supervision. This precious opportunity has significantly changed my life and I feel I am greatly indebted to him. It is from him I have learnt the right attitude of doing research. His priceless encouragement and guidance has hugely improved my writing and presentation skills which I would appreciate in my whole life. I will never forget the time he spent with me in preparing my papers/reports/presentations with full dedication. Personally, I think he is the best supervisor I have ever met, and also one of the greatest people as a friend with kindness and caring. I honestly think that I would not have done this PhD/thesis without him. I would also like to thank him and his wife, Dr. Philippa Reed, for their invaluable advice and support in the searching of my future career, also for their warm hospitality as being invited to their house.

Many thanks to Pechiney CRV (Centre de Recherches de Voreppe, France) for their full financial sponsorship throughout my PhD, without their financial support it is impossible to carry out this project. My greatest gratitude to the following people in Pechiney CRV: Dr. Jean-Christophe Ehrstöm, Dr. Julien Boselli, Dr. Bernard Bès, and Dr. Bruno Dubost for their stimulating questions and friendly discussions at meetings. My special thanks to Dr. Ehrstöm for his continuous interest, patient and support on my work. Dr. Richard Collins from Airbus (Filton, UK) is also deeply acknowledged with his active involvement in this project with invaluable and informative discussions at meetings.

I would like to thank people from INSA-Lyon (Lyon, France): Dr. Eric Maire, Dr. Walfgang Ludwig, and especially to Prof. Jean-Yves Buffière who has tirelessly offering help and support for the experiments at the ESRF (Grenoble, France). Their priceless expertise and knowledge have been second to none. Technical supports from Beamline ID19 at ESRF are also greatly acknowledged. It is my great pleasure to work with them in such a state-of-the-art facility.

My special thanks to Prof. Hiroyuki Toda, who was a visiting professor in our group from the Toyohashi University of Technology (Japan). He is such a nice person with great personality. I have learnt a lot from him about the right attitude of doing research. It is my great honour to have his involvement in this PhD project. On the other hand, I would like to thank Dr. Harvinder Singh Ubhi (Qinetiq, UK) and Dr. Shuncai Wang, who is from our group, for providing me with their invaluable expertise and help in the electron microscopy analysis work.

I would not have done all my experimental work without the help from technicians: Dave Beckett, Eric Bonner and Robert Barnes, my deepest gratitude to them. Gwyneth Skiller, our group secretary is also gratefully acknowledged as she is always the most cheerful, helpful and friendly person around.

My greatest and deepest gratitude to my fiancée, Candice Ka Wai Lau, who has been understanding and supportive throughout my PhD with her warmest love. Finally, I would like to thank my father, mother, sister and also my brother-in-law, without their understanding, love and support far away from home, I would not be what I am today.

NOMENCLATURE

2D	Two-Dimensional
3D	Three-Dimensional
3DAP	Three-Dimensional Atom Probe Methods
APFIM	Atom Probe Field Ion Microscopy
ASTM	American Society of Testing and Materials
BSE	Back-Scattered Electron
CA	Constant Amplitude
CCD	Charge-Coupled Device
CCT	Center-Cracked Tension
COD	Crack Opening Displacement
CPU	Centre Processing Unit
CT	Compact Tension
CTOD	Crack-Tip Opening Displacement
EBSD	Electron Back-Scattered Diffraction
EDS	Energy Dispersive Spectroscopy
EPMA	Electron Probe Microanalysis
ESRF	European Synchrotron Radiation Facility
FAST	Fatigue crack growth Analysis of Structures
FCGR	Fatigue Crack Growth Rate
FE	Finite Element
FEG-SEM	Field Emission Gun Scanning Electron Microscope
FRELON	Fast-Readout, Low-Noise
GP	Guinier-Preston
GPB	Guinier-Preston-Bagaryatsky
HREM	High Resolution Electron Miscroscopy
IADS	International Alloy Designation System
LEFM	Linear Elastic Fracture Mechanics
NDT	Non-Destructive Testing
ReX	Recrystallisation
RICC	Roughness-Induced Crack Closure
SEM	Scanning Electron Microscope

SEN	Single Edge Notched
TEM	Transmission Electron Microscope
OL	Overload
PD	Potential Drop
PFZ	Precipitates Free Zone
PICC	Plasticity-Induced Crack Closure
VA	Variable Amplitude
a	Half crack length
a^*	Small crack deflection section
a_d	Crack growth delay distance
a_t	Typical transverse dimension of the features in tomography sample
b	Burgers vector
B	Bending magnetic field
d_p	Particles diameter
d	Tomography sample-detector spacing
da/dN	Crack growth rate
$(da/dN)_b$	Baseline crack growth rate
$(da/dN)_t$	Transient crack growth rate
$(da/dN)_{CA}$	Constant amplitude crack growth rate
$(da/dN)_{VA}$	Variable amplitude crack growth rate
C	Scaling constant in Paris Law
$CTSD$	Crack Tip Shear Displacement
$CTSD_{max}$	Mode II crack tip shear displacement at maximum load
$CTSD_{IIImax}$	Mode III crack tip shear displacement at maximum load
$CTSD_{res}$	Mode II residual crack tip shear displacement
$CTSD_{IIIres}$	Mode III residual crack tip shear displacement
D	Distance over which the tilted crack advances along the kink crack
D_i	Mean diameter of intermetallic
D_f	Defocusing distance
el	Elongation
E	Young's modulus
f	Volume fraction of particles
G	Shear modulus

h	Effective displacement of a asperity tip that is left when the crack changes direction
h_{II}	Effective mode II displacement of a asperity tip that is left when the crack changes direction
h_{III}	Effective mode III displacement of a asperity tip that is left when the crack changes direction
k	Fitting parameter in Wheeler model
k_1	Local mode I stress intensity factor at the tip of a deflected crack
k_2	Local mode II stress intensity factor at the tip of a deflected crack
k_3	Local mode III stress intensity factor at the tip of a deflected crack
$k_{I(deflected)}$	Local mode I stress intensity factor at the tip of a deflected crack
K	Stress intensity factor
K_I	Mode I stress intensity factor
K_{II}	Mode II stress intensity factor
K_{III}	Mode III stress intensity factor
K_c	Fracture toughness of materials
K_{cl}	Crack closure stress intensity factor
K_{Ic}	Fracture toughness of materials in plane strain condition
$K_{I(undeflected)}$	Small undeflected mode I edge crack (of a length a^*) of mode I stress intensity
K_{min}	Minimum stress intensity factor in a fatigue cycle
K_{max}	Maximum stress intensity factor in a fatigue cycle
$K_{II\max}$	Maximum mode II stress intensity factor
$K_{III\max}$	Maximum mode III stress intensity factor
K_{op}	Crack opening stress intensity factor
K_{OL}	Maximum stress intensity during the overload cycle
K_{red}	Stress intensity factor used in the Willenborg model to reduce the applied crack tip stress intensity
l	X-ray source-sample distance
L	Crack deflection length
M	Scaling constant in Paris Law
n	Strain hardening coefficient
N^*_D	Number of cycles of retarded growth in a single-peak overload test
P	Applied load

r_c	Cyclic plastic zone size
r_F	Fresnel zone radius
r_p	plastic zone size
r_{pOL}	Monotonic plane strain plastic zone size
$r_{y(c)}$	Current plastic zone size
$r_{y(o)}$	Plastic zone size created by overload
R	Load ratio
S	Distance over which the plane of the growing crack is normal to the far-field tensile axis
t	Thresholding tolerance values
T_m	Melting temperature
u_y	Elastic displacement of the crack flank in the y-direction
U	Elber's effective 'shielding' parameter
V_f	Intermetallic volume fraction
W	Width of the tomography sample
Y	Geometrical compliance factor of the specimen and crack
Z	Atomic number of the material
Δa	Crack length increment
$\Delta CTSD$	Change in Crack Tip Shear Displacement
ΔK	Stress intensity factor range
ΔK_b	Baseline stress intensity factor range
ΔK_{app}	Applied stress intensity factor range
ΔK_{eff}	Effective stress intensity factor range
ΔK_{rms}	Root-mean-square value of the stress intensity factor range
ΔK_{th}	Threshold stress intensity factor range
ΔP	Applied loading range
$\Delta\sigma_{eff}$	Effective stress range
$\Delta\sigma_p$	Contribution of the particles to the yield strength of the alloy
α	Constraint factor in Newman's model
β	Scaling factor on the crack tip shear displacement
δ	Elastic crack opening displacements
δ_{cl}	Reduced crack opening displacement due to crack flank shear
δ_{min}	Minimum crack tip opening displacement

δ_{max}	Maximum crack tip opening displacement
δ_R	Plastic stretch to be appended to crack faces
δ_t	Crack tip opening displacement
ε_z	Strain in z direction
ϕ	Mode III crack deflection angle (twist)
λ	Scaling factor of plastic zone size in the RICC model
λ_c	Critical wavelength
λ_L	Mean linear intercept grain dimensions in L direction
λ_S	Mean linear intercept grain dimensions in S direction
λ_T	Mean linear intercept grain dimensions in T direction
μ	Linear attenuation coefficient which is related to the photon energy E
ρ	Material density
σ	Applied stress
σ_{op}	Crack opening stress
σ_{min}	Minimum stress in a fatigue cycle
σ_{max}	Maximum stress in a fatigue cycle
σ_{max2}	Maximum stress value of a second load block
σ_{UTS}	Ultimate tensile stress
σ_y, σ_{YS}, σ_Y	Yield stress
σ_z	Through thickness stress
σ_{xx}	Normal stress in x direction
σ_{yy}	Normal stress in y direction
σ_{zz}	Normal stress in z direction
θ	Mode I crack deflection angle (kink)
ν	Poisson ratio
ν_{gb}	Grain boundary interface tensions
ν_{sl}	Solid-liquid interface tensions
χ	Ratio of the mode II to the mode I displacement during unloading

1. INTRODUCTION

Accurate prediction of fatigue crack growth rates under variable amplitude load histories is clearly important in airframe lifing. Years of research have shown that, even during simple single peak load transients, many physical phenomena may influence crack growth, e.g. plasticity induced crack closure (PICC), roughness induced crack closure (RICC), residual stresses, crack tip blunting and monotonic failure modes [1-3]. Whilst many of these aspects are at least semi-quantitatively understood, the modelling approaches that have been developed to date to account for variable amplitude loading are of limited accuracy, offering limited precision over basic empirical methods [4]. Two key issues may be identified in this being the case: (i) the use of simplified, single mechanism models of variable amplitude effects, and (ii) the marked uncertainty that exists in interpreting real crack closure results in order to validate and/or calibrate any given modelling approach. To address these issues, recent collaborative research between Southampton, Airbus (Filton, UK) and Pechiney CRV (Voreppe, France), has focused on extrinsic and intrinsic crack growth processes during simple load transients in 2024-type aluminium alloys, with a view to providing an improved physical basis for alloy design and the development of accurate lifing methods. This work was progressed in both experimental and modelling aspects. Key results to date include significantly improved methods of crack closure detection, the clear identification of the critical role of closure processes, and novel finite element models of the combined effects of plasticity and roughness induced closure under constant and variable amplitude loading [5, 6].

Whilst significant progress has been made, further work is required to clarify & quantify microstructural contributions to crack shielding processes. Furthermore, with advances in sophisticated experimental methods, such as neutron and synchrotron radiation analysis, it is hoped that a more detailed understanding of closure mechanisms may be obtained over more conventional compliance-based closure analyses [7-11].

This project particularly addresses the materials assessment and potential optimisation of 2024-type aluminium alloys under constant amplitude (CA) and variable amplitude (VA) loading for fatigue resistance. The aims of the project can be summarised as following:

- To elucidate microstructural influences on closure mechanisms
- To improve the micro-mechanistic understanding of crack closure processes via the use of advanced three-dimensional (3D) imaging methods.

- Develop and apply appropriate physical models.

The key analysis techniques used in the present project include:

- Conventional constant amplitude and variable amplitude fatigue crack growth testing.
- Metallographic, fractographic and quantitative analysis of crack profiles/surfaces, carried out by a combination of 3D profilometry and electron back-scattered diffraction (EBSD) techniques.
- High resolution 3D imaging of crack opening and closing processes via synchrotron computed tomography at the European Synchrotron Radiation Facility (ESRF) (Grenoble, France).
- Application and enhancement of previous analytical modelling approaches to combine plasticity and roughness induced closure [5, 6, 12].

This thesis has been divided into 7 chapters. Chapter 2 presents a detailed literature review on fatigue behaviour of materials under constant amplitude and variable amplitude loading, and the principles of synchrotron X-ray tomography. Experimental techniques, and the materials characterisation of several 2024-type aluminium alloys are described in Chapter 3. Chapter 4 highlights the study of fatigue crack growth in 2024-type aluminium alloys under CA loading, considering crack closure measurement and assessment of the microstructural origin of fracture surface roughness and crack deflection. A novel analytical RICC model to predict crack closure level based on given fracture surface dimensions is also described and applied in this chapter. Chapter 5 describes specialised X-ray tomography procedures together with results from 3D crack closure assessment and analysis of the microstructural origin of crack deflection via 3D grain boundary and texture observation. Chapter 6 presents a study of fatigue crack growth behaviour under VA loading, where the results in this Chapter are linked with a parallel FE study [13]. Finally, Chapter 7 highlights the main achievement of this project and addresses areas where further work is needed.

References

[1] W. Elber, *Engineering Fracture Mechanics*, 1970. **2**: p. 37-45.

[2] W. Elber, *Damage Tolerance in Aircraft Structures, ASTM STP 486*, 1971, Philadelphia: ASTM, p. 230-242.

[3] S. Suresh and R.O. Ritchie, *International Metals Review*, 1984. **29**: p. 445-476.

[4] R.A. Collins, *Private communication, Fatigue Methods Group - Airbus (UK)*, 1998.

[5] M.R. Parry, *Finite Element and Analytical Modelling of Roughness Induced Fatigue Crack Closure*. PhD Thesis, University of Southampton. 2001.

[6] Y. Xu, *Closure assessment and overload transient behaviour in damage tolerant airframe materials*. Ph.D thesis, University of Southampton. 2001.

[7] J.-Y. Buffiere, E. Maire, P. Cloetens, G. Lormand, and R. Fougeres, *Acta Metallurgica*, 1999. **47**: p. 1613-1625.

[8] A. Guvenilir, T.M. Breunig, J.H. Kinney, and S.R. Stock, *Acta Metallurgica*, 1997. **45**: p. 1977-1987.

[9] A. Guvenilir, T.M. Breunig, J.H. Kinney, and S.R. Stock, *Philosophy Transaction of The Royal Society Lond.*, 1999. **A 357**: p. 2755-2775.

[10] A. Guvenilir and S.R. Stock, *Fatigue and Fracture Engineering Materials and Structures*, 1998. **21**: p. 439-450.

[11] P. Cloetens, M. Pateyron-Salome, J.-Y. Buffiere, G. Peix, J. Baruchel, F. Peyrin, and M. Schlenker, *Journal of Applied Physics*, 1997. **81**: p. 5878-5886.

[12] N. Kamp, M.R. Parry, K.D. Singh, and I. Sinclair, *Acta Materialia*, 2004. **52**(2): p. 343-353.

[13] K.D. Singh, *Modelling of combined roughness and plasticity induced closure effects in high strength Al-alloys*. PhD Thesis, University of Southampton. 2004.

2. LITERATURE REVIEW

This chapter consists of two main sections. These include a detailed literature review on fatigue crack growth under constant amplitude and variable amplitude loading, and also basics principle of synchrotron radiation X-ray tomography. In the interest of brevity general materials science (particularly in the Al-Cu-Mg-Mn alloy, AA2024) and fracture mechanics background to this work are detailed separately in Appendix A.

2.1 Fatigue

Fatigue of materials particularly refers to cracking or failure due to repeated load cycling, i.e. under fluctuating stresses or strains [1]. Under these circumstances it is possible that failure can occur at stress levels much lower than the tensile yield or fracture stress for a static load. Even if nominal stresses are well below the elastic limit, it must be noted that locally stresses may be above yield due to stress concentrations at second phase inclusions or other microstructural and/or micro-mechanical defects. As such, irreversible plastic phenomena may occur, giving rise to fatigue damage. Over many years, various approaches have been developed to quantify the fatigue behaviour of materials.

2.1.1 Fatigue Crack Initiation

There have been many mechanisms proposed over the years to describe the initiation of fatigue cracks. Woods originally proposed that under the action of cyclic loads, cracks can be initiated as a result of cyclic plastic deformation [2, 3]. It was suggested that repeated cyclic straining leads to different amounts of net slip on different glide planes, ultimately generating physical cracks. Forsyth and Stubbington [4] later identified 'intrusions' and 'extrusions' at slip bands formed on fatigued surfaces, serving as micro-notches for subsequent crack propagation. Hunche & Neumann [5] and Ma & Laird [6] have shown experimental evidence of crack initiation at the interface between persistent slip bands and surrounding material, which is a plane of discontinuity involving abrupt gradients in density and distribution of dislocations.

In commercial structural materials, the principal sites of fatigue crack nucleation include voids, inclusions, dents, scratches, and macroscopic stress concentrations, as

well as regions of microstructural and chemical non-uniformity. Surface grains are the most likely places for crack initiation for metals and alloys of high purity; the formation of fatigue cracks is feasible at both near-surface and interior locations in commercial alloys depending on the defect population and spatial distribution. Fatigue life and maximum fatigue strength of commercial alloys can be improved via reduced defects level such as inclusions and pores. The mechanisms of fatigue crack initiation at defects depend upon factors such as slip characteristics of the matrix, the relative strength values of the matrix and the defect, the strength of the matrix-inclusion interface and the relative susceptibility of the matrix and the inclusion to corrosion in the fatigue environment [1]. In aluminium alloys, coarse intermetallic particles such as *S*-phase (Al_2CuMg) and β-phase (Al_7Cu_2Fe), typically 1-10μm in diameter, provide common sites for fatigue crack nucleation. The type of cracking is however dependant on the microstructure and testing conditions. Grosskreutz and Shaw [7] noticed the debonding of the particle-matrix interface after cyclic damage within the matrix over a large number of fatigue cycles in a 2024-T4 aluminium alloy. Kung and Fine [8] showed the precipitous increase in particle cracking probability with an increase in the size of the intermetallic particles in 2x24 aluminium alloys.

2.1.2 Fatigue Crack Growth under Constant Amplitude (CA) Loading

The rate of crack growth under fatigue loading is commonly expressed in terms of the crack length increment per cycle, *da/dN*. Paris, Gomez & Anderson and Paris & Erdogan [9, 10] first applied the ideas of LEFM (Linear Elastic Fracture Mechanics) (see Appendix A) to fatigue crack growth, with characterisation of the rate of crack growth rates then being based on the stress intensity factor range, ΔK,

$$\Delta K = K_{\max} - K_{\min} \tag{2.1}$$

where K_{max} and K_{min} are the maximum and minimum values respectively of the stress intensity factor during the fatigue load cycle,

$$K_{\max} = Y\sigma_{\max}\sqrt{\pi a} \tag{2.2}$$

$$K_{\min} = Y\sigma_{\min}\sqrt{\pi a} \tag{2.3}$$

where σ_{max} and σ_{min} are the maximum and minimum values respectively of the stress cycle, a is the crack length and Y is the geometrical compliance factor. Paris *et al.* suggested that the rate of crack growth (da/dN) depends on ΔK by the power law relationship:

$$\frac{da}{dN} = C(\Delta K)^m \tag{2.4}$$

where C and m are scaling constants, influenced by variables such as material microstructure, environment and temperature (the latter two of which may promote a strong effect of cyclic load frequency and waveform), and load ratio, R, defined as,

$$R = \frac{\sigma_{\min}}{\sigma_{\max}} = \frac{K_{\min}}{K_{\max}} \tag{2.5}$$

Thus a plot of log (da/dN) vs log (ΔK) should be a straight line with a slope of m. However, the real relationships between log (da/dN) and log (ΔK) for common engineering materials commonly exhibit an approximately sigmoidal form, as depicted in Figure 2.1 [1].

2.1.2.1 Microscopic Mode of Fatigue Crack Growth

The microscopic mode of fatigue crack growth in metallic materials is known to be strongly affected by the slip characteristics of the material, characteristic microstructural dimensions, applied stress levels and the extent of near-tip plasticity. In general two stages of fatigue crack growth are widely identified in the literature [1], as illustrated in Figure 2.2 and 2.3.

During 'Stage I' crack growth [11] , cracks may exhibit serrated and faceted profiles. This is generally identified with low stress intensities, with the plastic zone size surrounding the crack tip being confined to within a few grain diameters; deformation then predominantly occurring by single shear in the direction of the primary slip system as shown in Figure 2.2.

At higher stress intensity values, when the plastic zone at the crack tip extends over many grain diameters, the attendant crack growth process tends to involve

simultaneous or alternating flow along two or more slip systems. Forsyth [11] has termed this duplex slip mechanism 'Stage II' crack growth. This results in a planar (Mode I) crack path which is normal to the far-field tensile axis, as illustrated in Figure 2.3.

Stage II crack growth may then involve the formation of fatigue 'striations'. Individual striations on the surfaces of fracture surfaces may be produced as the crack advances over one cycle, i.e. the striation spacing corresponds to the *da/dN* value. Following from this, Laird [12] has proposed a conceptual model of crack growth, linking the striation effect to the plastic blunting of the crack tip during each cycle, although circumstances where the presence of striation-type features on fatigue surfaces that are not explicitly linked to cycle-by-cycle crack advance are well known [12].

2.1.2.2 Regimes of Fatigue Crack Growth

For most engineering alloys, a plot of log *da/dN* against log ΔK exhibits a sigmoidal variation, as shown schematically in Figure 2.1. In this plot, three primary regimes of fatigue crack growth are noted: A, B and C.

- *Regime A*

In regime A, the average growth increment per cycle appears to drop dramatically with ΔK, and is commonly associated with the existence of a threshold stress intensity factor range ΔK_{th}. As $\Delta K \rightarrow \Delta K_{th}$, the rate of crack growth is thought to tend to zero. A common operational definition for ΔK_{th} is the point at which the rate of crack growth falls below 10^{-8} mm/cycle [1]. An important point is that these extremely slow crack growth rates represent an average crack advance of less than one atomic spacing per cycle where growth is then of necessity discontinuous. Crack growth in this regime may be highly sensitive to environmental effects due to the low growth rate [13, 14]. Stage I crack growth is commonly seen to the presence of a small plastic zone size effect. Further detail of microstructural characteristics in this near-threshold regime are discussed in the following section.

- *Regime B (Paris Regime)*

Regime B, known as the Paris regime, exhibits a linear variation of log (da/dN) with log (ΔK), i.e. as Equation (2.4). In the Paris regime, the rate of crack growth is commonly identified as weakly sensitive to microstructure and the load ratio R [1]. The key parameter governing crack growth is then ΔK. The microscopic mechanisms of fatigue crack growth are often identified with duplex slip and crack blunting and re-sharpening as outlined by the Laird model above.

- *Regime C*

Regime C pertains to high ΔK values where crack growth rates increase rapidly toward catastrophic failure when the K_{max} for the fatigue cycle approaches the fracture toughness of the material, K_c (or K_{Ic} in plane strain). The crack growth in this regime is seen to be sensitive to microstructure, load ratio, R, and stress state (i.e. plane stress and plane strain loading) [15]. However, crack propagation rates are too rapid to be affected strongly by the test environment. For a higher R ratio, catastrophic fatigue failure occurs at lower ΔK values. At such high ΔK levels approaching fast fracture, static fracture modes, such as cleavage and intergranular separation occur in addition to pure cyclic growth behaviour [16].

Regime	A	B	C
Terminology	Slow-growth rate (near-threshold)	Mid-growth rate (Paris regime)	High-growth rate
Microscopic failure mode	Stage I, single shear	Stage II, (striations) duplex slip	Additional static modes
Fracture surface features	Faceted or serrated	Planar with ripples	Additional cleavage or microvoid coalescence
Crack closure levels	High	Low	—
Microstructural effects	Large	Small	Large
Load ratio effects	Large	Small	Large
Environmental effects	Large	*	Small
Stress state effects	—	Large	Large
Near-tip plasticity†	$r_c \leq d_g$	$r_c \geq d_g$	$r_c \gg d_g$

*large influence on crack growth for certain combinations of environment, load ratio and frequency.

† r_c and d_g refer to the cyclic plastic zone size and the grain size, respectively.

Table 2.1 Characteristics of the three regimes of fatigue crack growth

Table 2.1 Summarises the common salient characteristics of crack advance in the three regimes of fatigue fracture, as has been identified in many papers over the last 20-30 years [1]. Details of this table are considered in the following sections.

From the literature, it has been consistently reported that there is a sequence of growth rate transition points in aluminium alloy crack growth curves for laboratory air conditions [17, 18]. Figure 2.4 shows typical constant amplitude fatigue crack growth rates for 2024-T351 aluminium alloy plate (at $R = 0.1$) where the three main transition points are respectively labelled as T_1, T_2 and T_3. Wanhill and Yoder [17, 18] have then suggested that there is a correlation between these various changes in slope along the crack growth curve and the crack tip plane stain cyclic plastic zone size (r_c). It was suggested that the transition points occur when r_c becomes equal to certain characteristic microstructural dimensions: T_1 corresponding to the mean planar distance between dispersoids, T_2 corresponding to subgrain and dislocation cell size, and T_3 relates to overall grain dimensions. In terms of the threshold stress intensity factor range (ΔK_{th}) of aluminium alloys, Wanhill [18] reported that the 2024-T351 alloy tested in laboratory air at $R = 0.1$ has a ΔK_{th} of ~ 2.9 MPa$\sqrt{m}$, while work from Venkateshwara Rao and Ritchie [19] showed a ΔK_{th} of ~ 3.6 MPa$\sqrt{m}$ for 2024-T351 test under the same conditions.

- *Additional mechanical and micromechanical considerations*

The existence of a fatigue crack growth threshold was first suggested by McClintock [20]. He used the criterion that fatigue crack growth occurs when a critical value of local strain or accumulated damage over certain characteristic distance ahead of the crack tip reaches a critical value. He argued that fatigue cracks may cease to advance when the extent of near-tip plasticity becomes comparable to some characteristic microstructural size scale. Frost [21] then represented experimental evidence to support the existence of a fatigue threshold. This was then followed by the work of Schmidt and Paris [22] showing that the threshold for the non-propagation of long fatigue cracks can be associated with a critical stress intensity factor range, ΔK_{th}. Conventionally, the *da/dN* curve and determinations of ΔK_{th} of a materials are measured experimentally via load-shedding techniques [23]. In this approach, the stress intensity range, ΔK is successively reduced, with cyclic frequency and R

typically being held constant. At each stage of constant ΔK, the fatigue crack is allowed to propagate distances of the order of 4 or more times the maximum current plastic zone size before the ΔK is reduced by an amount of the order of 5 – 10%. This process is repeated until the threshold, ΔK_{th}, for no crack growth or crack growth rate of 10^{-8}mm/cycle is reached. The choice of a particular gradient of ΔK is somewhat crucial, as if the ΔK drops too rapidly, the growth of the current crack tip through the greatest prior plastic zone induced at the previous higher load level may cause artificial retardation or even complete arrest of fatigue crack growth. However, if the ΔK values are reduced too slowly, the development of crack closure (see section 2.1.3) in some materials may once again result in premature closure of the crack faces and will lead to a high value of ΔK_{th} (e.g. due to fracture surface oxidation). Due to such uncertainties and errors in the measurement of ΔK_{th}, alternative methods have been suggested: Christman and Suresh [24] for example proposed a technique whereby ΔK_{th} is determined by load 'shedding-up' on cracks initiated under fully compressive loads fatigue (pre-cracked sample are cycled at successively increasing stress intensity levels until crack growth occurs). On the other hand, Herman *et al.* [25] introduced another method to measure an 'intrinsic' fatigue threshold: in this method, the R ratio is caused to rise in the load shedding process by imposing that K_{max} is held fixed whilst ΔK is progressively reduced. Since K_{max} is fixed, the maximum plastic zone at the crack tip remains unaltered; hence load reduction is not expected to cause retardation effects typical of variable amplitude fatigue. Furthermore, closure of the crack faces is virtually eliminated for the high load ratio levels at which ΔK_{th} is finally measured.

In the near-threshold regime (Regime A), fatigue crack growth rates and threshold value are strongly affected by microstructure and the load ratio, R. The work from Liaw *et al.* [26] indicate that most alloys show an increase of ΔK_{th} with decreasing R. The transition from the near-threshold regime to the intermediate stage (Paris regime) of fatigue crack growth is considered by many to be dependant on the microstructural size scale [17, 18], of which grain size and slip characteristics are particularly critical. The transition from near-threshold to Paris regime growth may occur when the size of the cyclic plastic zone, r_c becomes comparable to the characteristic microstructural dimension: indeed according to Wanhill and Yoder [17, 18], transitions in crack

growth may additionally occur when the r_c dimension approaches those of the mean planar distance between dispersoids, the subgrain size, the dislocation cell size, and the overall grain dimensions. They identify the mean planar distance between each type of feature with a transition points in the *da/dN* curve. However, even when the size of the cyclic plastic zone at the tip of a near-threshold crack is the same for two different microstructures (with the same grain size), different fatigue thresholds may result because of the differences in slip characteristics. The influence of slip behaviour on thresholds is best illustrated with the examples of a precipitation-hardened alloy system. Consider the case of under-aged and over-aged microstructures of an aluminium alloy (where two ageing conditions are designed to give the same macroscopic yield strength). In the under-aged alloy, the matrix consists of shearable and coherent precipitates. These strengthening particles are amenable to be shearable by slip bands ahead of a fatigue crack. Hornbogen and Zum Gahr [27] have suggested that in such heterogeneously deforming microstructures, dislocation glide occurs within grains predominantly along a single slip system. The single shear failure (equivalent to Stage I crack growth mode) promotes a highly serrated and tortuous crack path in the under-aged condition, with the wavelength of crack path tortuosity being of the order of the grain size. On the other hand, in the over-aged alloys, the incoherent precipitates are by-passed rather than sheared by dislocations, and a flat transgranular fracture profile results from the corresponding homogeneous deformation and Stage II-type crack growth.

Environmental effects have been well recognised as a significant factor that controls fatigue crack growth rate. The work of Piascik and Gangloff [14] shows the deleterious effects of hydrogenous environments on steady state, intrinsic fatigue crack propagation rates in Al-Li alloys for example. Their results indicated growth rates are equally unaffected by vacuum, purified helium, and oxygen environment, but are particularly accelerated in the low ΔK region in hydrogenous environment (such as pure water vapour and moist air). Increased crack growth rates are attributed to hydrogen embrittlement mechanisms as suggested in the literature [28-31], where atomic hydrogen produced by water vapour interaction with fresh metal surfaces at the crack tip, may be transported into the plastic zone ahead of the crack tip. High frequency and low R conditions may then reduce the effect of hydrogen

embrittlement. Christodoulou and Flower [28] showed that embrittlement which promotes intergranular failure may be caused by hydrogen in solution at grain boundary precipitates in an Al-Zn alloy which can act as hydrogen trap sites where bubbles of gaseous hydrogen are evolved. Further works from Piascik and Gangloff [13, 14] showed that in an Al-Li alloy in an inert environment, fatigue cracks propagate along {111} slip planes independent of ΔK, forming a crack path that is tortuous and dominated by twist deflection. They also showed that in hydrogenous environment, {100} or {110} "cleavage" cracking is dominant at low ΔK, while intersubgranular cracking with limited regions of {111} slip band cracking is observed at higher ΔK. {100} facets are small and nearly normal to the applied load compared to out-of-crack-plane {111} facets.

2.1.3 Fatigue Crack Closure

Fatigue crack closure is the general term used to describe the contact of crack surfaces in the wake of an advancing crack, which may then cause load transfer and a reduction in the cyclic 'driving force' for crack advance. This idea is generally attributed to Elber [32, 33]. Assuming that a crack could only propagate when it was fully open, Elber suggested that premature crack closure decreased the fatigue crack growth rate by reducing the effective stress intensity range. This concept is illustrated in Figure 2.5. Identifying the crack opening stress, σ_{op} at the point in the applied load cycle where crack face contact occurs, the effective stress range, $\Delta\sigma_{eff}$, and the corresponding effective stress intensity factor range, ΔK_{eff}, which are responsible for crack growth may be given by,

$$\Delta\sigma_{eff} = \sigma_{\max} - \sigma_{op} \tag{2.6}$$

$$\Delta K_{eff} = K_{\max} - K_{op}, if\ K_{\min} < K_{op} \tag{2.7}$$

$$= K_{\max} - K_{\min}, if\ K_{\min} > K_{op}$$

Elber further introduced an effective 'shielding' parameter, U,

$$U = \frac{\Delta K_{eff}}{\Delta K_{app}} = \frac{K_{\max} - K_{op}}{K_{\max} - K_{\min}} \tag{2.8}$$

Hence, the corresponding characterisation of fatigue crack growth rates based on LEFM becomes,

$$\frac{da}{dN} = C\left(\Delta K_{eff}\right)^m = C\left(U\Delta K_{app}\right)^m \tag{2.9}$$

where K_{app} is the remotely applied stress intensity factor range.

Following the work of Elber, many researchers have suggested that crack closure is a key factor in fatigue crack propagation. Suresh and Ritchie [32] have in particular identified five key of mechanisms for fatigue crack closure, they are (i) oxide-induced closure, (ii) closure induced by a viscous fluid, (iii) transformation-induced closure, (iv) plasticity-induced crack closure (PICC), and (v) roughness-induced crack closure (RICC). Among the mechanisms, PICC and RICC have been identified as the most significant influence on crack growth rates in engineering aluminium alloys in aerospace applications in non-aggressive environments [34]. Hence, PICC and RICC are the main concerns in the current study and they are discussed in more detail in the following section. Schematic illustrations PICC and RICC mechanisms are shown in Figure 2.6 and Figure 2.7.

Although different types of crack closure have been identified; there are some basic, common characteristics:

i. Generally, crack closure is more dominant at relatively low ΔK levels, and at lower R ratios, due to the smaller minimum crack opening displacements of the fatigue cycle.
ii. There is a characteristic size scale with each closure process, such as the height of the fracture surface asperities for RICC and the size of the residual plastic crack wake for PICC. When the size of this characteristic 'closure dimension' becomes comparable to the crack opening displacement, premature crack face contact may then exert a marked effect on the rate of fatigue crack growth.

iii. The extent of crack closure generally increases with an increase in crack length up to a saturation crack length, beyond which closure is normally crack length independent.

iv. Closure is produced by mechanisms which are operative both at the tip of the fatigue crack as well as in the wake of the fatigue crack tip, hence the fundamental fracture mechanics concept of similitude does not strictly apply.

Further to the work from Elber, crack closure understanding, as mentioned above, has been developed over the past twenty years to explain a wide variety of crack growth effects, such as short crack behaviour and overload effects. However, there are still significant controversies among researchers, where some deny a major influence of closure. For example, works from Vasudeven and co-workers [35] in recent years have suggested that the magnitude of closure contributions to fatigue are small or negligible. They suggest that PICC effects are non-existent and RICC effects are much smaller than those normally estimated from specimen compliance. An alternative, non-ΔK_{eff} based rationalisation of various fatigue phenomena is then proposed; however, it must be noted that the major body of experimental and theoretical evidence in the literature supports the action of crack closure (e.g. [36]).

2.1.3.1 Plasticity-Induced Crack Closure (PICC)

When a crack in a ductile metallic material (such as aluminium) is subjected to a far-field tensile load, material at the crack tip will undergo a tensile plastic deformation. During unloading, a degree of reverse plastic deformation will occur, however a residual tensile plastic deformation of the crack tip material will exist, i.e. reversed deformation is never complete. When the crack propagates, the previously plastically deformed material will be transferred into the crack wake. Constraint of the surrounding elastic material result in premature contact between crack faces on unloading. This phenomenon was first postulated by Elber [32, 33] as described above and it is illustrated by the schematic diagram in Figure 2.6. PICC is commonly identified as more pronounced in the plane stress condition rather than plane strain due to increased residual tensile deformation facilitated by contraction in the through-thickness direction. This is evidenced for example in experimental results of Fleck

and Smith [37] using a "push rod" compliance gauge method to measured deflections in the middle thickness section of thick compact tension specimens of a low strength steel.

- *Analytical models of PICC*

Budiansky and Hutchinson [38] applied the Dugdale [39] and Barenblatt [40] strip yield model to this problem and showed (for plane stress conditions at least) that the residual stretch in the plastic wake may indeed cause the crack faces to close at a positive remote stress. Based on the Dugdale approach, the plastic zone size and crack tip opening displacement, respectively are,

$$r_p = \frac{\pi}{8}\left(\frac{K}{\sigma_y}\right)^2, \quad and \quad \delta_t = \frac{K^2}{\sigma_y E} \tag{2.10}$$

With the origin of a Cartesian coordinate system located at the crack tip, the variation of plastic stretch over the distance for $0 \le x \le r_p$ (ahead of the crack tip) and the opening of the crack for $x < 0$ (in the crack wake) is given by,

$$\frac{\delta}{\delta_t} = g\left(\frac{x}{r_p}\right), \quad where \quad g(\xi) = \sqrt{1-\xi} - \frac{\xi}{2}\log\left|\frac{1+\sqrt{1-\xi}}{1-\sqrt{1-\xi}}\right| \tag{2.11}$$

where δ_t is the crack tip opening displacement at K_{max}. Given the possibility of compressive yielding over the distance, $r_c = r_p/4$ during unloading from K_{max} (see Appendix A), the residual plastic stretch at $K_{min} = 0$ over the region $0 \le x \le r_p/4$ and the crack opening displacement becomes,

$$\frac{\delta}{\delta_t} = g\left(\frac{x}{r_p}\right) - \frac{1}{2}g\left(\frac{4x}{r_p}\right) \tag{2.12}$$

For steady-state fatigue crack growth, a plastic stretch of magnitude $\delta_R/2$, which leads to crack closure all along the crack length at $K_{min} = 0$ (i.e for $R = 0$), is appended to the upper and lower crack faces. Using Muchkelishvili's complex potentials formulation with appropriate boundary conditions, it can be shown that $\delta_R/\delta_t = 0.8562$ at $R = 0$, in which the residual stretch left behind the advancing crack is ~ 86% of the

crack tip opening displacement at K_{max}. Their analysis also showed that upon unloading from K_{max}, crack faces may come into contact at a location very close to the crack tip at $K_{cl}/ K_{max} = 0.483$. As the fatigue crack is reloaded, the crack faces open by a gradual peeling process whereby the boundary of the contact region shifts toward the crack front. Crack opening is seen to occur fully at $K_{op}/ K_{max} = 0.557$, i.e. K_{op} is found to be slightly higher than K_{cl}. K_{op}/ K_{max} is found to be a function of load ratio R and not absolute stress intensity levels, with the predicted R-ratio effect showing reasonable agreement with Elber's empirical formula for thin sheet Al-alloy at high ΔK levels [32],

$$\frac{K_{cl}}{K_{\max}} = 0.5 + 0.1R + 0.4R^2 \tag{2.13}$$

The Hutchinson and Budiansky model provided the first detailed treatment of the phenomenon of crack closure, and establishes a theoretical justification for the use of ΔK_{eff} to characterise the fatigue crack advance (based on calculated crack tip opening behaviour). However, the model is fundamentally limited to the plane stress condition, does not invoke any mechanisms of fatigue crack growth, and addresses only one crack closure mechanism (i.e. microstructure and environmental effects are not taken into account).

A popular bar element model for crack closure (via PICC) was developed by Newman [41]. The formulation employed by Newman differs from Budiansky and Hutchinson in that Newman adopts a fracture mechanics approach, however the physical basis is essentially identical. Newman's model further removes the semi-infinite crack idealisation in Budiansky & Hutchison's work [38]. The associated computer program was originally developed for a central through crack in a finite-width specimen subjected to remote applied stress and called "FAST" (Fatigue crack growth Analysis of STructures). Later the use of 'small-crack' concepts was incorporated into "FASTRAN" [42]. In the model, the near-tip region is broken down into a series of rigid-perfectly plastic bar elements, with the intact elements ahead of the tip capable of carrying tensile and compressive stresses, and broken elements behind the tip capable of carrying compressive stresses only. The flow stress σ_o is taken as the average between the yield stress and ultimate tensile strength to account for possible

strain hardening effects. Unlike the original Dugdale model [39] and the mathematical analyses of Budiansky and Hutchinson, the Newman model is considered applicable to both plane stress and strain conditions. However, a constraint factor, α, has to be introduced to elevate the flow stress within the plastic zone (elements ahead of the crack tip) to account for the influence of stress state on plastic zone sizes and crack surface displacements. For plane stress conditions, α is equal to unity (the flow stress is unchanged, as for the original Dugdale model) and for plane strain conditions, α is set to values of the order of 2 - 3, in which the stress in the crack tip elements must reach the nominal flow stress for plastic deformation to occur multiplied by this factor. Although the constraint factor only gives an approximation for plane strain conditions, the model is identified as being able to produce crack surface displacements and crack opening stresses comparable to those calculated from elastic-plastic finite element analyses of crack growth and closure for finite-thickness plate [43]. The model is able to predict crack opening stresses as a function of crack length and load history. Newman [41-45] has obtained good agreement between predicted fatigue lives and experimental results for notched 2024-T3 aluminium alloy sheet specimens under a variety of load sequences. However, the validity of the results is highly dependant on the constraint factor α which must be calibrated to account for the influence of finite thickness of the samples. A further down-side of the FASTRAN model is the lack of consideration of other crack closure mechanisms such as RICC.

2.1.3.2 Roughness-Induced Crack Closure (RICC)

In general, roughness-induced crack closure (RICC) is termed as the premature contact crack closure behind a crack tip which is caused by a permanent shear deformation of crack surfaces that lead to mismatch between both surfaces upon unloading, as illustrated in Figure 2.7. Walker and Beevers [46], who studied fatigue crack growth in titanium samples, were the first who identified the possibility of crack roughness could leading to premature crack closure. The RICC effect was further confirmed by works from Minakawa and McEvily [47], Blom *et al.* [48] and Ritchie and Suresh [49]. It is commonly thought to result from the influences of microstructure on crack path, and the associated formation of asperities (crack deflection) on fracture surfaces behind the crack tip. Sources of crack deflection can

for example be identified with failure along grain boundaries, slip bands, secondary phases and reinforcement particles/fibres, depending on the system of interest.

RICC in metals is commonly linked to the near-threshold crack growth regime where Stage I growth (single slip mechanism) may lead to a serrated or faceted fracture morphology. Whilst fatigue cracks propagate under pure Mode I conditions on a global scale, crack deflection due to the microstructural features can lead to local mixed mode conditions at the crack tip. As illustrated in Figure 2.7 for crack deflection from the propagation direction, deviation from the maximum tensile opening plane gives rise to local Mode II displacements. Irreversible mixed mode sliding of crack faces may then cause mismatch and premature contact between the upper and lower crack face asperities, which in turn results in enhanced crack closure [47, 50-52]. Coarse-grained planar slip materials are commonly thought to produce a higher degree of surface roughness in fatigue, corresponding to increased RICC effects especially in low R ratios condition as shown by Gray *et al.* [53]. In their results, materials with different grain sizes have the same fatigue crack growth resistance at high load ratio (R = 0.7). However differences become pronounced at low load ratio (R = 0.05), where fine grained material is seen to exhibit higher growth rates than an equivalent coarse grained material. Hornbogen and Zum Gahr [27] also show that RICC effect is more pronounced in underaged materials, where the shearability of the strengthening precipitates by dislocations may lead to a highly inhomogeneous slip distribution and crystallographic crack growth, enhancing RICC influence. Overaged materials, which have non-shearable strengthening precipitates, dislocation bypassing of precipitates favours a wavy slip deformation pattern, hence causing a smoother fracture surface and associated reduced RICC effect.

Overall, it may be noted that RICC is promoted by:

i. Low stress intensity factor levels where plastic zone dimensions at the crack tip are typically smaller than an average grain dimension (favouring Stage I crack growth)
ii. Small crack opening displacements (at low ΔK levels and low R ratios) which are of a scale comparable to the height of the fracture surface asperities

iii. Microstructures containing coarser grains and shearable/coherent precipitates which generally favour heterogeneous planar slip

iv. Periodic deflections in crack path induced by grain boundaries, second phase particles, composite reinforcements or abrupt load changes

- *Analytical models of RICC*

Suresh and Ritchie [54] proposed one of the earliest RICC models, which uses a simple geometrical model of a deflecting crack to derive an expression for the closure stress intensity factor due to RICC as,

$$\frac{K_{cl}}{K_{\max}} = \sqrt{\frac{\delta_{cl}}{\delta_T}} = \sqrt{\frac{\chi \tan\theta}{1+\chi \tan\theta}} \tag{2.14}$$

Where δ_{cl} is the reduced crack opening displacement due to crack flank shear, δ_T is the initial (unsheared) crack opening displacement, θ is the crack deflection angle and χ is the ratio of the mode II to the mode I displacement that occurs during unloading, as shown schematically in Figure 2.8.

The model was later modified [55, 56] to describe periodic crack definition as shown in Figure 2.9. θ is the kink angle, D is the distance over which the tilted crack advances along the kink, and S is the distance over which the plane of the growing crack is normal to the far-field tensile axis. The following relationship was then proposed, taking into account both crack closure and deflection shielding processes,

$$\frac{\Delta K_I}{\Delta k_{eff}} \approx \left\{\frac{D\cos^2(\theta/2)+S}{D+S}\right\}^{-1} \left\{1-\sqrt{\frac{\chi \tan\theta}{1+\chi \tan\theta}}\right\}^{-1} \tag{2.15}$$

where ΔK_I is the nominal mode I stress intensity factor range. Thus, the nominal mode I stress intensity factor range ΔK_I required to propagate a deflected crack at the same rate as a straight crack is always greater than that for an undeflected crack by a factor equal to the right-hand side of Equation (2.15). This equation incorporates the closure level at any R where fracture surface contact is geometrically possible as a result of mismatch, i.e. for $\delta_{min} < D\ sin\theta$, where δ_{min} is the crack opening displacement at $K_I = K_{min}$.

Recent works by Parry and co-workers [57-60] also show the importance of deflection angle and deflection length in the determination of RICC effect via finite element and analogous analytical fracture mechanics models. In their FE model, the analyses of periodically deflected cracks show an increasing effect of crack deflection angle on RICC levels in general agreement with the simple analytical model of Suresh and Ritchie [54-56] as discussed above. However, more importantly, they suggested that the mechanism by which closure occurs has been shown to be more strongly dependent on residual plastic strains arising from the crack propagation process, rather than conventionally suggested 'global' shear displacement due to mixed-mode behaviour at the crack tip. The shear deformations at asperity tips in the wake of a deflecting crack have been identified as the primary factor in determining RICC influence (see Figure 2.10). They noted that when a crack is loaded at a given asperity tip, a degree of shear plastic deformation occurs at the tip (Figure 2.10 (a)). On unloading, the elastic constraint of the surrounding material causes a limited degree of reverse plastic deformation. Hence a degree of residual shear exists in the material surrounding the crack tip (Figure 2.10 (b)) analogous to the residual tensile strain that is identified with mode I loading under plane stress conditions. When crack deflection occurs, the residual shear deformation is left in the crack wake and leads to premature crack face contact. In terms of asperity size (i.e. deflection length), a non-linear, plateauing influence of increasing asperity size on closure behaviour has been identified.

Based on the above FE modelling, a novel simple analytical model has been developed to describe the effective residual shear associated with a crack passing through a single representative crack turning point (i.e. asperity tip) and the subsequent fracture surface contact that will arise as the crack tip moves away from this point, see Figure 2.11. In the model, it is assumed that the tensile crack opening of a small deflected section (of length a^*) at the tip of a long nominally mode I crack may be approximated by the opening of a mode I edge crack of equivalent mode I stress intensity loading. The value of local mode I stress intensity factor at the tip of a deflected crack $k_{I(deflected)}$ is a function of the remotely applied mode I stress intensity factor K_I and the deflection angle θ, with the elastic crack opening displacements, δ, then being approximated (from standard LEFM expressions) by:

$$\delta = 2u_y = \frac{K_I\left(1-\nu^2\right)\left(3\cos\frac{\theta}{2}+\cos\frac{3\theta}{2}\right)\sqrt{a^{*2}-x^2}}{E\sqrt{\pi a^*}} \tag{2.16}$$

where u_y is the elastic displacement of the crack flank in the y-direction at a distance x from the origin, ν is the Poisson ratio and E is the elastic modulus. In the formulation of the model, it is further assumed that the residual shear deformation of the asperity tip can be approximated by the residual crack tip shear displacement ($CTSD_{res}$). As shown in Figure 2.11, the residual shear deformation of a deflected crack tip may be considered to generate an effective displacement, h, of the asperity tip that is left when the crack changes direction (i.e. to generate a new crack wake asperity peak). In first approximation, h is then equated to the residual $CTSD_{res}$ associated with the crack at the point of turning. The $CTSD_{res}$ is then given as:

$$CTSD_{res} = h = \frac{\sqrt{3}K_{I\max}{}^2\left(1-\nu^2\right)\left(\frac{1}{2}+R-\frac{1}{2}R^2\right)\left(\sin\frac{\theta}{2}+\sin\frac{3\theta}{2}\right)^2}{16E\sigma_{YS}} \tag{2.17}$$

It can be seen from Figure 2.11 that crack closure will occur when $\delta = h\sin(2\theta)$. Combining Equation (2.16) and Equation (2.17) and rearranging them to express the closure level gives the following:

$$\frac{K_I}{K_{I\max}} = \frac{K_{cl}}{K_{I\max}} = \beta\frac{\sqrt{3\pi}K_{I\max}\left(\frac{1}{2}+R-\frac{1}{2}R^2\right)\left(\sin\frac{\theta}{2}+\sin\frac{3\theta}{2}\right)^2\sin 2\theta}{16\sigma_{YS}\sqrt{a^*}\left(3\cos\frac{\theta}{2}+\cos\frac{3\theta}{2}\right)} \tag{2.18}$$

As there is some variation in the analytical expressions available for determining $CTSD$ available in the literature [61, 62], β is used as a scaling factor on the $CTSD$ value which may be expected to take values between approximately 1 and 4. The predicted closure levels from this analytical model have shown good quantitative agreement with the FE model behaviour. The model is unique in the literature of analytical RICC models in that extent of shear offset of the fracture surfaces arises from within the model formulation and is not defined arbitrarily.

2.1.3.3 Crack Closure Measurement

Whilst crack closure has been an established aspect of fatigue analysis for many years, measurement methods remain the subject of debate. This is mainly due to the degree of scatter that may result from different measuring techniques. Measurement techniques can be mainly divided into four main groups, which are (i) direct observations of the crack tip, (ii) indirect observations based on fatigue crack growth, (iii) mechanical compliance measurement, and (iv) physical compliance measurement.

(i) *Direct observations of the crack tip*

The most direct observation of crack closure is to study the fatigue crack through a microscope during cyclic loading. Staal and Elen [63] adopted an optical system with a TV camera, with a maximum magnification of X800. Davidson *et al.* [64] has used the scanning electron microscope (SEM) to obtain higher magnifications when observing the crack, in conjunction with specially designed testing equipment for cyclic loading of the sample. Observation of the crack tip profile can also be made by applying replica techniques, however a number of replicas may be required to arrive at a crack opening stress level. Nisitani and Kage [65] for example used this method for small crack observations.

Several techniques have been developed to observe displacements around a crack tip during cyclic loading. Davidson [66] introduced the stereo-imaging technique on pictures obtained in an SEM. Photographs in the region of the crack made at minimum load may be compared in a stereoscope with photographs of the same region made at progressively larger loads. By this comparative technique, the open portion of the crack may be seen and directly measured. As the open portion of the crack approaches the crack tip, higher magnification photographs may increase the accuracy of the measurement. Fellows *et al.* [67] have used Moire interferometry to obtain high resolution near-tip displacement fields. The closure point on the surface of the sample is obtained through the careful monitoring of the variations of the displacement fields during unloading. Optical interferometry was adopted by other investigators in transparent polymeric materials [68]. Interferometric measurements of the crack opening in such a sample over the full area of a fatigue crack has confirmed that the crack opening stress level may be relatively high at the surface, and decrease

towards the interior of the material, with a minimum then occurring at the specimen mid-thickness.

Whilst three-dimensional images of crack closure processes may be obtained by testing transparent materials [69], Guvenilir *et al.* [70] has recently used high resolution X-ray computed tomography to image fatigue cracks within the interior of metallic specimens, with crack opening as a function of position across the crack face being measured and related to the three-dimensional crack face geometry: details of such imaging is presented in Section 2.2.

(ii) ***Indirect observations based on fatigue crack growth***

Based on the assumption adopted by De Koning [71] that crack growth does not occur in a load cycle of a variable amplitude load cycle history if $\sigma_{max}<\sigma_{op}$, the crack opening stress level may be determined in tests with simple *High-Low* block load histories. The maximum stress value of a second load block, σ_{max2}, which is just below the level to cause further crack growth is then supposed to be equal to σ_{op} associated with the last cycle of the first block. This method assumes that the smallest amount of crack opening is sufficient for further growth. A disadvantage of the method is the extensive experimental effort required.

Striations on fatigue fracture surfaces may be the most direct evidence of crack growth in individual cycles. Striations may thus give information on σ_{op}. Pelloux *et al.* [72] performed tests with two block load sequences. Both blocks used the same σ_{max}. After the large cycles at first block loading, a second block of loading was introduced with only 10 smaller cycles where different σ_{min} value are applied. When the striation spacings of the small cycles and the large cycles were equal, it is concluded that σ_{min} of the small cycles is equal to σ_{op} of the larger cycles.

(iii) ***Mechanical compliance measurement***

These methods are essentially based on measuring the variation of the mechanical compliance of a cracked sample for an effective varying crack length. Crack closure loads are then considered to be associated with initial deviation from linearity in mechanical compliance of a cracked specimen during unloading or loading. Elber [32] used a clip gauge (crack opening displacement (COD) meter), which he located 2mm

behind the tip of the crack. The more popular position for a clip gauge in such measurements is at the centre line of centre cracked tension (CCT) specimens, or at the load line of compact tension (CT) specimens. The advantage is that one does not have to replace the gauge as the crack grows. A similar argument applies to the use of back face strain gauges on CT or single edge notched (SEN) specimens. Strain gauges mounted on the side surface of a specimen near the crack tip may be used to record variations in the near tip surface strain with fatigue load. It has been stated that more accurate measurements can be made if the gauge is positioned closer to the crack tip in view of the larger apparent change of the compliance. However, a location too close to the crack tip might lead to misleading results due to the crack tip plasticity. Vasudevan *et al.* [35] showed that a change in compliance slope can occur if plastic relaxation (reverse plastic flow) occurs during unloading. This however is not consistent with, for example, the incidence of high apparent closure levels (from crack mouth compliance data analysis) in the near threshold regime, where the extent of plasticity will be very small in relation to any typical fatigue specimen format.

As mentioned earlier Fleck and Smith [37] developed a 'push-rod' complieance measurement approach. In their technique, two small holes (1.5mm) were drilled at the mid thickness of a relatively thick CT specimen (24mm). Both holes are parallel to the loading direction and just behind the crack front. The depth of one hole terminated 1mm above the crack and the other hole went 1mm below the crack. The COD can then be measured via mechanical connections through the holes at the sample mid-thickness. Results indicated a lower mid-thickness crack closure stress level than that observed on the outside on the specimen surfaces, which is consistent with through-thickness stress state effects on PICC in particular.

In terms of identifying deviations from linearity in mechanical compliance data, slope variation and tangent line intersection methods are the most commonly used to determine fatigue crack opening point [73]. In the slope variation method [74], linear regression analysis is made at the upper part of the compliance data; then, going down along the compliance curve, local averaged slopes are obtained by considering a number of neighbouring points on both sides of a data point. The σ_{op} is then determined based on a certain *nominal* difference in local & upper slope values (say 2% or 5%). The selection of the nominal difference will of course affect the level and

stability of the closure measurement results. In the tangent line intersection method, two tangent lines are drawn for the upper part and the lower part of the compliance curve respectively. The fatigue crack opening stress σ_{op} is defined as the intersection point of the tangent lines. The physical significance of this intersection point is however unclear.

Closure point estimations may also be made via direct visual observation of the deviation from linearity in 'unprocessed' compliance curves. This method is only a rough estimation of the closure point and it is clearly subjective. The accuracy of such the direct observations can be improved by applying the so-called offset method to the original compliance curve, as recommended by ASTM E647 [74]. The compliance curves are recorded as an offset value from a straight line fit to the upper part of the original compliance curves. The offset method may improve sensitivity to the non-linearity of the compliance curves, however, it is still subjective in identifying the closure point, and there is a degree of uncertainty in selecting the upper portion of the curve for the linear fit [75].

Recently, Xu *et al.* [76] have developed non-subjective fitting methods based on linear and quadratic functions. In this curve fitting, two methods were considered. In the first method, the compliance curves are divided into a linear part (upper part) and a second order polynomial curve (lower part) about a 'test' closure point along the curve. The closure point is obtained when the absolute difference in *co-ordinates* between the straight line and the second order polynomial sections at this point reaches a minimum as the test closure point is systematically varied. In the second method, based on the same curve fitting, the closure point was defined when the difference between the *slopes* of the straight line and the second order polynomial sections at the test closure point reaches a minimum. Their curve fitting results were compared with the results from conventional direct observation, offset observation and slope variations methods. The curve fitting technique appeared to provide consistency in closure measurements from conventional crack mouth clip gauge and near tip strain gauges. This method was thought to improve upon current ASTM suggested methods in terms of sensitivity, consistency and noise in the measurements.

(iv) *Physical compliance measurement*

These methods cover a variety of physical indications of effective crack length that may be monitored during loading and unloading. The electrical potential drop (*PD*) method has been successfully applied for automatic crack growth monitoring in fatigue tests, however, the measurements have to be made at a moment of a load cycle when the crack is definitely fully open. The experience with the potential drop method for measuring crack closure is not encouraging. Bachmann *et al.* [77] indicate the significance of oxide layers on the fracture surfaces, which can act as insulators. Also, fracture surface asperities may cause only local electrical short-circuiting, leading to 'false' indications of closure.

The application of the eddy current method to measure crack closure was reported by Lal *et al.* [78]. The eddy current probe was put in close proximity to the crack tip. There is some control on the depth of penetration of the eddy currents by adjusting the frequency. The possibilities have not yet been widely explored, but the famous arguments against the potential drop method may be seen to apply to this method as well.

Ultrasonic surface wave probes were adopted by Ho *et al.* [79]. The acoustic transmission of these waves through a crack was supposed to indicate whether closure was present. The problem of this method is the difficulty in distinguishing hydraulic noises and other physical processes from real closure events. Uncertainties may also exist regarding the relationship between acoustically closed cracks and mechanically closed cracks.

2.1.3.4 Evaluation of Various Closure Measuring Methods

Lee [80] employed an acoustic emission technique to measure crack closure of 2024 CT samples during fatigue tests. The results were then compared with the results obtained via crack tip opening displacement, back face strain and surface strain methods. There was evidence that the crack tip displacement and back face strain methods gave good agreement with each other while measuring the through-thickness mean value of the crack closure loads. On the other hand, surface strain and acoustic emission techniques were rather sensitive to local crack tip behaviour on a microscopic scale, resulting in higher closure level detection. Sensitivities of the

surface strain technique was dependent on the relative distance between the strain gauge and crack tip, therefore yielding inaccurate data if the strain gauge is wrongly placed.

Whilst studying crack closure via clip gauge measurements, Yisheng *et al.* [73] found that the closure results found from the tangent line intersection method were not sensitive to clip gauge position. They have suggested that the crack opening stress determined via this method may be a median stress level between the crack just fully open and the crack just fully closed. On the other hand, the position of the clip gauge was found to have systematic effect on the crack opening stress when using the slope variation method. The crack opening stress measured by this method increased if the clip gauge was located closer to the crack tip, and it was found to be of a value higher than that obtained by tangent line intersection.

Hudak *et al.* [81] reported that local closure measurements from a stereo-imaging technique gave significantly higher crack opening loads than the global closure measurements performed by Minakawa *et al.* [47] for the same material by using a clip gauge. Ward-Close *et al.* [82] shows that while measuring crack closure levels of a tensile overloaded samples, they found that the back face strain technique (which gives *global* closure measurement) shows little evidence in explaining the overload retardation behaviour. On the contrary, the near-tip local closure measurement obtained via the surface strain technique provided a superior interpretation of post-overload retardation behaviour. However, Allison *et al.* [83] reported that the closure measurements obtained by global measurements (clip gauge and back face strain) and local measurements (replicas) were similar.

From the above discussion, clearly there is a certain degree of variation in closure measurement made by the available techniques, with different underlying principles, sensitivities and accuracy depending on the location of measurement relative to the crack tip and overall specimen geometry. For example, using the ASTM suggested offset method, Venkateshwara Rao and Ritchie [19] reported closure levels (K_{cl}/K_{max}) of 2124-T351 alloy tested in laboratory air (R =0.1) are respectively at 0.6 and 0.35 at the ΔK of 4 MPa$\sqrt{m}$ and 8 MPa$\sqrt{m}$. Whilst at the same testing condition of side

grooved 2024-T351 alloy, at the same ΔK levels Xu [34] reported closure values of 0.75 and 0.4 by using the aforementioned curve fitting method. As such, discrepancies of the order of $0.1K_{max}$ are identifiable for similar test conditions but different curve analysis methods (consistent with Xu's own comparison of offset and curve fitting approaches).

2.1.4 Microstructural Aspects of Fatigue in High Strength Al-Alloys

In terms of fatigue crack growth rate (FCGR), slip character, slip length and slip reversibility are principal factors which may be considered to affect FCGR. Resistance to crack growth is generally superior in underaged micro-structures, attributable to because the marked planarity of slip from coherent shearable precipitate distribution promoting crack path tortuosity and hence enhanced RICC effects [84-86]. For example, in 7000-series alloys, underaged materials have been reported to have lower FCGR than overaged materials specifically in the near-threshold crack growth region [84, 86, 87]. In addition, pronounced deformation textures in aluminium alloys may also promote deflection along the crack front. For example, works from Yoda *et al.* [88] shows highly crystallographic crack facets (with included angles of ~ 60^{o}) in 2090 Al-Cu-Li alloys are identifiable with slip-plane orientations between component of the {110}<112> deformation texture of unrecrystalised plate, and the propensity for failure along {111} slip bands. It is also shown that different FCGR through-out the thickness of wrought plate may be associated with marked variations in crystallographic texture (i.e. different degree of recrystallisation). Furthermore, texture effect may also vary with crack plane orientation [89].

Dispersoids tend to homogenise slip and hence inhibit irregular fatigue crack paths [85, 90]. As noted in Appendix A, dispersoids give a pinning effect that may retard grain growth during processing. Therefore relatively low dispersoid densities may promote large grain structures which allow planar slip over large distances to give perturbed crack paths and high fracture surface roughness levels. This may then promote RICC effects and decrease FCGR [34, 91]. *Vice versa*, high dispersoid density may reduce fracture surface roughness by their retardation effect on grain

growth and inhibition of planar slip. Intermetallic particles may provide preferential crack paths ahead of a growing fatigue crack tip and thus decrease the propagation resistance, particularly at high stress levels [1, 92]. This may be associated with essentially monotonic void formation at the particles. Depending on the load levels of interest FCGR may then be reduced by reducing the volume fraction of intermetallic compounds in an alloy.

Regime	Relevant Mechanisms	Desirable Microstructural Features
Initiation	Slip band formation	Non-shearable precipitates, dispersoids, reduced grain size, reduced texture
	Particle failure	Uniform spatial distributions, small equiaxed particles
	Porosity	Improved processing procedures
	Grain boundary failure	'Remove' boundary PFZs & particles, limit slip band activity
Short Crack Growth	Slip band/Stage I	Small grain size, high angle boundaries
	Grain boundary growth	Triple points, large boundary particles
	Slip band/extended Stage I	Shearable precipitates, fewer dispersoids, increased grain size, increased texture
Long Crack Growth	Roughness induced closure	Shearable precipitates, fewer dispersoids, increased grain size, increased texture (texture effects vary with orientation)
	Deflection shielding	Shearable precipitates, fewer dispersoids, increased grain size, increased texture (texture effects vary with orientation)
	Plasticity induced closure	Lower strength, increasing cyclic work hardening

Table 2.2 Basic micro-structural influences on fatigue resistance in high strength monotonic Al-alloys [93].

Detailed discussions in microstructure effects in FCGR are given by Sinclair and Gregson [93] in a recent survey on fatigue optimisation in aerospace aluminium alloys. Table 2.2 presents a survey of basic microstructural influences on fatigue resistance in high strength monolithic Al-alloys.

2.1.5 Fatigue Crack Growth under Variable Amplitude (VA) Loading

While the study of constant amplitude fatigue provides valuable understanding into the mechanistic processes by which fatigue failure may occur, structural parts used in practical engineering structures are often subjected to a wide spectrum of stresses (variable amplitude loading) over their lifetime, thereby complicating the task of fatigue lifing. In contrast to constant amplitude loading where the increment of crack growth is essentially dependent on the present crack size and the applied loads, under variable amplitude loading the increment of fatigue crack growth is strongly dependent on the preceding loading history. Given the importance of VA loading, various intensive investigations have been made over the years e.g. see [94-99]. Whilst real time loading spectra are highly complex, much research has been focussed on understanding the simplest case of a single overload/underload inserted in a constant amplitude loading schedule with the general conclusion that crack growth retardation and acceleration occurs respectively for each case.

- *Transients Overload Effects*

The application of a single overload (a high loading cycle in a sequence of low amplitude cycles) is generally identified to perturb steady state fatigue crack growth, typically with a predominant decrease in growth rate for a number of cycles subsequent to the overload. This phenomenon is referred to as crack retardation. If the overload is large enough, crack arrest can indeed occur. However, as first observed by Corlby and Packman [100], the application of a tensile overload in a ductile solid generally exhibits an initial small amount of accelerated growth prior to retardation, a situation identified as "delayed retardation". The marking of the fracture surface corresponding to this rapid extension of the crack during the overload cycle is often referred to as the *stretch zone*. Stretch zones are commonly observed when K_{OL} is significantly greater than K_{max}, where K_{OL} is the maximum stress intensity during the

overload cycle and K_{max} is the maximum stress intensity of the baseline stress intensity factor range, ΔK_b.

As noted above, the accelerated crack growth is commonly followed by prolonged decelerated crack growth before the post-overloaded crack returns to the baseline stress intensity factor range [82, 96, 100, 101], as shown schematically in Figure 2.12. The deceleration of crack growth continues over a crack growth distance which is called the *delay distance*, a_d. By the end of the delay distance, the crack growth rate has returned to the pre-overload baseline value $(da/dN)_b$. However, there are also reports which suggest the absence of initial acceleration in crack growth rates [102, 103]. The overall transient behaviour after a single tensile overload is strongly dependant on the baseline loading ΔK_b, nominal load ratio R, the overload ratio $\%OL$ (see Figure 2.12 for definition), sequence of loading, specimen thickness, as well as the material microstructure and environmental factors. Von Euw [96] reported that the distance of delayed retardation from the overload location is approximately one-eight to one-quarter of the overload plastic zone size. In terms of crack front position in thick specimens, variation in post-overload crack growth response has also been reported [104]. At the surface of thick specimens (where conditions are close to plane stress), the behaviour of crack growth retardation may be similar to that of thin specimens, where plane stress condition apply. However, at the centre of the specimen, where plane strain conditions exist, retardation of crack growth occurs for a shorter distance compared to measurements made at the surface.

2.1.5.1 The Origin of Transient Effects after an Overload

To understand the origin of the growth transient effect after a tensile overload, many explanations have been proposed in the literature over the years [105, 106]. These include explanations based on enhanced PICC effects, residual compressive stresses, crack tip blunting, crack deflection, RICC effects, and strain hardening, as well as the activation near-threshold crack growth mechanisms. As one mechanism alone cannot fully explain observed retardation effects (e.g. see [1]), it therefore may be seen that overload transient behaviour can be caused by a combination of several of these mechanisms, dependent on various factors such as the type of material, loading condition, stress state overload ratio, environment, etc.

- *PICC Effects*

During the application of a tensile overload, as compared to the baseline ΔK_b, a larger plastic deformation zone is created in the wake of the fatigue crack. As discussed in Section 2.1.3.1, the residual plastically deformed material that is left behind a crack tip due to crack tip plastic deformation can cause premature crack surface contact which may affect the crack growth rate. Based on this fact, the larger plastic deformation zone produce by overloading along the crack wake has been argued to enhance the surface contact level of PICC, and in turn promote crack retardation post overload [32, 33]. In experimental observations on aluminium alloys it has been noted that striations on the fracture surfaces prior to an overload may "disappear" in the post-overload fracture surfaces. This phenomenon was indicated in the work of Von Euw *et al.* [96]; they suggested that increased levels of PICC can bring increased surface frictional contact that may obviate surface marking such as striations. Before crack retardation, a degree of crack growth is needed to pass through the overloaded plastic zone to cause this enhanced PICC effect; as such, delayed retardation can be reasonably explained based on this interpretation. However, results obtained at high overload ratio and/or ΔK_b levels suggest that immediate retardation can occur even if PICC is operative [107, 108]. In such cases however, the stretched ligament ahead of the crack tip may fracture during the overload cycle and the enhanced closure on the newly created surfaces negates the tendency for initial acceleration and prompts retardation without any delay.

Although the theory of enhanced PICC influence on overload transients has been widely considered in the literature, such closure processes cannot fully explain observed transient effects, and there are some inconsistencies with this mechanism. For example, while PICC intrinsically leads to higher crack closure levels in plane stress than in plane strain, increased levels of post-overload retardation indeed have been reported in some materials in plane strain than in plane stress [109]. In addition, some of the micromechanical characteristics of the post-overload retardation region have been identified to be inconsistent with pure PICC effects, where the changing of crack growth mode from Stage II to Stage I after overload is indicative of near-threshold mechanisms which may be expected to increased RICC effects [110, 111].

- *Residual Compressive Stresses*

It maybe noted that compressive residual stresses exist at a crack tip after cyclic loading (as discussed in Appendix A). After the application of an overload, and upon the removal of the overload, locally enhanced compressive stresses are developed surrounding the crack tip. The enlarged compressive stress zone might then be expected to reduce the driving force for crack propagation and hence cause fatigue crack retardation. The presence of an enlarged residual compressive zone following a tensile overload has been indicated by X-ray measurement of stress fields ahead of the fatigue cracks [112, 113]. Willenborg et al. [114] and Wheeler [115] have proposed these residual compressive stresses dominate post-overload crack growth, with the associated simple models being widely used to predict the retardation behaviour (see Section 2.1.5.2).

Although enhanced residual compressive stresses undoubtedly exist following an overload, they can not account for several post-overload observations. Due to the fact that residual compressive stresses only exist in the immediate vicinity of the overloaded crack tip, this theory can only predict instantaneous crack retardation or arrest after overload, and does not allow for delayed retardation. Moreover, this theory is also shown to contradict the experimental observation that retardation can continue even when the crack tip has passed through the predicted residual compressive stresses zone of an overload [109].

- *Crack Tip Blunting*

After tensile overload, a fatigue crack tip in a ductile material may be anticipated to be blunted. Under constant amplitude loading the shielding effect caused by crack blunting is stable. However, during a tensile overload, locally enhanced blunting has been suggested to behave like a notch, with less severe stress concentration than the original pre-overload sharp crack tip. The blunting of the crack tip by the overload cycle has been suggested to persist even during post-overload crack growth [116-118]. Rice [62] and Christensen [119] argued this can make a significant contribution to crack growth retardation. However based on experimental evidence from Fleck [120] it is suggested that blunting only causes retardation at extremely high overload

ratios. A direct experimental observation of dynamic crack tip blunting process has been made by Lankford and Davidson [117] via SEM observations.

Rao et al. [106] proposed an explanation of delayed retardation based on the incidence of crack tip blunting in conjunction with crack closure. Based on the experimental studies of transient fatigue crack growth behaviour following single overloads in a 2090 aluminium alloy, they argued that the immediate crack acceleration of crack growth after a tensile overload is associated with the crack tip blunting which increases crack opening displacements immediately after the overload, causing a decrease in crack closure levels. The reduced crack closure level may then cause temporarily acceleration in crack growth rates before the crack advances fully into the overload region and experiences enhanced closure levels (i.e. retardation).

- *Crack Deflection and RICC Effects*

Several investigators have found that the application of a tensile overload in a material with a propensity for planar slip deformation can promote deflection of the crack tip from the nominal mode I crack growth plane [109, 117, 121]. As discussed earlier, Suresh [55, 56] showed that when a crack tip is deflected from its nominal mode I growth direction, the effective driving force for growth is smaller than that of a straight crack of the same total (projected) length which is subjected to the same far-field ΔK. Based on analyses suggested by Bilby *et al.* [122] and Kitagawa *et al.* [123] for a semi-infinite crack with a kink at its tip, Suresh [109] shows a reduction of up to 19% in the effective stress intensity range can occur for a crack tip deflected at 45° from its nominal path after an overload (for a kink-to-straight crack length ratio of 0.01 or less). The reason of the growth of a fatigue crack along a deflected path after overloading however must be linked to the presence of a path of low crack propagation resistance away from the mode I growth plane, hence one can explain the acceleration in the crack growth rates during the application of an overload as due to the 'sudden' decreases in the crack propagation resistance in the preferred deflected crack path. Crack profile measurements have revealed the occurrence of enlarged 'humps' of stretched material on crack surfaces at an overload location can indeed be seen and be responsible for increased crack closure levels following an overload [98, 120].

It is worth noting that some investigators find crack growth retardation does not happen during post overload crack tip deflections, but only occurs after the fatigue crack has grown out of the influence of the deflection, back to the nominal mode I growth plane. This has been seen by Lankford *et al.* [117] for of various aluminium alloys. However, the initiation of crack tip deflection can be linked to an increase of crack roughness along the wake of the fatigue crack, therefore the retardation of crack growth may be linked to an influence of enhanced RICC from the crack deflection. For example, Rao *et al.* [106] have linked particularly high post-overload retardation levels in the Al-Li 2090 alloys compared to more conventional 2124 and 7150 alloys with the very high crack surface roughness levels in the 2090 alloy. However, arguments against crack path irregularities as a dominant cause of retardation are reported, where, for example stress relief treatments after an overload are found to fully eliminate (for steels) or greatly reduce (for aluminium alloys) retardation levels, in spite of the occurrence of deflected crack paths [97, 124].

- *Near-threshold Mechanisms*

The development of enhanced levels of PICC, residual compressive stresses or crack deflection after the application of tensile overloads on a fatigue crack can result in a post-overload stress intensity factor range whose effective value may be much lower than the nominal baseline value ΔK_b [109]. This means that even when the post-overload ΔK is well within the Paris crack growth regime, the effective ΔK value may fall into the near-threshold regime. In this case, the activation of additional mechanisms of fatigue crack growth retardation, which are of significant to CA near-threshold fatigue may also influence the post-overload regime. These additional retardation mechanisms may then involve stage I crack growth as well as RICC and OICC [125, 126].

- *Strain Hardening*

It has been suggested by Jones [127] that overloads will induce plastic strain hardening effects in the material ahead of the crack tip and this then leads to retarded crack growth due to reduced subsequent crack tip opening displacements at the crack tip. The phenomenon of strain hardening has been supported by the experimental results of Knott and Pickard [128] where it has been reported that under-aged

aluminium alloys which have more strain hardening capacity show more pronounced retardation effects than equivalent over-aged materials (i.e. with reduced less strain hardening) [129]. However, similar to other theories, due to the complex retardation effects following an overload, this strain hardening mechanism alone cannot account to give a full explanation of transient behaviour. This is evidenced from the work by Chaki and Li [130] where overload retardation is observed in metallic glasses which do not exhibit any high strain hardening.

2.1.5.2 Modelling Approaches

From the previous section it would appear that crack growth retardation following an overload is a potentially complicated phenomenon to model. In view of the variety of mechanisms that maybe underlying variable amplitude fatigue, there are a number of empirical or semi-empirical models that have been developed to estimate the service life of an engineering material subjected to complex loading histories.

- *Crack-tip Plasticity Models*

Two popular life prediction approaches that are based on crack-tip plasticity and notional residual stress expects are the Wheeler model [115] and the Willenborg model [114]. These models are based on the assumption that crack growth rates under variable amplitude loading can be related to the interaction of the crack tip plastic zones, and predict the retardation of crack growth by modifying the constant amplitude growth rates.

The Wheeler model relates crack growth rate to the overload plastic zone size and the current plastic zone size. The model multiplies the constant amplitude crack growth rate $(da/dN)_{CA}$ by a retardation factor to predict the variable amplitude crack growth rate $(da/dN)_{VA}$, where the retardation factor, ϕ is a function of the ratio of the sum of the distance a crack has grown since overload (Δa) and the current plastic zone size, $r_{y(c)}$, to the plastic zone size created by overload, $r_{y(o)}$.

$$\left(\frac{da}{dN}\right)_{VA} = \phi\left(\frac{da}{dN}\right)_{CA}, \quad \phi = \left(\frac{\Delta a + r_{y(c)}}{r_{y(o)}}\right)^{k} \tag{2.19}$$

k is a fitting parameter which is empirically chosen to obtain the best overall crack growth predictions for a given material and loading spectrum. The Wheeler model predicts that retardation decreases proportionally with the penetration distance of the crack into the overload plastic zone, with the maximum retardation occurring immediately after an overload. Crack retardation is assumed to occur as long as the current plastic zone is within the plastic zone created by the overload. As soon as the boundary of the current plastic zone leaves the boundary of the overload zone, retardation is assumed to cease and $\phi = 1.0$. A major disadvantage of this model is the material properties and stress spectrum dependent empirical constant, k, which is required to curve fit the model to test data.

The Willenborg model uses an effective stress intensity, which is the applied stress intensity reduced by an amount of compressive residual stress intensity, K_{red}. Similar to Wheeler's model, the reduction in K is a function of the forward plastic zone size associated with the current load cycle and the maximum plastic zone size produced by overloads. The decrease in stress intensity is proportional to the square root of the distance the crack has to propagate to be free of the residual stresses arising from an overload. The Willenborg model predicts that retardation occurs as long as the current plastic zone size is within the plastic zone created by previous overload (same as the Wheeler model). Crack growth retardation is predicted by this model if the minimum stress intensity factor K_{min} of the current loading cycle is less than K_{red}.

One shortcoming of both semi-empirical engineering models by Wheeler and Willenborg is that they require crack growth retardation to be immediate after an overload and do not allow for delayed retardation which has been experimentally observed. In addition, while residual compressive stresses may play a role in reducing effective stress intensity values over distances of the order of the reversed plastic zone size due to overload [62], the retarded crack growth distance can be up to an order of magnitude larger than the extent of the reversed plastic zone directly ahead of the crack tip, especially under plane strain conditions [34, 104, 110, 111].

- *The Characteristic Approach*

Based on a similitude concept, which presumes that similar stress-strain conditions at the fatigue-critical locations in two different specimens should produce similar fatigue

lives, Paris [131] has proposed that random variations of crack tip loading are describable in terms of the associated root-mean-square value of the stress intensity factor range, ΔK_{rms}. The variable amplitude crack growth rates are then given by the Paris-type relationship,

$$\frac{da}{dN} = C(\Delta K_{rms})^m, \quad \Delta K_{rms} = \frac{\sqrt{\left(\sum_{i=1}^{n} \Delta K_i^2\right)}}{n} \tag{2.20}$$

where C and m are material constants, ΔK_i is the stress intensity factor range in the ith cycle in a sequence consisting of n stress cycles. Under constant amplitude fatigue, $\Delta K_{rms} = \Delta K$. Based on the above equation, this characteristic approach suggests that the average crack growth rate in spectrum fatigue can be predicted from constant amplitude fatigue data. Although this approach is empirical, it has been used in some fatigue critical applications, such as variable amplitude fatigue of steel bridges [132]. However, in applications such as flight simulation of gust loading spectra for aircraft, random loading and statistically equivalent program loading are known to provide different results [133], highlighting a load sequence dependency that is ignored in this approach.

- *Numerical Models*

Over the last 20 – 30 years, many finite element (FE) models have been established to predict variable amplitude fatigue behaviour in terms of crack closure. Although quantitative agreement with experimental data has not always been achieved by most of the models, the general trend of a brief acceleration followed by prolonged retardation following a single overload has been reported by various researchers from both two dimensional [134-136] and three dimensional FE models [137, 138]. Newman's [139] FASTRAN model (closely related to the strip yield modelling of Budianski and Hutchinson [38]) can be applied to variable amplitude loading as described earlier in this chapter. One advantage of the Newman model is that it is notionally capable of *a priori* predictions, while empirical approaches such as the Wheeler model are merely able to relate crack growth data after the fact. It should also be noted that Newman's model is based on only one closure mechanics (i.e. PICC), and is not strictly applicable to plane strain conditions.

2.2 High Resolution Synchrotron X-Ray Microtomography

Tomography is referred to as the quantitative description of a slice of material within a bulk volume. There are several methods available which can deliver the specific images of interest (i.e. internal imaging), depending on the selected physical excitation source, such as using ultrasonics, magnetic fields, electric fields (impedance or capacitance tomography), X-rays or gamma-rays. In the field of industrial non-destructive testing (NDT) and material characterisation, X-ray tomography is the most widely used method today.

X-Ray tomography techniques have been widely used in medicine for the last 30 years, and have become a powerful tool to perform non-destructive investigations in materials science providing three-dimensional (3D) images of the interior of materials. Tomography has the potential to show a variety of microstructural features within a material (including second phases, cracks, pores, *etc.*) which induce a modification of the attenuation (or the optical phase) of an X-ray beam. Recently, with the availability of third-generation synchrotron radiation sources such as at the European Synchrotron Radiation Facility (ESRF), it is possible to obtain tomographic image resolutions as fine as 1 micron or less in voxel size. Such resolution levels may be identified with "X-ray microtomography". Synchrotron X-ray microtomography has been successfully applied to studies in material science and mechanical engineering, such as characterising the semi-solid microstructure of cast aluminium alloys [140], quantifying damage in SiC reinforced metal matrix composites [140-142], observing grain boundaries in polycrystalline aluminium [140] and investigating fatigue crack closure behaviour of high strength aluminium alloys [143, 144]. In-situ observation of specimens under different loading conditions can be carried out when the specimen is coupled with a loading stage during the x-ray microtomography scan [70].

2.2.1 Principles of X-Ray Tomography

There are basically three types of tomography technique, which are (i) transmission tomography, (ii) scattered photon tomography, and (iii) emission tomography. Of

most general interest is essentially transmission tomography, based on the application of Equation (2.21), the Beer-Lambert attenuation law:

$$\mu = K\rho\frac{Z^4}{E^3} \tag{2.21}$$

where μ is the linear attenuation coefficient of a material which is related to the photon energy E, ρ is the material density and Z is the atomic number of the investigated material. Contrast in conventional X-ray tomographic image is generated by detecting different local X-ray absorption values (i.e. μ) within an object. Figure 2.13 shows the basic concepts of the imaging process. When an X-ray beam passes through an object, the transmitted intensity across the object may be recorded as a 2D radiograph on a 2D detector. The information in this radiograph is a projection of the absorption density in the object onto the plane perpendicular to the X-ray beam. If the object is imaged many times at different angles for a full rotation, by logging a series of contiguous equidistant image slices, a 3D numerical image of the whole interior of the object can be obtained by using an appropriate image reconstruction algorithm based on "filtered back projection" which follows from the Radon transform [145, 146]. Figure 2.14 illustrates the 3D tomographic reconstruction of an object where it is performed offline in a slice by slice approach [147]: each line in the 2D projection images corresponds to the parallel projection of a given layer z of the object. The ensemble of parallel projection of a given layer for all different angular settings is called the *sinogram* (or Radon transform) of the layer and serves as input for the reconstruction.

Different set-ups may achieve different resolutions of tomography image [148]. For low to medium resolution tomography, conventional microfocus X-ray tubes may be used, which may then be used in a cone beam setup as illustrated in Figure 2.15. The divergent beam allows magnification to be controlled by simple positioning of the sample (see Figure 2.15). The maximum resolution of the image is mainly linked to the size of the microfocus: a focus size in the range of 5 – 10 μm is commonly used. Focus needs to be as small as possible to enhance resolution, but cuts down the beam power. In order to minimise imaging times at a small beam focus, the camera must be very sensitive. Performance effectively becomes a playoff between time to acquire an image (high power) and microfocus (low power). A polychromatic beam is used in

such set-ups, which tends to introduce artefacts that make quantitative reconstruction of μ values difficult due to the differential absorption of different photon energies from the beam (beam hardening).

To obtain better image quality at higher resolutions (maintaining high signal to noise ratios) synchrotron radiation beam sources may be used. For example, the beamline ID19 of the ESRF can deliver a very high intensity, monochromatic (after passage in a suitable monochromator), spatially and phase coherent (making it possible to obtain phase images by simply adjusting the sample-detector distance), and almost parallel X-ray beam with significant benefits for image quality.

2.2.2 Principles of Synchrotron Radiation

In general, synchrotron radiation is derived from ultra-relativistic electrons (energies of several GeV) held in a storage ring, where the electron beam is maintained at the operating energy, travelling with nearly the speed of light (e.g. at 2 GeV their velocity is around 0.9999 of the speed of light) and producing synchrotron radiation (synchrotron X-ray beam) when the electron beam is accelerated by magnetic fields which modify its trajectory. Figure 2.16 illustrates a basic plan of a typical synchrotron facility (such as ESRF) , as can be seen energetic electrons are produced initially from a linear accelerator (*linac*) giving energies from hundreds of MeV to several GeV. A small "booster synchrotron", sited in between the linac and the main synchrotron, is used during "start-up" (referred to as *injection*) to bridge the energy gap between the output-MeV of the linac and the input-GeV required for the main synchrotron ring. A key aspect of injection however, is that the electrons are injected in discrete *pulses* so that the electrons exist inside the storage ring as *bunches*, typically one or two hundred bunches distributed around the whole ring. This is essential for an effective action of another synchrotron component, a *radio-frequency generator/cavity*, of which there may be several around the ring. The purpose of the radio-frequency generator is to synchronously (hence the name *synchrotron*) feed energy to the electron bunches circulating in the ring to compensate for their energy losses during their emission of radiation. This current of electron bunches slowly decays with time due to collisions between the electrons and any molecules contained

within the ring; even with ultra-high vacuum conditions (typically 10^{-10} mbar) in the storage ring, a storage beam typically needs to be regenerated about every 24 hours.

- *Dipole Magnet*

As illustrated in Figure 2.16, the brown lines denote the paths of the synchrotron radiation emitted as the bunches of electrons pass through the dipole magnets (Figure 2.17). The dipole magnet has two vital roles in the synchrotron. First, according to basic electro-magnetic principle, an electron (see Figure 2.17) [149], travelling in a direction **v**, intersects a magnetic field **H** in a direction perpendicular to **v** then it will experience a force **F** (the *Lorentz* force) in a direction perpendicular to both **v** and **H** ("inwards" as shown in Figure 2.17). Since the electron is moving with velocity **v**, **F** produces a centripetal acceleration causing the electron to move in a deflected path. The second vital feature is that because the electron is being accelerated within the dipole magnet it will emit electromagnetic radiation, where this radiation extents from the radio-frequency to the X-ray region of the electromagnetic spectrum. By ganging up a series of such dipole magnets around a circle of the appropriate radius, it is obviously possible to make an electron move around a closed loop (see Figure 2.17) consisting of curved (within the dipole magnets) and straight (between the dipole magnets) sections.

- *Wiggler*

As shown in Figure 2.18, a wiggler is one of the so-called "insertion devices" that may be placed into the straight electron path sections between dipole magnets. The radiation emitted by a dipole magnet (illustrated in Figure 2.17 [149]) is characterised by the parameter λ_c, the critical wavelength by which the total power spectrum reaches 50%. A standard formula relates λ_c to the electron beam energy E (in GeV) and the bending magnetic field B (in Tesla):

$$\lambda_c = \frac{18.6}{E^2 B} \tag{2.22}$$

Therefore if for a given energy E we can increase B, and hence the radial acceleration, we would shift λ_c to a shorter wavelength thus the X-rays would on average have shorter, more penetrating, wavelengths. Such a device is therefore often referred to as

a wavelength shifter. A so-called wiggler is both an insertion device and a wavelength shifter, as illustrated in Figure 2.19. In its simplest form, the wiggler contains three magnets; the outer two magnets are opposed (magnetic field in opposite direction) to the central magnet. Basically the first (outer) magnet bends the electron path in the "wrong direction" (i.e. opposite curvature from the overall synchrotron ring), the second (middle) magnet over-compensates for this, and the third (outer) magnet brings the electron path back to its original direction (the overall motion could be described as a *wiggle*, hence the name). The over-compensation in the middle section is brought about by a very intense magnet (usually a super-conducting magnet with typically a 5-6 Tesla magnetic field strength) and the resulting tighter local curvature means that a greater radial acceleration is brought about with the consequent production of harder X-rays (i.e. higher energy photons).

- *Undulator*

An undulator is a magnetic device, made up of a complex array of small magnets, forcing electrons to follow an undulating, or wavy, trajectory (see Figure 2.20 [149]). It consists of many (typically 20-30) alternating low field magnetic poles. This therefore produces an alternating series of inward and outward electron accelerations (such motion being described as undulations) each with its individual radiation emission from each pole. At some point downstream from the undulator these radiation emissions will overlap and interfere with each other, sometimes constructively and sometimes destructively. By choosing the magnet parameters and interference point carefully, the undulator spectrum can be designed so that higher intensity can be obtained in the wavelength region of interest.

As can be seen in Figure 2.21, since the discovery of X-rays, the X-ray tube has steadily increased in power as a result of various technological improvements, particularly with the introduction of the rotating anode X-ray tube in the 1960s, and the curve then arches upwards dramatically with the introduction of the synchrotron [140]. Along with all 3rd generation synchrotron radiation sources (such as the ESRF), the introduction of insertion devices such as wiggler and undulator magnets have significantly improved the properties of the source. The original features of 3rd generation synchrotron radiation facilities, and more particularly the ESRF, which make it suitable for microtomographic application are [140]:

- The very high intensity of the X-ray beam (see Figure 2.21)
- The high energy (6 GeV) of the electrons producing the radiation, which implies the availability of high energy photons (beyond 100keV)
- The policy of providing each beamline, though appropriate choice of the insertion device, with the spectrum best suited to the experiment it is dedicated to
- The small size of the electron beam cross-section (<100 μm). This leads to high brilliance, but also to a very small angular extension of the source as seen from the point in the specimen, hence to a sizeable lateral coherence of the beam.

2.2.3 Phase Contrast

The spatial coherence of synchrotron radiation (such as that at ESRF) may be used to produce phase contrast effects in the image, where the phase contrast imaging can be used either in a qualitative way (typically for edge-detection) or in a quantitative way, involving numerical retrieval of the phase from images recorded at different distances from a sample. This spatial distribution of the photons occurs due to diffraction at internal interfaces (Fresnel diffraction): this is normally considered a nuisance in attenuation imaging, however, it facilitates phase imaging. The origin of the phase contrast effect is local variations in the refractive index for X-rays within the sample. The occurrence of contrast can be understood as due to interference between parts of the wavefront that have suffered slightly different angular deviations associated with different phase gradients between constituents of the material studied, such as holes, cracks, inclusions, reinforcing particles or fibres in a composite material. This phase difference induce contrast, is added to the classical attenuation contrast. Whilst the overlap between parts of the wavefront is only possible after propagation over a certain distance, the phase sensitivity maybe particularly obtained by choice of sample-detector distance, d (*propagation* technique). The latter determines the defocusing distance D through [150]:

$$D = \frac{d \times l}{d + l} \tag{2.23}$$

where l is the source-sample distance. In the case of the long ESRF beamline ID19 for example, where $d << l = 145$m, the defocusing distance and the sample-detector distance are practically equal, while the absorption radiograph corresponds to an image recorded close to the sample ($D \approx 0$). The region of the object mainly contributing to the corresponding point of the image contrast (the first Fresnel zone) has a radius equal to:

$$r_F = \sqrt{\lambda D} \tag{2.24}$$

In order for an image to be characterised in the optimum 'edge-detection regime', r_F has to be small compared to the typical transverse dimension a_t of the features in the sample ($r_F << a_t$). A separate fringe pattern will then show up for every border in the sample, and three-dimensional reconstruction of the boundaries inside the volume is then feasible. At larger distance ($r_F \approx a_t$), several interference fringes may show up in the radiographs and these can deform images and give incorrect information on the sample [140].

Phase contrast imaging has been shown to be an excellent way of improving the detection of cracks in material even in their early stages of development (i.e. where they are not widely open) [142, 151, 152]. This is also crucial when the attenuation contrast of different phases in the sample are small, for instance when observing light materials, and when seeking to distinguish absorbing constituents with similar X-ray attenuation. The detection of isolated features smaller than the nominal voxel resolution has been demonstrated thanks to the interference patterns produced, enhancing the effective image quality.

2.2.4 Application to Current Study

Most engineering materials or structures of practical interest are opaque to all intents and purposes, but many processes depend closely on internal/bulk conditions (for example, the first order influence of stress states in many failure processes). In the present study, a commercial high strength aluminium alloy developed for damage tolerant airframe applications (AA2024-T351) has been used for synchrotron X-ray microtomography experiments for the *in-situ* observation of steady state plane strain fatigue crack failure processes, particularly utilising enhanced resolution levels

associated with synchrotron tomography facilities. The high resolution imaging particularly enables the visualisation of minute microstructural features providing a unique possibility to assess the local mixed-mode (I, II and III) nature of crack opening behaviour.

As discussed earlier, fatigue crack closure has been recognised as a significant potential factor in determining fatigue crack growth rates. In terms of the application of synchrotron X-ray microtomography to mechanical damage and crack problems, Buffière *et al.* [142] and Stock *et al.* [143] have identified that it can be possible to detect features occupying areas as small as one-tenth of a voxel size. This corresponds to crack opening slightly greater than 0.5 μm for typical isotropic voxels (6.0 - 6.6 μm) [142, 143] which is in fact reasonable to detect the incidence of microscopic damage events. Guvenilir *et al.* [143, 144] in particular have shown the application of this technique in the *in situ* investigation of crack closure behaviour of Al-Li materials, where their work shows the evidence of mixed mode crack asperities contact during crack loading cycle. Whilst with an average crack opening at maximum load of ~ 4 mm in their study (which corresponds to about 60% of the voxel size (6.4 mm)), the resolution in their work may be considered to be relatively 'low' compared to the typical crack opening distance, therefore sub-voxel interpolation was needed to obtain an estimation of the 'real' crack opening. However, recent advances in imaging facilities now have allowed order of magnitude improvements in resolution levels.

To understand the contributions of crack closure mechanisms such as PICC and RICC to fatigue properties, three-dimensional understanding is clearly valuable. However, within the available experimental literature, such a three-dimensional viewpoint has been largely neglected since such three-dimensional crack closure behaviour is difficult to address either by post failure analyses such as fracture surface observation, or by conventional *in-situ* surface observation. As such it would appear that in-situ X-ray tomography provides a unique possibility to assess crack closure processes.

References

[1] S. Suresh, *Fatigue of Materials*. 2nd ed. 2001, Cambridge: Cambridge University Press.

[2] A.S. Tetelman and A.J. McEvily, *Fracture of Structural Materials*. 1967, New York: John Wiley & Sons Inc.

[3] W.A. Wood, *Recent Observations on Fatigue in Metals, ASTM STP 237*. 1958, p. 110-121.

[4] P.J.E. Forsyth and A. Stubbington, *Journal of the Institute of Metals*, 1955. **84**: p. 173-175.

[5] A. Hunsche and P. Neumann, *Acta Metallurgica*, 1986. **34**: p. 207-217.

[6] B.T. Ma and C. Laird, *Acta Metallurgica*, 1989. **37**: p. 325-336.

[7] J.C. Grosskreutz and G.G. Shaw, *Fracture 1969*, ed. P.L. Pratt. 1969, Oxford: Pergamon, p. 620-629.

[8] C.Y. Kung and M.E. Fine, *Metallurgical Transactions*, 1979. **10A**: p. 603-610.

[9] P.C. Paris, M.P. Gomez, and W.P. Anderson, *The Trent in Engineering*, 1961, 13, p. 9-14.

[10] P.C. Paris and F. Erdogan, *Journal of Basic Engineering*, 1963. **85**: p. 528-534.

[11] P.J.E. Forsyth, *Crack Propagation: Proceedings of Cranfield Symposium* 1962, London: Her Majesty's Stationery Office, p. 76-94

[12] C. Laird, *Fatigue Crack Propagation, ASTM STP 415*, 1967, Philadelphia: ASTM, p. 131-168.

[13] R.P. Gangloff and R.S. Piascik, *Metallurgical Transactions*, 1993. **24A**: p. 2751-2762.

[14] R.P. Gangloff and R.S. Piascik, *Metallurgical Transactions*, 1993. **24A**: p. 2415-2428.

[15] K. Walker, *Effects of Environment and Complex Load History on Fatigue Life*, 1970, Philadelphia: ASTM, p. 1-14.

[16] C.E. Richards and T.C. Lindley, *Engineering Fracture Mechanics*, 1972. **4**: p. 951-978.

[17] G.R. Yoder, L.A. Cooley, and T.W. Crooker, *NRL Memorandum Report 4787*, 1982.

[18] R.J.H. Wanhill, *Engineering Fracture Mechanics*, 1988. **30**(2): p. 233-260.

[19] K.T. Venkateshwara Rao and R.O. Ritchie, *International Materials Reviews*, 1992. **37**: p. 153-185.

[20] F.A. McClintock, *Fracture of Solids*, 1963. **20**: p. 65-102.

[21] N.E. Frost, *Proceedings of the First International Conference on Fracture*, eds., T. Yokobori, T. Kawasaki, and J.L. Swedlow, 1966, Sendai, Japan: Japan Society for Strength and Fracture of Materials, p. 1433-1459

[22] R.A. Schmidt and P.C. Paris, *Progress in Flaw Growth and Fracture Testing, ASTM STP 536*, 1973, Philadelphia: ASTM, p. 79-94.

[23] ASTM-E647-95a, *Annual Book of ASTM Standards*. 1996, Philadelphia, PA: ASTM International, p. 565-601.

[24] T. Christman and S. Suresh, *Engineering Fracture Mechanics*, 1986. **23**: p. 953-964.

[25] W.A. Herman, R.W. Hertzberg, and R. Jaccard, *Fatigue & Fracture of Engineering Materials & Structures*, 1988. **4**: p. 303-320.

[26] P.K. Liaw, T.R. Leax, and W.A. Logsdon, *Acta Metallurgica*, 1983. **31**: p. 1581-1587.

[27] E. Hornbogen and K.H.Z. Gahr, *Acta Metallurgica*, 1976. **24**: p. 581-592.

[28] L. Christodoulou and H.M. Flower, *Acta Metallurgica*, 1979. **28**: p. 481-487.

[29] R.P. Gangloff, *Environment Induced Cracking of Metals*, eds. R.P. Gangloff and M.B. Ives. 1990, Houston, TX: NACE, p. 55-109.

[30] T.H. Shih and R.P. Wei, *Engineering Fracture Mechanics*, 1983. **18**: p. 827-837.

[31] R.P. Wei and R.P. Gangloff, *Fracture Mechanics: Perspectives and New Directions, ASTM STP 1020*, eds. R.P. Wei and R.P. Gangloff. 1989, Philadelphia: ASTM, p. 233-264.

[32] W. Elber, *Damage Tolerance in Aircraft Structures, ASTM STP 486*, 1971, Philadelphia: ASTM, p. 230-242.

[33] W. Elber, *Engineering Fracture Mechanics*, 1970. **2**: p. 37-45.

[34] Y. Xu, *Closure assessment and overload transient behaviour in damage tolerant airframe materials*. Ph.D thesis, University of Southampton. 2001.

[35] A.K. Vasudeven, K. Sadananda, and N. Louat, *Materials Science and Engineering*, 1994. **A188**: p. 1-22.

[36] J.C. Newman and W. Elber, *Mechanics of fatigue crack closure, ASTM STP 928*. 1988, Philadelphia: ASTM.

[37] N.A. Fleck and R.A. Smith, *International Journal of Fatigue*, 1982. **4**: p. 157-160.

[38] B. Budiansky and J.W. Hutchinson, *Journal of Applied Mechanics*, 1978. **45**: p. 267-276.

[39] D.S. Dugdale, *Journal of the Mechanics and Physics of Solids*, 1960. **8**: p. 100-108.

[40] G.I. Barenblatt, *Advances in Applied Mechanics*, 1962. **VII**: p. 55-129.

[41] J.C. Newman, *Methods and Models for Predicting Fatigue Crack Growth Under Random Loading, ASTM STP 748*, eds. J.B. Chang and C.M. Hudson. 1981, Philadelphia: ASTM, p. 53-84.

[42] J.C. Newman, *Behaviour of Short Cracks in Airframe Components, Proceedings 328, Advisory Group for Aerospace Research and Development*, ed. H. Zocher, 1983, p. 6.1-6.26

[43] J.C. Newman, *FASTRAN-II - A fatigue crack growth structural analysis program, NASA Technical Memorandum 104159*. 1992.

[44] J.C. Newman, *Journal of Engineering Materials and Technology*, 1995. **117**: p. 433-39.

[45] J.C. Newman, *Analyses of fatigue crack growth and closure near threshold conditions for large-crack behaviour, NASA Technical Memorandum 209133*. 1999.

[46] N. Walker and C.J. Beevers, *Fatigue & Fracture of Engineering Materials & Structures*, 1979. **1**: p. 135-148.

[47] K. Minakawa and A.J. McEvily, *Scripta Metallurgica*, 1981. **15**: p. 633-636.

[48] A.F. Blom, A. Hadrboletz, and B. Weiss, *4th International Conference on Mechanical Behaviour of Materials*, 1983: p. 755-762.

[49] R.O. Ritchie and S. Suresh, *Metallurgical Transactions*, 1982. **13A**: p. 937-940.

[50] H. Nowack, K.H. Trautmann, K. Schulte, and G. Lutjering, *Fatigue Mechanics, ASTM STP 677*, ed. C.W. Smith. 1979, Philadelphia: ASTM, p. 36-53.

[51] M.D. Halliday and C.J. Beevers, *Journal of Testing and Evaluation*, 1981. **9**: p. 195-201.

[52] S. Suresh and R.O. Ritchie, *Materials Science and Engineering*, 1981. **15**: p. 61-69.

[53] G.T. Gray, J.C. Williams, and A.W. Thompson, *Metallurgical Transactions*, 1983. **14A**: p. 421-433.

[54] S. Suresh and R.O. Ritchie, *Metallurgical Transactions*, 1982. **13A**: p. 1627-1631.

[55] S. Suresh, *Metallurgical Transactions*, 1983. **14A**: p. 2375-2385.

[56] S. Suresh, *Engineering Fracture Mechanics*, 1985. **21**: p. 453-463.

[57] M.R. Parry, *Finite Element and Analytical Modelling of Roughness Induced Fatigue Crack Closure*. PhD Thesis, University of Southampton. 2001.

[58] M.R. Parry, S. Syngellakis, and I. Sinclair, *Materials Science and Engineering A*, 2000. **291**: p. 224-234.

[59] M.R. Parry, S. Syngellakis, and I. Sinclair, *Materials Science Forum*, 2000. **331**: p. 1473-1478.

[60] M.R. Parry, S. Syngellakis, and I. Sinclair, *Damage and Fracture Mechanics 2000*, eds., C.A. Brebbia and A.P.S. Selvadurai, 2000, Montreal, Canada, p. 313-322

[61] C. Li, *Acta Metallurgica et Materialia*, 1990. **38**: p. 2129-2134.

[62] J.R. Rice, *Fatigue Crack Propagation, ASTM STP 415*, 1967, Philadelphia: ASTM, p. 247-309.

[63] H.U. Staal and J.D. Elen, *Engineering Fracture Mechanics*, 1979. **11**: p. 275-283.

[64] D.L. Davidson and A. Nagy, *Journal of Physics E, Scientific Instruments*, 1978. **11**: p. 207-210.

[65] H. Nisitani and M. Kagi, *Fracture 1979 (ICF4)*, 1979. **2**: p. 1099-1108.

[66] D.L. Davidson, *Engineering Fracture Mechanics*, 1991. **38**: p. 393-402.

[67] L.J. Fellows, D. Nowell, and D.A. Hills, *Advances in Fracture Research, Proc. 9th Int. Conf. On Fracture*, eds., W.E. Frazier, K. Jata, and N.J. Kim, 1997, Sydney, Australia, p. 2552-2558

[68] W.N. Shapre and A.F. Grandt, *Mechanics of Crack Growth, ASTM STP 590*, 1976, Philadelphia: ASTM, p. 302-330.

[69] F.J. Pitoniak, A.F. Grandt, L.T. Montulli, and P.F. Packman, *Engineering Fracture Mechanics*, 1974. **6**: p. 663-670.

[70] A. Guvenilir, T.M. Breunig, J.H. Kinney, and S.R. Stock, *Acta Metallurgica*, 1997. **45**: p. 1977-1987.

[71] A.U.D. Koning, *NLR TR 81141 L, National Aerospace Laboratory NLR, Amsterdam, The Netherlands*, 1981.

[72] R.M. Pelloux, M. Faral, and W.M. McGee, *Fracture Mechanics: Proceedings of the Twelfth National Symposium on Fracture Mechanics, ASTM STP 700*, ed. J.B. Wheeler. 1980, Philadelphia: ASTM, p. 35-48.

[73] W. Yisheng and J. Schijve, *Fatigue & Fracture of Engineering Materials & Structures*, 1995. **18**: p. 917-921.

[74] ASTM-E647-95a, *Annual Book of ASTM Standards*. Vol. Vol.03.01. 1995, Philadelphia, PA: ASTM International, p. 578-614.

[75] J.J. Lee and W.N.J. Sharpe, *American Society for Testing and Materials, ASTM STP 982*. 1988, Philadelphia: ASTM, p. 270-278.

[76] Y. Xu, P.J. Gregson, and I. Sinclair, *Materials Science and Engineering*, 2000. **A284**: p. 114-125.

[77] V. Bachmann and D. Munz, *Journal of Testing and Evaluation*, 1976. **4**(4): p. 257-260.

[78] K.M. Lal, S.B.L. Garg, and I. LeMay, *Journal of Engineering Materials and Technology*, 1980. **102**: p. 147-152.

[79] C.L. Ho, O. Buck, and H.L. Marcus, *Progress in Flaw Growth and Fracture Toughness Testing, ASTM STP 536*, 1973, Philadelphia: ASTM, p. 5-21.

[80] C.S. Lee, C.G. Park, and Y.M. Chang, *Materials Science and Engineering*, 1996. **A216**: p. 131-138.

[81] S.J.J. Hudak and D.L. Davidson, *Mechanics of Fatigue Crack Closure, ASTM STP 982*, 1988, Philadelphia: ASTM, p. 121-138.

[82] C.M. Ward-Close and R.O. Ritchie, *Mechanics of Fatigue Crack Closure, ASTM STP 982*, 1988, Philadelphia: ASTM, p. 93-111.

[83] J.E. Allison, R.C. Ku, and M.A. Pompetzki, *Mechanics of Fatigue Crack Closure, ASTM STP 982*, 1988, Philadelphia: ASTM, p. 171-185.

[84] S. Suresh, A.K. Vasudevan, and P.E. Bretz, *Metallurgical Transactions A*, 1984. **15A**: p. 369-379.

[85] E.A.J. Starke and J.C. Williams, *Fracture Mechanics Perspectures and Directions, ASTM STP 1020*, 1989, Philadelphia: ASTM, p. 184-205.

[86] E. Zaiken and R.O. Ritchie, *Materials Science and Engineering*, 1985. **70**: p. 151-160.

[87] R.D. Carter, E.W. Lee, E.A. Starke, and C.J. Beevers, *Metallurgical Transactions A*, 1984. **15A**: p. 555-563.

[88] G.R. Yoder, P.S. Pao, M.A. Imam, and L.A. Cooley, *Scripta Metallurgica*, 1989. **23**: p. 1455-1460.

[89] K.T. Venkateshwara Rao, W. Yu, and R.O. Ritchie, *Metallurgical Transactions A*, 1988. **19A**: p. 549-561.

[90] F.J. Grau, A. Gysler, and G. Lutjering, *Proceedings of 4th International Conference on Aluminium Alloys*, eds., T.H. Sanders and E.A. Starke, 1994, Atlanta: GIT, p. 709-714

[91] M. Nakai and T. Eto, *Materials Science and Engineering*, 2000. **A285**: p. 62-68.

[92] I.J. Polmear, *Light Alloys*. 3rd ed, eds. R. Honeycombe and P. Hancock. 2000, Oxford: Butterworth-Heinemann.

[93] I. Sinclair and P.J. Gregson, *Aerospace Materials (Series in Materials Science and Engineering)*, eds. B. Cantor, H. Assender, and P. Grant. 1998, Bristol: Institute of Physics Publishing.

[94] L.P. Borrego, J.M. Ferreira, J.M. Pinho da Cruz, and J.M. Costa, *Engineering Fracture Mechanics*, 2003. **70**: p. 1379-1397.

[95] G. Wheatley, X.Z. Hu, and Y. Estrin, *Fatigue & Fracture of Engineering Materials & Structures*, 1999. **22**: p. 1041-1051.

[96] E.F.J. Von Euw, R.W. Hertzberg, and R. Roberts, *Stress Analysis and Growth of Cracks, ASTM STP 513*, 1972, Philadelphia: ASTM, p. 230-259.

[97] C.S. Shin and N.A. Fleck, *Fatigue & Fracture of Engineering Materials & Structures*, 1987. **9**: p. 379-393.

[98] C.S. Shin and S.H. Hsu, *International Journal of Fatigue*, 1993. **15**: p. 181-192.

[99] R.S. Vecchio, R.W. Hertzberg, and R. Jaccard, *Fatigue & Fracture of Engineering Materials & Structures*, 1984. **7**: p. 181-194.

[100] D.M. Corlby and P.F. Packman, *Engineering Fracture Mechanics*, 1973. **5**: p. 479-497.

[101] K.T. Venkateshwara Rao and R.O. Ritchie, *Acta Metallurgica*, 1988. **36**: p. 2849-2862.

[102] H.S. Goel and S. Chand, *Journal of Engineering Materials and Technology*, 1994. **116**: p. 168-172.

[103] P.C. Paris and L. Herman, *Fatigue Threshold, Fundamental and Engineering Applications*, 1982. **1**: p. 11-33.

[104] P.J. Bernard, T.C. Lindley, and C.E. Richards, *Materials Science and Engineering*, 1977. **12**: p. 390-398.

[105] M. Skorupa, *Fatigue & Fracture of Engineering Materials & Structures*, 1998. **21**(8): p. 987-1006.

[106] K.T.V. Rao and R.O. Ritchie, *Acta Metallurgica*, 1988. **36**: p. 2849-2862.

[107] D. Damri and J.F. Knott, *Fatigue & Fracture of Engineering Materials & Structures*, 1991. **14**: p. 709-719.

[108] C.M. Ward-Close, A.F. Blom, and R.O. Ritchie, *Engineering Fracture Mechanics*, 1989. **32**: p. 613-638.

[109] S. Suresh, *Engineering Fracture Mechanics*, 1983. **18**: p. 577-593.

[110] G.R. Chanani, *Flaw growth and fracture, ASTM STP 631*, 1977.

[111] R.P. Wei, N.E. Fenelli, K.D. Unangst, and T.T. Shih, *Journal of Engineering Materials and Technology*, 1980. **102**: p. 280-292.

[112] S. Taira and K. Tanaka, *Transactions of the Iron and Steel Institute of Japan*, 1979. **19**: p. 411-418.

[113] J.E. Allison, *Fracture Mechanics, ASTM STP 677*, ed. C.W. Smith. 1979, Philadelphia: ASTM, p. 550-562.

[114] J. Willenborg, R.M. Engle, and H. Wood, *Technical REport TFR 71-701*, 1971.

[115] O.E. Wheeler, *Journal of Basic Engineering*, 1972. **94**: p. 181-186.

[116] J. Lankford and D.L. Davidson, *Journal of Engineering Materials and Technology*, 1976. **98**: p. 17-23.

[117] J. Lankford and D.L. Davidson, *Advances in Fracture Research*, 1981, 2, p. 899-906.

[118] S. Suresh, *Scripta Materialia*, 1982. **16**(8): p. 995-999.

[119] R.H. Christensen, *Metal Fatigue*. 1959, New York: McGraw-Hill.

[120] N.A. Fleck, *Basic Questions in Fatigue, ASTM STP 924*, eds. R.P. Wei and R.P. Gangloff. 1988, 1, Philadelphia: ASTM, p. 157-183.

[121] J. Schijve, *Engineering Fracture Mechanics*, 1974. **6**: p. 245-252.

[122] B.A. Bilby, G.E. Cardew, and I.C. Howard, *Fracture*, 1977. **3**: p. 197-200.

[123] H. Kitagawa and R. Yuuki, *Fracture*, 1977. **3**: p. 201-211.

[124] P.M. Powell, P.J.E. Forsyth, and T.R.G. Wiliams, *Advances in Fracture Research, Proceeding 5th International Conference on Fracture*, 1981. **4**: p. 1781-1788.

[125] R.J. Bucci, A.B. Thakker, T.H. Sanders, R.R. Sawtell, and J.T. Staley, *Effect of Load Spectrum Variables on Fatigue Crack Initiation and Propagation, ASTM STP 714*, eds. D.E. Bryan and J.H. Potter. 1980, Philadelphia: ASTM, p. 41-78.

[126] S. Suresh, G.F. Zamiski, and R.O. Ritchie, *Metallurgical Transactions*, 1981. **12A**: p. 1435-1443.

[127] R.E. Jones, *Engineering Fracture Mechanics*, 1973. **5**: p. 585-604.

[128] J.F. Knott and A.C. Pickard, *Materials Science and Engineering*, 1977. **11**: p. 399-404.

[129] J. Petit, R. Tintillier, N. Ranganathan, M.A. Abdedaim, and G. Chalant, *Fatigue crack growth under variable amplitude loading*, eds. J. Petit, D.L. Davidson, S. Suresh, and P. Rable. 1988, London: Elsevier Applied Science, p. 162-179.

[130] T.K. Chaki and J.C.M. Li, *Scripta Metallurgica*, 1984. **18**: p. 1675-1678.

[131] P.C. Paris, *The growth of crack due to variations in loads, Ph.D thesis, Lehigh University*. 1960.

[132] J.M. Barsom, *Fatigue Crack Growth Under Spectrum Loads, ASTM STP 595*, 1976, p. 217-235.

[133] J. Schijve, *Engineering Fracture Mechanics*, 1973. **5**: p. 269-280.

[134] S. Pommier and P. Bompard, *Fatigue & Fracture of Engineering Materials & Structures*, 2000. **23**: p. 129-139.

[135] N.A. Fleck and H.R. Shercliff, *Proceedings of the 7th International Conference on Fracture ICF7* 1989, Houston, USA, p. 1405-1415

[136] F. Ellyin and J. Wu, *Fatigue & Fracture of Engineering Materials & Structures*, 1999. **22**: p. 835-847.

[137] J.Z. Zhang, M.D. Halliday, P. Bowen, and P. Poole, *Engineering Fracture Mechanics*, 1999. **63**: p. 229-251.

[138] R.G. Chermahini, K.N. Shivakumar, and J.C. Newman, *Mechanics of Fatigue Crack Closure, ASTM STP 982*, 1988, Philadelphia: ASTM, p. 398-413.

[139] J.C. Newman, *Design of Fatigue and Fracture Resistant Structures, ASTM STP 761*, eds. P.R. Abelkis and C.M. Hudson. 1982, Philadelphia: ASTM, p. 255-277.

[140] J. Baruchel, J.-Y. Buffiere, E. Maire, P. Merle, and G. Peix, *X-Ray Tomography in Material Science*. 2000, Paris: Hermes Science Publications.

[141] T. Hirano, K. Usami, Y. Tanaka, and C. Masuda, *Journal of Materials Research*, 1995. **10**: p. 381.

[142] P. Cloetens, M. Pateyron-Salome, J.-Y. Buffiere, G. Peix, J. Baruchel, F. Peyrin, and M. Schlenker, *Journal of Applied Physics*, 1997. **81**: p. 5878.

[143] A. Guvenilir and S.R. Stock, *Fatigue and Fracture Engineering Materials and Structures*, 1998. **21**: p. 439-450.

[144] A. Guvenilir, T.M. Breunig, J.H. Kinney, and S.R. Stock, *Philosophy Transaction of The Royal Society Lond.*, 1999. **A 357**: p. 2755-2775.

[145] G.T. Herman, *The Fundamentals of Computerised Tomography*, 1980, New York: Academic Press.

[146] A.C. Kak and M. Slaney, *Principles of computerised tomographic imaging*. 1987, New York: IEEE Press.

[147] W. Ludwig, *Development and applications of synchrotron radiation microtomography*. PhD Thesis, University of Munich. 2001.

[148] E. Maire, J.-Y. Buffiere, L. Salvo, J.J. Blandin, W. Ludwig, and J.M. Letang, *Advanced Engineering Materials*, 2001. **3**(8): p. 539-546.

[149] P. Barnes, S. Jacques, and M. Vickers, Advanced certificate in powder diffraction on the web, School of Crystallography, Birkbeck College, University of London, 1997.

[150] M. Born and E. Wolf, *Principle of Optics*. 6th ed. 1980, New York: Pergamon Press.

[151] J.-Y. Buffiere, E. Maire, P. Cloetens, J. Baruchel, and R. Fougeres, *Alluminium Alloys, Proceeding of ICAA-6*, 1998. **1**: p. 529-534.

[152] J.-Y. Buffiere, E. Maire, P. Cloetens, G. Lormand, and R. Fougeres, *Acta Metallurgica*, 1999. **47**: p. 1613.

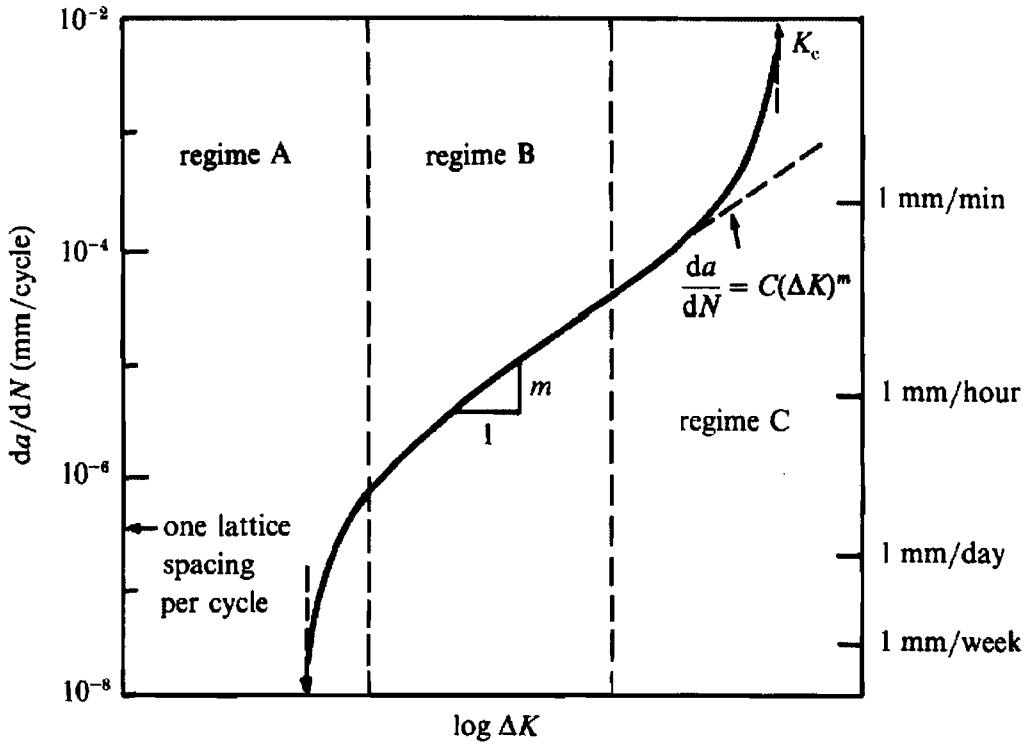

Figure 2.1 Schematic illustration of the regimes of stable fatigue crack propagation [1].

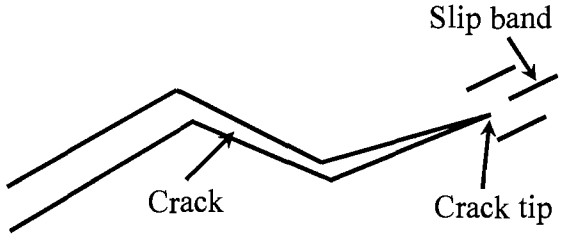

Figure 2.2 Schematic illustration of Stage I fatigue crack growth.

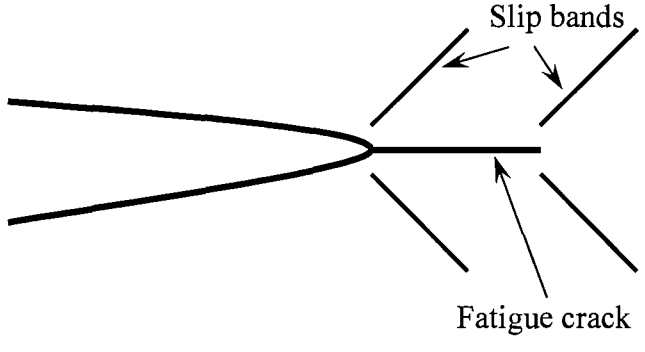

Figure 2.3 Schematic illustration of Stage II fatigue crack growth.

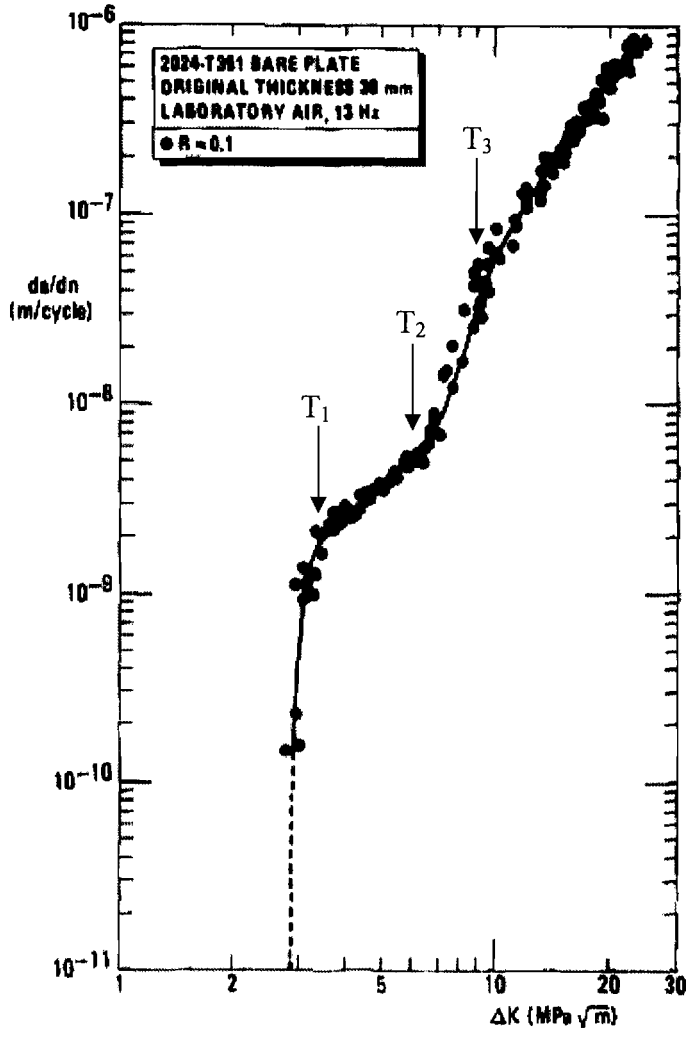

Figure 2.4 A typical constant amplitude fatigue crack growth rates for 2024-T351 plate (at $R = 0.1$) showing three transition points [18].

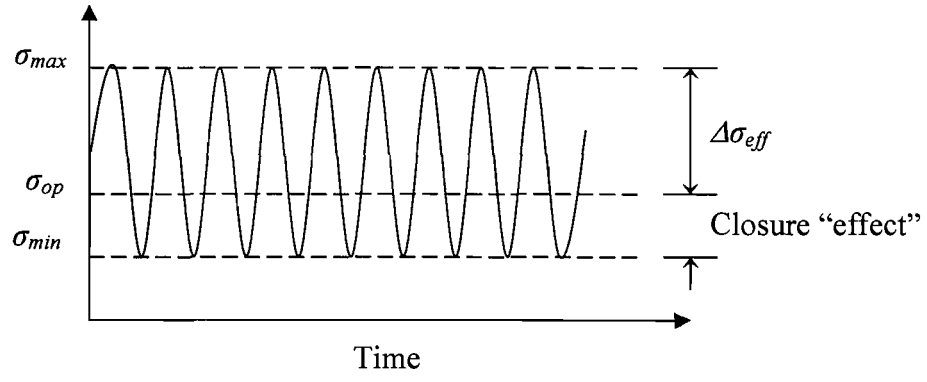

Figure 2.5 Schematic illustration of crack closure effect in relation to cyclic loading.

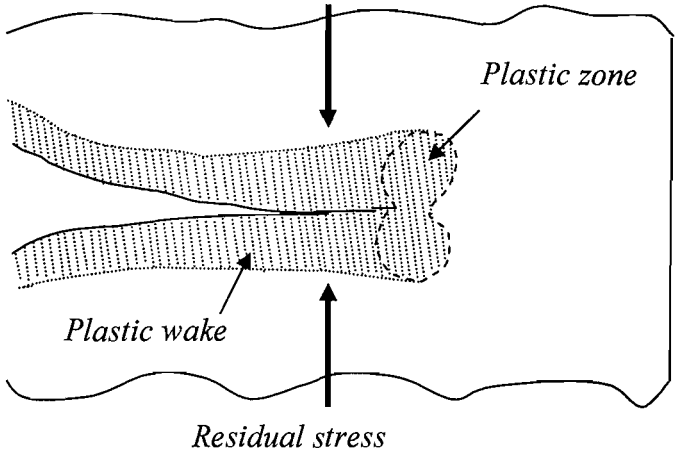

Figure 2.6 Schematic illustration of plasticity-induced crack closure (PICC).

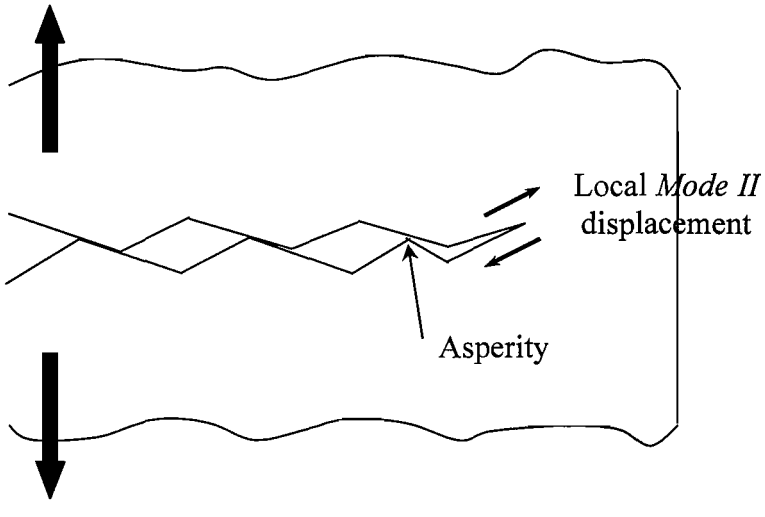

Figure 2.7 Schematic illustration of roughness-induced crack closure (RICC).

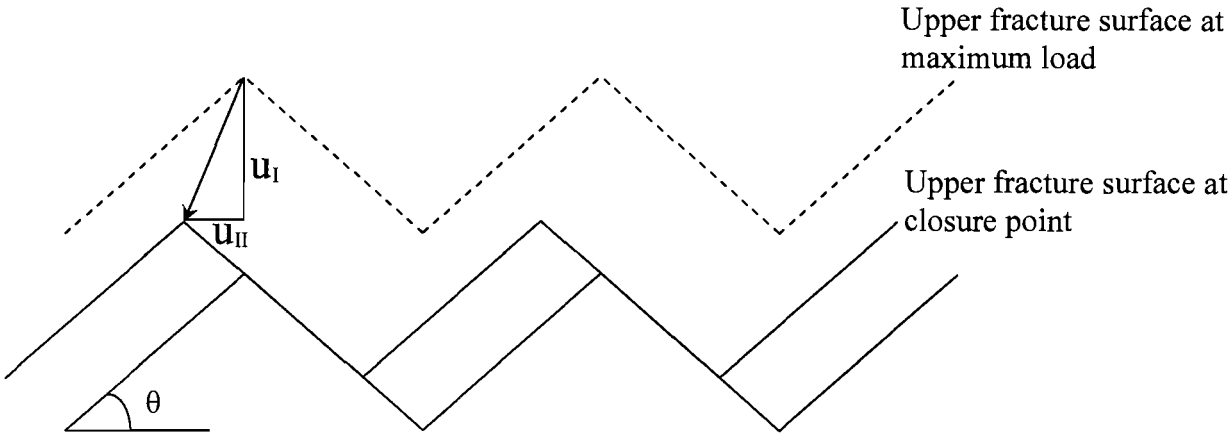

$$\chi = u_{II} / u_I$$

Figure 2.8 Detail of the geometrical model of roughness induced crack closure of Suresh and Ritchie [54].

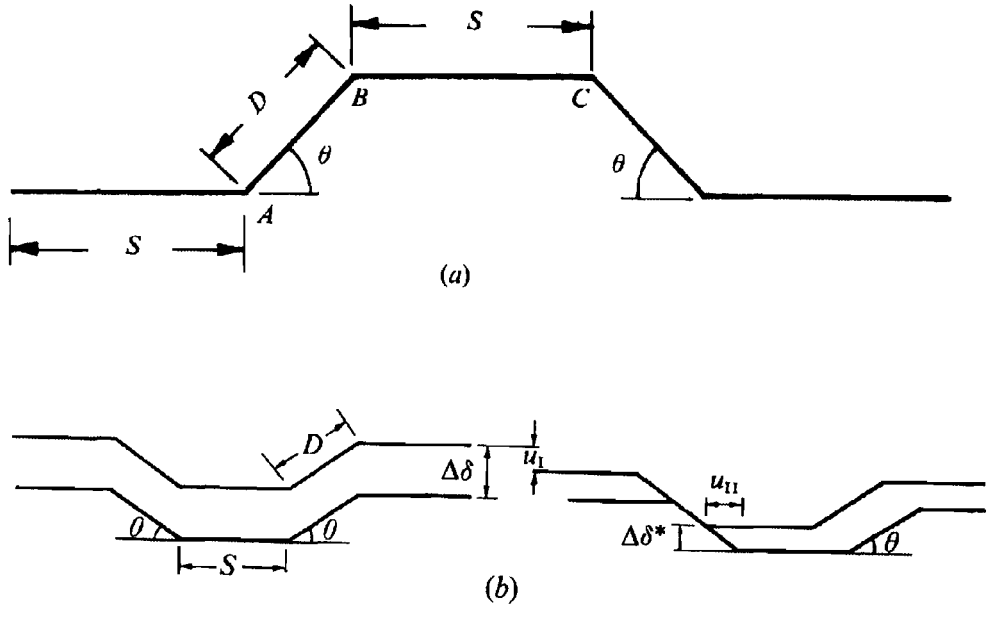

Figure 2.9 (a) Idealisation of a segment of a deflected crack with periodic tilts, (b) Schematic representation of a deflected crack in the fully opened condition at the peak load of the fatigue cycle (on the left) and relative mismatch between the crack faces leading to premature crack closure during unloading (on the right) [55, 56].

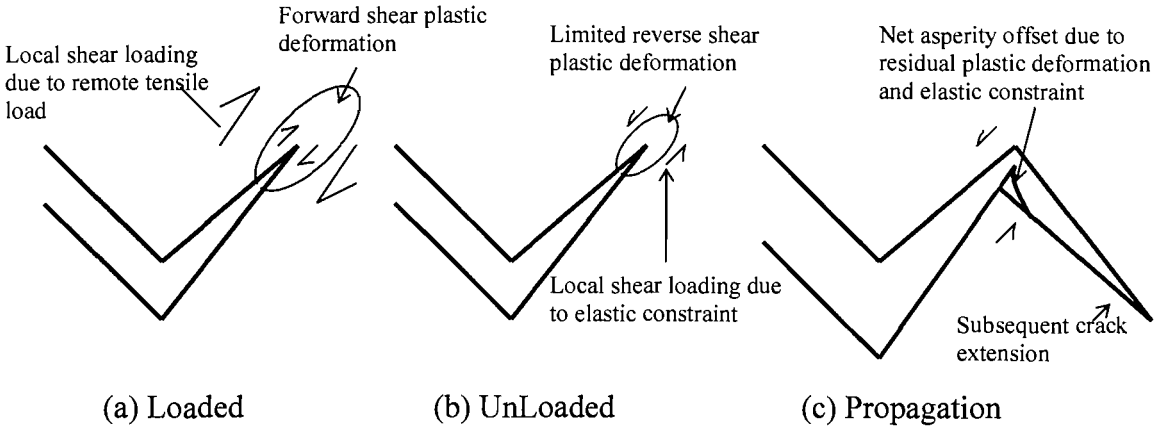

Figure 2.10 Schematic illustration of RICC arising from residual crack shear at asperities.

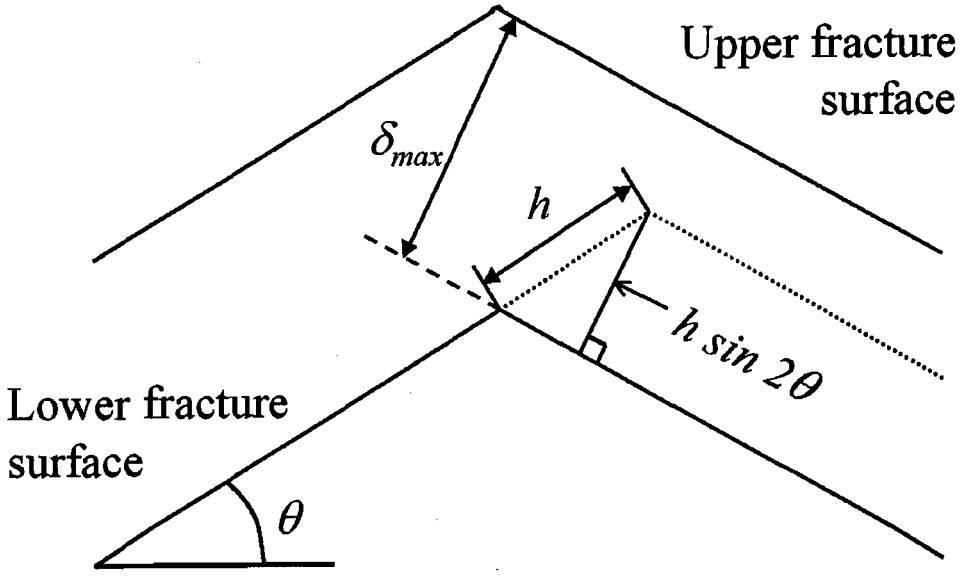

Figure 2.11 Geometry of residual shear crack closure model.

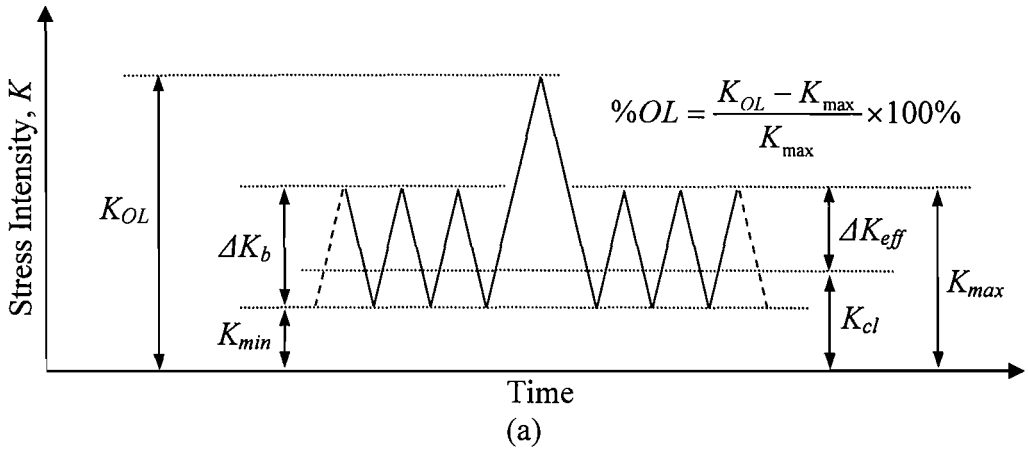

(a)

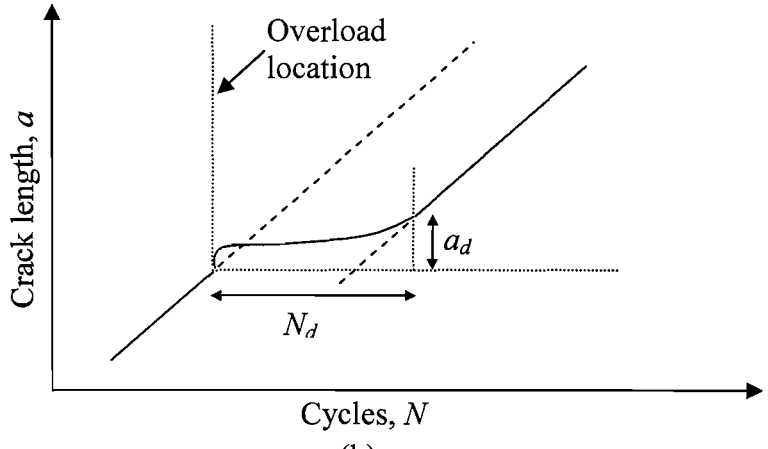

(b)

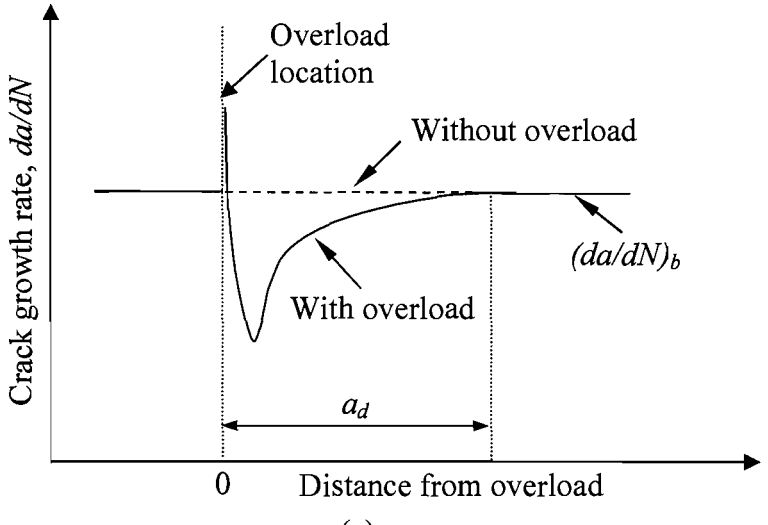

(c)

Figure 2.12 Schematic illustration of the effect of a single tensile overload, showing (a) loading nomenclature, (b) crack length vs number of cycles behaviour, and (c) crack growth rate vs crack length behaviour.

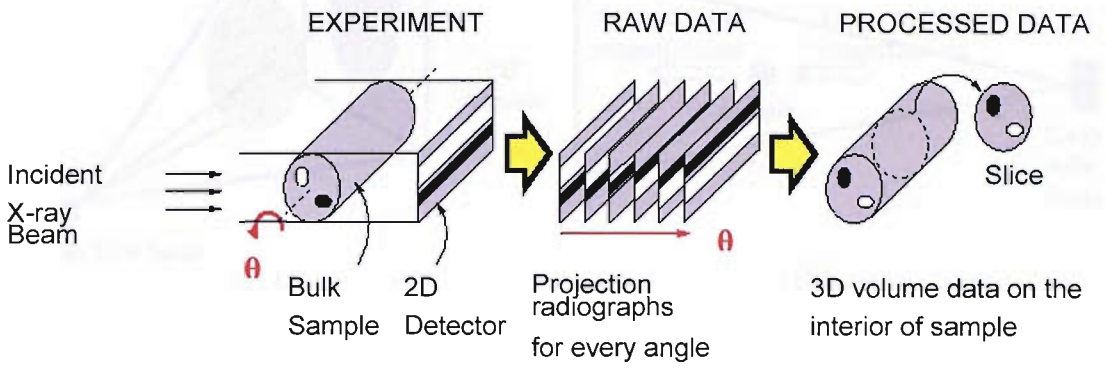

Figure 2.13 Schematic diagram of the tomographic imaging process.

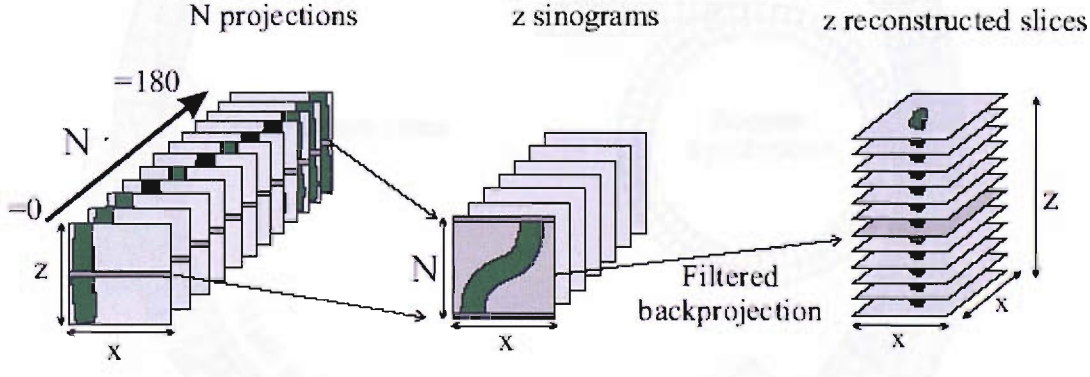

Figure 2.14 Reconstruction of a 3D object in the parallel beam geometry: N two-dimensional projections are recorded while the sample is rotated stepwise over 180°. Each projection contains z lines and x columns. The projections are reorganised into z sinograms, containing N lines and x columns (Radon transform of one object layer) and the volume (z slices) is then reconstructed slice by slice [147].

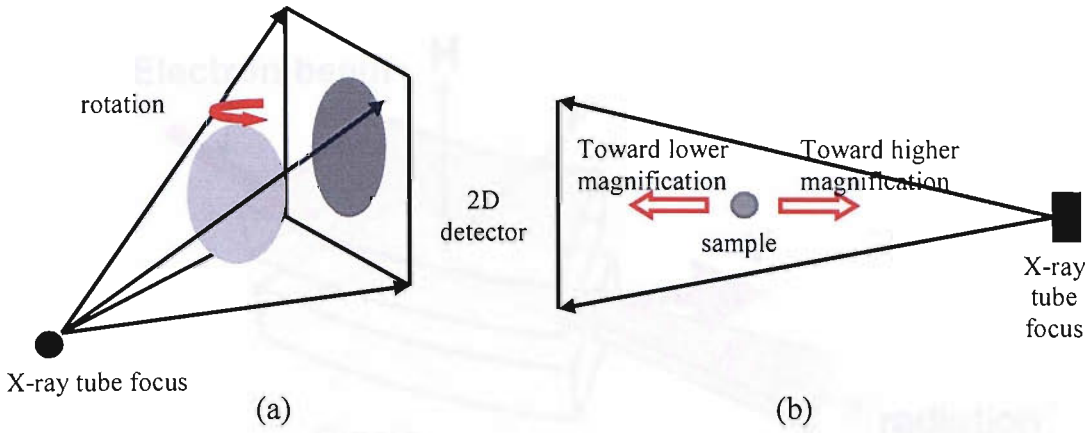

Figure 2.15 (a) Cone beam scanner, (b) Geometry for modification of magnification.

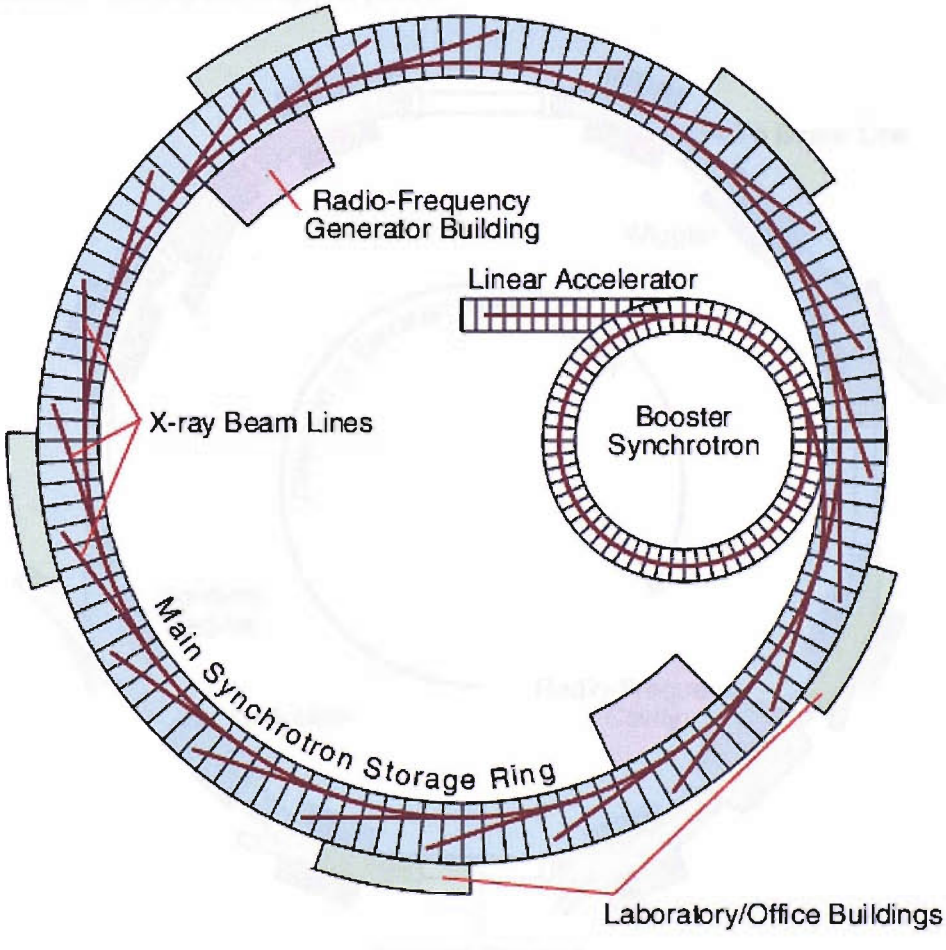

Figure 2.16 Basic plan of a synchrotron radiation facility [149].

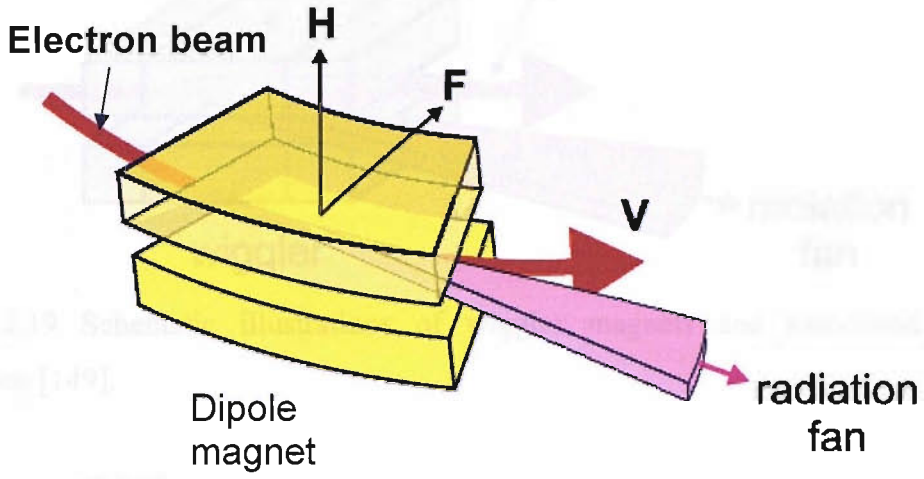

Figure 2.17 The emission of synchrotron radiation as electron bunches are radially accelerated by the dipole magnets [149].

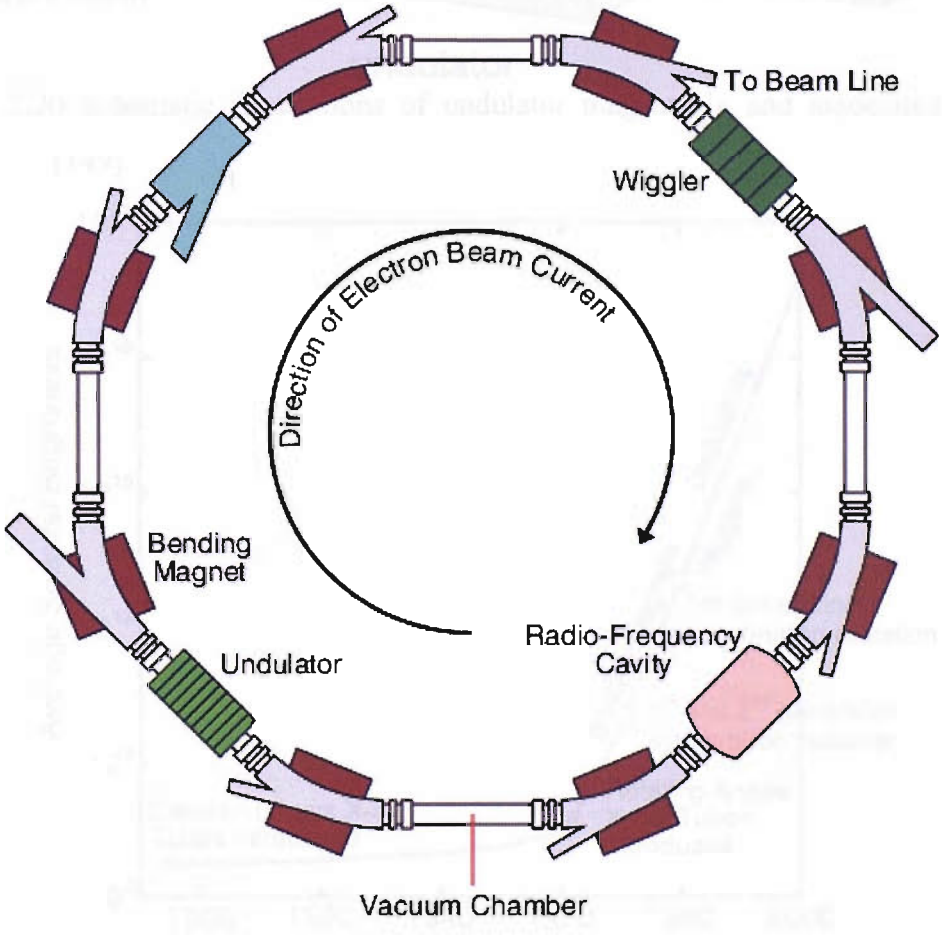

Figure 2.18 Schematic diagram of a simplified synchrotron storage ring with insertion devices [149].

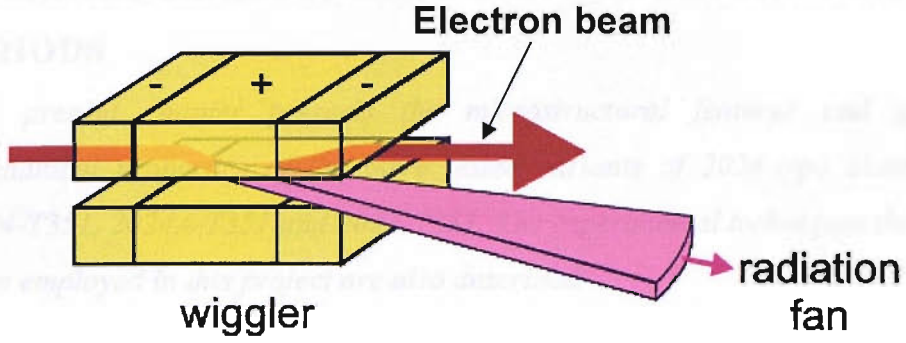

Figure 2.19 Schematic illustrations of wiggler magnets and associated beam generation [149].

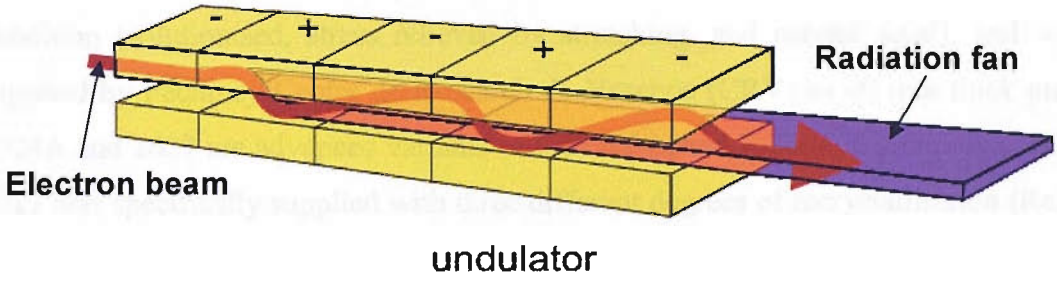

Figure 2.20 Schematic illustrations of undulator magnets in and associated beam generation [149].

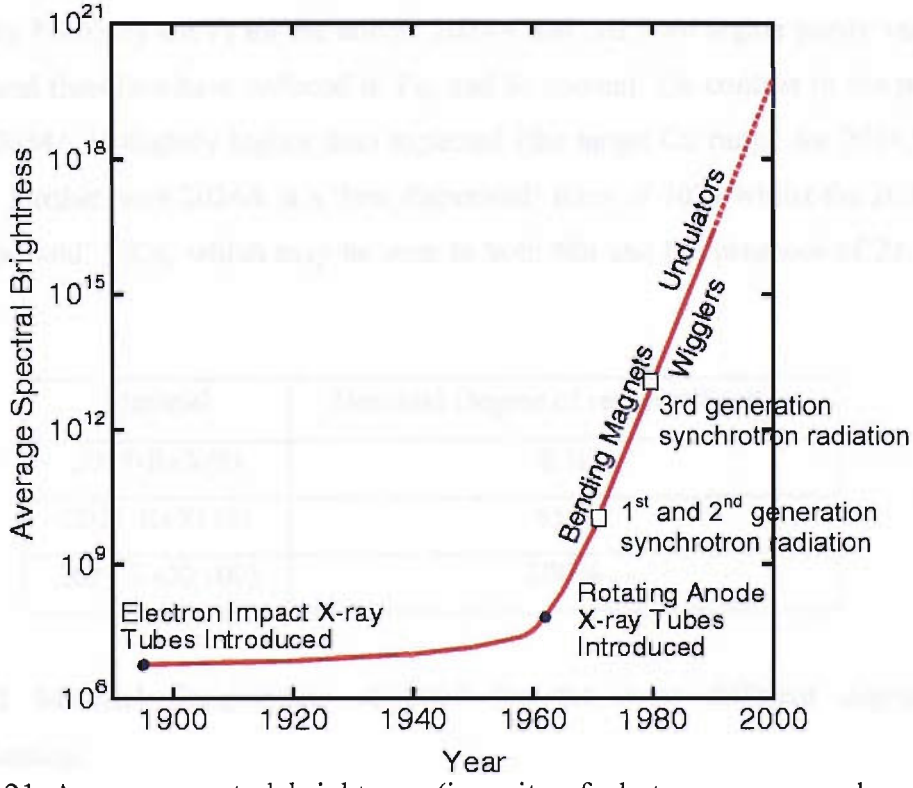

Figure 2.21 Average spectral brightness (in units of photons per second per 0.1% bandwidth per mrad^2) of X-ray sources from the discovery of X-rays to 3rd generation synchrotron facilities [140].

3. MATERIALS CHARACTERISATION AND EXPERIMENTAL METHODS

The present chapter presents the microstructural features and general mechanical properties of the three tested variants of 2024-type aluminium: 2024-T351, 2024A-T351 and 2027-T351. The experimental techniques that have been employed in this project are also described.

3.1 Materials Characterisation

Three types of heat-treatable airframe aluminium alloy have been considered in this work, designated 2024, 2024A and 2027. All have been examined in the T351 condition (solutionised, stress relieved by stretching, and natural aged), and were supplied by Pechiney Centre de Research de Voreppe (CRV) as 40 mm thick plate. 2024A and 2027 are advanced variants of the established 2024-type aluminium alloy. 2027 was specifically supplied with three different degrees of recrystallisation (ReX); nominally 8%, 55%, and 100% (determined by etching at Pechiney CRV). They are individually designated in this report as 2027-ReX(8), 2027-ReX(55) and 2027-ReX(100) as listed in Table 3.1. Table 3.2 shows the chemical composition (data supplied by Pechiney CRV) for the alloys. 2024A and 2027 are higher purity versions of 2024, and therefore have reduced in Fe, and Si content: Cu content in the present batch of 2024A is slightly higher than expected (the target Cu range for 2024A is ~ 4.1 wt%). Furthermore 2024A is a 'low dispersoid' form of 2024 whilst the 2027 is a 'high dispersoid' 2024, which may be seen in both Mn and the presence of Zr in the 2027.

Material	Nominal Degree of recrystallisation
2027-ReX(8)	8 %
2027-ReX(55)	55%
2027-ReX(100)	100%

Table 3.1 Material designations of 2027 for the three different degrees of recrystallisation.

Material	Si	Fe	Cu	Mg	Mn	Zr
2024	0.121	0.203	4.065	1.360	0.537	-
2024A	0.049	0.160	4.510	1.440	0.330	-
2027-ReX(8)	0.050	0.090	4.300	1.300	0.650	0.100
2027-ReX(55)	0.045	0.092	4.005	1.365	0.590	0.100
2027-ReX(100)	0.046	0.085	4.075	1.347	0.640	0.096

Table 3.2 Composition (wt%) of the major alloying elements in the Pechiney supplied alloys (as supplied by Pechiney CRV from wet chemical analysis).

3.1.1 Tensile Properties

Table 3.3 shows the tensile properties of the alloys measured according to ASTM E8M-96 based on 3 tests in each material [1]. In general, 2024A has the lowest tensile strength properties whilst 2027 has the highest tensile strength (decreasing with increasing degree of recrystallisation).

Materials	Tensile Drection	σ_{ys}(0.2%) (MPa)	σ_{UTS} (MPa)	*el* (%)	*n*
2024	L-direction	372	483	21.4	0.1
	T-direction	313	474	17.6	N/A
2024A	L-direction	345	434	25.2	0.09
	T-direction	312	449	13.4	N/A
2027-ReX(8)	L-direction	394	533	15.7	0.14
	T-direction	343	494	19.5	0.15
2027-ReX(55)	L-direction	385	515	16.3	0.13
	T-direction	335	485	19.1	0.13
2027-ReX(100)	L-direction	368	475	21.9	0.13
	T-direction	328	480	17.8	0.14

Table 3.3 Tensile properties of 2024, 2024A and three 2027 material [2, 3], where *el* (%) is the elongation percentage and *n* is the strain hardening coefficient, typically scatter in σ_{ys} and σ_{UTS} values are ±3 MPa, ±2 % in elongation, and ±0.02 in *n* values.

3.1.2 Grain Structure

- ***Optical Microscopy***

Metallographic samples were taken from all alloys and polished to a final finish of 0.25 μm. Grain structures were revealed by etching with Keller's reagent. Typical 'pancake' plate grain structure images were obtained as illustrated in Figure 3.1 and Figure 3.2.

Table 3.4 shows the grain sizes measured in term of mean linear intercept grain dimensions. It may be seen that the grain structure of 2024A is the largest, in that it is coarser than 2024 by a factor of approximately 2, with the mean of the L, T and S dimensions corresponding to 163 μm and 328 μm for the 2024 and 2024A respectively. Mean grain dimension in the three alloys of 2027 fall between the 2024 and 2024A, but have generally small through-thickness intercept lengths than those in the 2024 and 2024A. It may be seen that grain dimensions become more equiaxed with increasing ReX levels in the 2027.

Materials	λ_L (μm)	λ_T (μm)	λ_S (μm)	$\overline{\lambda}$ (μm)
2024	312	121	57	163
2024A	690	216	78	328
2027-ReX(8)	592	223	40	285
2027-ReX(55)	545	179	42	255
2027-ReX(100)	362	146	53	187

Table 3.4 Mean linear intercept grain dimensions (λ_L, λ_T, and λ_S corresponding to the L, T and S directions, respectively) with $\overline{\lambda}$ representing the average of these three firgues, taken at the t/2 plate position [2, 3].

- ***Electron Backscattered Diffraction Assessment***

Electron backscattered diffraction (EBSD) assessment has been carried out on all alloys. Samples in the S-T plane were taken and polished to a final finished of 0.25 μm. The samples were then electropolished in a methanol-nitric acid solution (with liquid nitrogen cooling down to -30°C) for 20 seconds to remove any deformed layer from the prepared surfaces. Grain structure EBSD mapping was then carried out with

a step size of 5 μm at an accelerating voltage of 15 kV and a specimen tilt of 55° in a Jeol 6500f field-emission scanning electron microscope (FEG-SEM), using the commercial 'HKL' EBSD analysis [4].

Figure 3.3 to Figure 3.7 show representative EBSD grain structure maps of the 2024, 2024A and three 2027 alloys. Two types of grain boundary are defined in the maps, with the high angle boundaries in black (more than 12° of misorientation), and the low angle boundaries in red (between 2° and 12° of misorientation). Individual grain colours are based on orientation in relation to the primary directions of the plate (i.e. L, T and S). The mapping areas of all the alloys are identical. As shown in Table 3.5, they have covered some 400 to 1000 individual grains.

Materials	No. of Grains Detected
2024	662
2024A	377
2027-ReX(8)	1132
2027-ReX(55)	1076
2027-ReX(100)	780

Table 3.5 Number of grains detected in the EBSD grain mapping areas.

Looking at the 2024 alloy grain boundary map (Figure 3.3), around ~ 50% of the grains are sub-structured, containing low angle grain boundaries, i.e. unrecrystallised. More distinct equiaxed grains without sub-structure can also be seen, corresponding to the remainder of the material (i.e. recrystallised grains). As shown in Figure 3.4, the 2024A shows significantly larger grains than the 2024, with a recrystallised fraction approximately ~ 80%. The three 2027 alloys show grain structures consistent with the order of nominal recrystallisation levels. However, the observed degree of recrystallisation at the centre line for the 2027-ReX(55) would appear somewhat lower than has been suggested: the material appears to be ~ 30% ReX compared to the suggested 55%. The 2027-ReX(100) shows some evidence of un-ReX grains, although it is clear that microstructure is indeed dominated by ReX grain (~ 90%), see Table 3.6 for a summary of apparent recrystallisation conditions. Differences in ReX level apparently detected in the 2027-ReX(55) may in the first instance be linked to

the present results only being drawn from the centreline of the plate (where all mechanical test coupons were subsequently drawn).

Material	Suggested Degree of ReX	Estimated Degree of ReX
2024	--	~50%
2024A	--	~80%
2027-ReX(8)	8%	~8%
2027-ReX(55)	55%	~30%
2027-ReX(100)	100%	~90%

Table 3.6 Comparison of suggested and EBSD estimated degree of recrystallisation.

Textures of each alloy were also assessed via the EBSD data. Figure 3.8 shows representative {100}, {110} and {111} pole figures of each alloy. The 2027-ReX(8) and ReX(55) materials show distinct, reasonably strong plate deformation textures [5], with peak intensities of ~ 10 and 8 times random for the ReX(8) and ReX(55) condition respectively (see Figure 3.9 for a schematic {111} pole figure with typical deformation texture components). Weaker texture are evident in the remaining three materials (~ 4 – 5 times random peak intensities), with deformation components still being evident in the 2024 and 2024A materials. A reasonable inverse correlation is seen between pole peak intensities and ReX levels (whilst 2024A may show a slightly high pole peak intensity, it is clear that the strongest texture peaks are associated with the lower ReX materials).

3.1.3 Dispersoid and Intermetallic Particle Distributions

To assess the differences of these alloys in term of dispersoid content, they were specifically observed in the FEG-SEM in the back-scattered electron (BSE) mode to image the larger Mn containing dispersoids. Figure 3.10 (a) - (e) respectively shows images of 2024A, 2024 and 2027 at magnifications of 5000x. The images were taken on polished S-L planes of each alloy. Each individual image is representative of a number of images (10 for each material) taken at random locations. It was qualitatively evident from micrographs such as Figure 3.10 that dispersoid point densities were indeed higher in 2027 than those in the 2024 and 2024A, consistent with the high Mn content of this alloy. Differences in particle density between the 2024 and 2024A material were not considered to be clear without further

quantification. As illustrated in Figure 3.11, marked variations in local dispersoid distribution and morphology were also evident in the alloys, complicating their comparison. Similar elongated particle morphologies were seen in the alloys, with particles appearing up to ~ 1μm in length. They have been identified by energy dispersive spectroscopy (EDS) as Mn rich, and are likely to be $Al_{20}Mn_3Cu_2$ [6]. As has been reported in the literature, Zr containing dispersoids (based on the β', Al_3Zr phase) are also expected in the 2027 materials, characteristically forming spherical particles in the 20 – 50 nm diameter range [6].

Materials	L-T	L-S	T-S	All Data
2024	3.0±0.15	2.6±0.11	2.7±0.07	2.8±0.08
2024A	3.2±0.06	3.2±0.11	3.3±0.24	3.2±0.09
2027-ReX(8)	1.4±0.2	1.4±0.26	1.4±0.16	1.4±0.2
2027-ReX(55)	1.9±0.5	1.6±0.26	1.5±0.3	1.7±0.6
2027-ReX(100)	1.9±0.3	2.1±0.2	1.8±0.25	1.9±0.25

Table 3.7 Mean intermetallic area fraction (%) results

Table 3.7 shows measured area fraction values of the coarse intermetallic particles in the various materials. Area fraction for each material was measured optically from 10 random sites in the three surface orientations (L-T, L-S and T-S) at a magnification of 100x. Results in Table 3.7 show that area measurements for the three orientations were reasonably consistent, with 2024A having a slightly higher intermetallic content, contrary to the basic design of this alloy [7]. The higher intermetallic level in 2024A may be attributed to the relatively high Cu content in this particular batch [7], therefore coarse S may be expected to be present. Consistent with the chemical composition, the 2027, which has lower Cu, Fe, and Si, shows lower intermetallic content. Table 3.8 shows length, breadth and aspect ratio of intermetallic particles for all materials. Measurements were taken at a magnification of 500x for each material, with a smaller particle size being identified in the 2027.

Materials	Length (μm)	Breadth (μm)	Aspect Ratio
2024	2.9	1.9	1.5
2024A	2.5	1.6	1.6
2027-ReX(8)	1.4	0.9	1.55
2027-ReX(55)	1.4	0.9	1.55
2027-ReX(100)	1.6	1.1	1.6

Table 3.8 Mean intermetallic particles length, breadth, and aspect ratios

Figure 3.12 shows representative intermetallic particles for the 2024, 2024A and 2027-ReX(55) in the L-S plane. EDS analyses of these alloys showed that large S (Al_2CuMg) phase particles and Cu-Fe-Mn rich clusters made up the majority of the intermetallic particles population in the materials. S phase particles are generally rounded compared to the Cu-Fe-Mn cluster. Based on known common constituent phases in 2024-type materials [6], the Cu-Fe-Mn clusters may be identified in the first instance as a mixture of Al_7Cu_2Fe + $Al_{20}Cu_2Mn_3$, with Al_7Cu_2Fe in the majority.

In addition to EDS analysis, electron probe microanalysis (EPMA) has also been applied (at CRV, Voreppe, France) for quantitative mapping of major alloying elements in the alloys. EPMA mapping have been carried out on 2024, 2024A and one of the 2027 (2027-ReX(8)). The results in Figure 3.13, Figure 3.14 and Figure 3.15 show quantitative maps of each alloy in each element. It is worth noting that for the same element map, each colour scale has been set to the identical threshold level in order to give a direct comparison. The most significant differences among these three alloys are the differences of the dispersoid alloying elements (as reported above). As can be seen in the three Mn maps, 2024A has lowest Mn content, whereas 2027-ReX(8) has the highest. Looking at the Zr map, again 2027-ReX(8) stands out as it is the only alloy that contains Zr. It is interesting to see the distinct bands in the distribution of the Zr in this alloy (band width up to ~ 50 μm) [8]. Some large particles, which are recognised as the coarse intermetallics, can be seen in the EPMA maps with chemical make-ups consistent with the presence of coarse S and Cu-Fe-Mn containing particles, as noted earlier.

3.2 Fatigue Test Methods

The great majority of fatigue testing in this work was carried out using the centre cracked tension sample format (CCT). Constant amplitude (CA) and variable amplitude (VA) CCT fatigue crack growth tests were carried out using an Instron 8501 servo hydraulic fatigue testing machine. All CCT specimens were machined from the plate mid-section (t/2) in an L-T orientation. Figure 3.16 shows overall dimensions of the test specimens. All specimens were side-grooved along the nominal crack growth plane to a depth of 1 mm with an internal angle of 30° on both faces of the specimen. The side grooves were essentially to alleviate plane stress effects from the surface of the specimen which may be expected to complicate closure measurements (i.e. give rise to both plane stress and plane strain effects in the compliance curves) [2].

Figure 3.17 shows the overall CCT testing set-up. A pulsed four-probe potential drop (PD) system was used to monitor the physical crack length (offering higher accuracy and stability than a two-probe system). Four strain gauges (two attached on each face of the specimen at symmetrical positions) were used to ensure good alignment of the specimen in the test machine before testing was started. For CA fatigue crack growth, all specimens were tested at an R-ratio, of 0.1 according to ASTM Standard E647 [9]. Step-wise load shedding methods (with fixed ΔK values at each step) were used to obtain $da/dN \sim \Delta K$ curves for all the materials. The reduction in ΔK of adjacent ΔK steps was about ~ 10% of the previous ΔK until reaching the ΔK_{th} (i.e. cracks stop to grow). Crack growth rate measurements were taken during the load shedding process: whilst this is not part of the ASTM E647 standard, care were taken to ensure the crack growth had stabilised during each growth step (a minimum crack extension of 0.50 mm or 5 times the previous monotonic plastic zone size was used). Experience of the stability of the equipment shows sensitivity to changes in crack length measurement is of the order of 10 μm. A conventional crack mouth clip gauge was used to record crack opening displacements (COD) proving global specimen compliance curves.

It must be noted that in some experiments, whilst considerable effort was made in ensuring accurate initial alignment of the samples, problems were encountered with asymmetric crack fronts. In the first instance, this has attributed to slipping in the plate

grips during loading. To overcome this problem, the plate grips were redesigned to give better alignment to the samples. Fresh gripping faces were cut and additional alignment pins inserted through the CCT panel and grips.

For overload testing, similar to the CA tests, the PD system was used to monitor physical crack length increments. Near-tip strain gauges were employed to record local compliance curves which are later used to define closure points. Figure 3.18 shows a typical VA CCT fatigue crack growth testing experimental setup. It should be noted that additional mechanical tests were performed as part of the synchrotron tomography investigations reported in Chapter 5: given the rather specific nature of these tests and the details of the associated specimen preparation, the relevant experimental description is provided in Chapter 5.

3.3 Fractographic Assessment

Fractographic studies were carried out via FEG-SEM, in which the fatigue crack surfaces at different ΔK levels were studied and compared for each of the materials. Three-dimensional (3D) fracture surface topography was also quantified via Rank-Hobson Talysurf stylus surface contact profilometry and "Taicaan" polychromatic source (white light) optical profilometry to study the influences of fracture surface asperity roughness on fatigue crack closure (see Chapter 4 and 6). The operating principle of the Talysurf is quite simple: a stylus runs over a surface, and its height displacements are recorded via capacitance transducer, then yielding a profile of the surface (see Figure 3.19). Whilst the depth resolution of the Talysurf is dependent upon surface geometry and stylus radius, a value of the order of 0.1μm is expected [10]. Figure 3.20 illustrates the Taicaan system and its working principle. A poly-chromatic light source is used, with a mirror then feeding reflected light to a spectrometer for the detection of the light frequency in focus on the surface; for example, the λ3 wavelength is shown to be in focus in Figure 3.20 (b). By calculating the focus distances between the sample surface and lens from the corresponding wavelength at each point, a 3D surface profile can be obtained [11]. In terms of resolution, Taicaan is a significant improvement over the Talysurf, providing detail measurement down to ~ 10 nm [12].

Parts of the cracked samples from the CCT tests were also sectioned in the L-T and L-S planes to measure crack profiles in conjunction with EBSD for local grain structure and texture assessment. Figure 3.21 shows an example of the sample preparation route for EBSD assessment of crack profiles in the L-S plane. Sections of crack profile were cut from each sample at different ΔK levels by using a low speed diamond saw to limit any damaging effect to the fracture surface. Before the sections were cold-mounted in epoxy resins, the fracture surface was protected by applying a soluble varnish layer. The mounted sections were then mechanical polished down to a 0.02 μm. This was followed by electropolishing to remove any deformed layer on the surface prior to EBSD analysis (see Chapter 4 for details). The samples were broken out of the mounting resin and the varnish layer removed for simultaneous imaging of the fracture surfaces and underlying grain structure in the SEM.

References

[1] ASTM-E8M-96, *Annual Book of ASTM Standards*. 1996, Philadelphia, PA: ASTM International, p. 76-96.

[2] Y. Xu, *Closure assessment and overload transient behaviour in damage tolerant airframe materials*. Ph.D thesis, University of Southampton. 2001.

[3] F. Lefebvre, *Fatigue crack growth and shielding in damage tolerant aluminium alloys*. Ph.D First year report, University of Southampton. 2001.

[4] HKL Technology, Denmark (http://www.hkltechnology.com).

[5] A.W. Bowen, *Materials Science and Technology*, 1990. **6**: p. 1058-1071.

[6] I.J. Polmear, *Light Alloys*. 3rd ed, eds. R. Honeycombe and P. Hancock. 2000, Oxford: Butterworth-Heinemann.

[7] T.J. Warner, R.A. Shahani, P. Lassince, and G.M. Raynaud, *Research Report of Pechiney*. 1998, Pechiney CRV, France.

[8] J.D. Robson and P.B. Prangnell, *Acta Materialia*, 2001. **49**: p. 599-613.

[9] ASTM-E647, *Annual Book of ASTM Standards*. 1996, Philadelphia, PA: ASTM International, p. 565-601.

[10] Taylor Hobson Ltd., UK (http://www.taylor-hobson.com).

[11] J. McBride and C. Maul, *IEICE Transactions on Electronics*, 2004. **E87-C(8)**: p. 1261-1267.

[12] Taicaan Technology Ltd., UK (http://www.taicaan.com).

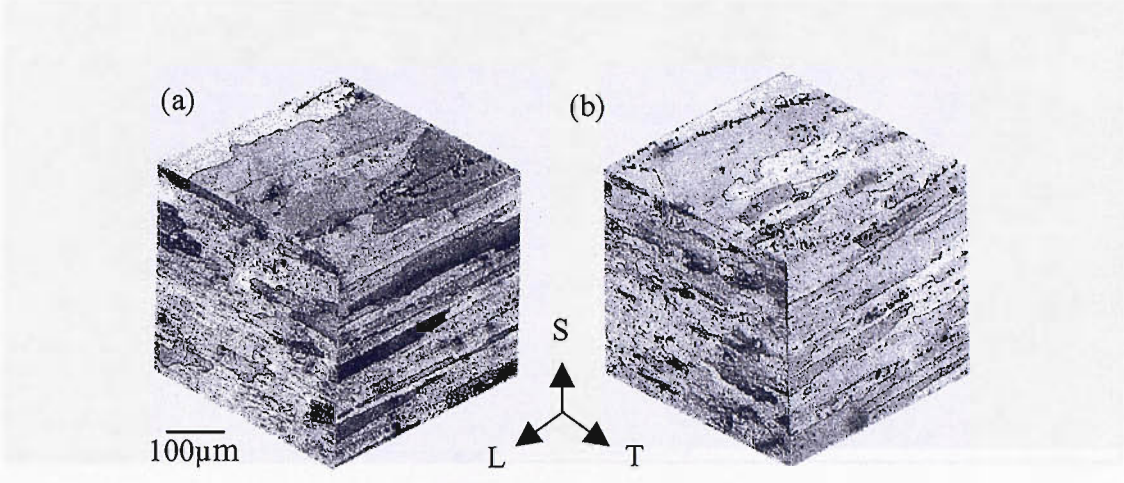

Figure 3.1 Grain structures of (a) 2024A, (b) 2024 [2].

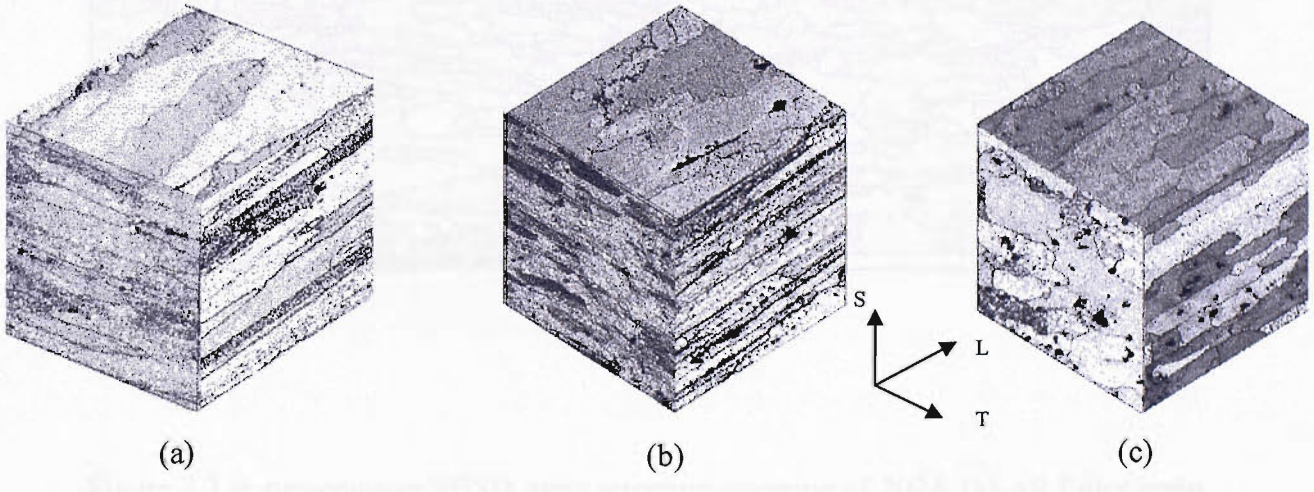

Figure 3.2 Grain structures of (a) 2027- ReX(8), (b) 2027- ReX(55), and (c) 2027- ReX(100) [3].

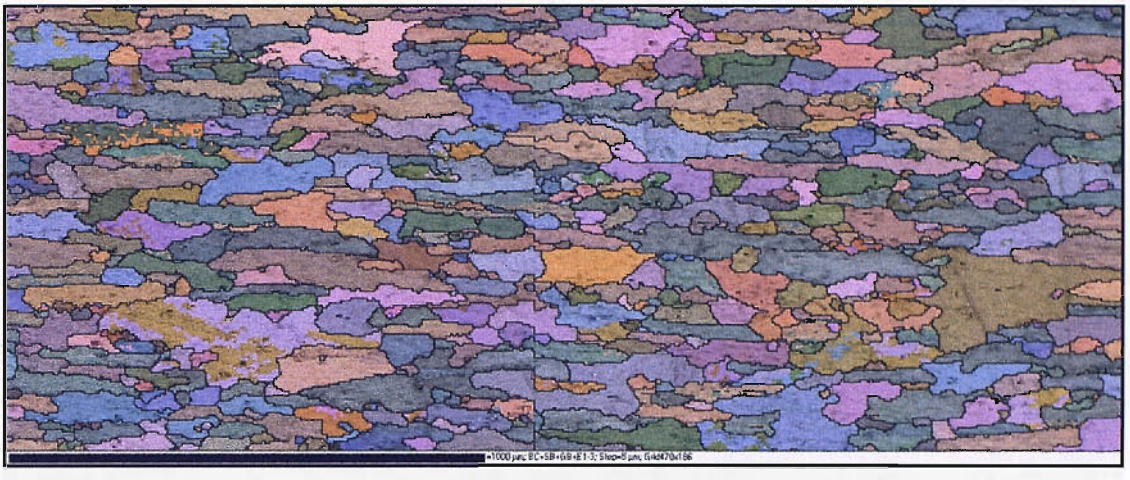

(a)

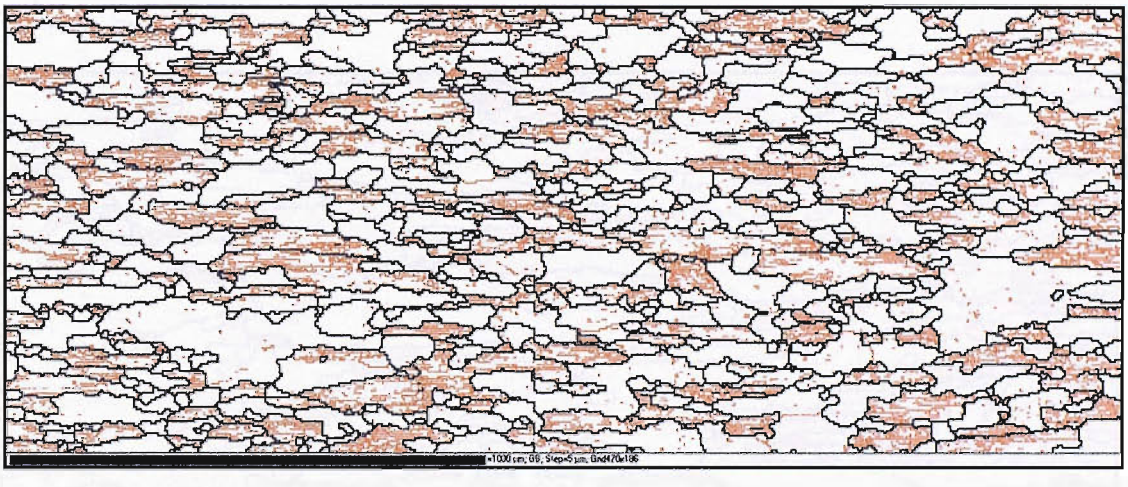

(b)

Figure 3.3 Representative EBSD grain structure mapping of 2024. (a) All Euler grain map with band contrast, (b) High angle and low angle grain boundary map.

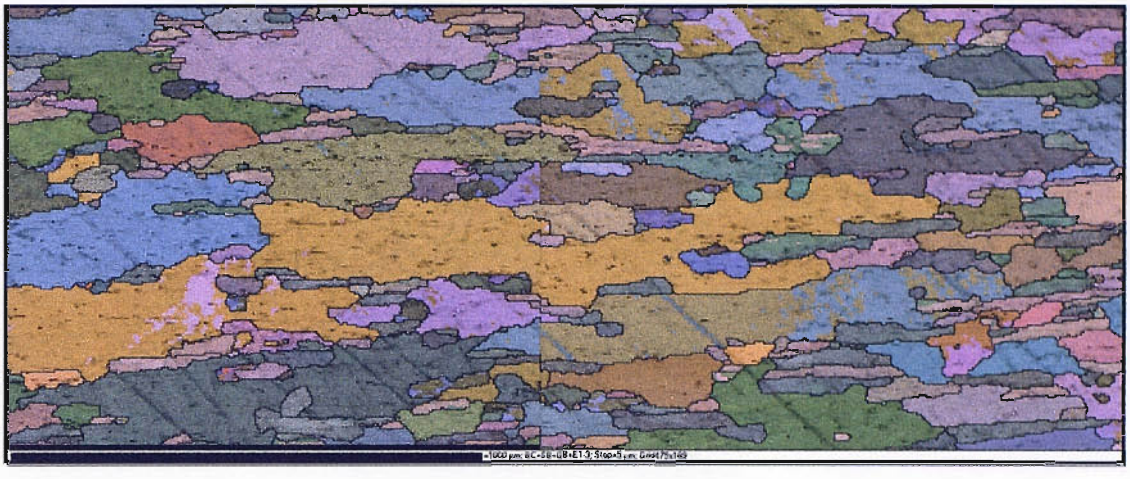

(a)

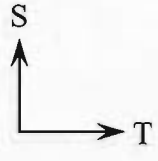

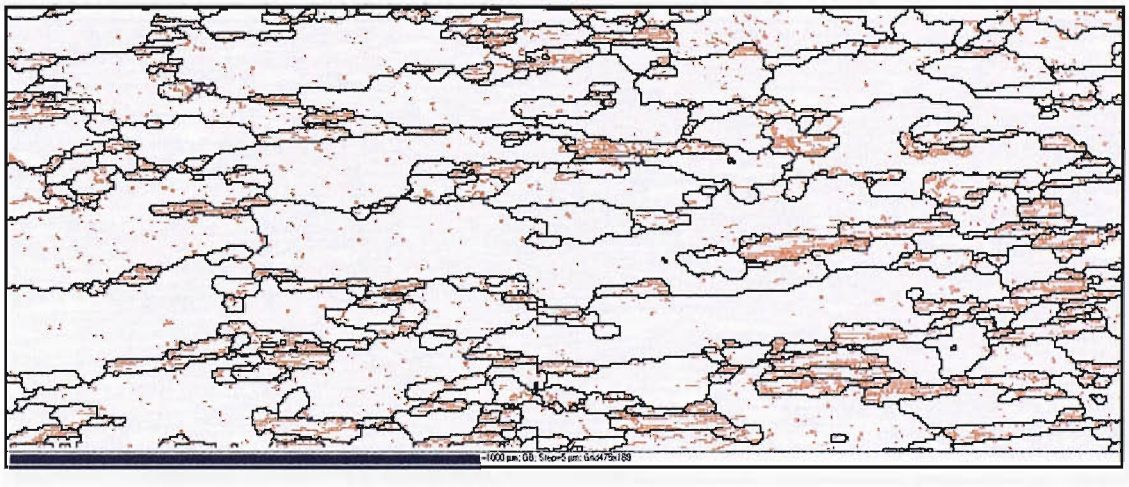

(b)

Figure 3.4 Representative EBSD grain structure mapping of 2024A. (a) All Euler grain map with band contrast (b) High angle and low angle grain boundary map.

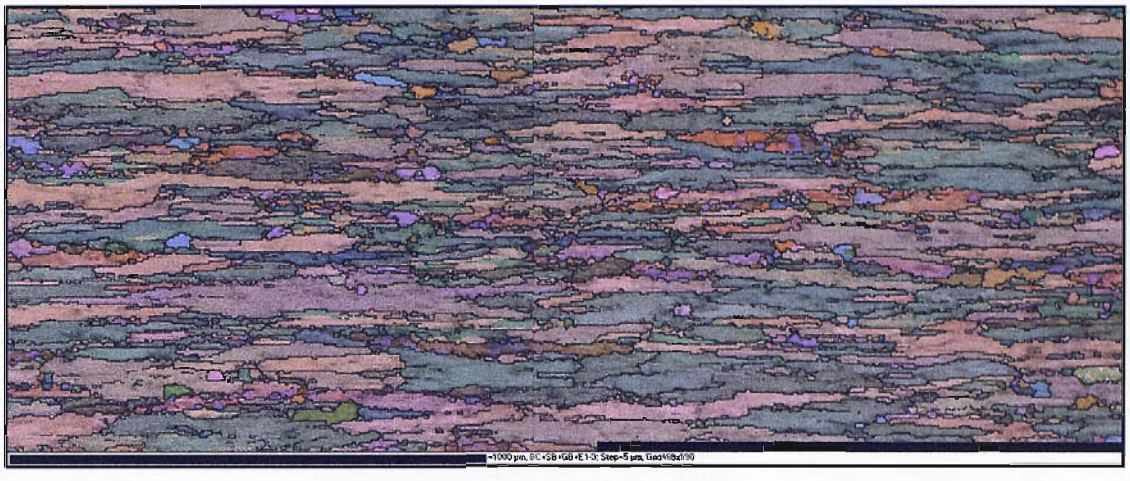

(a)

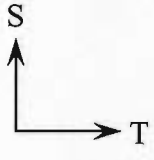

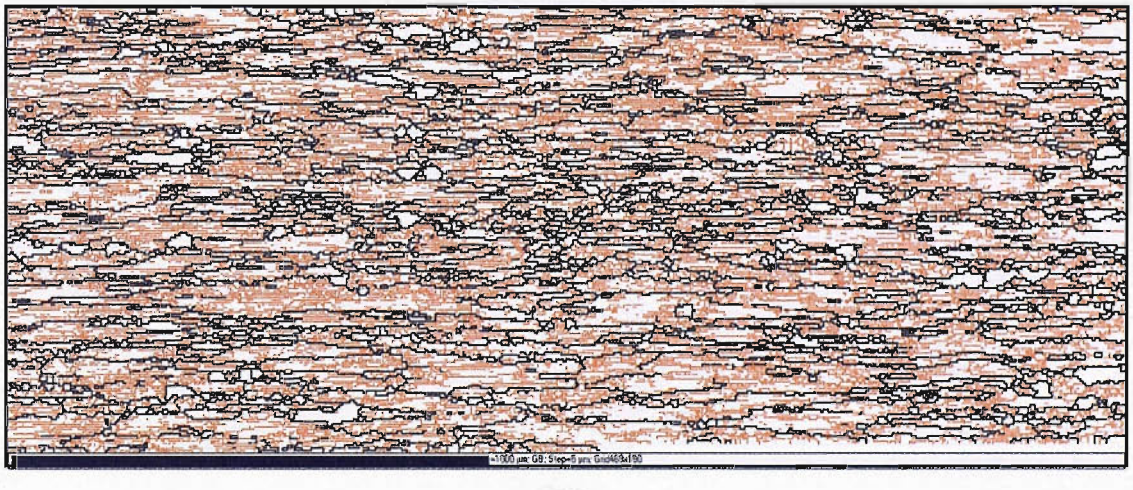

(b)

Figure 3.5 Representative EBSD grain structure mapping of 2027- ReX(8). (a) All Euler grain map with band contrast (b) High angle and low angle grain boundary map

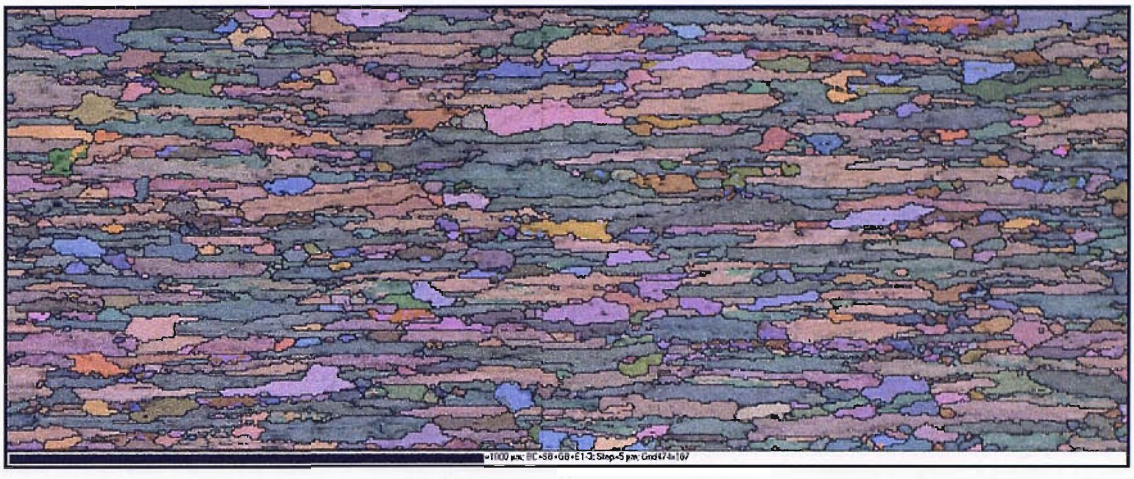

(a)

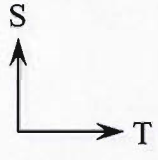

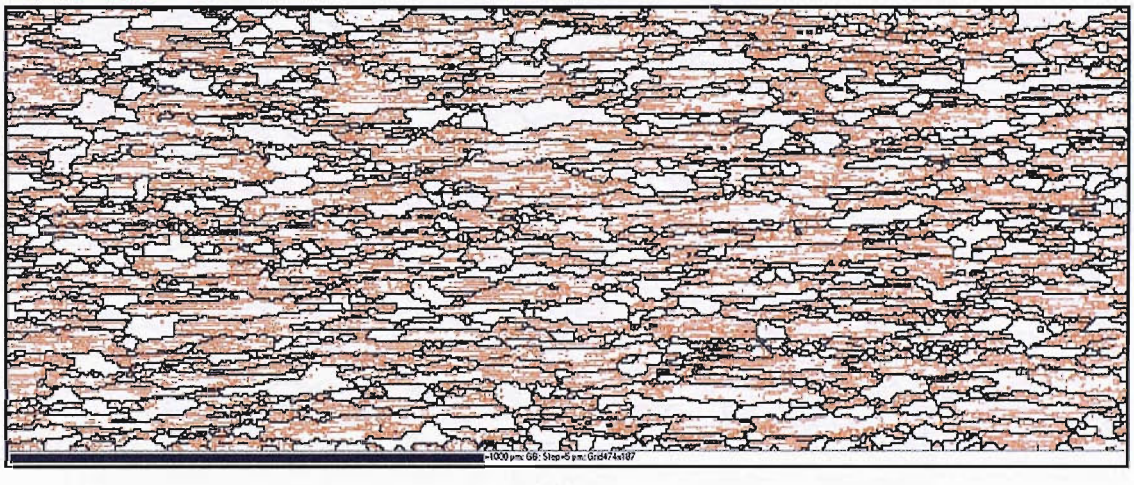

(b)

Figure 3.6 Representative EBSD grain structure mapping of 2027- ReX(55). (a) All Euler grain map with band contrast (b) High angle and low angle grain boundary map.

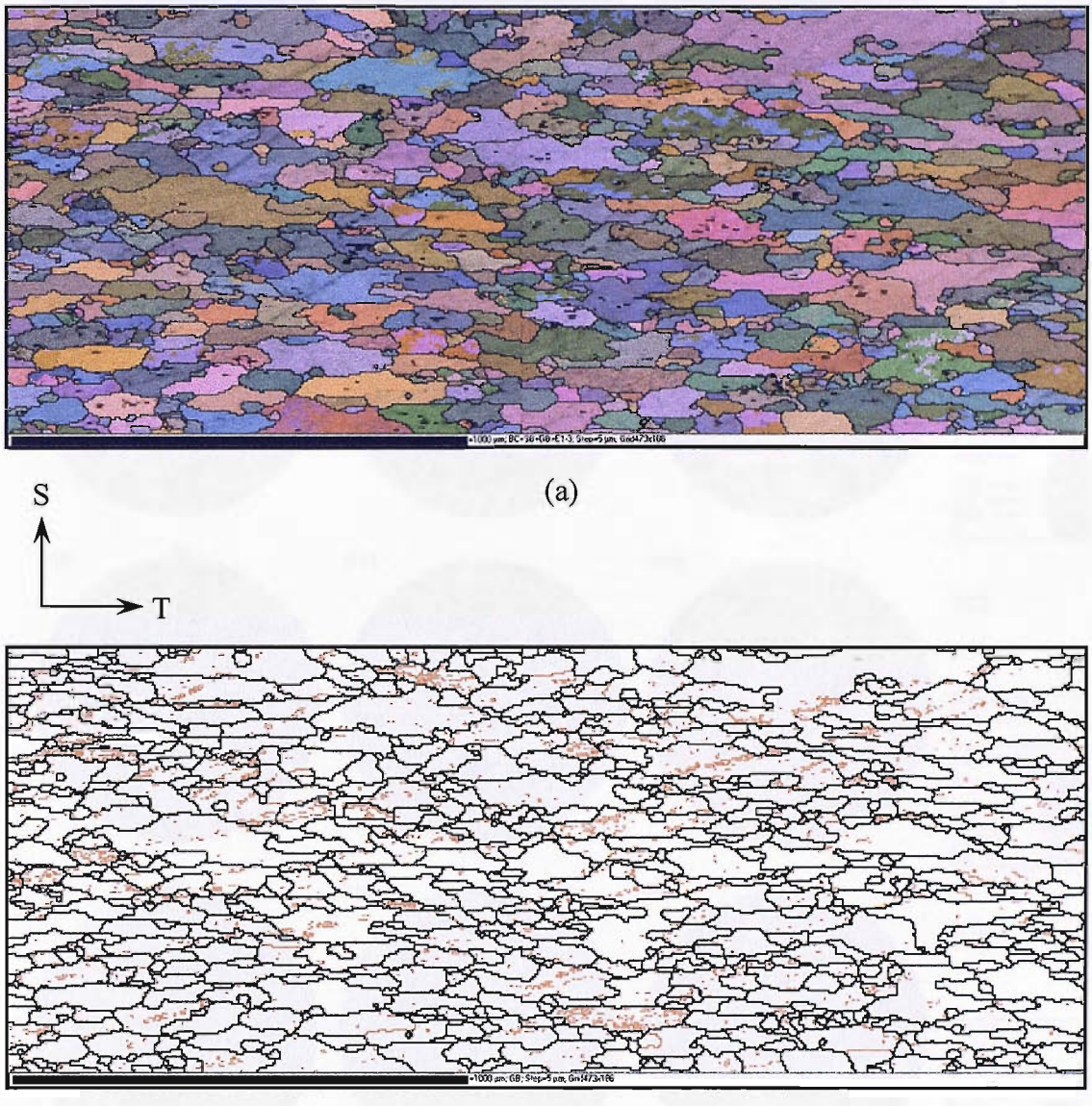

(a)

(b)

Figure 3.7 Representative EBSD grain structure mapping of 2027- ReX(100). (a) All Euler grain map with band contrast (b) High angle and low angle grain boundary map.

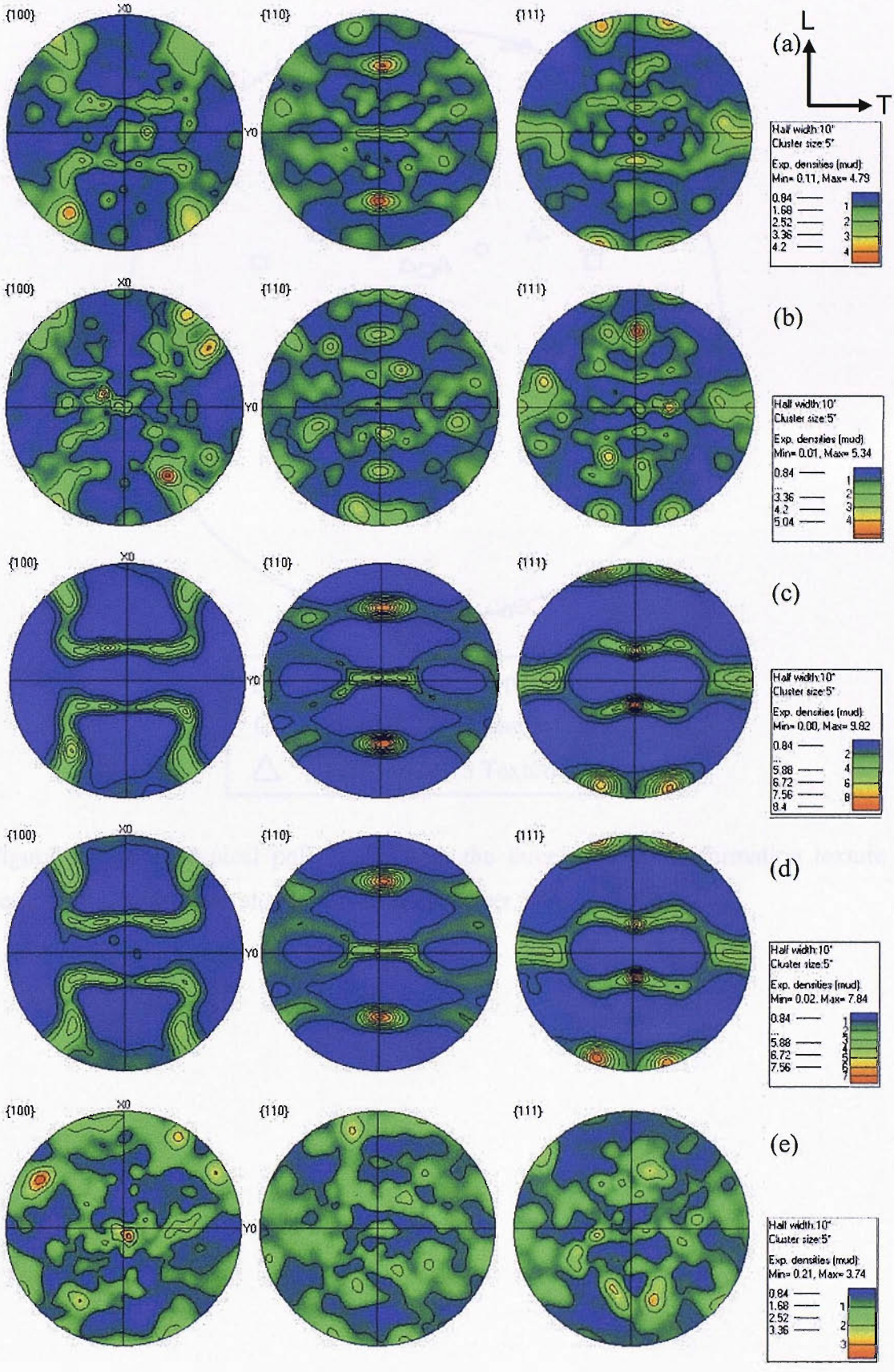

Figure 3.8 Representative {100}, {110} and {111} pole figures of (a) 2024-T351, (b) 2024A-T351, (c) 2027- ReX(8), (d) 2027- ReX(55) and (e) 2027- ReX(100).

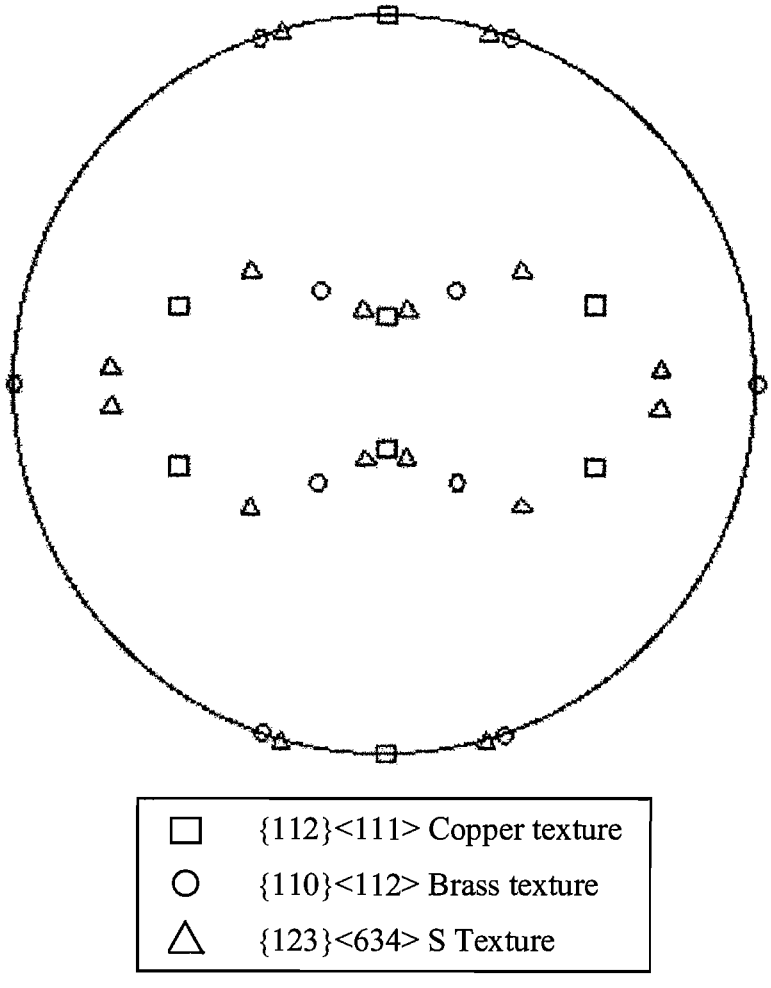

Figure 3.9 {111} typical pole figure with the three common deformation texture components in wrought aluminium alloys (Copper, Brass and S).

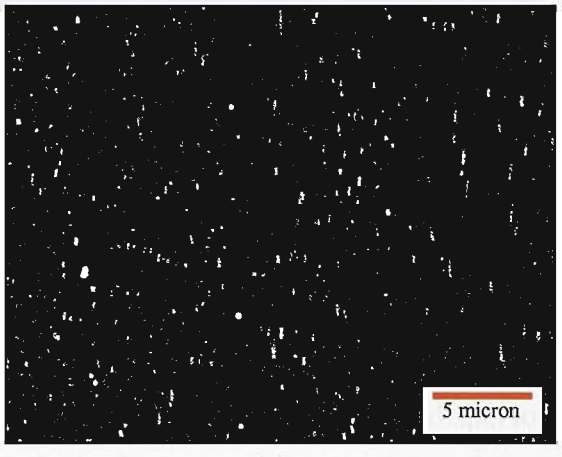

(a)

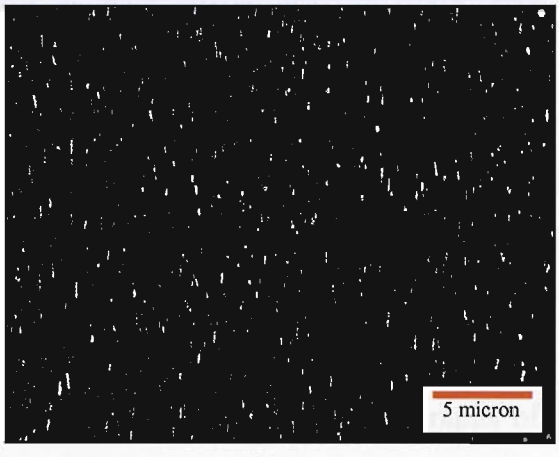

(b)

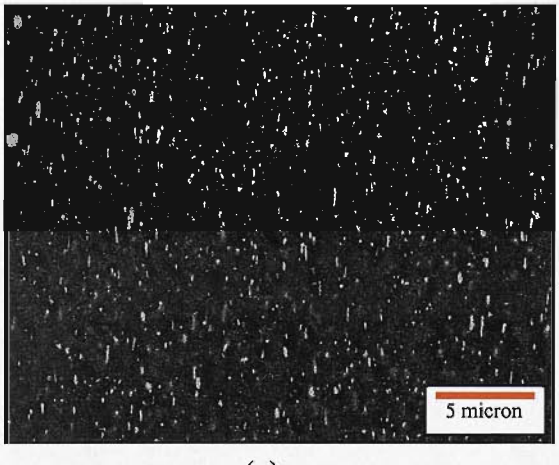

(c)

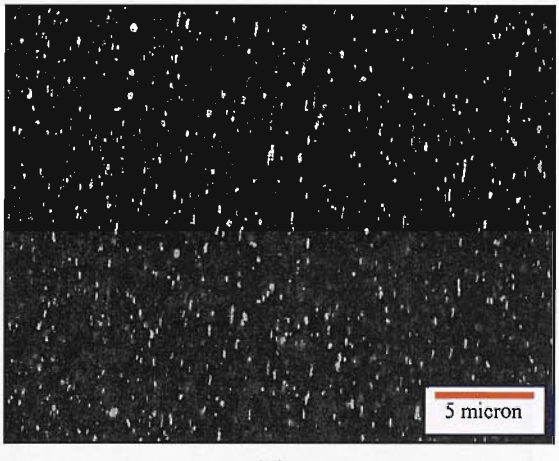

(d)

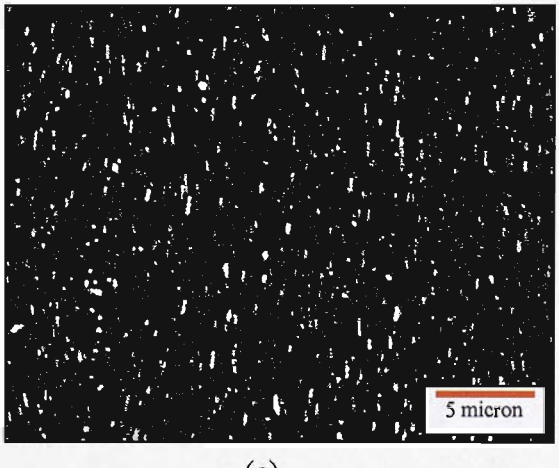

(e)

Figure 3.10 FEG-SEM back scattered electron images of dispersoid distributions in (a) 2024A, (b) 2024, (c) 2027-ReX(8), (d) 2027-ReX(55), and (e) 2027-ReX(100).

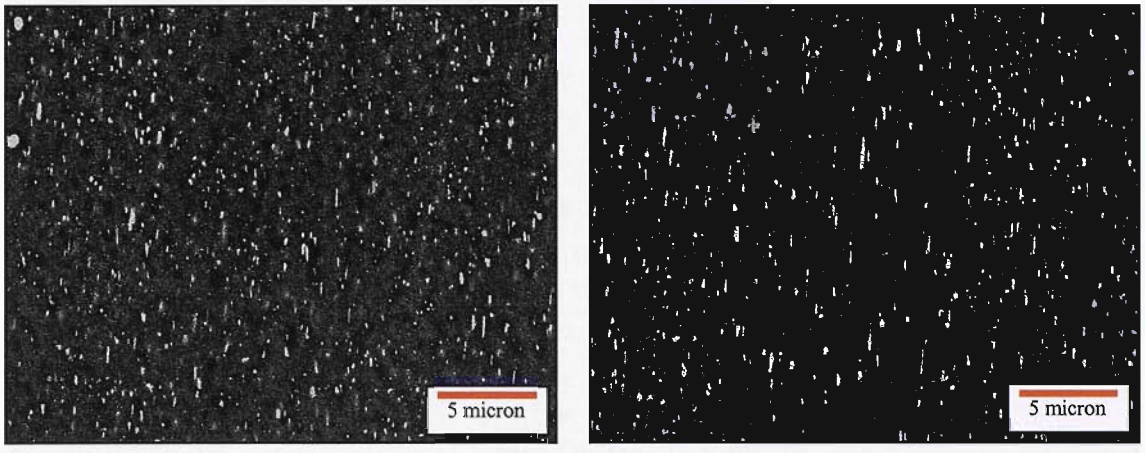

Figure 3.11 Variations in local dispersoid distribution in equivalent micrographs of 2027-ReX(8).

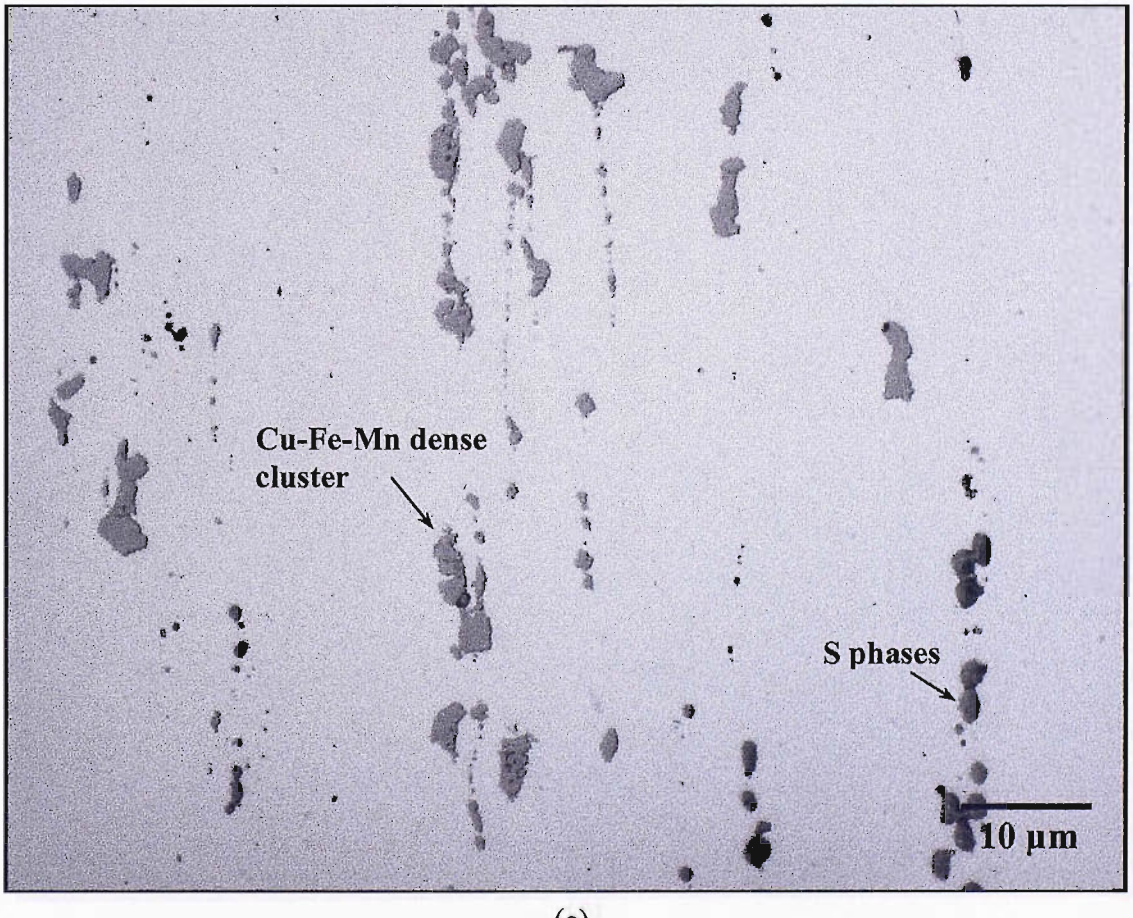

(a)

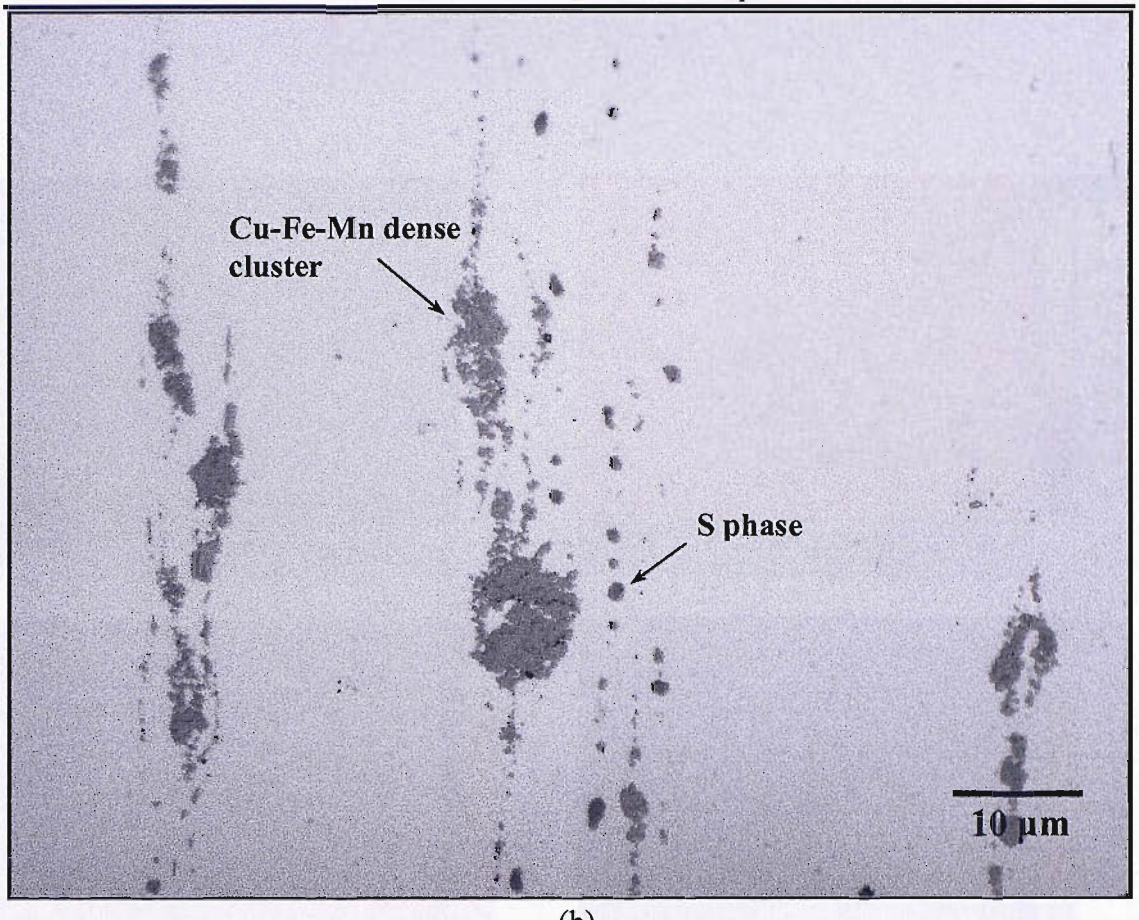

(b)

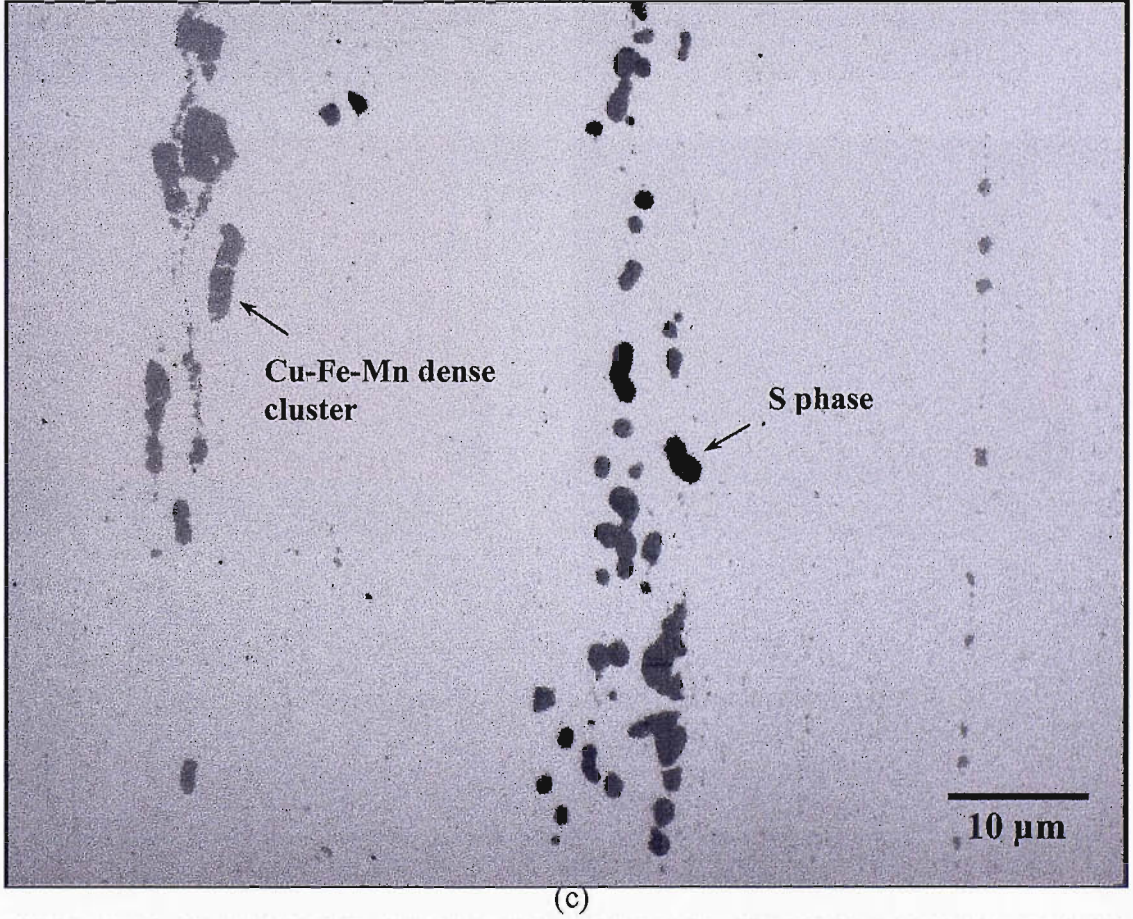

(c)

Figure 3.12 Representative intermetallic particles in (a) 2024, (b) 2024A and (c) 2027-ReX(55), in the L-S plane.

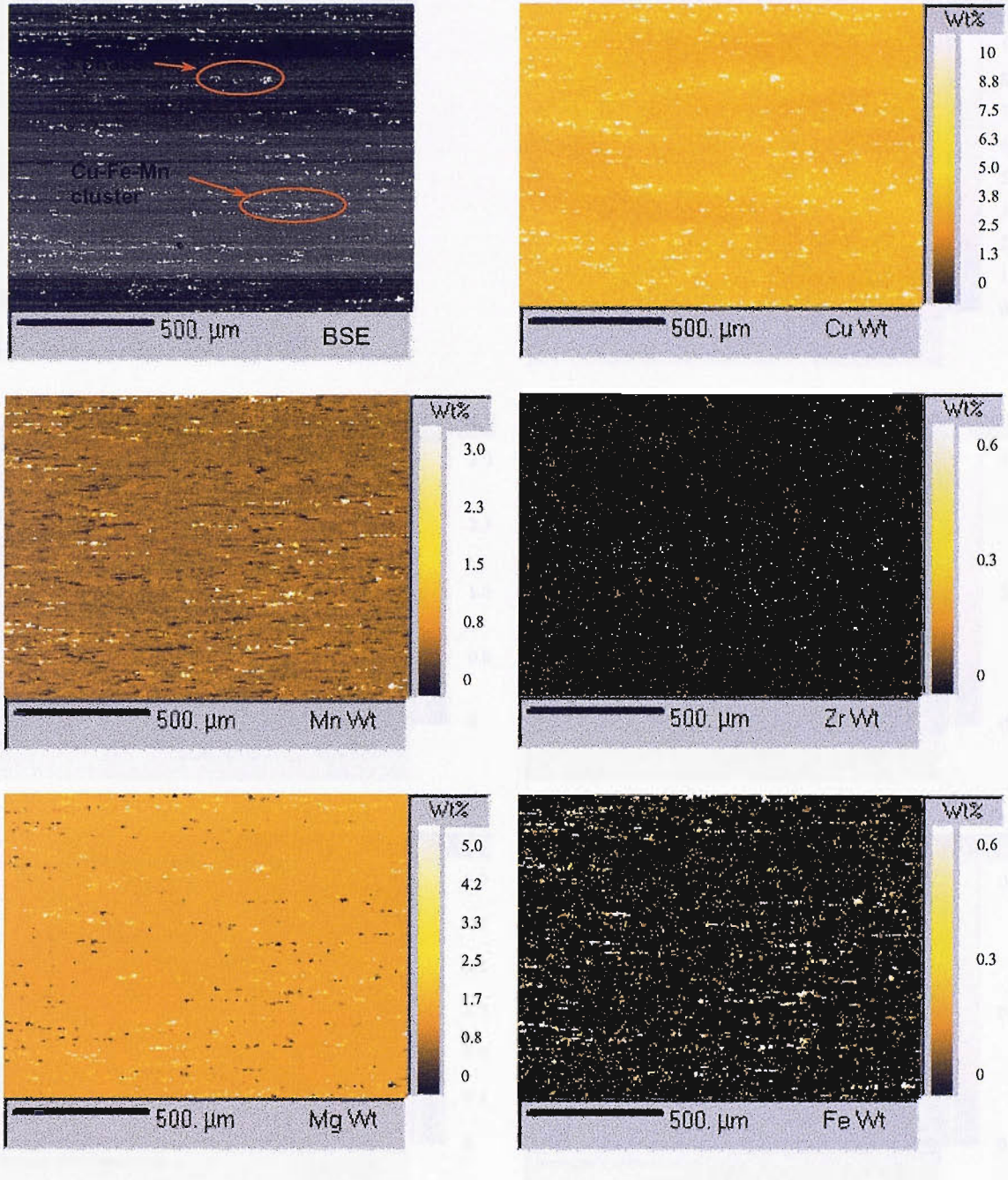

Figure 3.13 EPMA quantitative alloying element mapping of 2024.

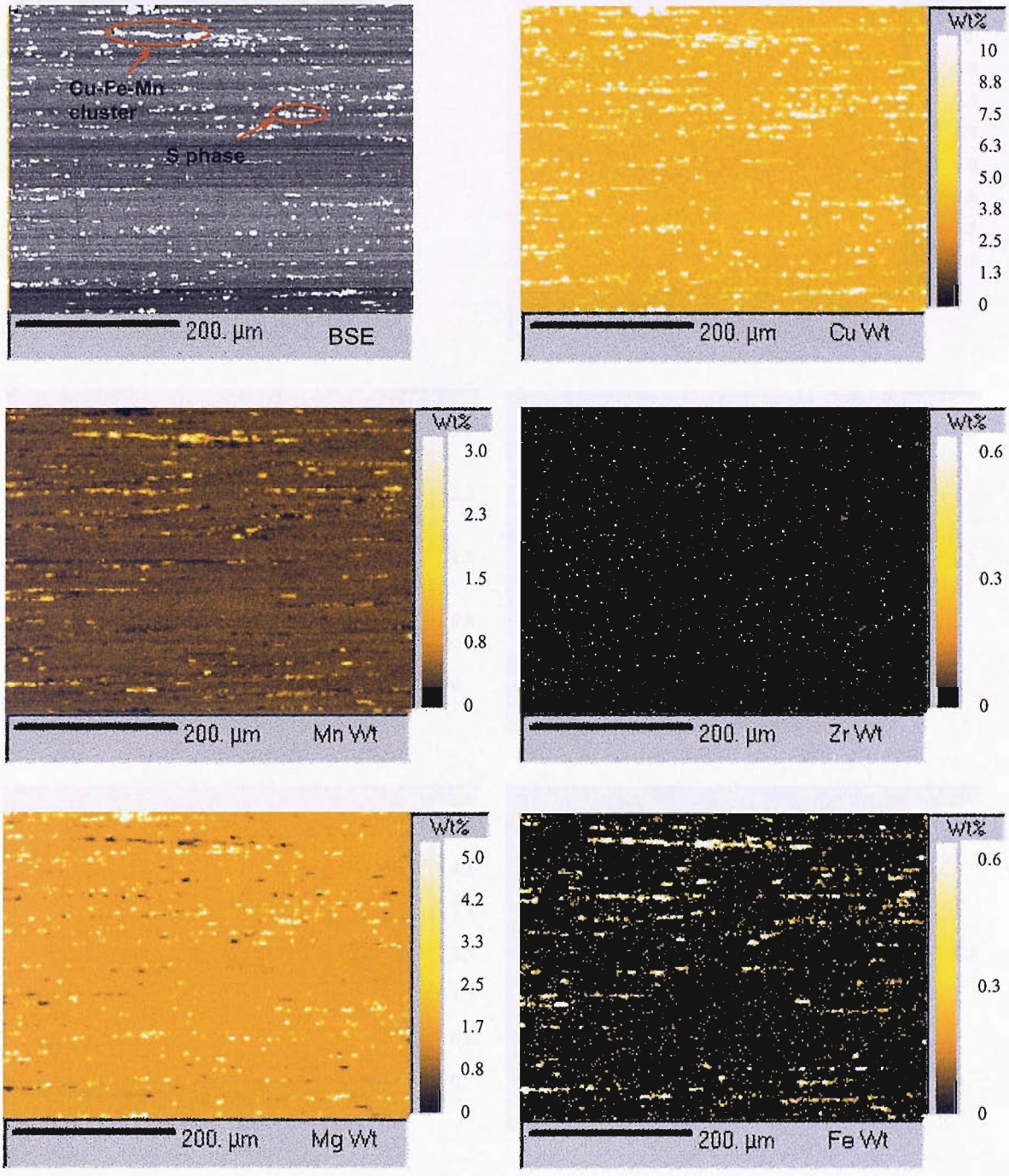

Figure 3.14 EPMA quantitative alloying element mapping of 2024A.

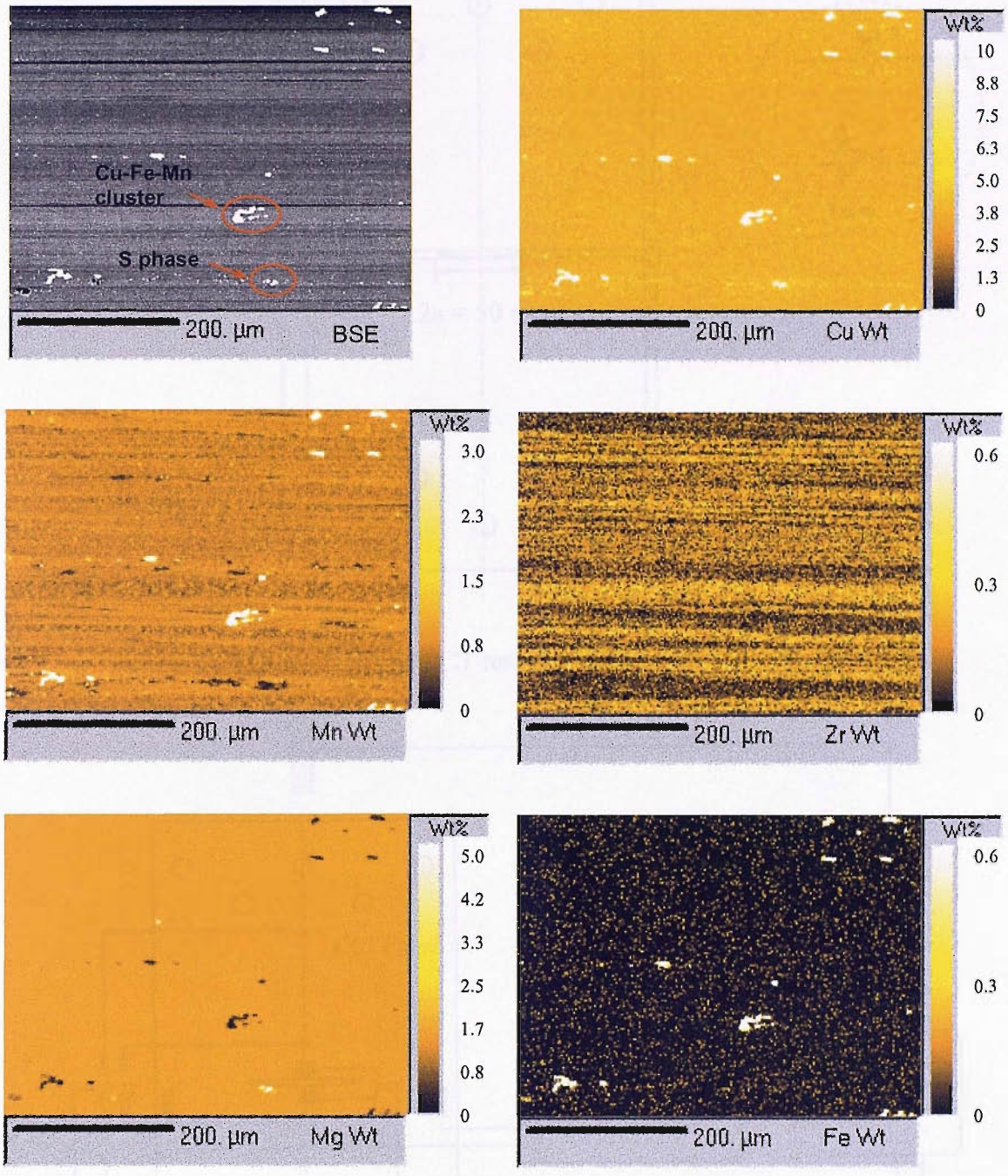

Figure 3.15 EPMA quantitative alloying element mapping of 2027-ReX(8).

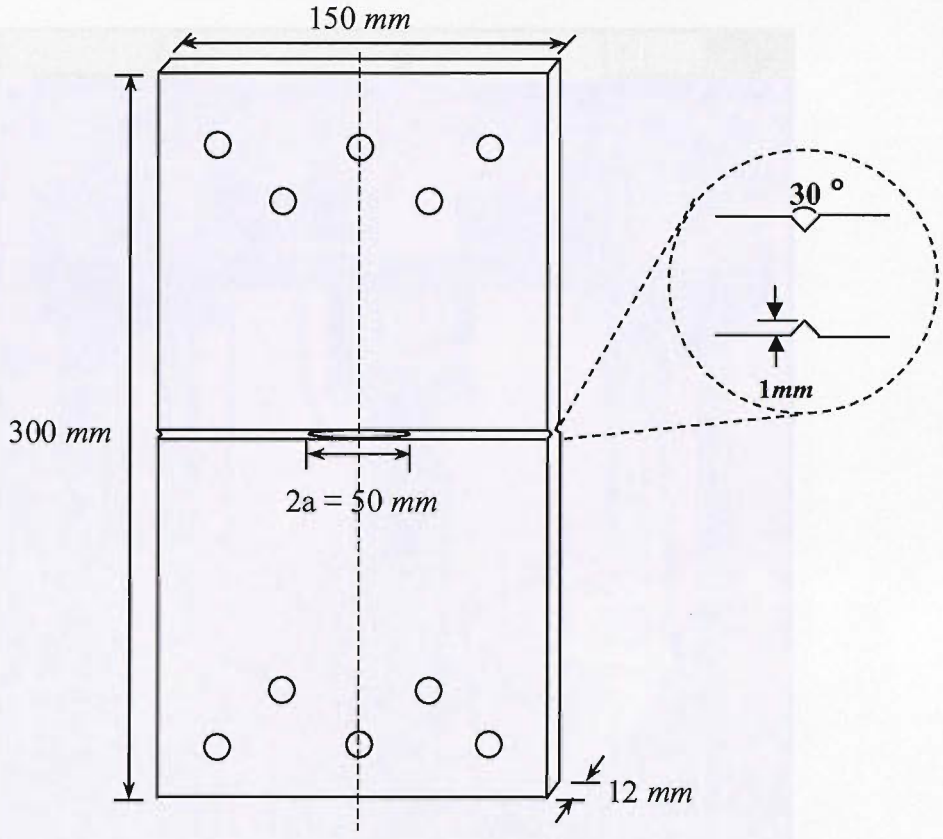

Figure 3.16 Dimensions of CCT test specimens used for fatigue testing.

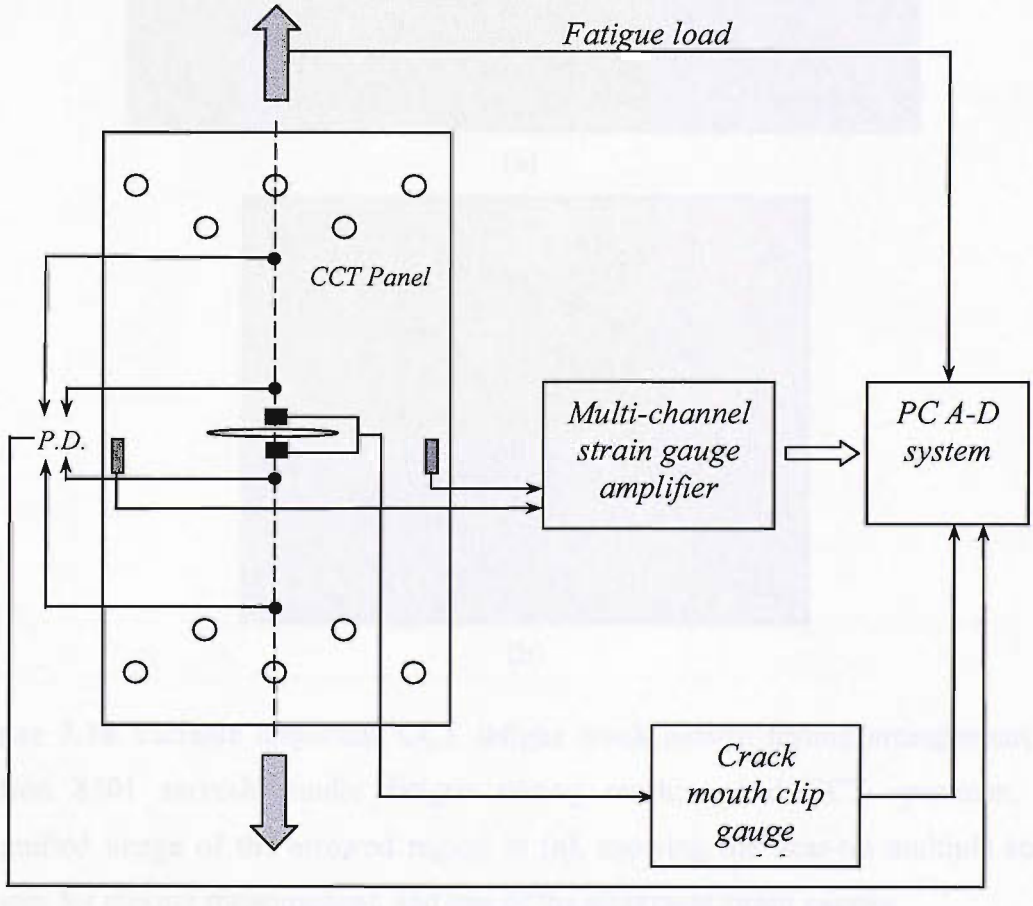

Figure 3.17 Schematic diagram of the CCT fatigue test set-up.

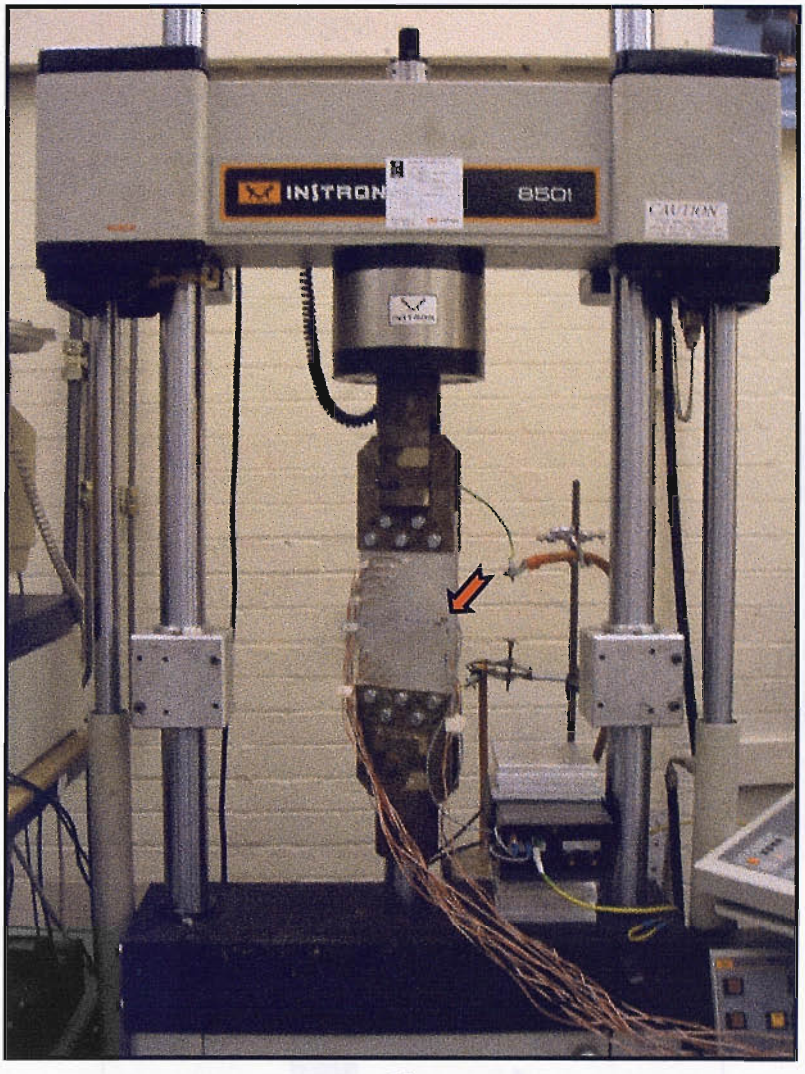

(a)

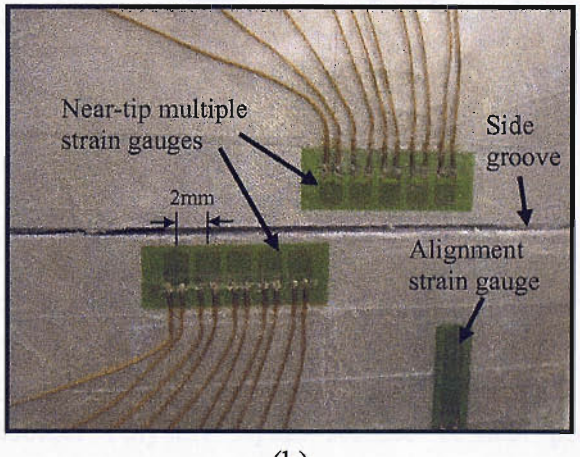

(b)

Figure 3.18 Variable amplitude CCT fatigue crack growth testing arrangement (a) Instron 8501 servo-hydraulic fatigue testing machine and CCT specimen, (b) magnified image of the arrowed region in (a), showing the near-tip multiple strain gauges for closure measurement, and one of the alignment strain gauges.

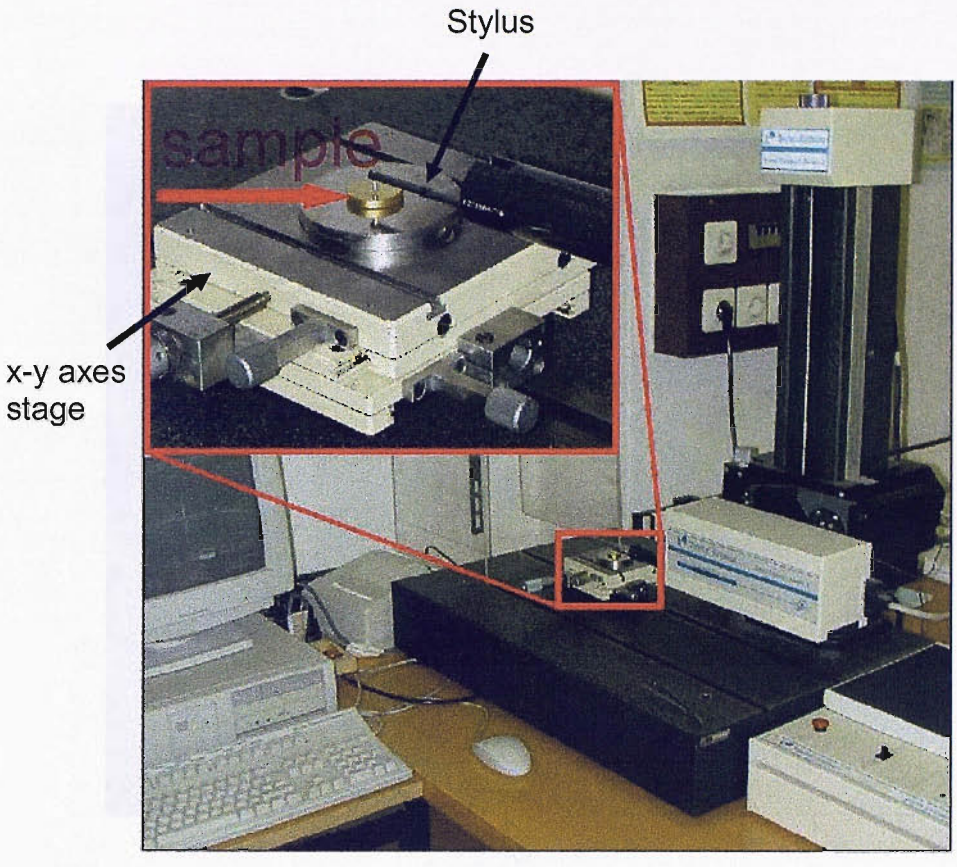

(a)

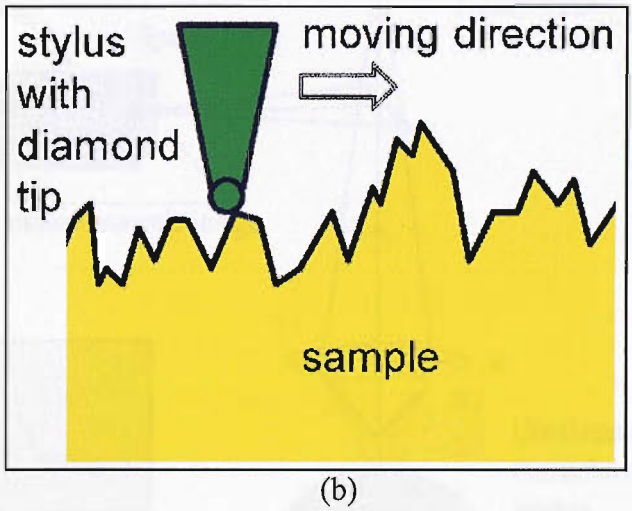

(b)

Figure 3.19 Rank-Hobson Talysurf stylus surface contact profilometry; (a) The Talysurf system. (b) Schematic diagram of working principle.

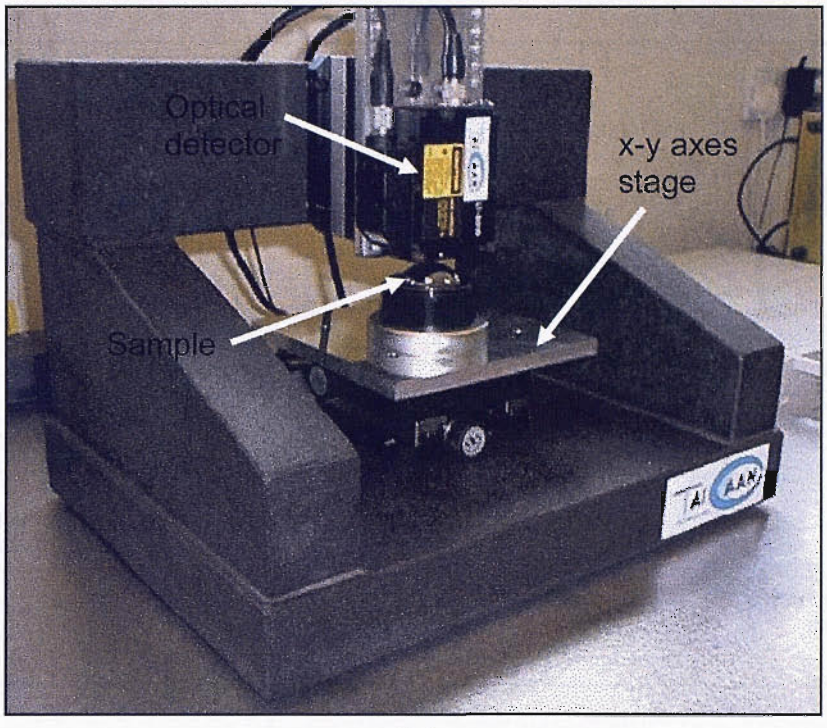

(a)

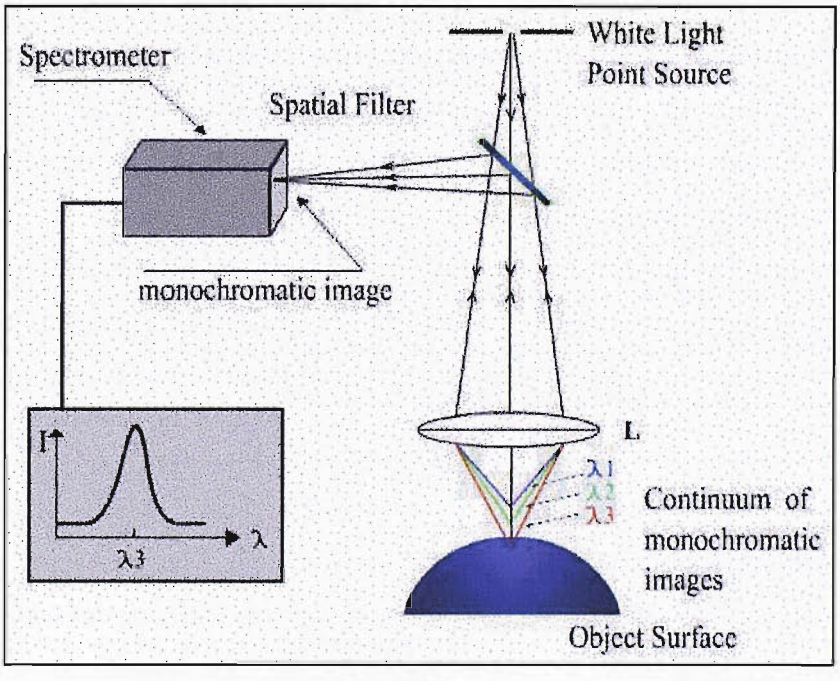

(b)

Figure 3.20 Taicaan white light optical profilometry; (a) the Taicaan system. (b) schematic diagram of working principle [11].

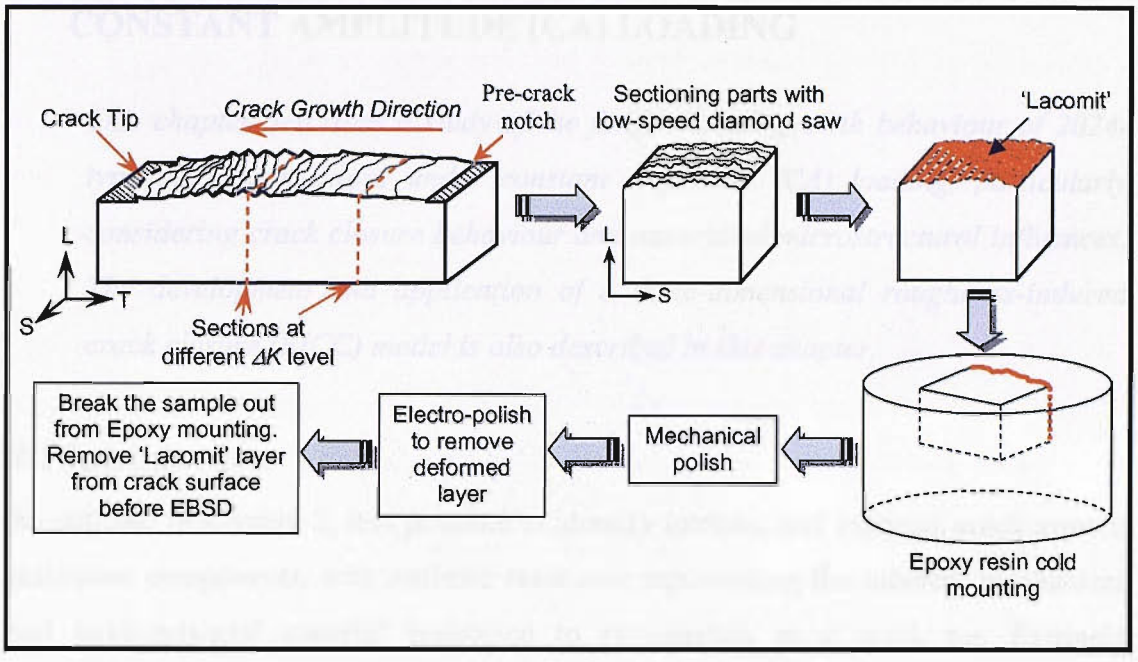

Figure 3.21 Sample preparation route for EBSD assessment of crack profiles.

4. FATIGUE CRACK GROWTH BEHAVIOUR AND ROUGHNESS-INDUCED CRACK CLOSURE MODELLING ASSESSMENT OF 2024-TYPE ALUMINIUM ALLOYS UNDER CONSTANT AMPLITUDE (CA) LOADING

This chapter describes a study of the fatigue crack growth behaviour of 2024-type aluminium alloys under constant amplitude (CA) loading, particularly considering crack closure behaviour and associated microstructural influences. The development and application of a three-dimensional roughness-induced crack closure (RICC) model is also described in this chapter.

4.1 Introduction

As outlined in Chapter 2, it is possible to identify intrinsic and extrinsic crack growth resistance components, with intrinsic resistance representing the inherent mechanical and environmental material resistance to propagation at a crack tip. Extrinsic resistance represents a variety of localised internal mechanical influences that tend to attenuate the crack driving force experienced at a crack tip. Since the crack closure shielding concept was first proposed by Elber [1, 2], it has been recognised by a wide variety of authors as a major extrinsic influence on fatigue crack growth behaviour in common structural materials [3, 4].

In term of PICC, over the years, various numerical and analytical model have been developed by different investigators: among the most popular crack closure models, the work of Newman [5-9] may be recognised, however, it is only based on PICC effects without explicit treatment of other closure mechanisms. RICC may be particularly identified with the influences of microstructure on crack path, and is associated with mismatch between crack surfaces exhibiting surface asperities behind the crack tip. Several attempts have been made to model RICC, e.g. see [10-13]. Whilst these models adopt a variety of approaches, all of the available approaches, to the best of the authors knowledge, suffer from an essentially arbitrary treatment of the shear offsets required for the asperities in a crack wake to come into physical contact during unloading. Recent work by Parry and co-workers [14-16] has shown a novel description of RICC processes via finite element and analytical modelling that include a quantitative description of shear deformation as a function of the crack path. The

results suggest that the mechanism by which closure occurs is strongly dependent on residual plastic strains arising from the crack propagation process, rather than conventionally suggested 'global' shear displacement due to mixed-mode behaviour at the crack tip. The shear deformation at asperity tips in the wake of a deflecting crack has been identified as the primary factor in determining RICC influence. It is however worth noting that there of course certain limitations in this FE model, where the crack path for example is 'pre-determined' by the user, i.e. the crack deflection angle and length is pre-set for the crack to grow along. Whilst the crack path is predetermined, parametric studies in terms of deflection angle (θ), stress intensity range (ΔK) and deflection length (L) have been quantitatively explored for the various parameters involved, as described in the work of both Parry [17] and Singh [18]. Therefore, the effort is still thought to provide an invaluable insight of the micromechanisms of RICC. To date this previous work has only considered 2-dimensional representations of crack growth where only mode II shear offsets may generate crack closure. However, recent tomography data [19] highlight the potential role of mode III contacts that may arise in crack wakes (see Chapter 5 for details). The present study extends the previous analytical model [14-16] and particularly seeks to: (a) estimate mode II and III shear effects on crack closure, and (b) assess model performance against real materials behaviour. Several advanced variants of the established aerospace alloy 2024-T351 (with different dispersoid contents and degrees of recrystallisation, as described in Chapter 3) are particularly studied for their micromechanistic influences on fatigue crack growth behaviour. 3D surface profilometry techniques are applied to obtain crack deflection parameters (deflection angles and length-scales) from fatigue fracture surfaces. In order to understand the fatigue crack growth behaviour in term of microstructural effects, detailed assessment of texture variant distributions, grain orientations and, grain boundary separations was carried out via EBSD.

4.2 Materials and Experimental Details

4.2.1 Materials

Detailed materials characterisation of the three materials tested are described previously in Chapter 3. Key points are as follows:

- 2024A and 2027 represent advanced variants of the 2024-type aluminium alloy (reduced Fe, Si).
- There are three 2027 conditions with different degrees of recrystallisation (ReX): nominally 8%, 55%, and 100%.
- 2024A and 2027 can respectively be considered as a *low* and *high* dispersoid variants of 2024, with 2027 having both high Mn levels and Zr alloying additions.
- 2024A has the largest scale grain structure.
- 2024A and 2027 have the lowest and highest tensile strength respectively, with strength levels decreasing with increasing degree of recrystallisation.

4.2.2 Fatigue Testing

As detailed in Chapter 3, constant amplitude centre-cracked tension (CCT) fatigue crack growth tests were carried out in laboratory air via load shedding in the LT orientation. A conventional crack mouth clip gauge was used to record crack opening displacements (COD), providing global compliance curves for crack closure measurement. Tests were carried out for the three 2027 materials, with three repeated tests being carried out for each material. Crack growth and closure data for 2024 and 2024A were made available from a previous project [20] using identical test arrangements.

4.2.3 Closure Measurement

The determination of closure point from mechanical compliance data was based on the two curve fitting approaches developed by Xu *et al.* [20]. The two curve fitting methods are based on a combination of fitting linear and quadratic functions to the upper and the lower parts of a compliance curve (see Figure 4.1) as outlined in Section 2.1.3.3 (under " mechanical compliance measurement"). A closure point is said to be valid when there is agreement from both curve fitting criteria indicating a good fit to the linear and quadratic functionality. Experience from repeat measurement of closure levels in different samples at the same stress intensity levels shows that that reproducibility of this measurement method is in the order of ±0.025 (in terms of $\Delta K_{eff}/\Delta K_{app}$).

4.3 Analytical RICC Model Formulation

As outlined in Section 4.1, previous work by Parry *et al.* [14-16] has identified residual shear deformation at asperity tips in the wake of a deflecting crack as the primary factor in determining RICC, as summarised in Figure 4.2. The simple 2D analytical modelling approach describes the mode II effective residual shear associated with a crack passing through a single representative crack turning point (i.e. asperity tip) and the subsequent fracture surface contact that will arise as the crack tip moves away from this point, see Figure 4.3. The main elements of this model are therefore estimating the crack opening along the deflected crack path as a function of applied load, and the mode II residual shear deformation at the crack turning point that will interfere with this opening (i.e. to generate crack closure). In the current study, a modified and improved analytical model has been developed and implemented in conjunction with the work of Singh and Kemp [16, 18] by considering fracture surface features in three-dimensions. In the following section, the general formulation of the 2D model, as originally developed by Parry [14-16], is described and summarised (i.e. only considering mode II asperity tip deformation), and then extended to consider additional mode III residual shear deformation (i.e. 3D effects).

4.3.1 Formulation of the 2D Analytical Model

- ***Crack opening***

The crack opening profile of a crack of length *2a*, lying in the *x-z* plane, parallel to the *x*-axis, in an infinite plate of a linear elastic material, under far-field tension σ, (as shown in Figure 4.4), under plane strain conditions, can be found from the equations of the elastic field displacements [21],

$$u_y = \frac{2\sigma}{E}\left(1-\nu^2\right)\sqrt{a^2-x^2} \tag{4.1}$$

where u_y is the elastic displacement of the crack flank in the *y*-direction at a distance x from the origin, E is the elastic modulus, ν is the Poisson ratio.

To express the opening behaviour of a deflected crack tip in this RICC model, as shown in Figure 4.5, if the assumption is made that the tensile opening of the final deflected section of the long nominally loaded mode I crack (of length a^*) behaves like a small undeflected mode I edge crack (also of a length a^*) of equivalent mode I stress intensity loading, with $k_{I(deflected)} = K_{I(undeflected)}$, then an approximation to the opening behaviour of the final deflected section of the crack can be expressed as,

$$u_y = \frac{2\sigma}{E}(1-\nu^2)\sqrt{a^{*2}-x^2} \tag{4.2}$$

with the elastic crack opening displacement δ being,

$$\delta = 2u_y = \frac{4k_{1(deflected)}(1-\nu^2)\sqrt{a^{*2}-x^2}}{E\sqrt{\pi a^*}} \tag{4.3}$$

The value of $k_{1(deflected)}$ is a function of the remotely applied mode I stress intensity factor K_I and the deflection angle θ. If the assumption that the final deflected section of the crack can be equated to a kink off a straight crack, as shown in Figure 4.6, then when a^*/b is small, the local mode I stress intensity factor k_1 is approximated by the following (elastic) expression for the stress intensity factor at the tip of a pupative kink [22],

$$k_1 = \frac{1}{4}\left(3\cos\frac{\theta}{2}+\cos\frac{3\theta}{2}\right)K_I \tag{4.4}$$

Combining Equation (4.3) and Equation (4.4) gives:

$$\delta = \frac{K_I(1-\nu^2)\left(3\cos\frac{\theta}{2}+\cos\frac{3\theta}{2}\right)\sqrt{a^{*2}-x^2}}{E\sqrt{\pi a^*}} \tag{4.5}$$

- ***Residual asperity deformation***

On the basis that forward plastic deformations associated with fatigue crack tip displacements are of necessity larger than those occurring in reverse (i.e. on unloading), residual shear deformations of a deflected crack tip may be considered to generate an effective mode II displacement, h_{II}, of the asperity tip that is left when the

crack changes direction (i.e. to generate a new crack wake asperity peak), see Figure 4.3. In first approximation, h_{II} is then equated to the residual crack tip shear displacements ($CTSD_{res}$) associated with the crack at the point of turning.

Considering a Dugdale-type strip yield model under far field mode II loading, the *CTSD* at maximum load under plane strain conditions can be expressed as [23]:

$$CTSD_{\max} = \frac{\sqrt{3}K_{\mathrm{II}\max}{}^{2}\left(1-\nu^{2}\right)}{E\sigma_{YS}} \tag{4.6}$$

Where $K_{II\max}$ is the maximum mode II stress intensity factor and σ_{YS} is the yield strength.

Upon unloading a degree of reversed crack tip sliding will occur. The effective yield stress controlling the reverse crack tip sliding displacement ($\Delta CTSD$) may be approximated as twice the yield stress for forward yielding [23], hence the change in *CTSD* (i.e. $\Delta CTSD$) due to cyclic mode II stress field, characterised by ΔK_{II}, is given by,

$$\Delta CTSD = \frac{\sqrt{3}\Delta K_{\mathrm{II}}{}^{2}\left(1-\nu^{2}\right)}{2E\sigma_{YS}} \tag{4.7}$$

Hence, the residual crack tip sliding displacement, $CTSD_{res}$ is given by,

$$CTSD_{res} = CTSD_{\max} - \Delta CTSD$$

$$CTSD_{res} = \frac{\sqrt{3}K_{\mathrm{II}\max}{}^{2}\left(1-\nu^{2}\right)\left(\frac{1}{2}+R-\frac{1}{2}R^{2}\right)}{E\sigma_{YS}} \tag{4.8}$$

$CTSD_{res}$ of a crack under a far field mode II load can be correlated to the $CTSD_{res}$ of a deflected crack by replacing $K_{II\max}$ by k_2, the local mode II stress intensity factor at the tip of a deflected crack. As in Equation (4.4), k_2 may be estimated by the local mode II stress intensity factor at the tip of a pupative kink:

$$k_2 = \frac{1}{4}\left(\sin\frac{\theta}{2}+\sin\frac{3\theta}{2}\right)K_I \tag{4.9}$$

Combining Equation (4.8) and Equation (4.9) gives:

$$CTSD_{res} = h_{II} = \frac{\sqrt{3}K_{\mathrm{I}\max}{}^{2}(1-\nu^{2})\left(\frac{1}{2}+R-\frac{1}{2}R^{2}\right)\left(\sin\frac{\theta}{2}+\sin\frac{3\theta}{2}\right)^{2}}{16E\sigma_{YS}} \tag{4.10}$$

There is some variation in the analytical expressions available for determining *CTSD* within the literature [23, 24]. The value for h_{II} which is used in the analytical model is therefore replaced by βh_{II}, where β is a scaling factor which may be expected to take values between approximately 1 and 4.

- ***Estimation of crack closure***

It can be seen from Figure 4.3 that crack closure will occur when $\delta = h_{II}\sin(2\theta)$. Combining Equation (4.5) and Equation (4.10) and rearranging to express the closure level, it follows:

$$\frac{K_I}{K_{\mathrm{I}\max}} = \frac{K_{cl}}{K_{\mathrm{I}\max}} = \beta\frac{\sqrt{3\pi}K_{\mathrm{I}\max}\left(\frac{1}{2}+R-\frac{1}{2}R^{2}\right)\left(\sin\frac{\theta}{2}+\sin\frac{3\theta}{2}\right)^{2}\sin 2\theta}{16\sigma_{YS}\sqrt{a^{*}}\left(3\cos\frac{\theta}{2}+\cos\frac{3\theta}{2}\right)} \tag{4.11}$$

4.3.2 Formulation of the 3D analytical model

The additional considerations in the 3D model compared to the 2D model are the crack twist angle (ϕ) and the mode III residual asperity shear deformation (h_{III}) in the through-thickness direction, as schematically illustrated in Figure 4.7. In this 3D model, to simplify the model, for the first instance, the through-thickness crack geometry was assumed to be trapezoidal. Based on the same general approach applied in the 2D model, by considering the contribution of mode III to the *CTSD* at maximum load, the $CTSD_{IIImax}$ can be expressed as,

$$CTSD_{III\max} = \frac{\sqrt{3}K_{\mathrm{III}\max}{}^{2}(1+\nu)}{E\sigma_{YS}} \tag{4.12}$$

Upon unloading a degree of reversed crack tip sliding will occur,

$$\Delta CTSD_{III} = \frac{\sqrt{3}\Delta K_{III}{}^2(1+\nu)}{2E\sigma_{YS}} \tag{4.13}$$

Hence, the $CTSD_{IIIres}$ is given by,

$$CTSD_{IIIres} = \frac{\sqrt{3}K_{III\max}{}^2(1+\nu)\left(\frac{1}{2}+R-\frac{1}{2}R^2\right)}{E\sigma_{YS}} \tag{4.14}$$

$CTSD_{IIIres}$ of a crack under a far field mode III load can be correlated to the $CTSD_{IIIres}$ of a deflected crack by replacing K_{IIImax} by k_3, the local mode III stress intensity factor at the tip of a twisted crack. k_3 is given by the equation for local mode III stress intensity factor at the tip of pupative kink after Faber and Evans [25],

$$k_3 = K_{31}(\phi)K_I$$
$$with \quad K_{31}(\phi) = \cos^4\left(\frac{\theta}{2}\right)\left[\sin\phi\cos\phi\left(\cos^2\left(\frac{\theta}{2}\right)-2\nu\right)\right] \tag{4.15}$$

Considering pure twist in the determination of k_3, i.e. $\theta = 0$, hence k_3 becomes,

$$k_3 = K_I[\sin\phi\cos\phi(1-2\nu)] \tag{4.16}$$

Combination of Equation (4.16) and (4.14) gives the residual mode III displacement, h_{III},

$$CTSD_{IIIres} = h_{III} = \frac{\sqrt{3}K_{I\max}{}^2(1+\nu)\left(\frac{1}{2}+R-\frac{1}{2}R^2\right)[\sin\phi\cos\phi(1-2\nu)]^2}{E\sigma_{YS}} \tag{4.17}$$

Figure 4.7 (c) illustrates a simple proposed superposition of asperity offsets created by the local mode II and mode III effects. Thus crack closure is estimated to occur when,

$$\delta = h = h_{II}\sin(2\theta) + h_{III}\cos\theta\sin\phi \tag{4.18}$$

Hence, combination of Equation (4.3), (4.10) and (4.17) gives the overall closure level,

$$\frac{K_{cl}}{K_{\mathrm{Imax}}} = \beta \frac{\sqrt{3\pi} K_{\mathrm{Imax}} \left(\frac{1}{2} + R - \frac{1}{2} R^2 \right)}{16 \sigma_{YS} \sqrt{a^*} \left(3\cos\frac{\theta}{2} + \cos\frac{3\theta}{2} \right)} \times$$

$$\left[\left(\sin\frac{\theta}{2} + \sin\frac{3\theta}{2} \right)^2 \sin 2\theta + \frac{16(1+\nu)}{(1-\nu^2)} \cos^8\left(\frac{\theta}{2}\right) \cos\theta \sin^3\phi \cos^2\phi \left(\cos^2\left(\frac{\theta}{2}\right) - 2\nu \right)^2 \right] \tag{4.19}$$

With Equation (4.19) being implemented in relation to each crack turning point, it is clear that the model exhibits a singularity at each turning point, i.e. when a^* tends to zero (there is a $1/\sqrt{a^*}$ relationship). Therefore, when considering the occurrence of crack closure immediately following a deflection, it is legitimate to assume that the crack must propagate some distance into the deformed material at the asperity turning point for that material to effectively move into the crack wake to generate crack closure, i.e. shielding due to residual strains at the asperity turning point cannot act instantaneously on the crack tip as the formulation of the analytical model implies. The distance over which the crack needs to propagate in order for deformation at the asperity tip to act fully in the closure process may be expressed as some fraction (or multiple of) the plastic zone size, λr_p, as length dimensions of the crack tip plastic deformation field can be expected to scale with $(K/\sigma_{YS})^2$. Hence it can be considered that the analytical model described in Equation (4.19) is not valid for $a^* < \lambda r_p$. Considering the requirement for residual displacements to pass into the crack wake to cause crack closure, it may be noted that h must effectively tend to zero as $a^* \rightarrow 0$, as illustrated in Figure 4.8. To represent the transition in shielding in the region $0 \leq a^* < \lambda r_p$ we then identify the term h' to describe the effective component of h as a function of a^* (normalised by λr_p):

when $a^* < \lambda r_p$

$$h' = h'(a^*) = h.\left(\frac{a^*}{\lambda r_p} \right)^m \tag{4.20}$$

and when $a^* \geq \lambda r_p$

$$h' = h$$

where m is an empirical factor to be determined and h is given by Equation (4.18). In the first instance m is arbitrarily considered to be 1, i.e. a simple linear interpolation is used to represent the effective influence of asperity deformation at small a^* values.

4.4 Results and Discussions

4.4.1 Fatigue Crack Growth Rate

Crack growth rate results for the three different degrees of recrystallisation in the 2027 material are shown in Figure 4.9 based on multiple tests of side-grooved CCT samples of each material. A typical sequence of growth rate transitions points (T_1, T_2 and T_3) was seen in each material, consistent with various aluminium alloy crack growth rate results in the literature for laboratory air conditions [26, 27]. It may be seen that the three 2027 materials show very similar fatigue crack growth rate behaviour with similar transition points, i.e. limited recrystallisation effects on crack growth behaviour are evident. All three 2027 materials exhibit ΔK_{th} at ~ 3 MPa$\sqrt{m}$, which is close to the values reported by Wanhill [27] for 2024-T351 tested under similar conditions, and slightly lower than the value reported by Venkateshwara Rao and Ritchie [28] for 2124-T351 with a ΔK_{th} of ~ 3.6 MPa$\sqrt{m}$. It should be noted however that results obtained by Wanhill and Venkateshwara *et al.* are from non-side grooved samples (in keeping with the vast majority of the literature), in contrast to the side grooved samples specifically used in the present work to avoid mixed stress state influences on closure measurement (i.e. direct comparisons are somewhat restricted).

Xu *et al.* [29] suggested that dispersoid content may be a key factor in controlling the fatigue crack growth resistance in 2024 materials. In their work they showed that the lower dispersoid content alloy (2024A) has higher fatigue crack growth resistance than conventional 2024 material. Figure 4.10 shows the comparison of crack growth rate data obtained of 2027 with that for identical test conditions in 2024 and 2024A [29]. Whilst scatter bands (based on multiple tests for each material) can be clearly seen to be overlapping in places, the scatter band of crack growth rate for each

material is considered to be consistent with ASTM E647 [30] suggested levels, i.e. crack growth rate scatter is within a factor of 2. Crack growth trend behaviour for each material can be discerned from the trend lines shown in Figure 4.11: all three alloys exhibit the same form of *da/dN* curve, with several slope transitions. 2027 exhibits higher crack growth rates than 2024A for the whole load range tested (by a factor in excess of 2). 2027 growth is also generally faster than that in 2024, although the data bands clearly overlap more at moderate ΔK levels. The comparison of results shown here is consistent with Xu *et al.*, where the key implication would then appear to be a controlling influence of dispersoid content on crack growth rates, as the dispersoid content increases in the order 2024A → 2024 → 2027. Wanhill and Yoder [27, 31] have suggested that there is a correlation between the various changes in slope that occur along crack growth curves for such materials and scale of crack tip plasticity, with the lowest curve transition (T_1) being linked to cyclic plastic zone size exceeding the spacing of dispersoid particles. In the present work it may be seen that whilst T_1 points are difficult to exactly specify, this transition may indeed be lowest in the 2027 alloy, which is then consistent with a reduced dispersoid spacing in the 2027. Given the higher yield strength of the 2027, it can be seen that differences in T_1 due to dispersoid spacing may in fact be moderated as higher stress intensities are required to achieve a given plastic zone size. Given the proposed link between T_1 and cyclic plastic zone size, it is of course be necessary to consider crack closure level differences between the materials, which are discussed in the next subsection.

4.4.2 Crack Closure Measurement

Crack closure results for three 2027 materials were obtained from clip gauge compliance datas by using the aforementioned curve fitting approaches. 2027 closure results are compared with Xu's [29] 2024 and 2024A results (obtained in identical samples by the same curve fitting methods) in Figure 4.12 in terms of $\Delta K_{eff}/\Delta K_{app}$, where,

$$\Delta K_{app} = K_{\max} - K_{\min} \tag{4.21}$$

$$\Delta K_{eff} = K_{\max} - K_{cl} \tag{4.22}$$

ΔK_{app} is the applied stress intensity factor range, ΔK_{eff} is the effective stress intensity factor range, K_{max} is the maximum stress intensity level, K_{min} is the minimum stress intensity level, and K_{cl} is the stress intensity level at the measured onset of closure. As can be seen in Figure 4.12, the three 2027 materials with different degrees of recrystallisation have similar closure levels, consistent with their growth rate behaviour, particularly considered in relation to Xu's data shown for 2024 and 2024A. Overall, a good agreement with the growth rate trends can be seen between these materials, at least qualitatively, where crack growth resistance is increasing as closure levels increase (i.e. decreasing $\Delta K_{eff}/\Delta K_{app}$). The current closure data is obtained from side grooved samples and via a unique curve fitting algorithm, hence there are no results available in the literature for a direct comparison: comparison with work from Venkateshwara Rao and Ritchie [28] maybe noted however, with their 2124-T351 material (non-side grooved sample) tested at $R = 0.1$, showing closure levels that are slightly lower than have been measured here by Xu for the comparable similar material (2024-T351). For example, at $\Delta K_{app} \sim 8$ MPa$\sqrt{m}$, Venkateshwara Rao *et al.* reported a $\Delta K_{eff}/\Delta K_{app}$ of ~ 0.72 as compared to Xu's value of 0.6 at the same ΔK_{app} level. It should be noted that closure detection method being used in the present study is expected to be more sensitive to the onset of closure method than the conventional offset method used by Venkateshwara Rao *et al.*, consistent with Xu's lower $\Delta K_{eff}/\Delta K_{app}$ results.

To assess the crack growth rate influences more quantitatively, the crack growth rate of the three 2027 materials are plotted as a function of ΔK_{eff}, and again compared with Xu's 2024 and 2024A data, in Figure 4.13. As Xu [29] reported, the 2024 and 2024A growth rates are closely rationalised in terms of ΔK_{eff}: looking at the 2027 data, much of the divergence from the 2024 alloy growth rates is indeed explained, however, in the region 2 MPa$\sqrt{m} \leq \Delta K_{eff} \leq 6$ MPa$\sqrt{m}$, there is evidence of greater intrinsic growth rate resistance in the 2027 compared to the 2024 and 2024A.

Considering the crack growth rate curve transitions for the 2027 data in Figure 4.13, T_1, T_2 and T_3 (transitions moving from low to high ΔK levels) may be suggested to lie at ~ 1.2, 3 and 7 MPa$\sqrt{m}$ respectively for the three grain structure conditions; exact transition values are however considered difficult to define, particularly for the lower,

T_1 case. Similarity in growth rate curves may still be taken to imply a limited dependence of growth rate transitions on cyclic plastic zone size and underlying substructure and/or grain size in the 2027, contrary to the suggestions of Wanhill [27] and Yoder *et al.* [31]. A lack of substructure influence may be highlighted by the range of substructure condition in the 2027 variants, i.e. going from almost fully substructured, to an essential absence of substructure. In terms of grain dimension changes, three dimensional anisotropy will of course complicate direct comparisons, however it is seen from Chapter 3 that mean 3D intercept measurements vary by ~50% between the ReX(8) and ReX(100) materials, whilst in-plane dimensions (perhaps most relevant to plane strain deformation) vary by ~60%. Any simple correlation of crack growth rate transition with such changes in grain size (via cyclic plastic zone dimensions) would then be expected to manifest in transition shifts of the order of 20-25% in ΔK_{eff}, which is not supported by the current data. In this case, yield strength variation between the 2027 materials (corresponding to ~7%) may be expected to augment differences in grain size related transitions, as the higher strength ReX(8) material exhibits the larger in-plane grain dimensions. The possibility of maximum plastic zone size control of transitions can of course also be considered and assessed in relation to Figure 4.10 as the present tests were carried out at a fixed R-ratio (i.e. K_{max}, controlling maximum plastic zone size, is then directly proportional to ΔK_{app}). Within the 2027 data there is again a lack of conclusive microstructural influence in the data.

Overall, a lack of sensitivity of transition points to microstructural change may then be seen to support environmental control of the transition phenomenon as indicated by Gangloff and Piascik [32, 33]. Considering the 2027, 2024 and 2024A data together it may be noted that the clearest apparent distinction in growth rate curve transitions is between the Zr containing (2027) and non-Zr containing (2024 and 2024A) materials in Figure 4.13, with the presence of Zr appearing to shift the T_2 growth rate curve transition to higher stress intensities. To the best of the authors' knowledge similar direct comparison of Zr and non-Zr containing alloy intrinsic growth transitions has not been reported in the literature. Simple correlation of plastic zone size and separation of slip blocking features does not appear to explain this transition shift as *additional* dispersoids would be expected to displace a transition to lower stress

intensities. Variations in the environmental sensitivities of alloys with the additional dispersoid population may then be considered in the first instance (e.g. via changes in slip character [34]), following Gangloff and Piascik's proposed control of the transitions; however investigation/quantification of such environmental influence is beyond the scope of the current project.

In keeping the work of Xu, closure measurements indicate a distinct adverse extrinsic effect of dispersoids on crack growth in the 2027 materials in relation to results seen in 2024 and 2024A. Three main mechanisms of crack closure may be expected to apply to these alloys: (i) PICC, (ii) RICC and (iii) OICC. In terms of PICC, it is important to note that the present closure results were specifically obtained from thick side-grooved samples where the results should closely represent pure plane strain condition. Although it has been reported that PICC may occur to some extent under plane strain conditions (e.g. see Ref.[35]), the reported closure levels are significantly lower than those observed here. In term of OICC, consistent with what have been observed by Xu, there was little evidence of the build-up of an extensive oxide layer on the fracture surface when approaching threshold in these tests (i.e. the distinct blackening of fracture surfaces by aluminium oxide reported by Suresh *et al.* [36]). A strong RICC effect on crack growth behaviour in the present materials is therefore considered likely.

4.4.3 Fractographic Assessment

Representative fracture surface views from each of the 2027 materials are given in Figures 4.14, 4.15 and 4.16. In all images, the 2027-ReX(100) shows the largest general scale in fracture features, in keeping with the large underlying grain size (evident in the *S* direction in particular). Figure 4.14 shows a comparison of the fracture surfaces near threshold, at $\Delta K \sim 3$ MPa$\sqrt{m}$. Faceted fracture with a mixture of large, nearly planar facets and 'feathery' crystallographic features were evident in all the materials. Figure 4.15 shows the fracture surfaces at $\Delta K \sim 6$ MPa$\sqrt{m}$. Again, all of the materials show quite similar 'feathery' crystallographic fracture characteristics, but with rougher faceted features. Figure 4.17 highlights a typical faceted fracture surface from the 2027-ReX(8) material in this region. Some faceted areas have been

analysed by EDS indicating the local presence of oxide, i.e. indicative of discrete crack closure point due to the rubbing (fretting) of contact areas, see Figure 4.18. Figure 4.16 shows fracture surfaces of the three 2027 materials at $\Delta K \sim 9$ MPa$\sqrt{m}$, showing rather more ductile fracture surfaces. Striations consistent with classical Stage II growth can be observed at higher ΔK levels, with Figure 4.19 showing typical features from the 2027-ReX(100) material corresponding closely to the corresponding macroscopic crack growth rate.

From the observations described above, the three 2027 materials show quite consistent and equivalent fatigue fracture features and transitions in fracture surfaces throughout the crack growth range studied. Macroscopic observations however show that surface roughnesses in each material are distinct, particularly for crack growth below a $\Delta K \sim 7$ MPa$\sqrt{m}$, as shown in Figure 4.20 (the rough region lying just above the $\Delta K \sim 7$ MPa$\sqrt{m}$ line in this figure). It should be noted that whilst the samples show asymmetric crack fronts, the crack shapes are still within ASTM E647 [30] guidelines where the crack length differences measured from each side of the sample should be less than 25% of the width of the sample (i.e. < 3 mm in the case of 12 mm thick sample). As such, 3D Talysurf profilometry were used to map 2 mm x 2 mm fracture surface areas for the three 2027 materials at ΔK levels of ~ 9 and 6 MPa$\sqrt{m}$ to quantify the surface roughnesses, as can be seen in Figures 4.21 and 4.22 (representative of multiple mapping at the same ΔK region and corrected for any mean plane tilt). From the surface maps, it may be seen that at ΔK of 9 MPa$\sqrt{m}$ (Figure 4.21), the two higher ReX materials show similar levels of surface roughness, with a relatively flat and ductile fracture mode being seen in the surface SEM images of all three alloys. This can be seen more clearly from the side view of the 3D maps: the height of the surface asperities are within a range of approximately 0.1 mm, with the 2027-ReX(100) material exhibiting slightly rougher fracture surfaces (up to 0.15mm). Figure 4.22 shows the fracture surface mapping of the three materials at a ΔK of ~ 6 MPa$\sqrt{m}$: as observed macroscopically, fracture surface roughness levels increased with the decrease of the degree of ReX (more deflected crack growth can indeed be clearly seen in all three materials compared to Figure 4.21). The difference of the fracture surface asperity heights can again be observed more clearly from the side view of the maps. The 8% ReX material was seen to exhibit a consistently (over

~ 4 such maps for each material) greater asperity height range (> 0.35 mm), followed by the 55% ReX material (~ 0.3 mm), and whilst the 100% ReX material had a smaller asperity height range (~ 0.25 mm): more quantitative descriptions of the fracture surfaces is considered later in Section 4.4.5.1.

The overall growth mode transition behaviour seen in all three alloys is broadly consistent with classical interpretation of fatigue behaviour at low growth rates/stress intensity levels [4]. The incidence of a more ductile crack growth mode with increasing ΔK may of course correlate to a transition from heterogeneous/single slip to homogeneous/multiple slip deformation with decreasing plastic zone size. In the present materials, the most distinct crystallographic to ductile transition in fracture surface roughnesses and crack growth mode was associated with ΔK levels of ~ 7 MPa$\sqrt{m}$ (close to the upper growth rate curve transition point), and was independent of the ReX condition of the material. An independence of substructure, texture and grain structure is then implied for this growth mode transition. Previous work by Xu [37] has implied a primary dependence of crystallographic severity of fatigue failure on dispersoid content in 2024 and 2024A type materials, which would appear to be consistent with the present tests, in that the common feature of the 2027 alloy is indeed the dispersoid content.

4.4.4 Crack Deflection Assessment

In term of the micro-mechanical origins of increased fracture surface roughness as the degree of recrystallisation decreased (specifically at the region of ΔK ~ 6 MPa$\sqrt{m}$ which shows more significant differences), it may be of course be noted that in-plane grain dimensions increase in reverse order to the degree of recrystallisation. Results in the literature [38] also identify the role of strong textures of unrecrystallised material in promoting extended crystallographic deflections over multiple grains in high strength Al-alloys. As such it may be expected that increased texture intensity in the 2027-ReX(8) materials might also enhance fracture surface roughness levels via co-planar facet extension across regions of similar orientation. In the first instant, crack profiles of the samples have been examined in the L-T plane via EBSD. Figure 4.23 shows a crack profile of the 2027-ReX(55) material in the L-T plane at a ΔK of ~ 6

MPa√m showing a correlation between the grain structure and crack deflections. Black lines and red lines in the EBSD grain map are again correspondingly high (> 12°) and low angle (between 2° and 12°) boundaries. Major crack deflections are seen to be of a similar scale to the grain dimension in this plane, where a simple 1-to-1 correlation between crack turning point and the high angle grain boundary locations may be noted in Figure 4.23. However, when looking at the through-thickness direction (S-direction), it may be noted that the wavelength of the large crack deflections far exceeds the S-direction grain size (most significantly at ΔK of ~ 6 MPa√m, see Figure 4.22), i.e. crack deflections must grow across many grains at a time in the through-thickness direction to accommodate this. To understand how such through-thickness crack profiles develop (in the L-S plane) local texture have been investigated via EBSD at the most deflected and faceted region of interest (i.e. ΔK ~ 6 MPa√m), as well as at higher ΔK region ~ 9 MPa√m for comparison. The two most extreme microstructural cases (2027-Rex(8) and 2027-ReX(100)) were chosen for the assessment as they show the most significant differences in fracture surface roughness. Figure 4.24 to 4.27 show through-thickness crack profiles and explicitly corresponding EBSD grain maps highlighting overall grain structure together with the main texture components, at ΔK ~ 9 and ~ 6 MPa√m for both materials. The five common ideal texture components for wrought plate Al-alloys are individually highlighted in the grain maps with each colour representing a different texture variants, as shown in Table 4.1 [39].

Texture Components	**Variants**	
	(hkl)	**<uvw>**
Brass	(110)	$<1\bar{1}2>$
	$(1\bar{1}0)$	$<\bar{1}12>$
Copper	(112)	$<11\bar{1}>$
	$(\bar{1}\bar{1}2)$	$<1\bar{1}\bar{1}>$
S	$(\bar{1}23)$	$<\bar{6}3\bar{4}>$
	(123)	$<\bar{6}34>$
	$(\bar{1}2\bar{3})$	$<63\bar{4}>$
	$(12\bar{3})$	$<634>$
Cube	(100)	<001>
Goss	(110)	<001>

Table 4.1 Texture components and variants.

Figures 4.24 to 4.27 highlight the through-thickness fracture surfaces in the 2027-ReX(8) and 2027-ReX(100) materials, where the 2027-ReX(8) samples clearly exhibit the finer through-thickness grain size. In term of texture intensity, the 2027-ReX(100) material clearly exhibits reduced texture levels compared to the 2027-ReX(8) material, see Figure 3.8. The 2027-ReX(8) material in particular shows classical deformation components for rolled aluminium, and high peak intensity levels. As shown in Figure 4.24 and 4.25, at $\Delta K \sim 9$ MPa$\sqrt{m}$, both materials show relatively flat crack profile with no obvious link between significant local large crack deflection and texture components. On the other hand, at $\Delta K \sim 6$ MPa$\sqrt{m}$, as shown in Figure 4.26 and 4.27, crack profiles in this region becomes more deflected, in particular it may be seen that whilst the 2027-ReX(8) sample has a much finer through-thickness grain size, planes of sustained crack deflection (extending over distances of the order of 200μm and angles of 30°) are evident.

In terms of qualitative and quantitative understanding of relationships between local texture and fracture surface features, two broad concepts may be identified to support large crack deflections (i.e. extending over multiple grains), as illustrated in Figure 4.28. Firstly a simple common texture effect may be identified, where local blocks of grains are close to a particular texture component, or, if not an actual block, possibly a region where one texture component is predominant (but not entirely so) that may then 'force-through' a common crack plane in some fraction of neighbouring grains. A second condition may be based on the existence of a common fracture surface plane where a region of varying local orientations exists with a common zone/plane which crack growth then occurs along.

Based on the potential influence of common texture components, a quantitative analysis of deflected crack slopes has been carried out along the through-thickness crack path of 2027-ReX(8) material in particular, as shown in Figure 4.29. It is worth noting the difficulty in defining the extent of an individual deflection along a crack path, therefore, only a number of 'obvious' large deflections have been analysed. Individual deflected crack slopes are highlighted in Figure 4.29 along with the main texture components present (Br = Brass, Cu = Copper and S). Looking at the texture components in detail, there are no obvious indications that the large crack deflections

were supported by simple blocks of a given texture[†]: slope No. 3 appears close to a single block of Copper texture, but the effect was not ubiquitous. Rather than looking for monolithic blocks of a particular texture, analysis has also been carried out in terms of locally increased component content levels. Results of such an analysis are shown in Figure 4.30. Figure 4.30 (a) shows the normalised local texture contents of individual crack deflection slopes as illustrated in Figure 4.29 where the y-axis indicates the local volume fraction of that texture component, divided by the average volume fraction of that component for the whole material. When this figure goes above 1, a component is clearly disproportionally present: below 1 indicates a local deficiency of the component. Figure 4.30 (b) considers all of the slopes together to give an average indication of texture component predominance, taking standard errors on the averages. On this basis, there is an indication that a high local copper texture component tends to support large through-thickness crack path deflections in the material, although, as noted earlier, the effect is not uniform for all locations analysed. An interesting point to consider in relation to slopes 1 and 2 is the fact the Brass and S texture components are relatively close, and can in fact overlap, which might then suggest that slopes 1 and 2 are related to high combined S and Br component levels controlling the crack when the Copper component is low. Further statistical assessment of such effects would be valuable to validate/refine these findings, however, given the time consuming and demanding nature of the measurements, must be identified as an area for future research.

Based on the common fracture surface plane suggestion, further analysis was carried out on the same fracture profiles. In order to determine the possible crack plane on each deflection with the available EBSD grain crystallographic information, two crack deflection angles need to be considered of course: i.e. the angle of the crack 'kinks', θ (mode II deflection) and 'twists', ϕ (mode III deflection). ϕ can be readily measured from the available SEM images, while a 3D fracture surface profile behind the crack is needed to measure the θ. As such, the Taicaan optical surface profilometry technique was applied to map the 3D fracture surfaces immediately behind the crack profile illustrated in Figure 4.31. Figure 4.32 illustrates a typical example of crystallographic indexing of a section of deflected crack. Taking slope No.

[†] Texture identification is based on ±10° from ideal orientation

6 as an example, Figure 4.32 shows a combination of SEI crack profile image and the Taicaan 3D fracture surface, together with the corresponding {100}, {110} and {111} pole figure for that sub-region (i.e. the grains immediately below that section of fracture surface). Knowing the fracture slope, and comparing with the various pole peaks, it is interesting to note the strongest texture peaks that are closest to the slope of the region shown are in the {110} pole figure, suggesting a preferred {110} orientation. Further assessment of the other fracture surfaces slopes confirmed a frequent proximity to {110} plate orientation peaks. Treating the whole section of a multiple grain crack deflection as a single crystallographic 'unit' however be inappropriate in this type of analysis. This is evidenced in Figure 4.33, where it shows a close-up view of slope No. 6. When the slope of the deflection is observed in detail, the flank is indeed built up by small deflections with locally varying angle, which must of course be considered for accurate fracture plane determination. With the current observation, it is difficult to achieve the required resolution of slope measurement, and it will be shown in Chapter 5 how 3D synchrotron X-ray tomography may be used to address this matter.

4.4.5. RICC Modelling

As discussed in Section 4.4.2, RICC may constitute a key extrinsic factor in controlling fatigue crack growth rate in the 2024-type materials of interest here. In Section 4.4.4, visual investigation of fracture surface roughness via three-dimensional surface mapping indicated some distinct differences in fracture surface morphology between the three 2027 materials at different ΔK levels. Based on simple RICC understanding, differences in fracture surface roughness may then be expected to give rise to different crack growth rates. However, all three 2027 materials showed similar crack growth resistance, in keeping with the similar experimentally measured crack closure levels. From the literature [14, 15, 17, 40-43], it has been widely suggested that key parameters in the determination of RICC effects are crack deflection angle and deflection lengths. Parry's finite element model [14, 15, 17, 43] suggests that the crack deflection angle may be rather more dominant in controlling the RICC effect than deflection length, while indicating the effect of crack deflection length may become more significant when it becomes less than the active plastic zone size.

Therefore, to quantify the real RICC effect, it is necessary to consider the various loading and fracture surface aspects quantitatively.

4.4.5.1 Fracture Surface Features Quantification

In terms of quantifying fracture surfaces, the available surface stereology literature shows no established parameters of direct value to the current closure analysis [44]. As such a novel micromechanism-based approach has been established to measure crack deflection angles and lengths from the available profilometry data. As illustrated in Figure 4.34, the profilometry surface mapping points along a crack path may be used to define asperities in terms of a sign change in crack slope measured in-plane. Given that the present analytical model of RICC uses k_2 just *before* crack turning points to calculate $CTSD_{res}$, θ just before each turning point may be identified as most critical and therefore most relevant to measure from the fracture surfaces. Furthermore, the analytical model is based on growth distance *after* a turning point in controlling closure levels, so the deflection length, L is measured from the present fracture surfaces as the distance after a given turning point up to the next one (it is worth noting that the 'real' deflection length applied in the model is $L/cos\theta$ but not the horizontally measured L). Crack twist angle (ϕ) associated with each in-plane asperity may then be obtained from the 3D profilometry data. In term of spatial resolution, the profilometry measurements were taken at a nominal 12μm grid spacing (for computational and consistency with initial Talysurf investigations. Finite element modelling by Parry [17] indicates that deflections or asperities significantly smaller than the plastic zone size will have limited RICC effect. For a ΔK of 6 MPa$\sqrt{m}$, a maximum plastic zone size of ~ 40μm may be identified in the present materials, i.e. for load levels of this order, or higher, crack deflection scales less than 12μm should then be negligible in relation to RICC. To obtain the 3D fracture surface, for the first instance, the Talysurf surface profilometry technique was used for the 3D mapping. However, this technique uses a needle shape stylus that runs across the fracture surface during mapping, due to the contacting nature of this technique, occasionally technical problems were encountered, especially when mapping rougher fracture surfaces. Some non-continuity of surface measurement is then attributable to a 'jammed and jumping' stylus. The round tip of the stylus may also fail to pick up some detailed features from the surface. To achieve higher accuracy of measurement,

the Taicaan optical profilometry technique is used to replace the Talysurf for surface quantification.

Clearly the angle and length measurement associated with all asperity points on a given fracture surface will give rise to a wide range of measurement, where it may be anticipated that wedging of the fracture surface at closure "high points" will mean that many asperities may not in fact come into contact during unloading. From recently reported work by the authors [19] and Chapter 5, crack closure observations via the high resolution synchrotron X-ray tomography of such materials confirm that only a small number of points on a fracture surface actually come into contact along the crack path, consistent with common tribological understanding of contact between rough surfaces [45]. Based on this assertion, each individual line profile of the crack surface running back from the crack tip making up the 3D profilometry maps has been considered in itself and the point with the highest individual closure effect identified on each line profile based on its parameters, θ, ϕ and L. An average value of these parameters from each overall fracture surface profile was then applied to the analytical model as describe in Section 4.3 (i.e. Equation (4.19)) to estimate the overall closure level for the corresponding fracture surface. Figure 4.35 shows a typical Taicaan 3D fracture surface (covering 2 mm x 2 mm of mapping area), with an illustration of the process of extracting the relevant surface parameters.

4.4.5.2 Deflection Angles and Asperity Size Effect

As noted earlier, the current model is a development of a previous 2D model [14-16] where fracture surface features are now considered in 3D (i.e. with the addition of mode III crack twisting angle, ϕ). To assess the effect of ϕ in terms of overall closure level prediction by the current 3D model compared to the previous 2D model, Figure 4.36 shows the closure predictions with varying ϕ, where the analysis was performed using fixed crack deflection length of L = 30 μm at ΔK = 6 MPa$\sqrt{m}$. The values of λ and β using in this analysis were chosen in accord with the previous 2D FE studies of RICC [17] and they are fixed respectively at 0.4 and 2.0 through out all the following analyses. The value of λ is in fact entirely based on previous FE studies and has not been used as a fitting parameter at all in the present work. The value of β is however

identified in Section 4.3.1 as between 1 and 4 to be physically reasonable. The choice of $\beta = 2$ is utilised here as simply a nominal value for parametric investigation of the RICC model, and it's significance in relation to experimental results is considered later in this section. In general, an increase in closure level prediction can be seen with increase in θ value in Figure 4.36: the application of mode III crack twisting angle, ϕ to the model is also seen to consistently increase the overall closure predictions although the most significant parameter appears to be θ. For moderate tilt and twist angles of 30° degrees, it may be seen that crack twist (i.e. ϕ = 30°) may increase crack closure levels by ~ 35% over a non-twisted crack (equivalent to the 2D model formulation) undergoing 30° zig-zag crack growth about the nominal growth direction.

Figure 4.37 shows the effect of different, fixed asperity size/crack deflection lengths in term of closure prediction at different ΔK levels, where in this case θ and ϕ are fixed at nominal values of 35° and 25° respectively (for illustrative purposes only: as evident in the present materials, fracture surface geometry is more commonly a function of ΔK level). It is interesting to see that at high ΔK level the increase of L leads an increase in closure levels; however, as the ΔK decreases, closure levels reach a plateau condition in terms of L, i.e. the effect of crack deflection length disappears. Within this modelling frame work, this is linked to the saturation of closure influence when asperities are larger than the active plastic zone size (conversely, $K_{cl}/K_{max} \rightarrow 0$ as $L/r_p \rightarrow 0$). This effect can be seen more clearly in Figure 4.38 where the closure predictions are plotted against normalised deflection lengths over plastic zone size, L/r_p. As the relative size of the asperities increases, there is a monotonic increase in the closure levels, up to a normalised deflection length of approximately unity, after which the closure levels plateau. For large L/r_p, this result is consistent with a residual plastic shear-based closure mechanism, in that the extent of the residual asperity deformation, and hence the level of crack closure, is governed by the local shear loading near the points of the crack deflections, which is not a strong function of asperity size, but is a strong function of deflection angle. The fact the closure levels fall for small L/r_p is of course consistent with the fact that RICC effects must disappear as the fracture surface tends to an undeflected (straight crack) form (asperities become vanishingly small). Hence, relationship between deflection length

(or surface asperity size) and closure levels, is highly dependent on the plastic zone size and hence applied stress intensity levels.

4.4.5.3 Comparison with Experimental Results

The Taicaan 3D optical profilometry fracture surface mapping was carried out here on the three 2027 and 2024A samples. For each material, profilometry measurement covering 2mm x 2mm of fracture surface area have been obtained at two different ΔK levels, corresponding to the ΔK levels at the flattest region of crack growth (9 MPa$\sqrt{m}$) and at the roughest region (6 MPa$\sqrt{m}$). For each ΔK level, two maps were measured to give average θ, ϕ and L values which are shown in Table 4.2 (following the peak extraction procedure outlined in Section 4.4.5.1).

Materials	Parameter	ΔK level	
		9 MPa$\sqrt{m}$	6 MPa$\sqrt{m}$
2027-ReX(8)	L (μm)	25.27	26.81
	θ (°)	29.24	34.77
	ϕ (°)	16.07	28.09
2027-ReX(55)	L (μm)	24.78	32.12
	θ (°)	31.93	33.05
	ϕ (°)	13.57	22.36
2027-ReX(100)	L (μm)	22.52	28.81
	θ (°)	31.33	30.69
	ϕ (°)	18.19	23.53
2024A	L (μm)	22.33	25.23
	θ (°)	38.55	39.24
	ϕ (°)	28.54	31.35

Table 4.2 Averaged crack profile deflection parameters measured from Taicaan 3D profilometry fracture surface maps of the 2027 and 2024A materials.

Measurements shown in Table 4.2 indicate that for both ΔK levels, the three 2027 materials indeed exhibit similar surface roughness parameters in terms of the measurements suggested to be critical to RICC by the present mechanistic understanding. Increased surface roughness on 2024A is not particularly evidenced in a significantly increased asperity size (L) in these measurements, however, 2024A does show higher crack deflection angles (in both θ and ϕ) compared to the 2027 materials.

Based on the measured average crack profile deflection parameters in Table 4.2, the corresponding predicted closure levels predicted by the analytical model for each material at the two ΔK levels are shown in Figure 4.39 (using $\lambda = 0.4$ and $\beta = 2.0$), where it should be noted that the error bars in Figure 4.39 are based on repeat measurements of different individual areas of fracture surface at the same ΔK level, showing the range of predicted closure levels from different sets of measurements. It can be seen that the trend of decreasing K_{cl}/K_{max} with increasing ΔK is in fact reasonably well represented in the closure levels predicted by the analytical model[‡]. They are of the correct order, where all three recrystallisation conditions of the 2027 material are indeed expected to exhibit similar closure levels (at least within the scatter of experimentally measured results), and, perhaps more importantly, higher closure levels are evidenced in the 2024A material, although corresponding measured closure levels at 9 MPa$\sqrt{m}$ are somewhat underpredicted. While all materials seem to have similar L values, the higher closure levels in 2024A appear to be predominantly attributed to higher crack deflection angles.

Whilst Figure 4.39 indicates that reasonable crack closure levels may be predicted by the present analytical model, the modelling parameter β has essentially be regarded as a fitting parameter (but with its value of 2 being within reasonable bounds as noted earlier). In the context of the present work, the main issue is not considered to be the exact fitting of experimental closure data but the fact that closure prediction levels for the three conditions of the 2027 are in fact similar and higher closure levels is successfully predicted in 2024A materials. The increase in closure effect with decreasing stress intensities is also captured. In considering the quantitative significance of Figure 4.39, it may be noted that the procedure of measuring θ, ϕ and L clearly has its own potential effects on the results. For example, a more statistical treatment of the 'peak' asperities on a surface map might be considered, rather that just the closure high points along individual lines of crack extension, which may then affect the fitted value of β. The important point however is that for a reasonable first order analysis of the fracture surfaces, a good correlation with experimental trends is

[‡] It is noted again that by using the same λ and β value, the current 3D model may be seen to increase the closure levels prediction by ~ 35% over the previous established 2D model (i.e. ignoring mode III deflection by setting ϕ to zero), as shown in Figure 4.36.

seen for a physically reasonable value of β. The present modelling approach may not be considered to be explicitly proven, however a reasonably consistent combination of model formulation and experimental assessment has been achieved for the materials considered here.

With the results as discussed above, indicating that deflection angles remain the key influence to closure level, it is therefore interesting to consider the microstructural origins in the 2024A material which may have contributed the measured deflection angles. In the first instant, fracture surfaces at $\Delta K \sim 6$ MPa$\sqrt{m}$ may be chosen to examine whether there is particular evidence of strong crystallographic features that may cause 2024A to have higher asperities angles. Figure 4.40 shows the comparison of typical SEM fracture surface images of 2027-ReX(8), 2027-ReX(100) and 2024A materials at $\Delta K \sim 6$ MPa$\sqrt{m}$ under 150x magnification. Significant differences in term of the scale of fracture features can be seen, where the 2024A generally shows larger features than the two 2027 materials. The change in scales and the complexity of the fracture surface features makes quantitative comparisons very difficult. In addition to the range of fracture surfaces that individual grains appear to manifest, oxide debris is also evident (Figure 4.40 (c) particularly), obfuscating the underlying fracture morphology in the areas of greatest potential interest (i.e. those features giving rise to surface contact). Bearing in mind these factors, inspection of the 2024A fracture surfaces does indicate a greater incidence of sharp, blocky faceting, as highlighted in Figure 4.40(c). This is consistent with the results of Xu, where increased faceting levels were identified in 2024A in relation to 2024 [37]. In the first instance, the increased presence of sharp faceting is intuitively consistent with the increasing severity of crack deflection angles that appear to be controlling crack closure levels (and hence fatigue performance) in the present work: the implication here is that, for this family of materials, it is more the relative incidence/proportion of sharp faceting that a microstructure can support that controls fatigue performance, rather then the overall scale of fracture surface features involved.

In practice there is clearly a convolution of parameters that may control both aspects of fracture surface development. Given the interrelated nature of the microstructural features of the present test materials, it is not possible to entirely separate the

variables involved. Given the consistent environmental test conditions of this work (lab. air), the relative incidence of faceted crack growth may be most directly linked to strain localising and strain homogenising microstructural features within the materials. The alloys are all in the naturally aged condition so are expected to present equivalent precipitate conditions in terms of shearability. Variations in strain homogenising features of the materials are however present, with decreasing grain size, decreasing texture levels and increasing dispersoid content all potentially suppressing slip band formation and hence faceted crack growth[§]. Taken in isolation, the three 2027 materials imply an absence of texture, grain size and sub-structure effects on the fracture surface features that control RICC levels, although the influence of compensatory effects between the three parameters cannot be ruled out. The 2024 alloy behaviour is then of some interest in relation to the 2027ReX(100) material, where texture and grain dimensions are similar (in relation to the other materials at least): a controlling influence of dispersoid levels on closure is then clearly implied by this comparison, consistent with the highest closure levels seen in the 2024A tests. Given the grain dimensions of the various materials, it is not possible to rule out some contributory effect of the large grain size in the 2024A to the measured crack closure levels (2024A presenting a distinctly coarser structure than the other materials investigated), although this would be interpreted as contributing to strain localisation capacity within the material, rather than the scale of surface features.

Within the framework of the present RICC understanding (as expressed in the modelling), the influences of crack deflection angles, asperity size, stress intensity level and material yield strength are all reflected: it must then be recognised that the understanding of microstructural influence developed here for 2024-type materials must be carefully re-assessed for other alloy systems. For example, distinct texture influences on crack closure in Al-Li alloys have been reported on a number of occasions, e.g. see [28], and indeed contrasted with relative insensitivity to texture in conventional Al-alloys. Qualitatively at least this may be rationalised by the fact that

[§] The implied incidence of {111} oriented, slip band crack growth is not *prima facia* supported by the crystallographic assessment of Section 4.4.4: this must be considered against the results to be shown in Chapter 5 and the fact that {100} and {110} oriented crack growth may arise from conjugate {111} deformation [46] G.G. Garrett and J.F. Knott, *Acta Metallurgica*, 1975. **23**: p. 841..

the Al-Li alloys in question have an exceptional propensity for faceted crack growth, with a greater proportion of the fracture surfaces therefore being controlled by underlying crystallography. Extension of the present RICC modelling and experimental validation effort over wider ranges of fracture surface scale and relative plastic zone size (e.g. room temperature testing of Ni-superalloy single crystals) would therefore be of value in extending the present understanding of crack closure processes and the corresponding potential for microstructural control of materials performance.

4.5 Conclusions

1. Degrees of recrystallisation level have been seen to have limited influence on constant amplitude crack growth resistance and closure levels in the advanced 2024 alloy variant, 2027. The results are particularly consistent with Xu's [29] assertion that dispersoids are a key factor controlling fracture surface faceting levels and hence, closure processes in commercial 2024-type materials, i.e. prevalence of crystallographic features may be more important to RICC levels than texture and grain size in the present microstructures.

2. In terms of fracture surface profiles, local balance in texture components may favour the formation of large facets, particularly in terms of the Copper preferred orientation. In terms of common fracture plane analysis on the large facets, a frequent correlation with {110} plate orientation peaks have been observed. Further analysis and clarification at a microscopic scale is however presented in Chapter 5.

3. Physical interpretation of RICC effects in terms of residual shear displacements at three-dimensional crack wake asperities has been compared to a variety of experimental results. For constant amplitude loading conditions, where the model is most readily applied, predictions of plane strain crack closure levels from real fracture surface features has been shown to be in reasonable functional accord with experimental data.

References

[1] W. Elber, *Engineering Fracture Mechanics*, 1970. **2**: p. 37-45.

[2] W. Elber, *Damage Tolerance in Aircraft Structures, ASTM STP 486*, 1971, Philadelphia: ASTM, p. 230-242.

[3] J.C. Newman and W. Elber, *Mechanics of fatigue crack closure, ASTM STP 928*. 1988, Philadelphia: ASTM.

[4] S. Suresh, *Fatigue of Materials*. 2nd ed. 2001, Cambridge: Cambridge University Press.

[5] J.C. Newman, *Methods and Models for Predicting Fatigue Crack Growth Under Random Loading, ASTM STP 748*, eds. J.B. Chang and C.M. Hudson. 1981, Philadelphia: ASTM, p. 53-84.

[6] J.C. Newman, *Behaviour of Short Cracks in Airframe Components, Proceedings 328, Advisory Group for Aerospace Research and Development*, ed. H. Zocher, 1983, p. 6.1-6.26

[7] J.C. Newman, *FASTRAN-II - A fatigue crack growth structural analysis program, NASA Technical Memorandum 104159*. 1992.

[8] J.C. Newman, *Journal of Engineering Materials and Technology*, 1995. **117**: p. 433-39.

[9] J.C. Newman, *Analyses of fatigue crack growth and closure near threshold conditions for large-crack behaviour, NASA Technical Memorandum 209133*. 1999.

[10] S. Suresh and R.O. Ritchie, *Metallurgical Transactions*, 1982. **13A**: p. 1627-1631.

[11] J. Wasen, K. Hamberg, and B. Karlsson, *Materials Science and Engineering A*, 1988. **102**: p. 217-226.

[12] J. Lllorca, *Fatigue & Fracture of Engineering Materials & Structures*, 1992. **15**: p. 655.

[13] N. Chen and F.V. Lawrence, *Fatigue and Fracture Mechanics, ASTM STP 1332*, eds. T.L. Panontin and S.D. Sheppard. 1999, Philadelphia: ASTM, p. 535-551.

[14] M.R. Parry, S. Syngellakis, and I. Sinclair, *Materials Science and Engineering A*, 2000. **291**: p. 224-234.

[15] M.R. Parry, S. Syngellakis, and I. Sinclair, *Materials Science Forum*, 2000. **331**: p. 1473-1478.

[16] N. Kamp, M.R. Parry, K.D. Singh, and I. Sinclair, *Acta Materialia*, 2004. **52**(2): p. 343-353.

[17] M.R. Parry, *Finite Element and Analytical Modelling of Roughness Induced Fatigue Crack Closure*. PhD Thesis, University of Southampton. 2001.

[18] K.D. Singh, *Modelling of combined roughness and plasticity induced closure effects in high strength Al-alloys*. PhD Thesis, University of Southampton. 2004.

[19] H. Toda, I. Sinclair, K.H. Khor, J.-Y. Buffiere, E. Maire, T. Connolley, M. Joyce, and P. Gregson, *Philosophical Magazine*, 2003. **83**(21): p. 2429-2448.

[20] Y. Xu, P.J. Gregson, and I. Sinclair, *Materials Science and Engineering*, 2000. **A284**: p. 114-125.

[21] H. Tada, P.C. Paris, and G.R. Irwin, *Stress Analysis of Cracks Handbook*. 1973, Hellertown: Del Research Corporation.

[22] B.A. Bilby, G.E. Cardew, and I.C. Howard, *Fracture*, 1977. **3**: p. 197-200.

[23] J.R. Rice, *Fatigue Crack Propagation, ASTM STP 415*, 1967, Philadelphia: ASTM, p. 247-309.

[24] C. Li, *Acta Metallurgica et Materialia*, 1990. **38**: p. 2129-2134.

[25] K.T. Faber and A.G. Evans, *Acta Metallurgica*, 1983. **31**(4): p. 565-576.

[26] G.R. Yoder, L.A. Cooley, and T.W. Crooker, *NRL Memorandum Report 4787*, 1982.

[27] R.J.H. Wanhill, *Engineering Fracture Mechanics*, 1988. **30**(2): p. 233-260.

[28] K.T. Venkateshwara Rao and R.O. Ritchie, *International Materials Reviews*, 1992. **37**: p. 153-185.

[29] Y. Xu, P.J. Gregson, and I. Sinclair, *Materials Science Forum*, 2000. **331**: p. 1525-1530.

[30] ASTM-E647, *Annual Book of ASTM Standards*. 1996, Philadelphia, PA: ASTM International, p. 565-601.

[31] G.R. Yoder, P.S. Pao, M.A. Imam, and L.A. Cooley, *Scripta Metallurgica*, 1989. **23**: p. 1455-1460.

[32] R.P. Gangloff and R.S. Piascik, *Metallurgical Transactions*, 1993. **24A**: p. 2751-2762.

[33] R.P. Gangloff and R.S. Piascik, *Metallurgical Transactions*, 1993. **24A**: p. 2415-2428.

[34] B. Holper, H. Mayer, A.K. Vasudevan, and S.E. Stanzl-Tschegg, *International Journal of Fatigue*, 2003. **25**(5): p. 397-411.

[35] N.A. Fleck and J.C. Newman, *Mechanics of Fatigue Crack Closure, ASTM STP 982*, 1988, Philadelphia: ASTM, p. 319-341.

[36] S. Suresh, G.F. Zamiski, and R.O. Ritchie, *Metallurgical Transactions*, 1981. **12A**: p. 1435-1443.

[37] Y. Xu, *Closure assessment and overload transient behaviour in damage tolerant airframe materials*. Ph.D thesis, University of Southampton. 2001.

[38] I. Sinclair and P.J. Gregson, *Aerospace Materials (Series in Materials Science and Engineering)*, eds. B. Cantor, H. Assender, and P. Grant. 1998, Bristol: Institute of Physics Publishing.

[39] A.W. Bowen, *Materials Science and Technology*, 1990. **6**: p. 1058-1071.

[40] J. Llorca, *Fatigue & Fracture of Engineering Materials & Structures*, 1992. **15**: p. 655-669.

[41] S. Suresh, *Metallurgical Transactions*, 1983. **14A**: p. 2375-2385.

[42] S. Suresh, *Engineering Fracture Mechanics*, 1985. **21**: p. 453-463.

[43] M.R. Parry, S. Syngellakis, and I. Sinclair, *Damage and Fracture Mechanics 2000*, eds., C.A. Brebbia and A.P.S. Selvadurai, 2000, Montreal, Canada, p. 313-322

[44] K.J. Stout, P.J. Sullivan, W.P. Dong, E. Mainsah, N. Luo, T. Mathia, and H. Zahouani, *Report EUR15178, Programme for Applied Metrology and Analysis*, 1993, European Commission, Brussels.

[45] I.M. Hutchinson, *Friction and Wear of Engineering Materials*. 1992, UK: Edward Arnold.

[46] G.G. Garrett and J.F. Knott, *Acta Metallurgica*, 1975. **23**: p. 841.

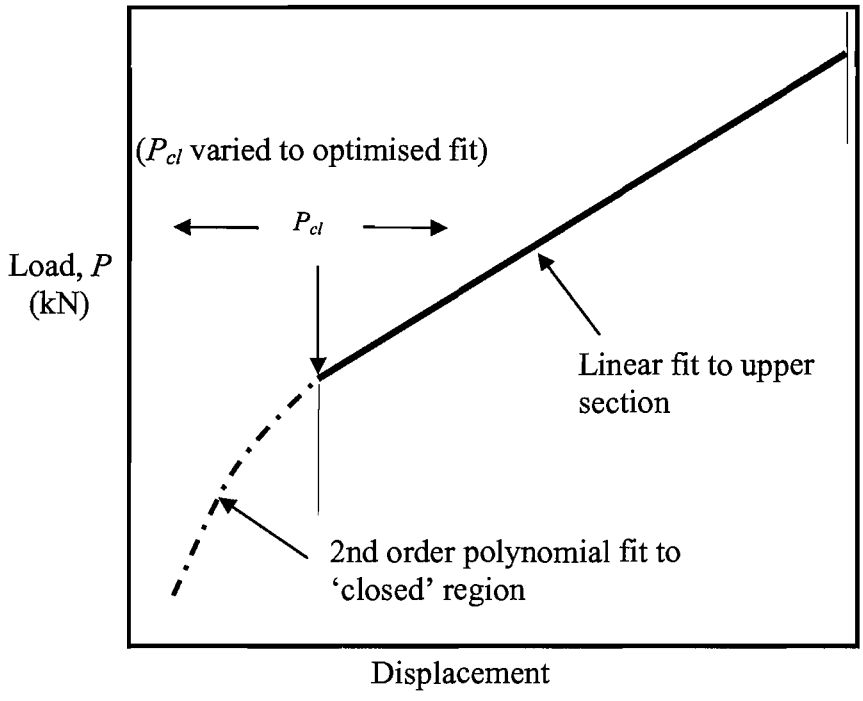

Figure 4.1 Schematic illustrations of compliance curve fitting methods for closure determination, in which P_{cl} is the closure load.

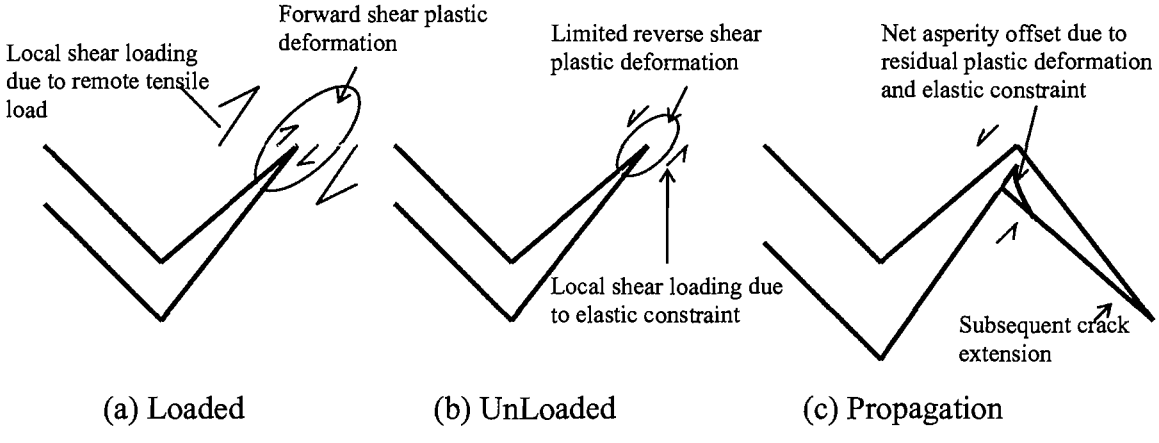

Figure 4.2 Schematic illustration of RICC arising from residual crack shear at asperities.

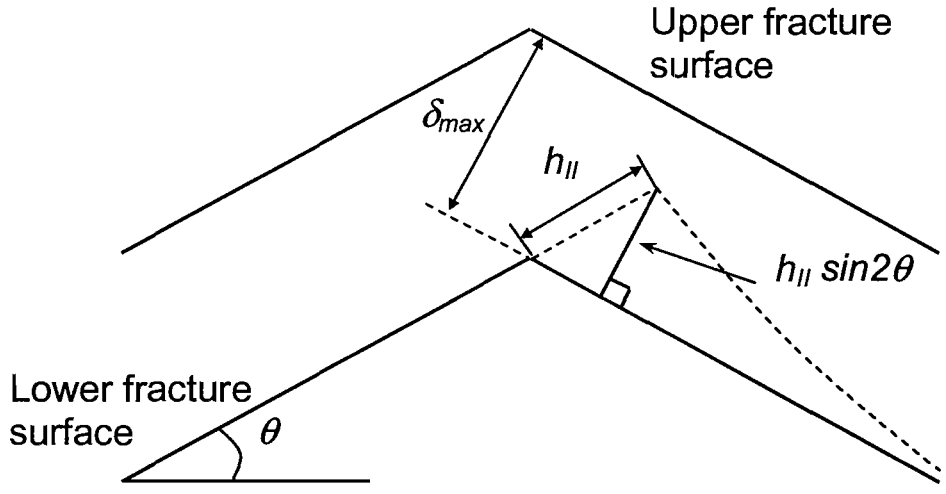

Figure 4.3 Geometry of the crack deflection model.

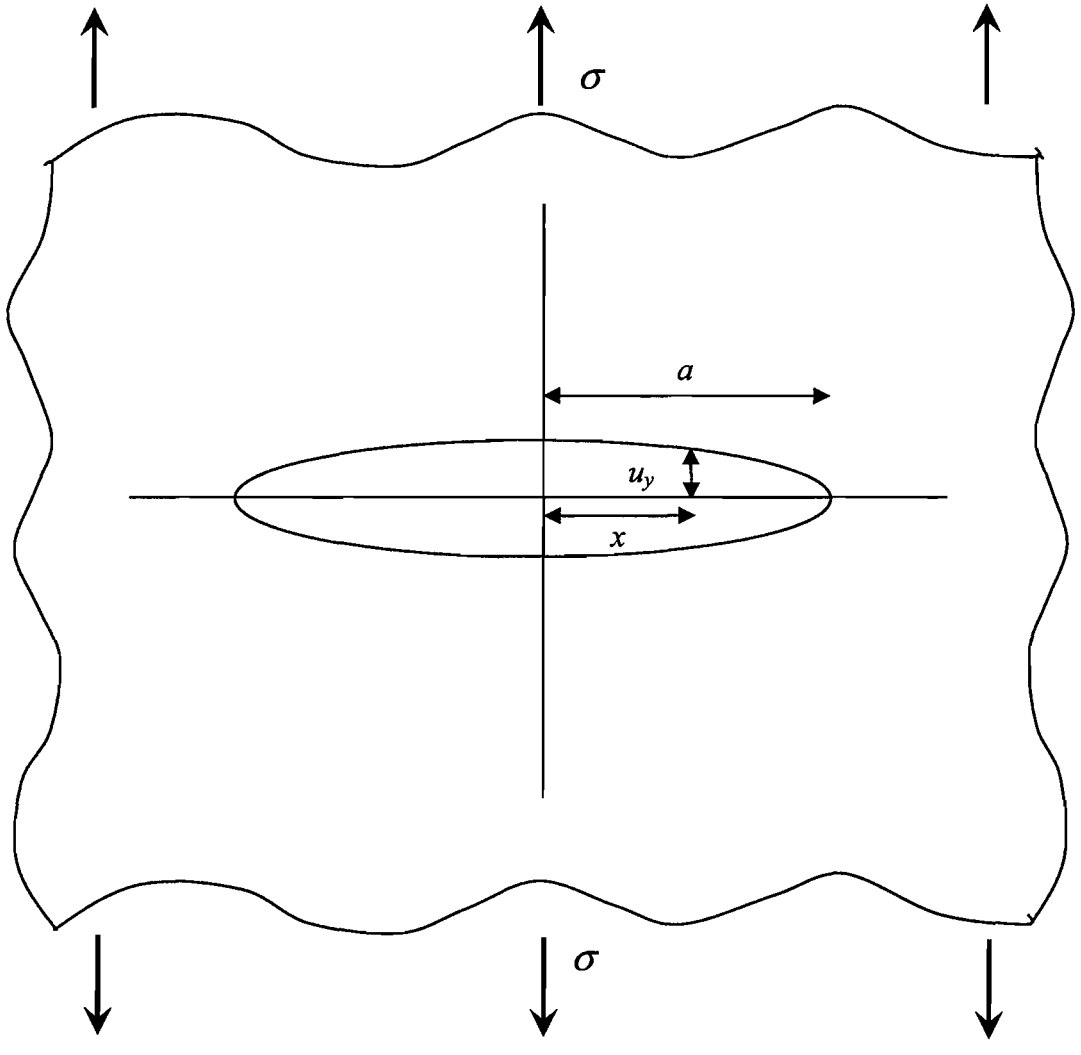

Figure 4.4 A crack in an infinite plate.

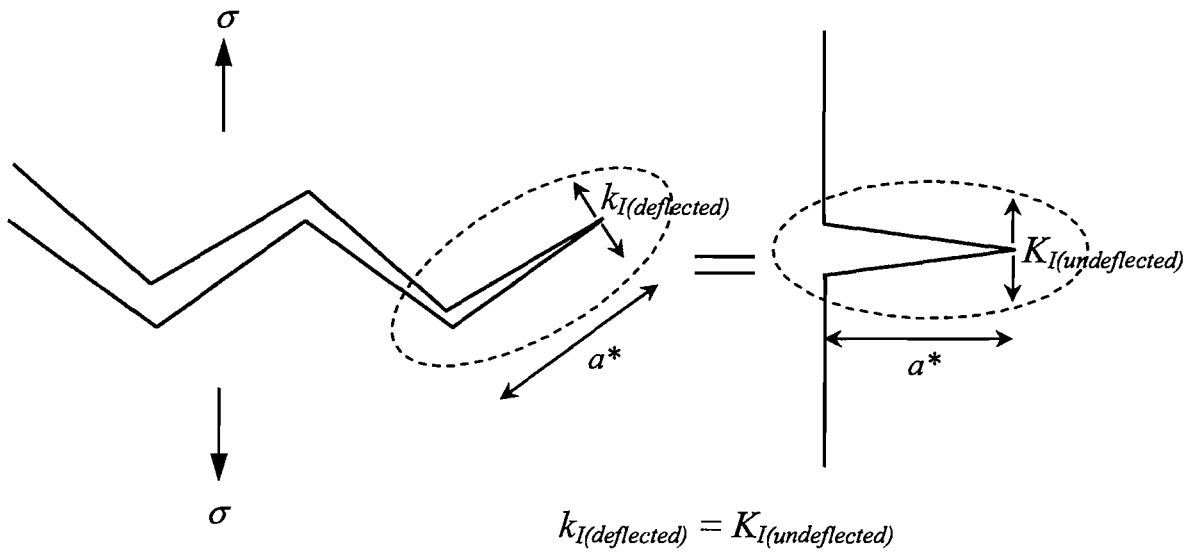

Figure 4.5 Approximation of the final deflected crack section, to a undeflected crack of the same length.

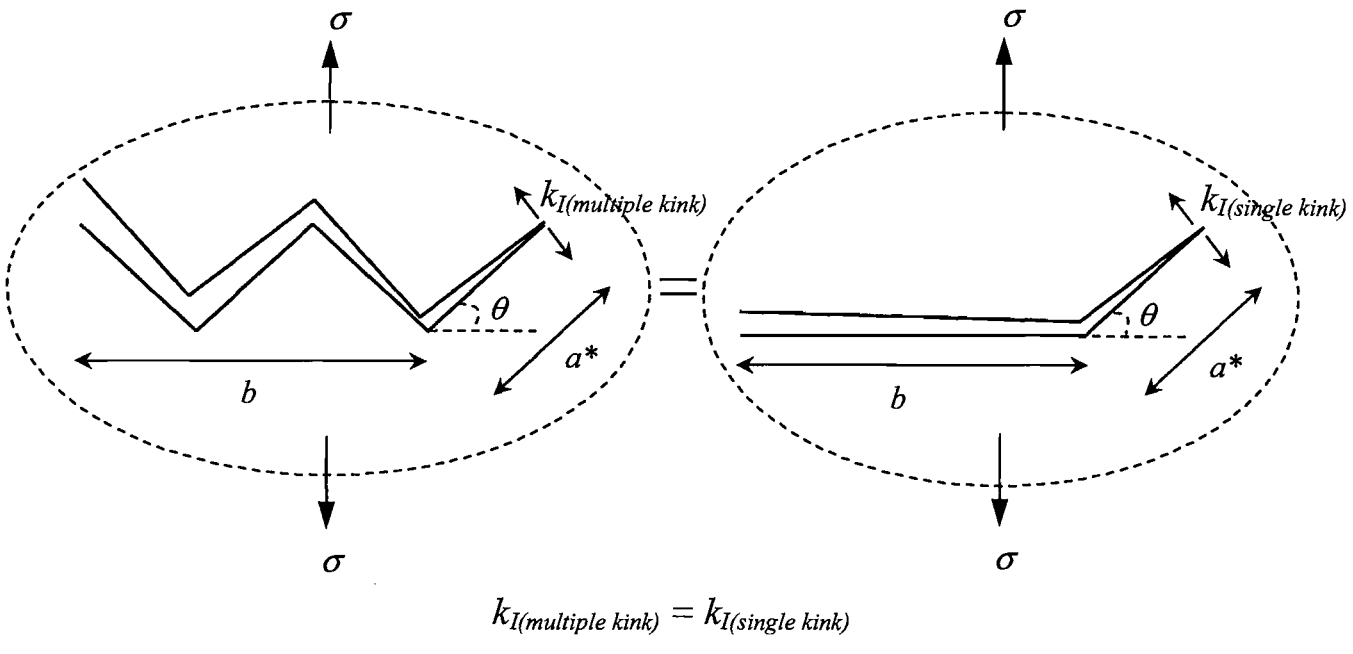

Figure 4.6 Approximation of the final deflected crack section, to a single pupative kink (i.e. $a^* << b$) off a straight crack.

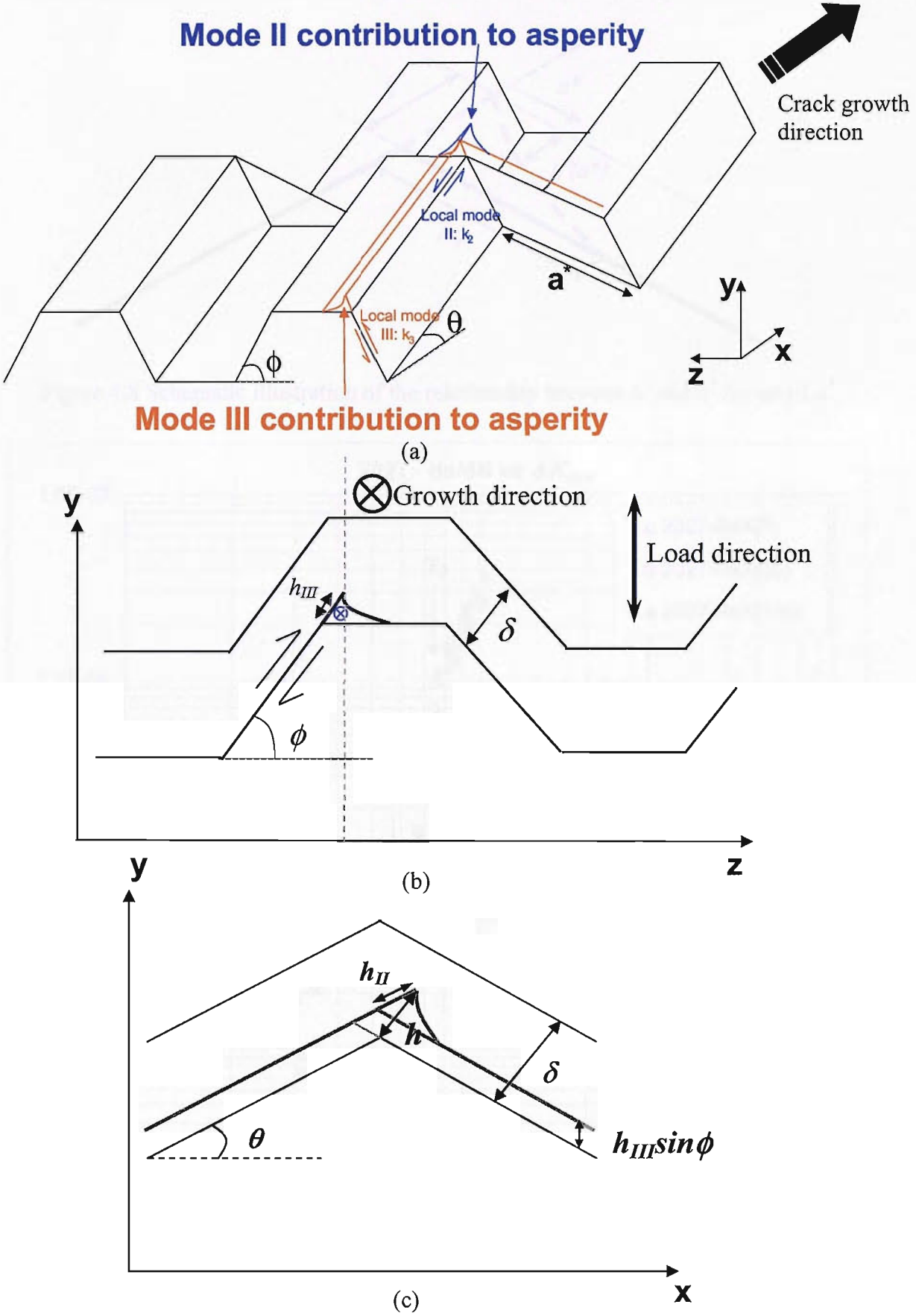

Figure 4.7 Schematic illustration of (a) overall 3D crack deflection model geometry, (b) trapezoidal through-thickness (*y*-*z*) crack deflection geometry, and (c) combination of mode II and mode III effects on the formation of asperities.

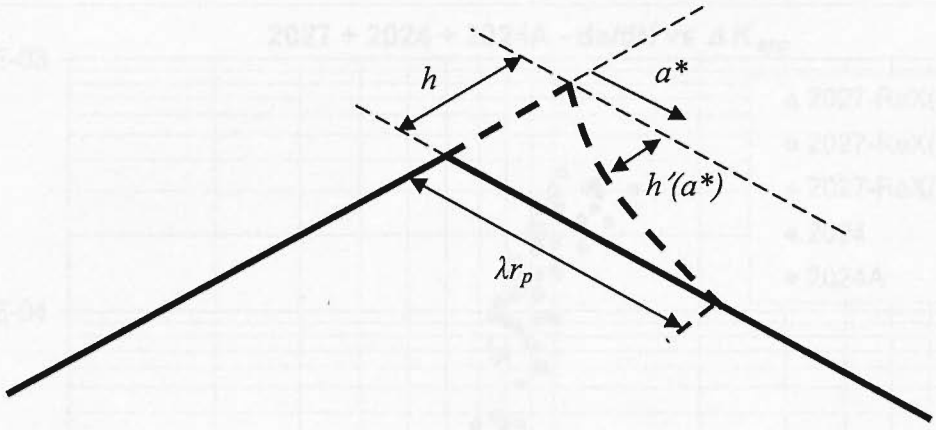

Figure 4.8 Schematic illustration of the relationship between h' and a^* for small a^*.

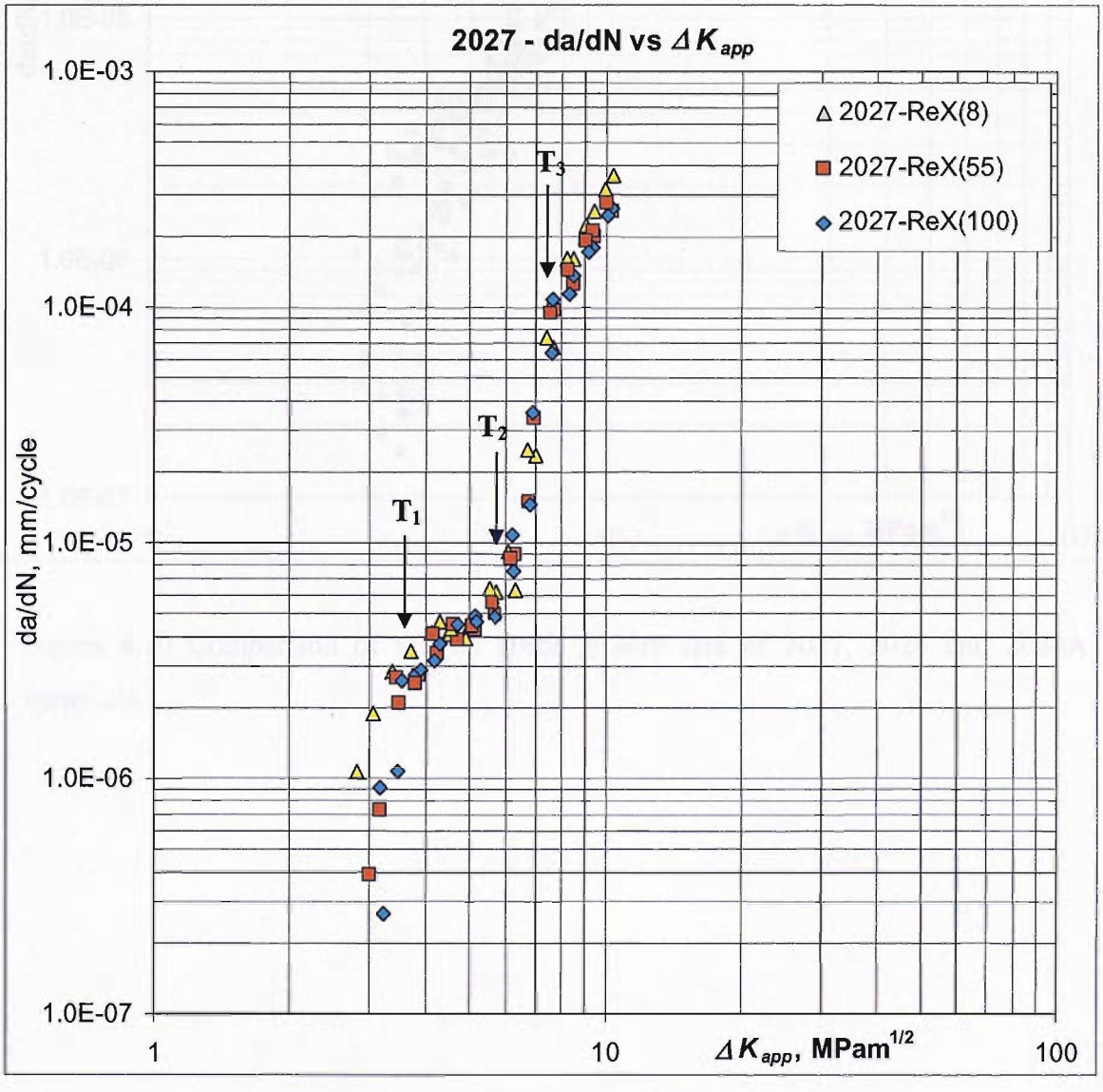

Figure 4.9 Fatigue crack growth rate, da/dN versus ΔK_{app} plot from multiple tests results of nominally 8%, 55% and 100% recrystallised 2027 materials. (Note: $\Delta K_{app} = K_{max} - K_{min}$)

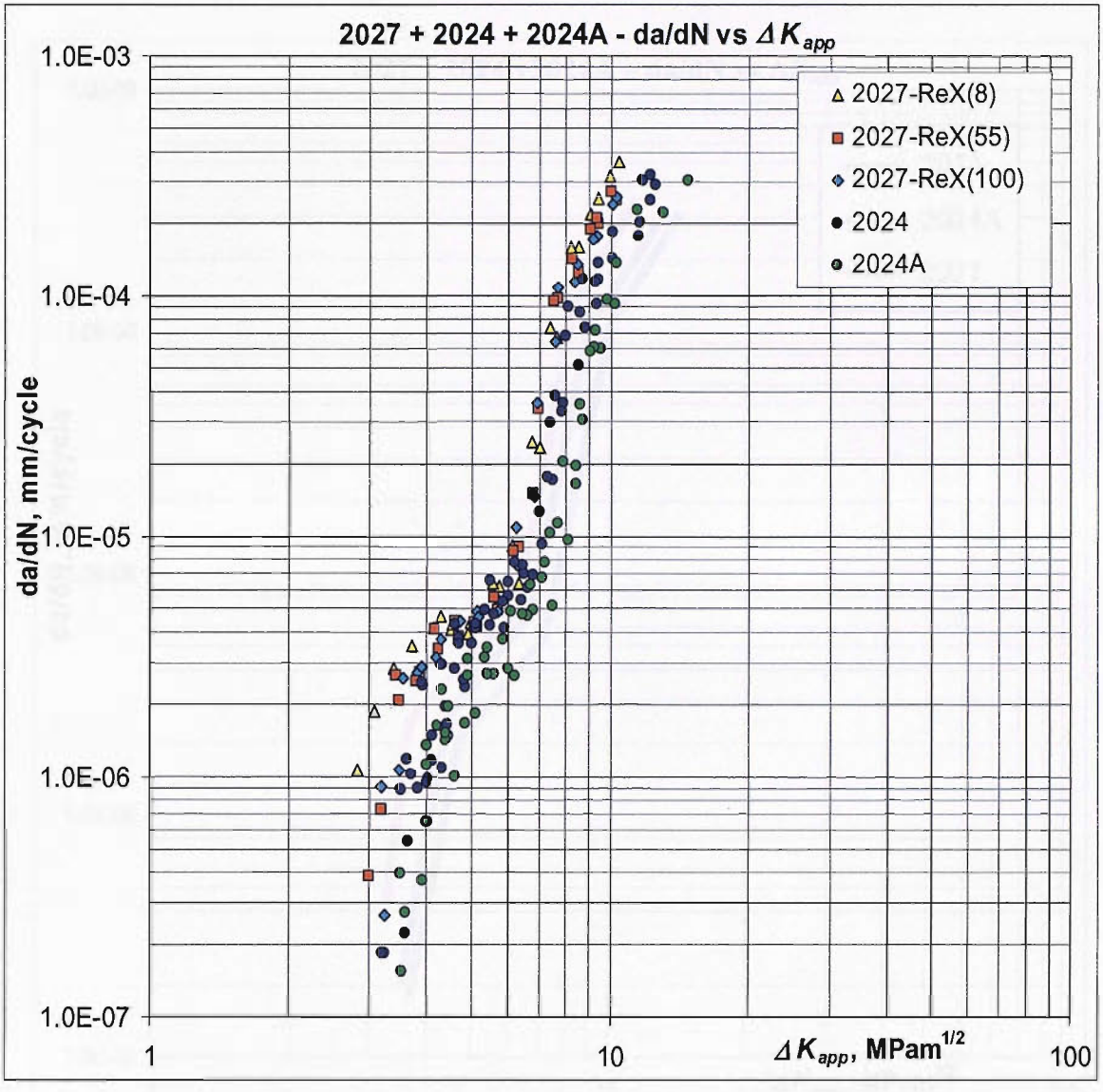

Figure 4.10 Comparison of fatigue crack growth rate of 2027, 2024 and 2024A materials.

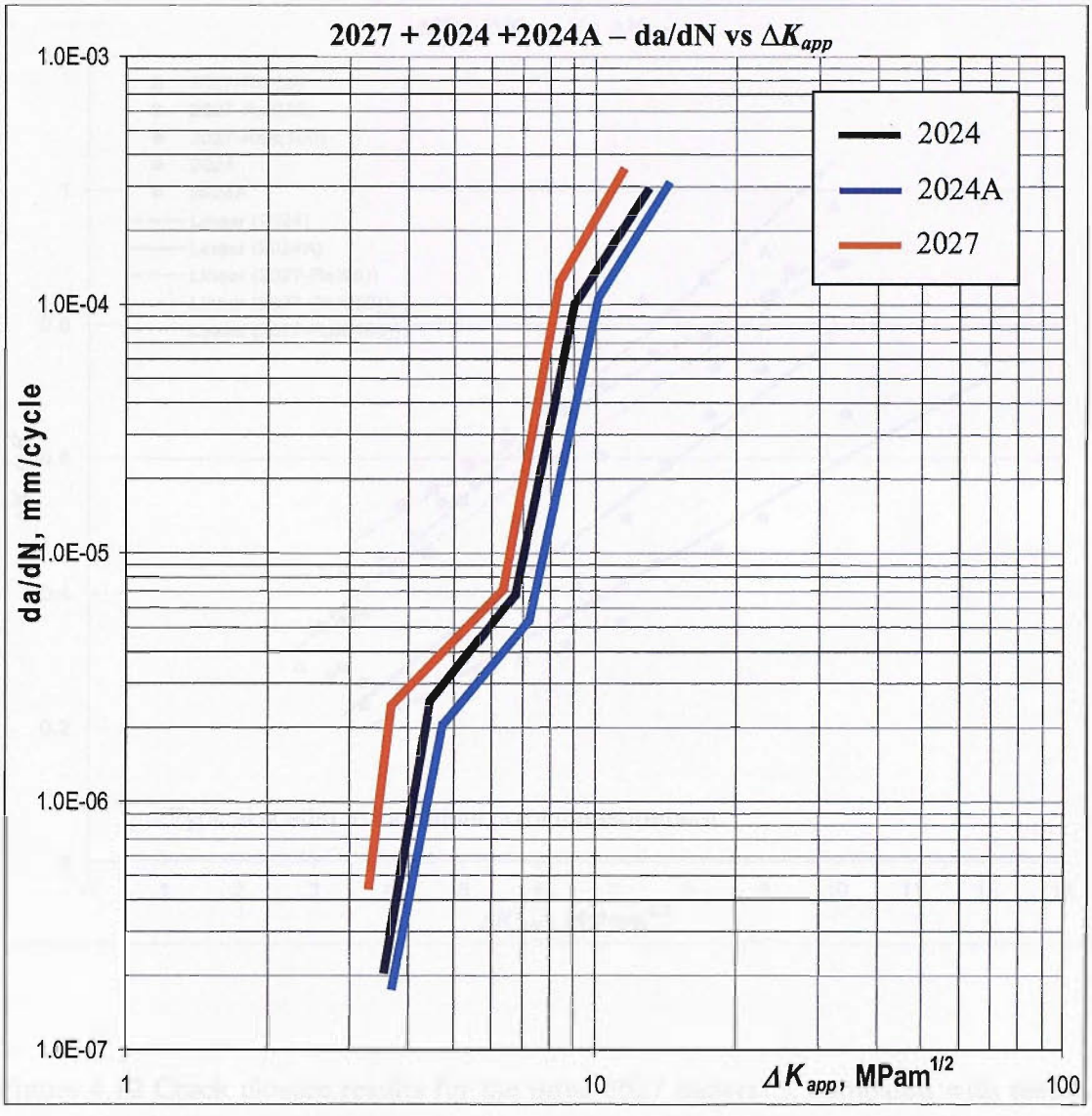

Figure 4.11 Schematic fatigue crack growth band of 2027, 2024 and 2024A materials.

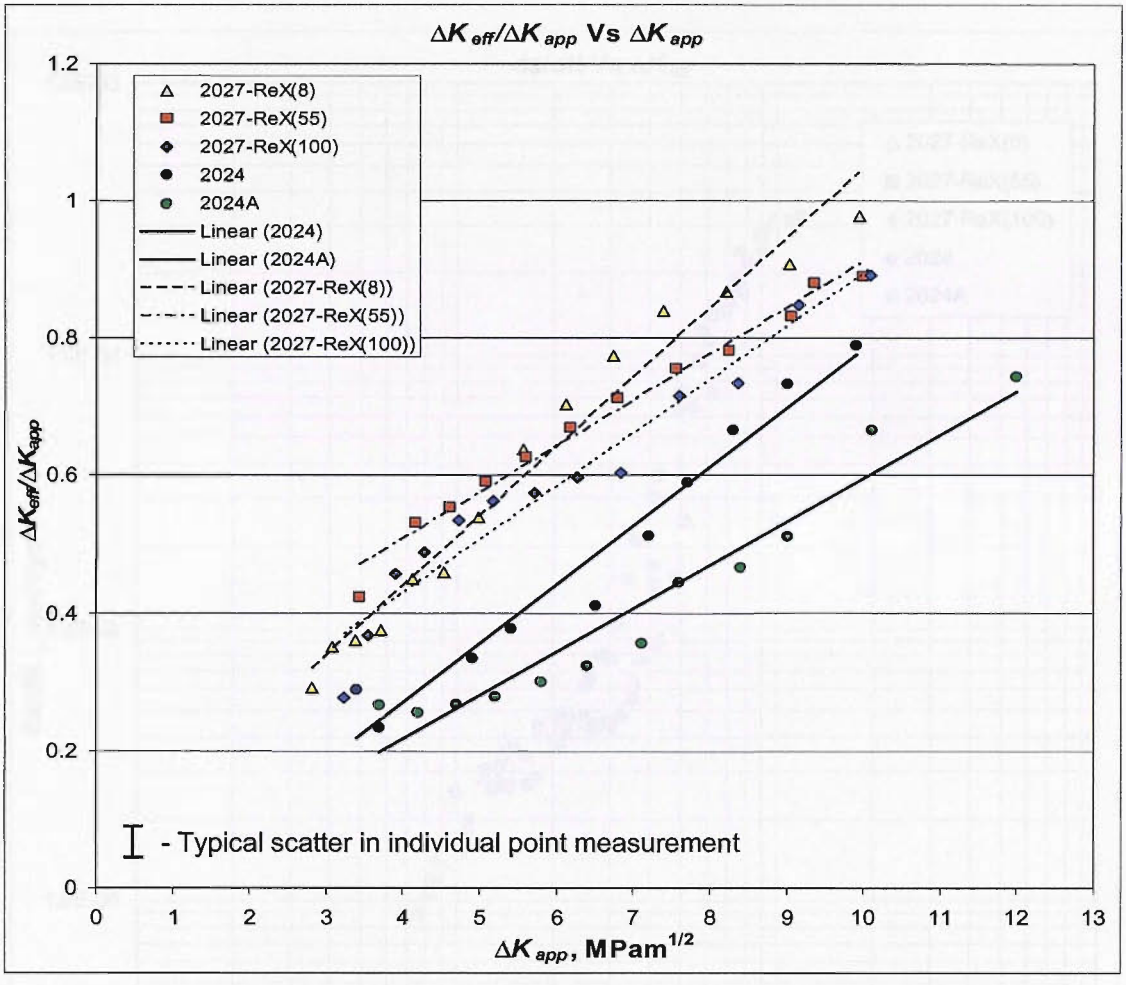

Figure 4.12 Crack closure results for the three 2027 materials, compared with results for 2024 and 2024A. (Note: linear fits shown in the plot are for illustrative purposes only, i.e. no mechanistic understanding/relationship is implied)

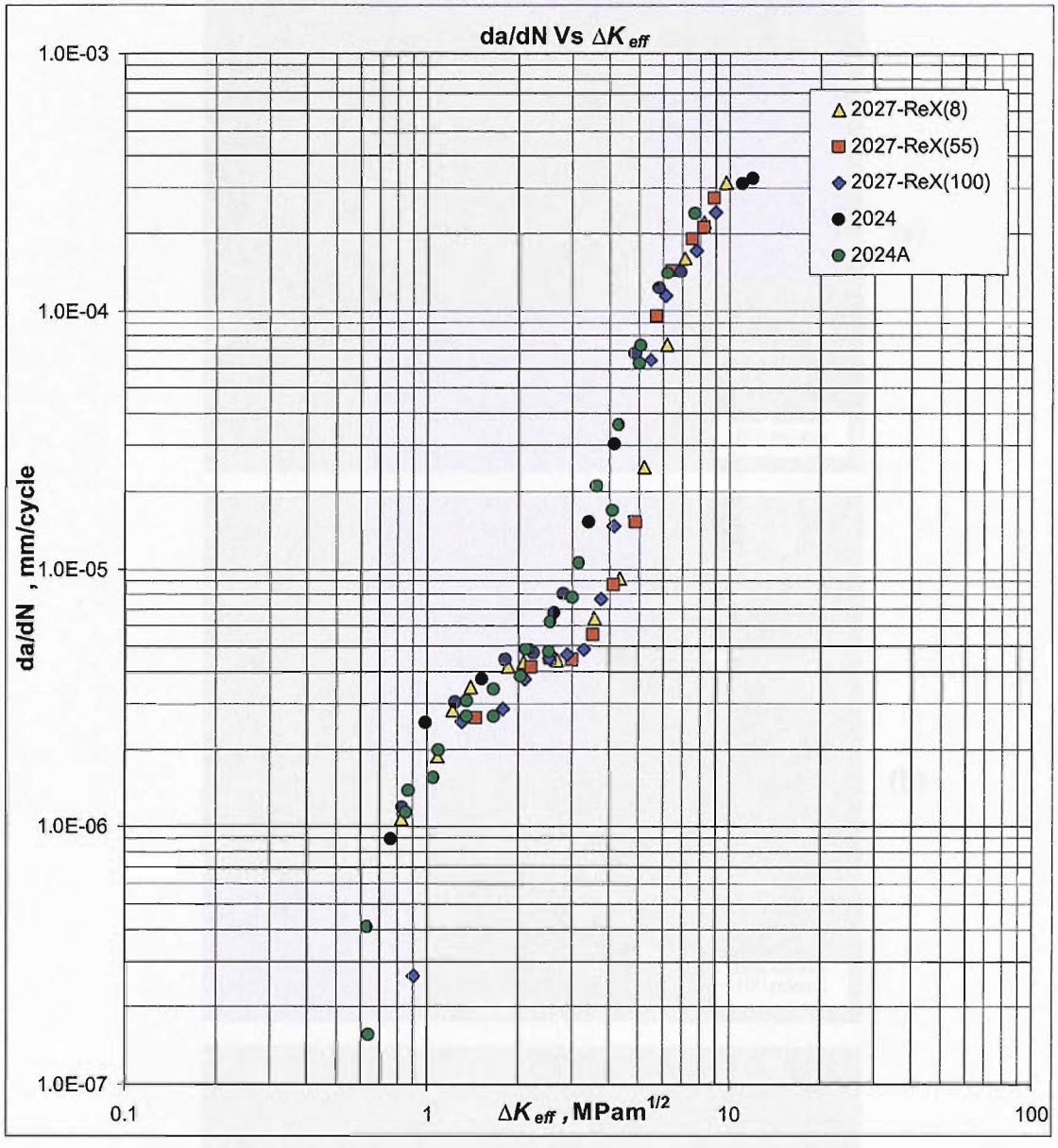

Figure 4.13 Comparison of fatigue crack growth rates in 2027, 2024 and 2024A alloys as a function of ΔK_{eff}.

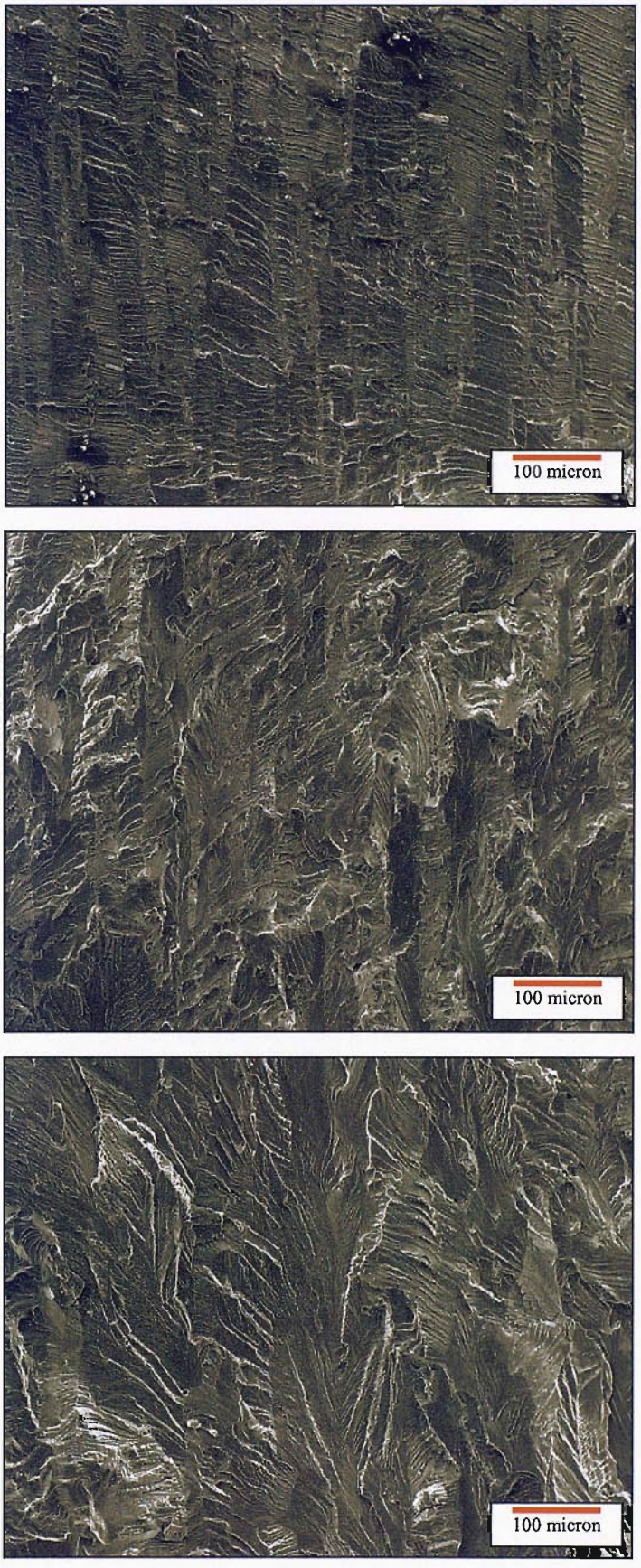

Figure 4.14 Fracture surfaces observed at $\Delta K \sim 3$ **MPa**$\sqrt{\mathbf{m}}$; (a) 2027-ReX(8), (b) 2027-ReX(55), and (c) 2027-ReX(100).

Figure 4.15 Fracture surfaces observed at $\Delta K \sim 6$ **MPa$\sqrt{\text{m}}$**; (a) 2027-ReX(8), (b) 2027-ReX(55), and (c) 2027-ReX(100).

Figure 4.16 Fracture surfaces observed at $\Delta K \sim 9$ **MPa**$\sqrt{\mathbf{m}}$; (a) 2027-ReX(8), (b) 2027-ReX(55), and (c) 2027-ReX(100).

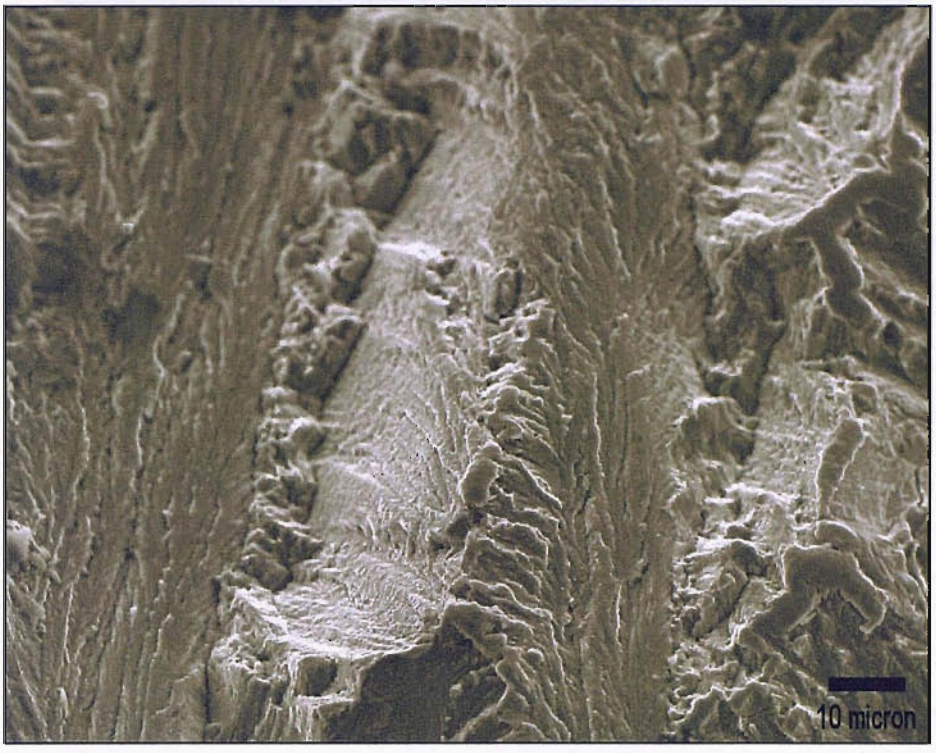

Figure 4.17 Faceted fracture surface features in, 2027-ReX(8) at $\Delta K \sim 6$ MPa$\sqrt{m}$.

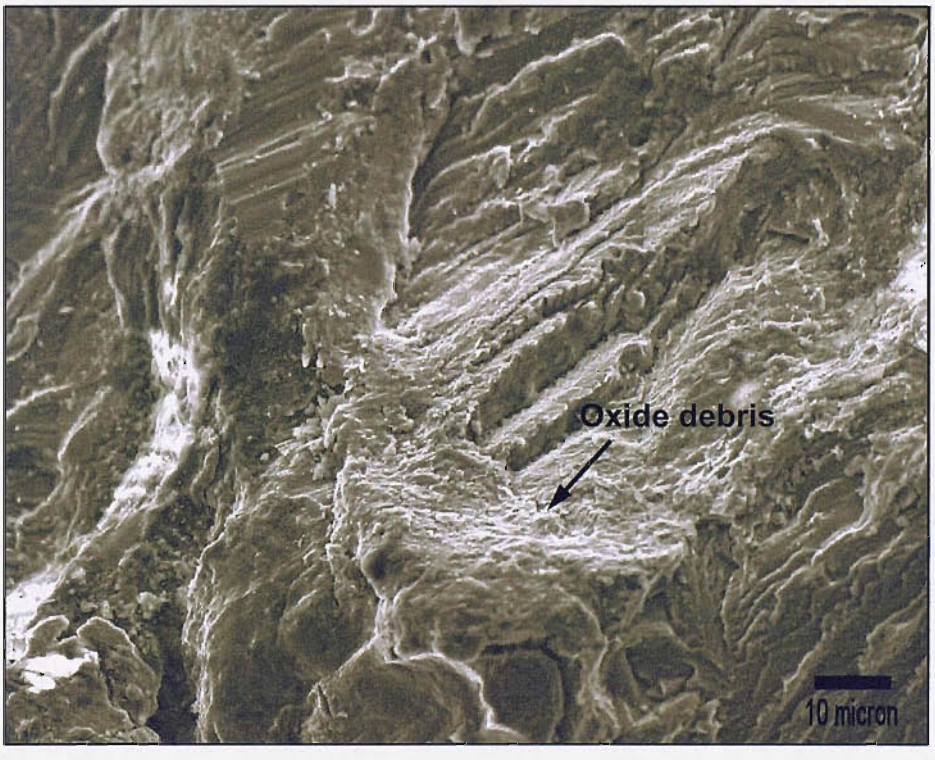

Figure 4.18 Fracture surface oxide debris, 2027-ReX(55) at $\Delta K \sim 6$ MPa$\sqrt{m}$.

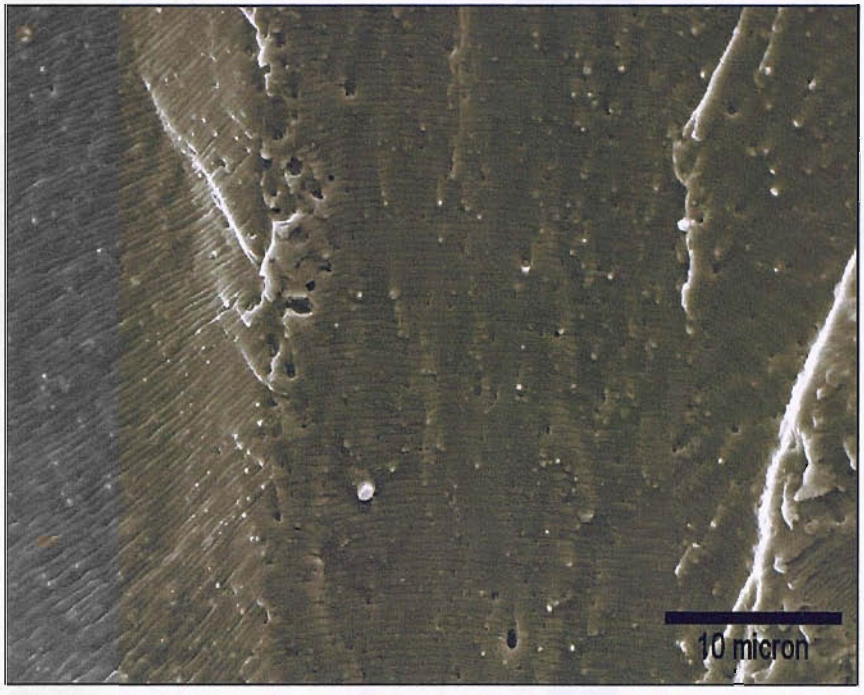

Figure 4.19 Typical striations fracture surface features at higher ΔK, 2027-ReX(100) ($\Delta K \sim 12$ MPa$\sqrt{m}$).

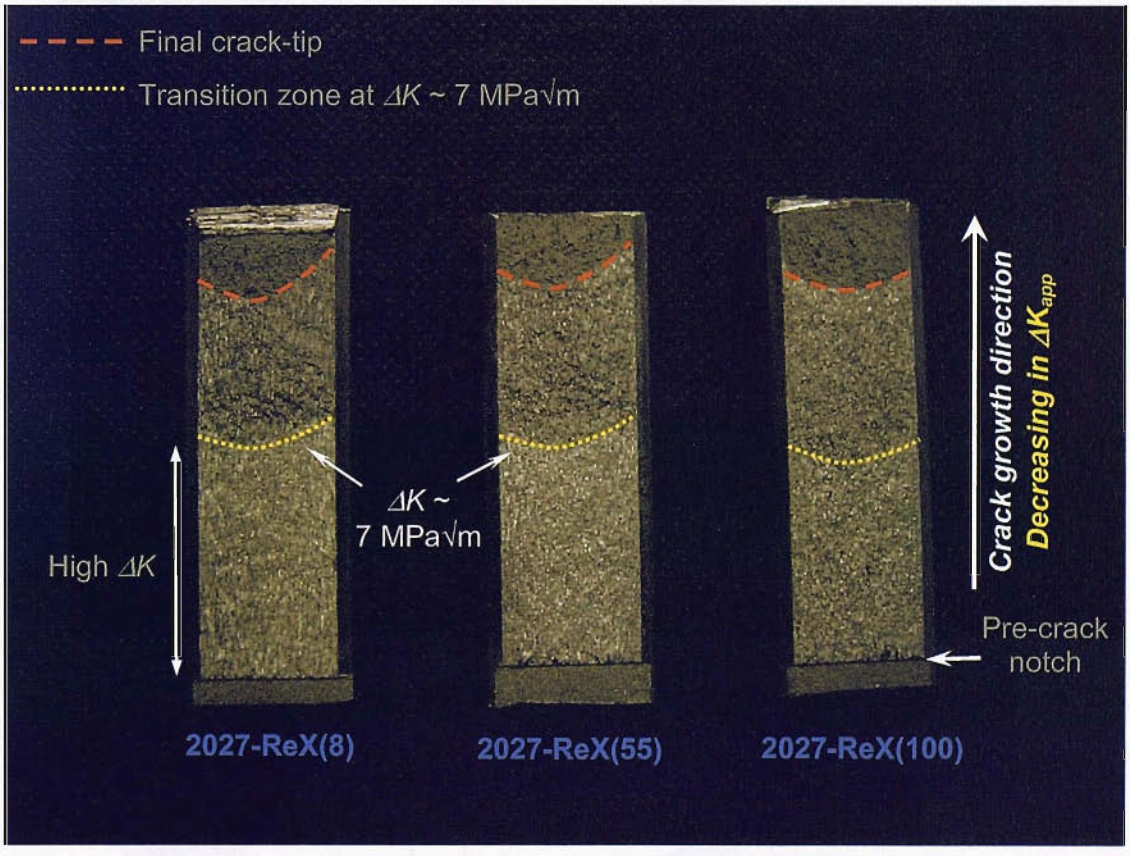

Figure 4.20 Macroscopic observations of fracture surface roughnesses in 2027 materials.

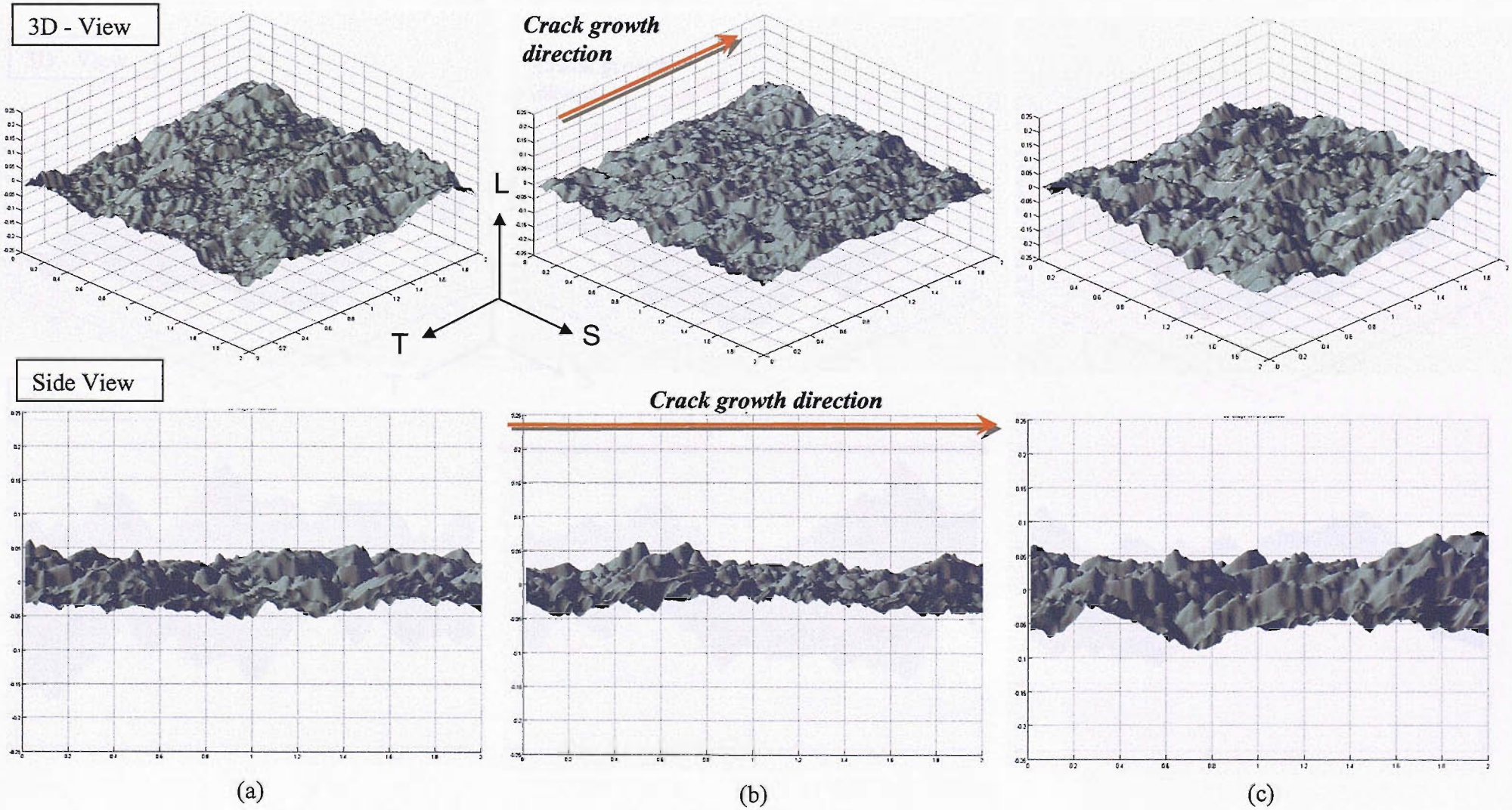

Figure 4.21 3D fracture surface roughness mapping at ΔK **of ~ 9 MPa$\sqrt{m}$:** (a) 2027-ReX(8), (b) 2027-ReX(55), and (c) 2027-ReX(100) (unit in mm).

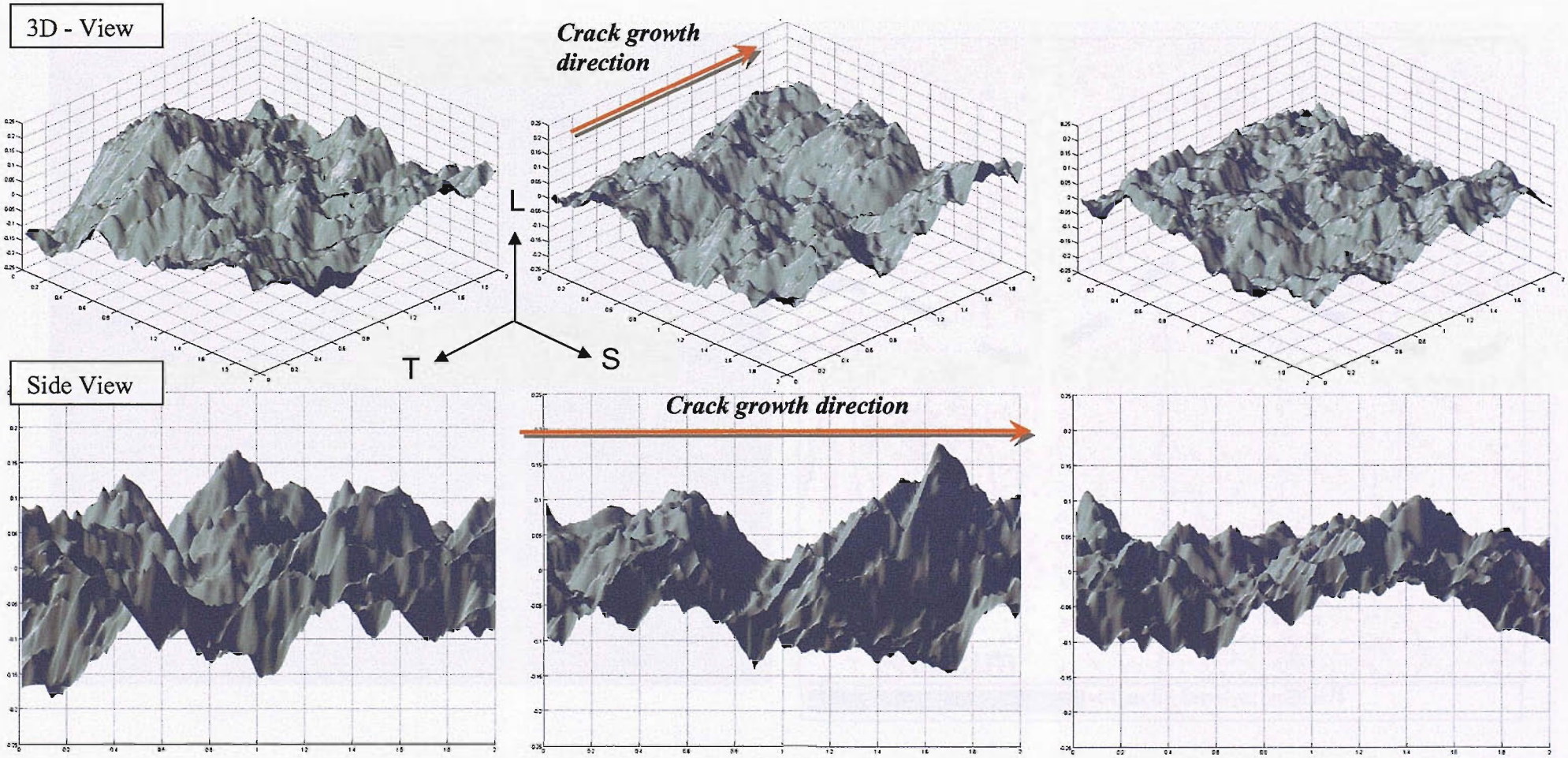

Figure 4.22 3D fracture surface roughness mapping at ΔK **of ~ 6 MPa$\sqrt{m}$:** (a) 2027-ReX(8), (b) 2027-ReX(55), and (c) 2027-ReX(100) (unit in mm).

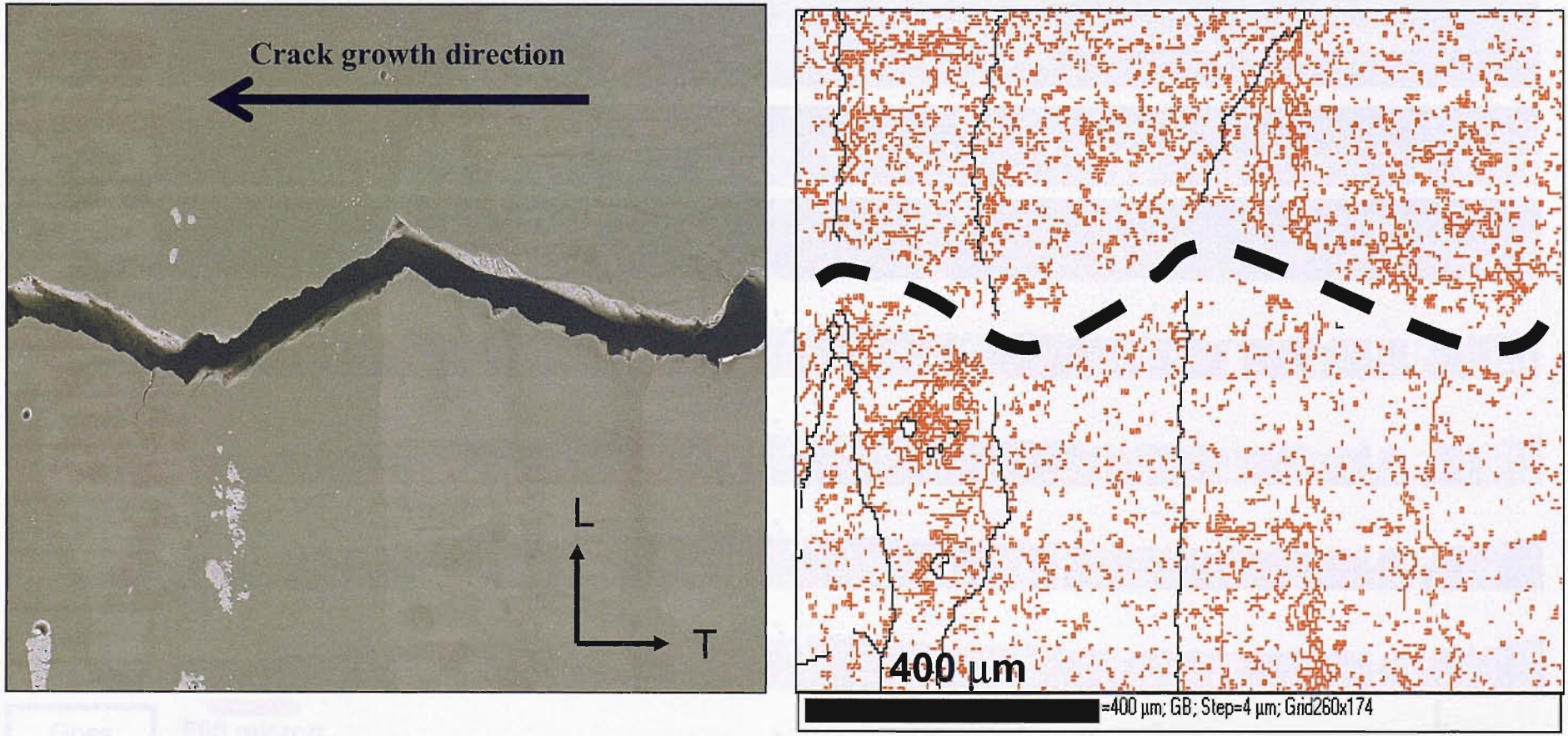

Figure 4.23 Polished section crack profiles of 2027-ReX(55) material in L-T plane at $\Delta K \sim 6$ **MPa$\sqrt{m}$:** (a) Secondary electron image (SEI), (b) corresponding EBSD grain boundaries map with crack path highlighted by dashed line.

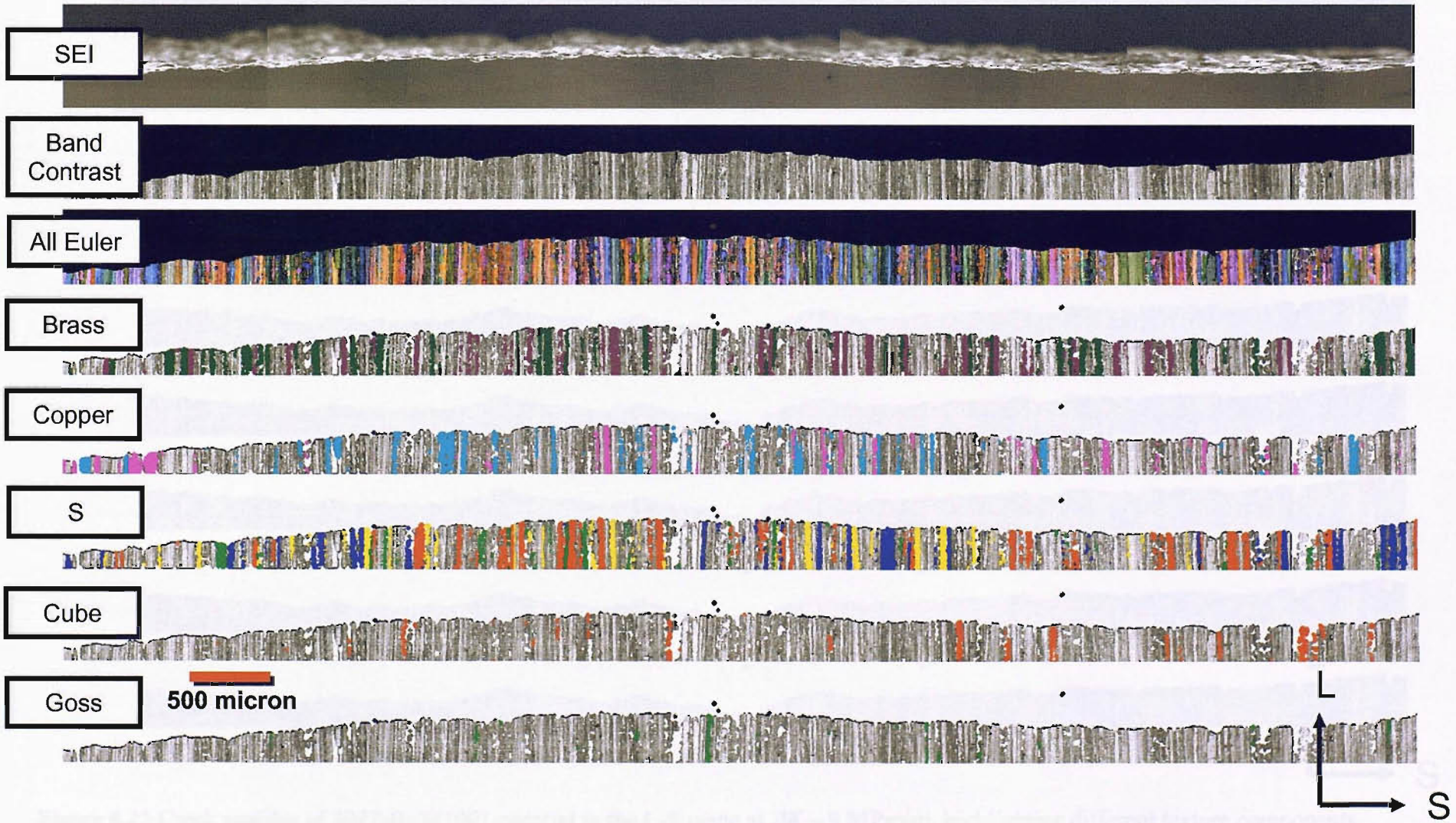

Figure 4.24 Crack profiles of 2027-ReX(8) material in the L-S plane at $\Delta K \sim 9$ **MPa$\sqrt{\text{m}}$**, highlighting different texture components.

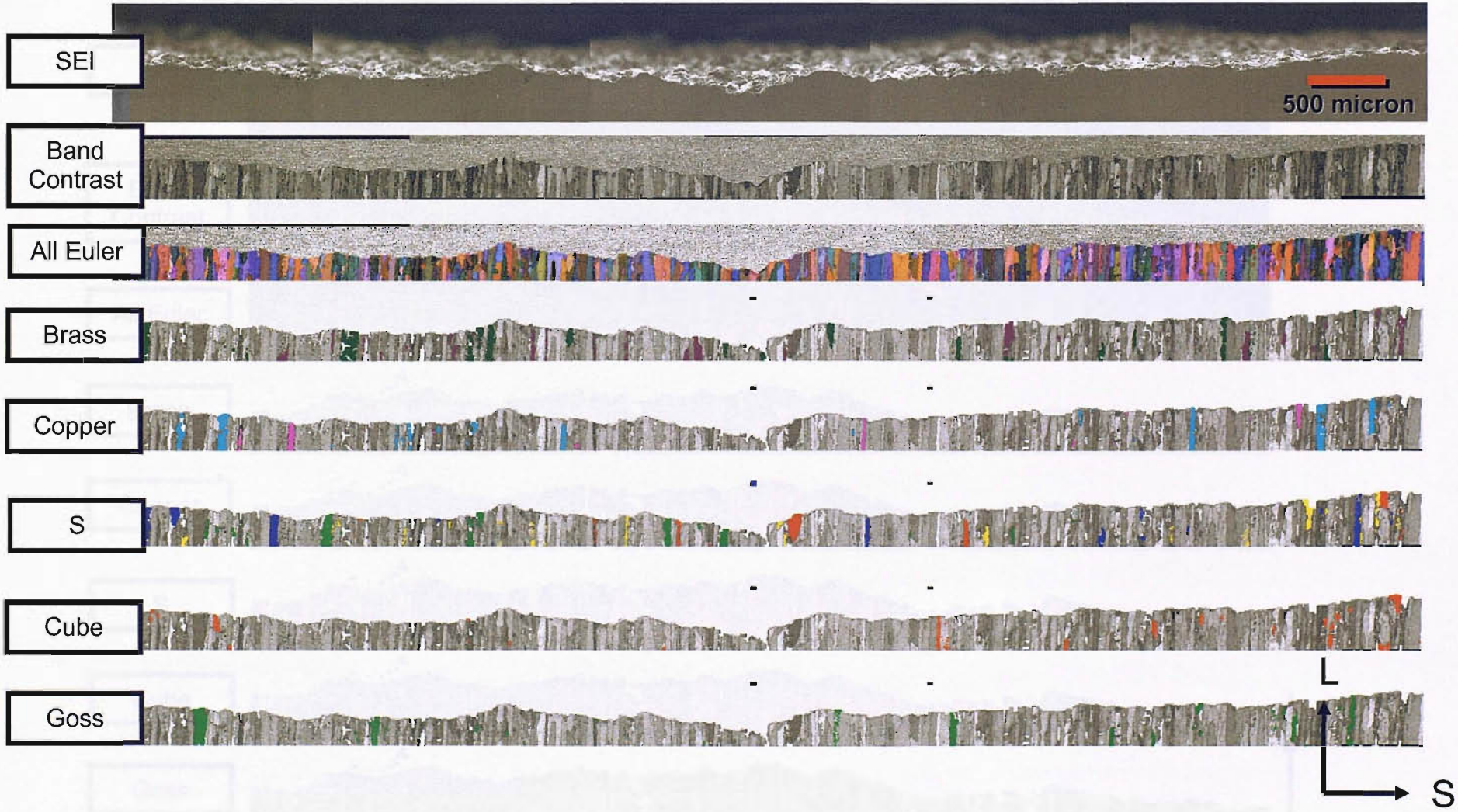

Figure 4.25 Crack profiles of 2027-ReX(100) material in the L-S plane at $\Delta K \sim 9$ **MPa$\sqrt{\text{m}}$**, highlighting different texture components.

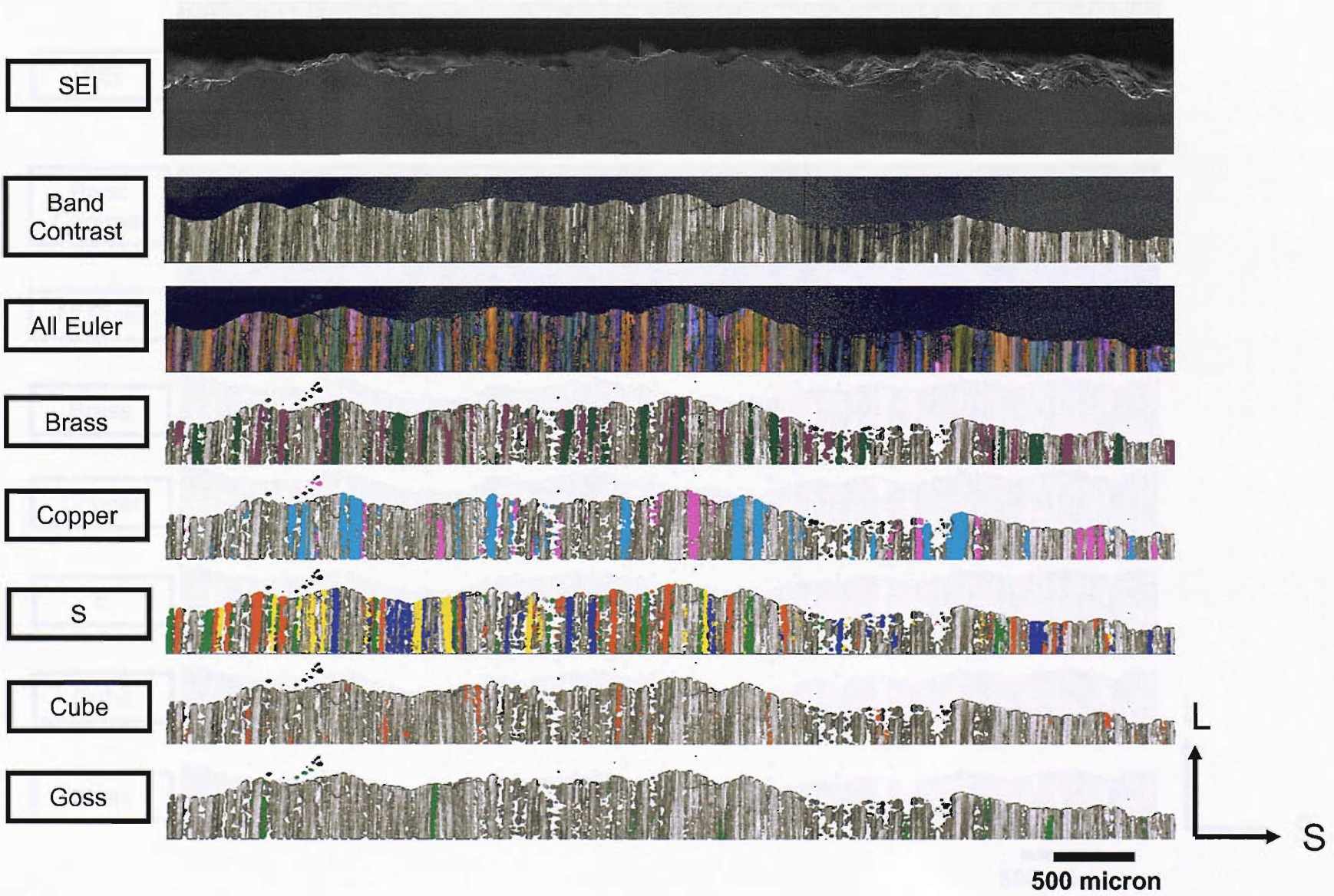

Figure 4.26 Crack profiles of 2027-ReX(8) material in the L-S plane at $\Delta K \sim 6$ **MPa$\sqrt{\text{m}}$**, highlighting different texture components.

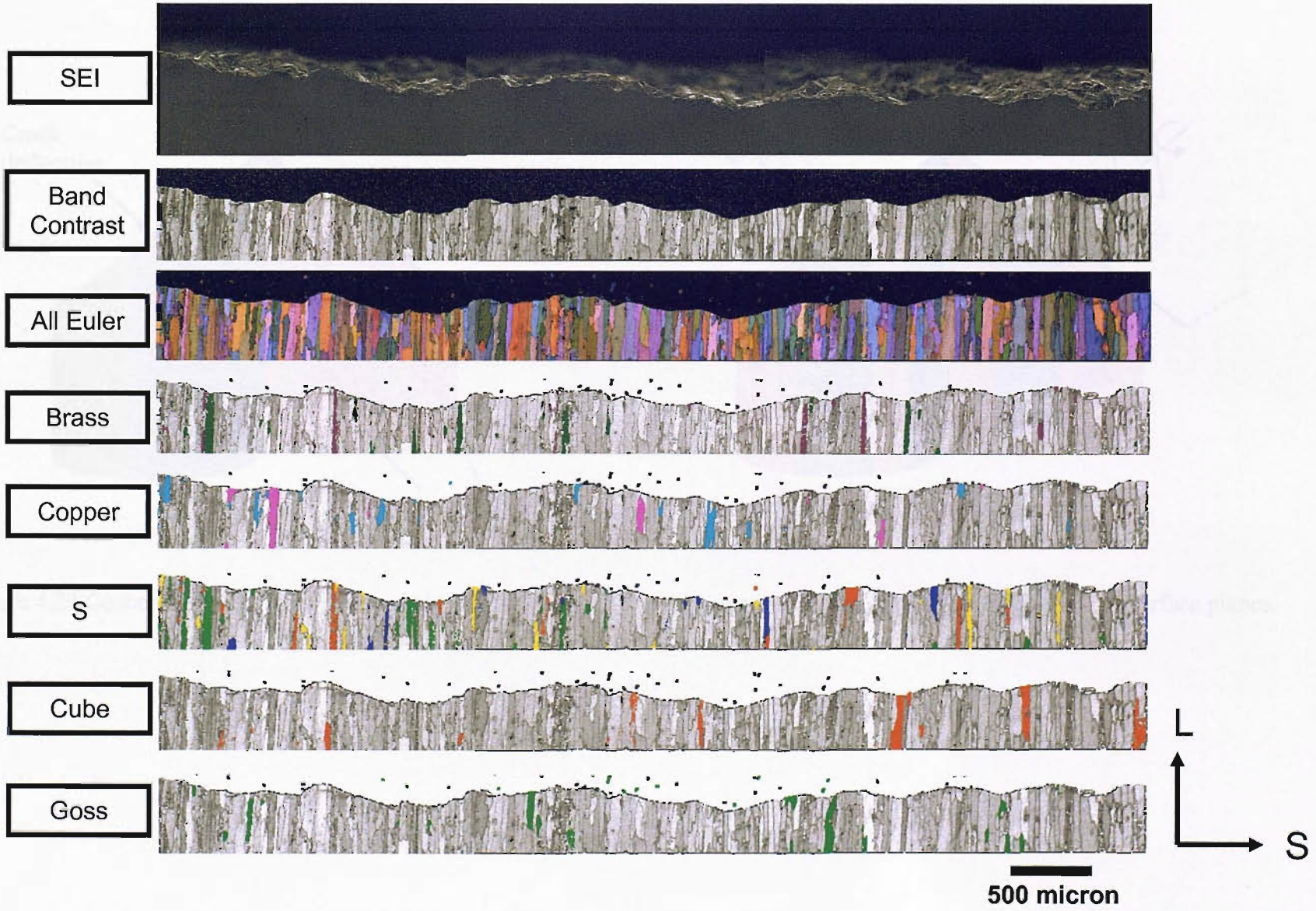

Figure 4.27 Crack profiles of 2027-ReX(100) material in the L-S plane at $\Delta K \sim 6$ **MPa$\sqrt{\text{m}}$**, highlighting different texture components

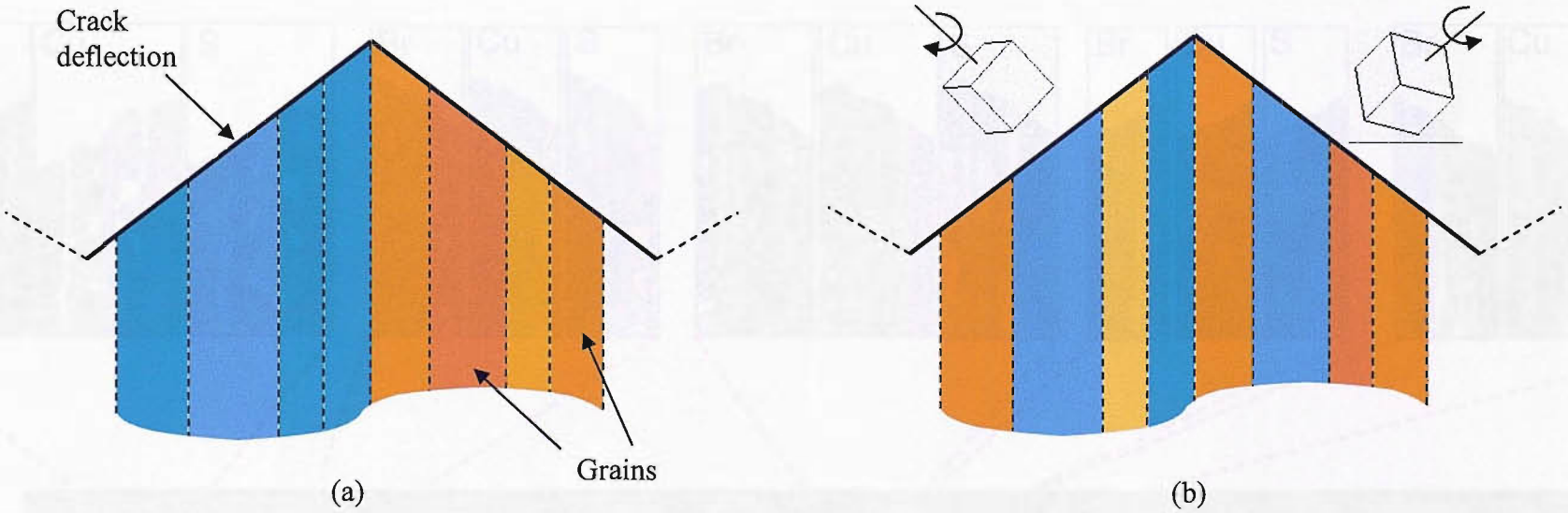

Figure 4.28 Concepts of multiple grain crack deflection; (a) common texture components, and (b) common fracture surface planes.

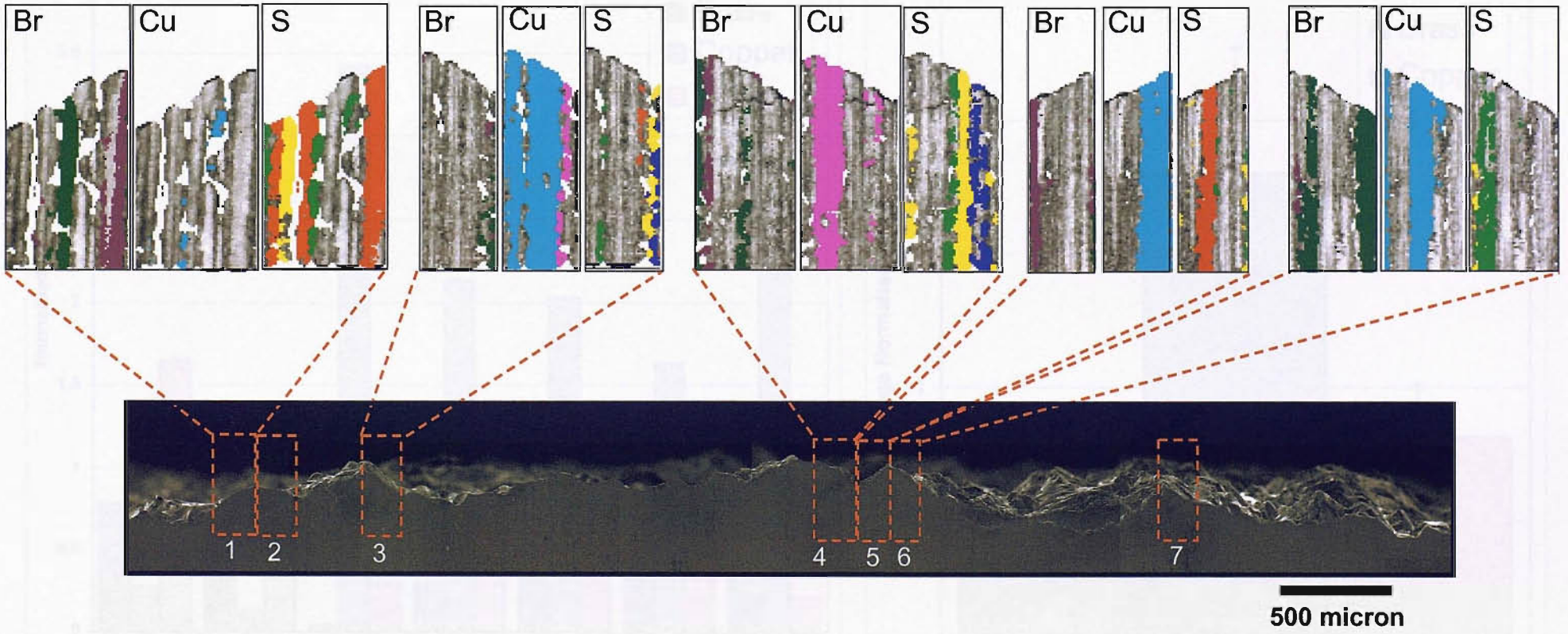

Figure 4.29 Texture components associated with deflected crack slopes in 2027-ReX(8) materials (at $\Delta K \sim 6$ **MPa**$\sqrt{\mathbf{m}}$).

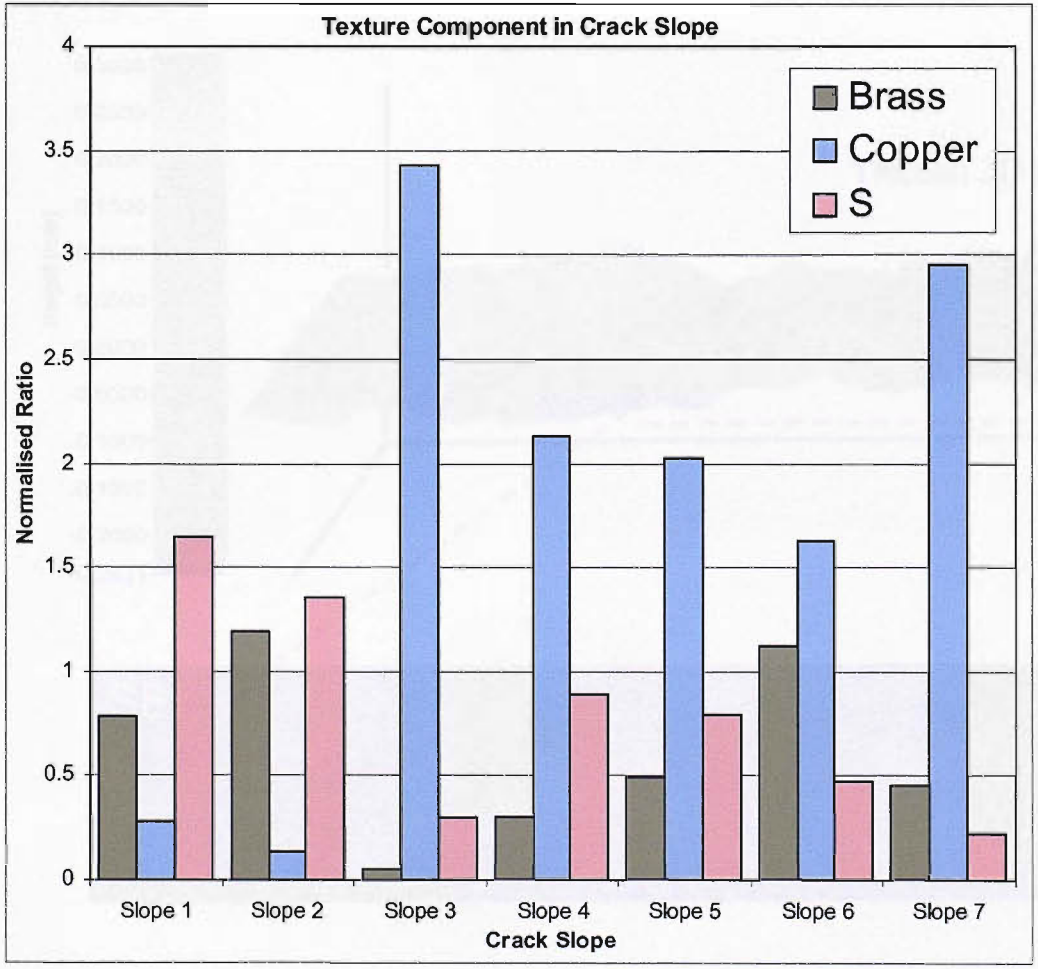

(a)

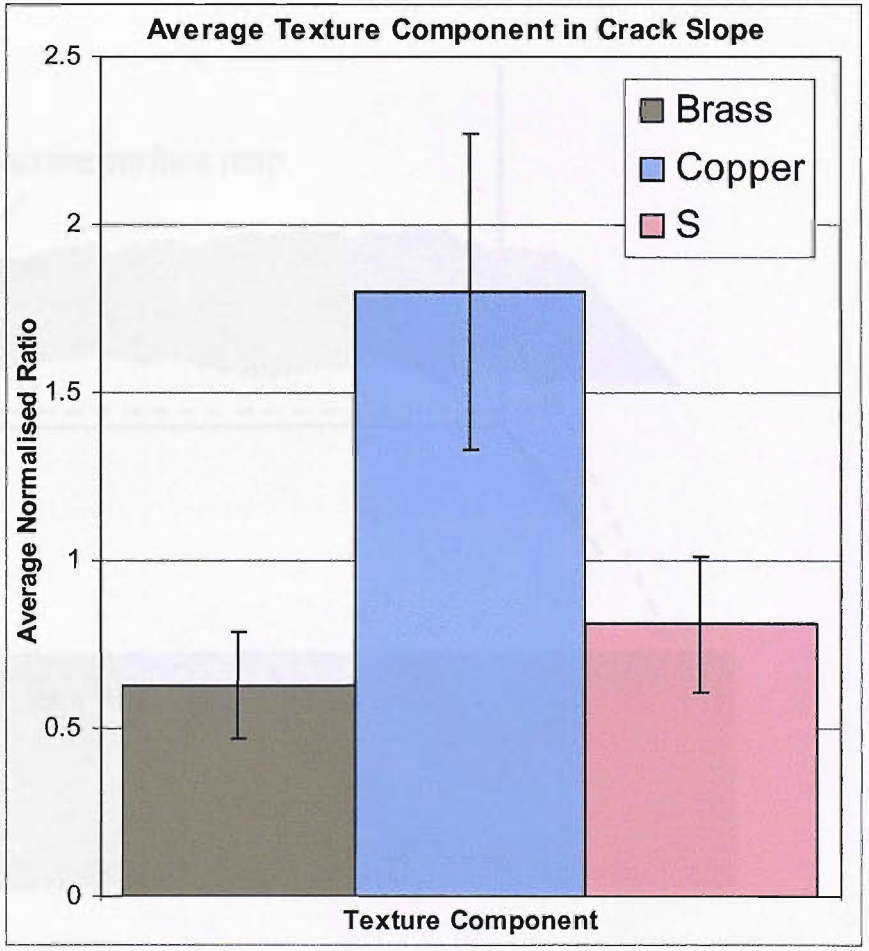

(b)

Figure 4.30 Statistical assessment of texture components associated with deflected crack slopes in 2027-ReX(8) material (at $\Delta K \sim 6$ MPa$\sqrt{m}$).

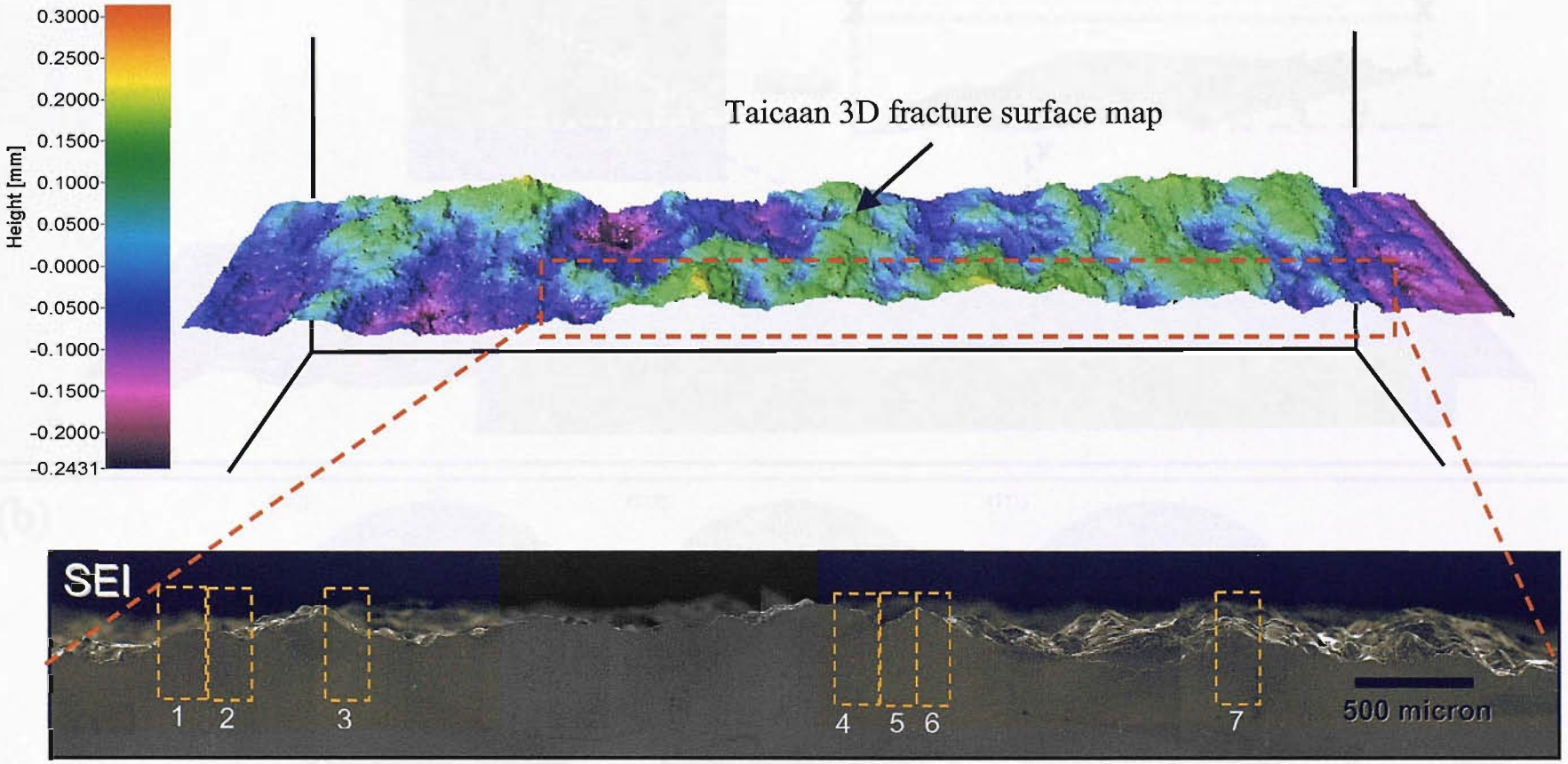

Figure 4.31 Taicaan 3D fracture surface mapping of area behind the crack profile of the 2027-ReX(8) materials at $\Delta K \sim 6$ **MPa$\sqrt{m}$** (Note: The same crack profile as shown in Figure 4.26 and analysed in Figure 4.29).

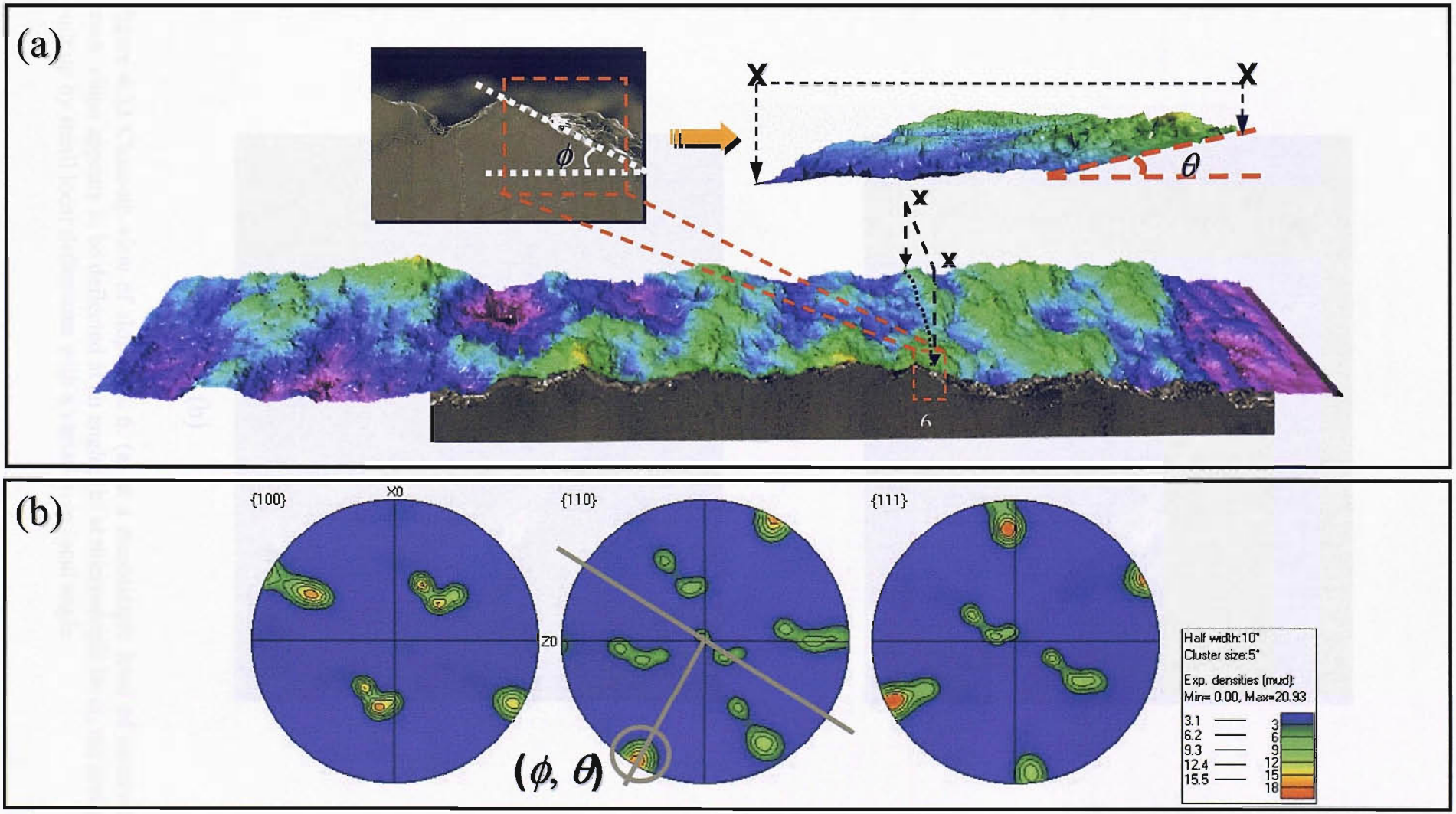

Figure 4.32 A typical example of crystallographic indexing of a section of crack deflection; (a) Crack deflection angles (θ, ϕ) determination from the combination of SEI image and Taicaan 3D fracture surface, (b) Peak determination at the sub-section {100}, {110} and {111} pole figures of the highlighted area in (a) by using measured (θ, ϕ).

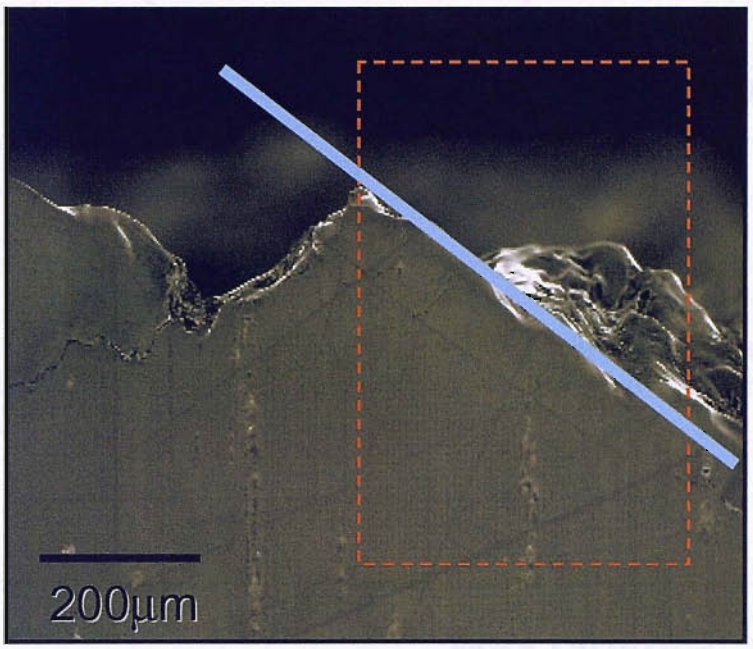

(a)

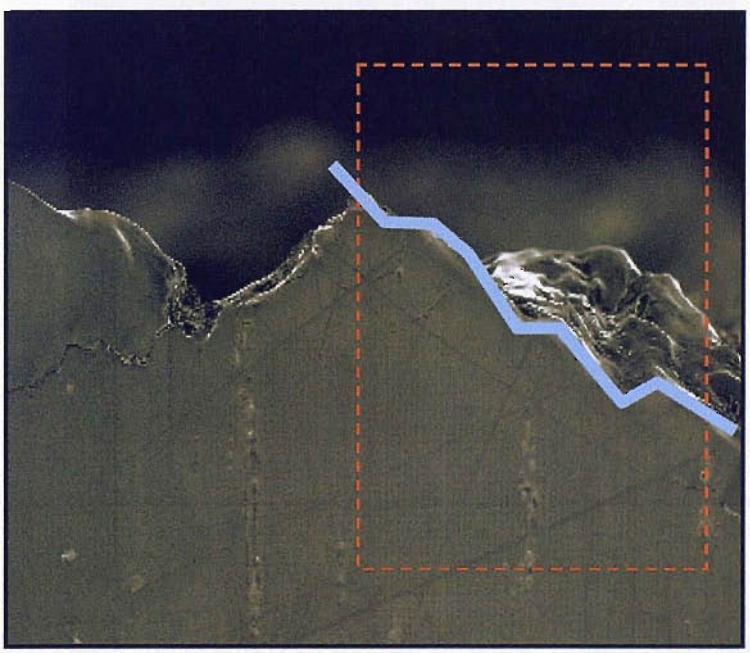

(b)

Figure 4.33 Close-up view of slope No. 6. (a) at a mesoscopic level of observation, crack slope appears to be deflected at an angle; (b) at microscopic level, the section is built up by small local deflections with a variation in local angle.

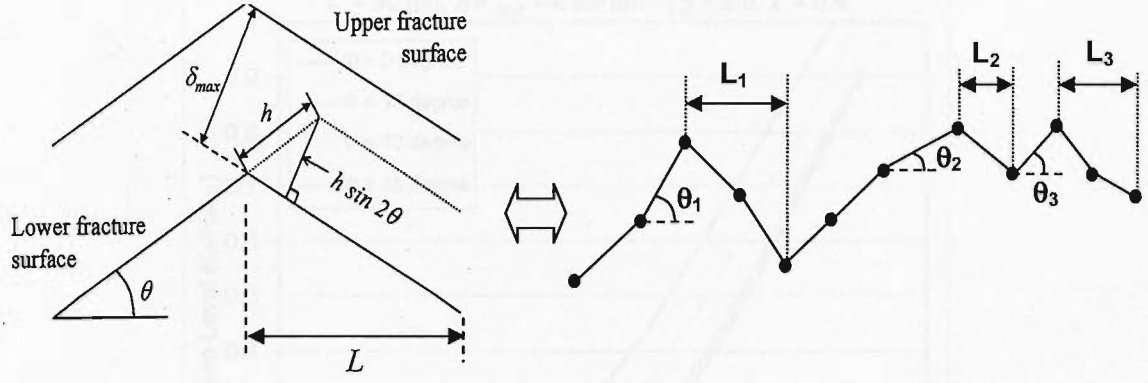

Figure 4.34 Schematic illustration of the correlation between the analytical RICC model definitions and micromechanism-based approach to measurement of real fracture surfaces.

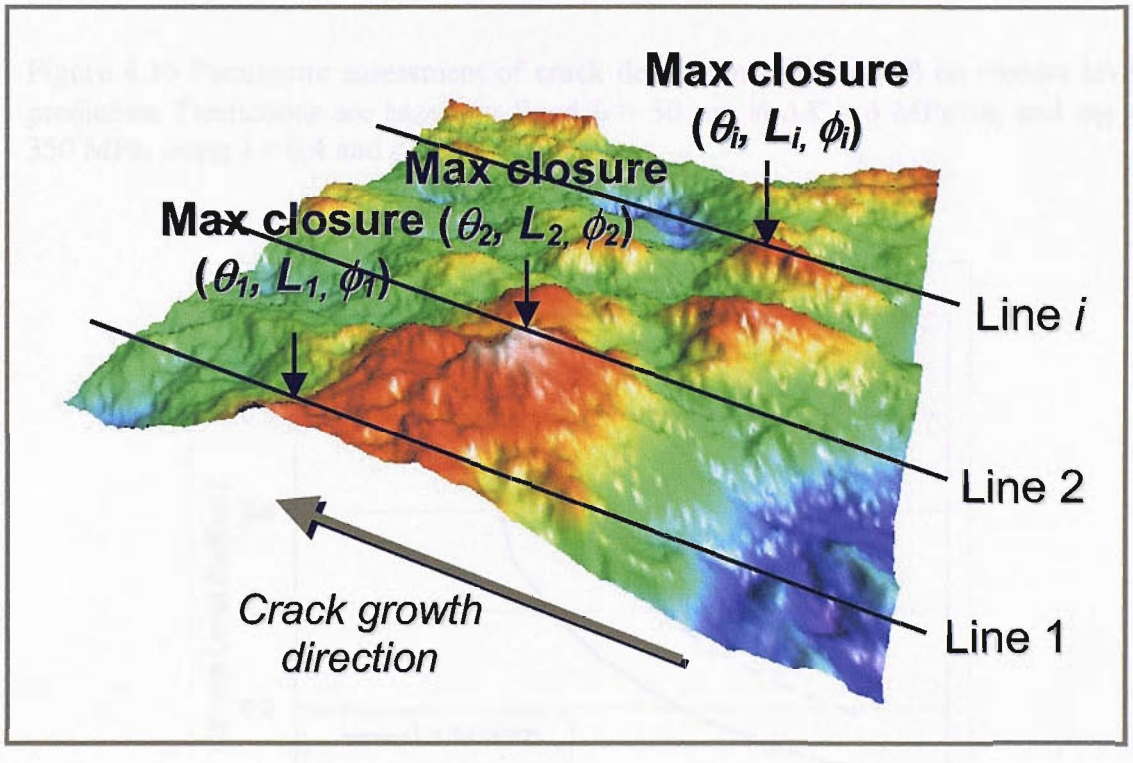

Figure 4.35 Schematic illustrations of overall θ, ϕ and L extraction from a typical 3D fracture surfaces mapped by Taicaan optical profilometry.

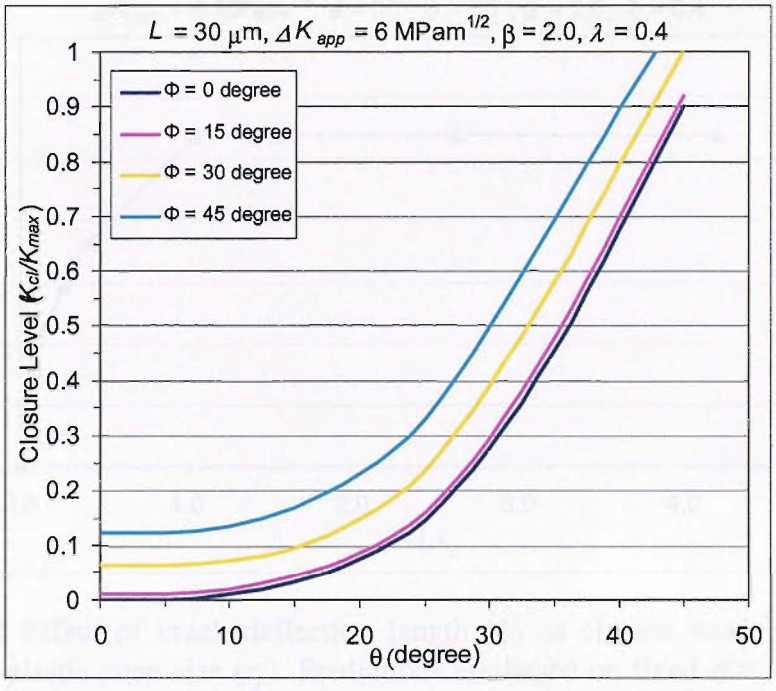

Figure 4.36 Parametric assessment of crack deflection angles (θ, ϕ) on closure level prediction. Predictions are based on fixed L = 30 μm at ΔK = 6 MPa√m, and σ_{YS} = 350 MPa, using $\lambda = 0.4$ and $\beta = 2.0$.

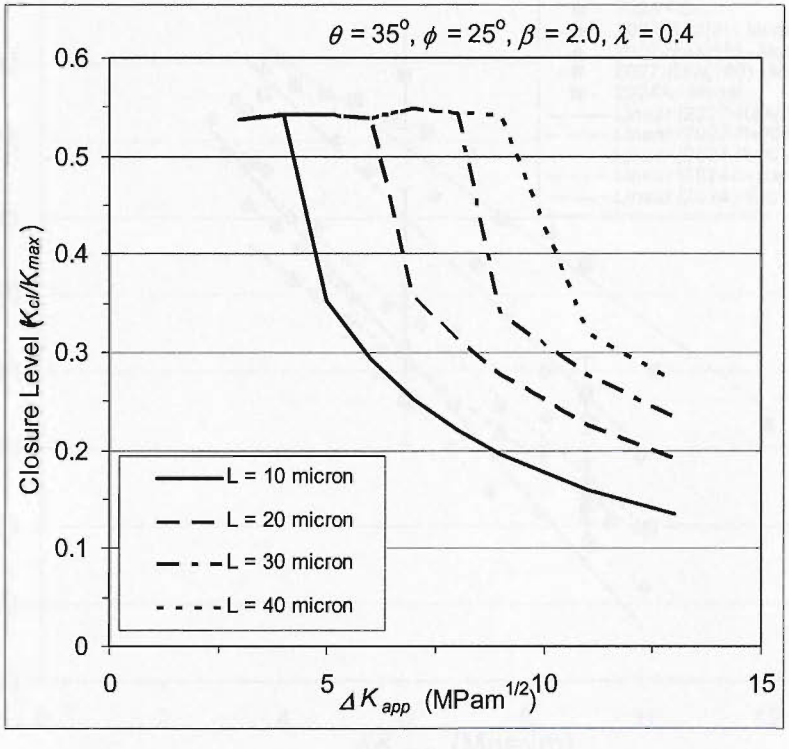

Figure 4.37 Parametric assessment of the effect of crack deflection length (L) in closure level prediction. Predictions are based on fixed $\theta = 35°$, $\phi = 25°$, σ_{YS} = 350 MPa, using $\lambda = 0.4$ and $\beta = 2.0$.

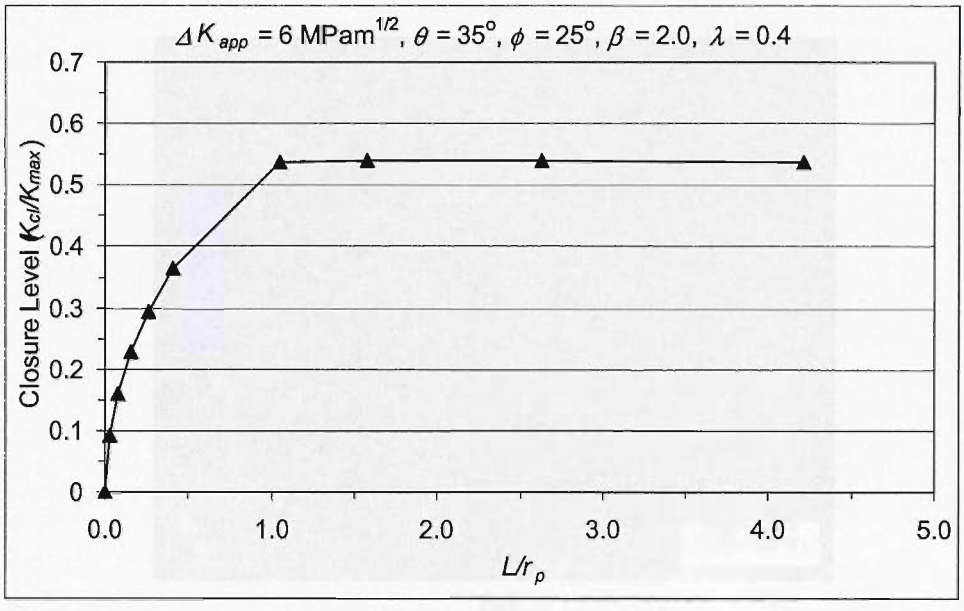

Figure 4.38 Effect of crack deflection length (L) in closure level prediction as a function of plastic zone size (r_p). Predictions are based on fixed $\theta = 35°$, $\phi = 25°$, at $\Delta K = 6$ MPa$\sqrt{m}$, $\sigma_{YS} = 350$ MPa, using $\lambda = 0.4$ and $\beta = 2.0$.

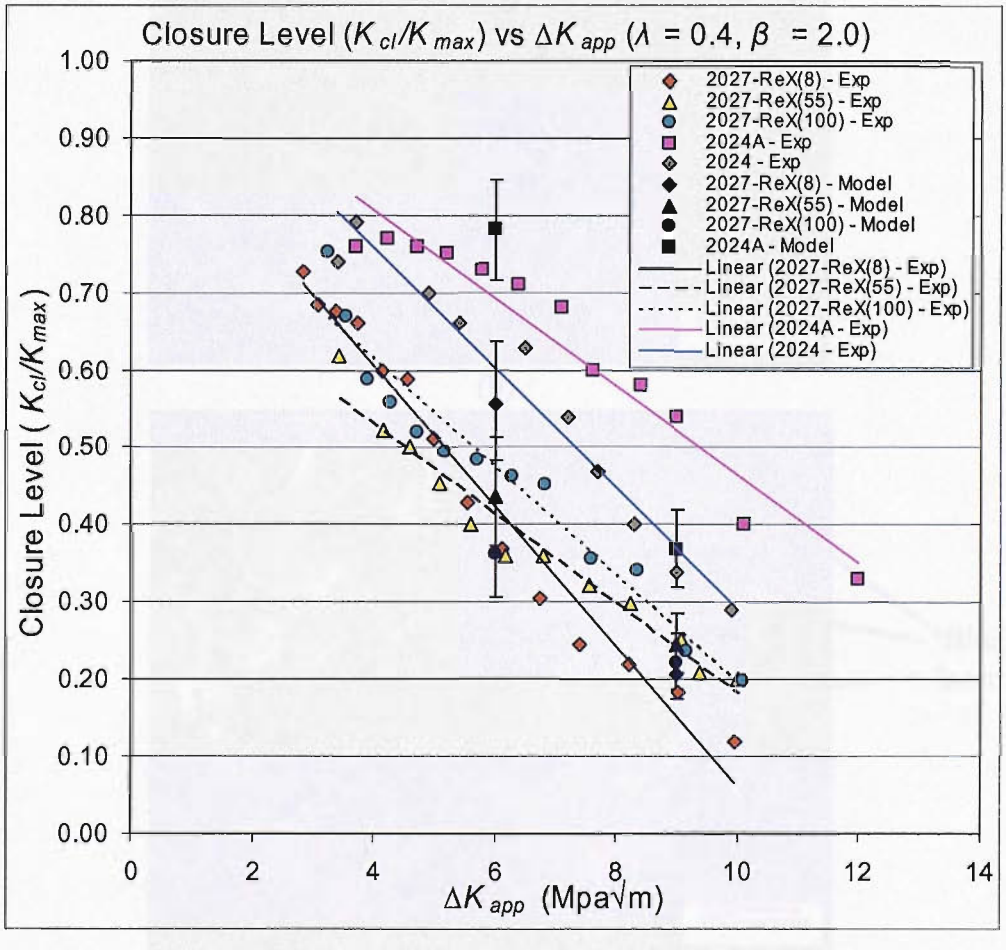

Figure 4.39 Comparison of experimentally measured closure levels with 3D analytical model predictions for three 2027 and the 2024A materials ($\lambda = 0.4$ and $\beta = 2.0$).

(a)

(b)

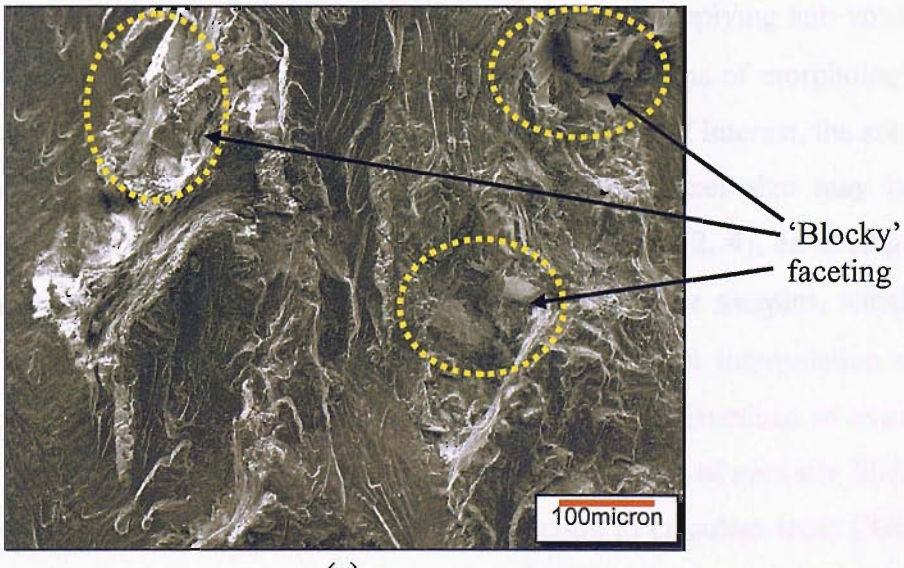

(c)

Figure 4.40 Comparison of typical SEM fracture surface images of (a) 2027-ReX(8), (b)2027-ReX(100), and (c)2024A materials at $\Delta K \sim 6$ MPa$\sqrt{m}$.

5. HIGH RESOLUTION SYNCHROTRON X-RAY TOMOGRAPHY OF CRACK CLOSURE MICROMECHNISMS

This chapter describes an innovative study of fatigue crack closure behaviour and micromechanisms in 2024 and 2024-type materials by using in-situ high resolution synchrotron X-ray tomography 3D imaging technique at Beamline ID19 of the European Synchrotron Radiation Facility, Grenoble, France. The feasibility of the application of this technique to the study is assessed and a variety of measurement methods are to extract quantitative information from the tomography data.

5.1 Introduction

Historically, X-ray computed tomography has been utilized as an advanced technique in diagnostic medical radiology. In this context, typical spatial resolution would be of the order of a few hundred micrometers. Recently, third-generation synchrotron radiation facilities have been identified as ideal sources for X-ray tomography, providing high intensity energy X-ray beams with excellent lateral coherence and monochromaticity. Microtomography of metallic samples performed at synchrotron radiation facilities has enabled the reconstruction of volumes with a typical spatial resolution of 6.5 ~ 14 μm [1]. In terms of the application of synchrotron X-ray microtomography to mechanical damage and crack problems, Guvenilir *et al.* [2, 3] have demonstrated the use of tomography to detect cracks fatigue crack closure in a bulk Al-Li sample with an crack opening as small as 0.5 μm by applying sub-voxel interpolation at an isotropic voxel size of 6.0 μm. However, in terms of morphology and quantification, where crack topology, COD and other features of interest, the sub-voxel interpolation used to define features smaller than the voxel size may be questioned. Specifically in the work of Guvenilir and co-workers [2, 4], an average crack opening at maximum specimen load was about 4 μm in their samples, which corresponds to about 60 % of voxel size (6.4 μm): i.e. sub-voxel interpolation is required to obtain any crack opening information from the results. Fractions of crack opening in individual voxels was estimated by a linear interpolation of partially filled voxel gray levels, and then summed in the opening direction to calculate local COD levels. Differentiation of the crack from the matrix may be identified as somewhat

arbitrary due to the lack of physical meaning of the linear attenuation coefficient used. Other factors, such as noise and interface fringes due to phase contrast were not considered.

In synchrotron X-ray microtomography, differences in phase induced on each side of an interface between two constituents of a material may be effectively added to classical attenuation contrast, potentially enhancing edge imaging quality, as discussed in Chapter 2. Phase sensitivity may be particularly obtained simply by varying sample-detector distance when using a coherent beam source. This has been shown to improve the detection of cracks even in the very earliest stages of their development (i.e. when they are not widely open) [5-7]. The major factors affecting spatial resolution in the reconstructed image are the sample size, the performance of the optical setup and the use of phase contrast imaging. Owing to recent developments in optical systems, an order of magnitude improvement in resolution has been enabled over the aforementioned studies of Guvenilir and co-workers.

In the present study, fatigue crack closure behaviour has been investigated by utilizing synchrotron X-ray microtomography with a resolution level of 0.7μm (isotropic voxel size). In addition, a liquid Gallium (Ga) grain boundary wetting technique has been investigated in conjunction with the microtomography to visualise and analyse simultaneously the correlation between the 3D structures of grains and fatigue cracks. The visualisation of the grains is based on the penetration of liquid Ga into the Al grain boundaries serving as a selective contrast agent [8]. Subsequently, electron backscattering diffraction (EBSD) assessment of grain orientation in the computed tomography samples provides detailed crystallographic information on possible crack propagation mechanisms.

5.2 Experimental Methods

The technique of X-ray tomography was applied in the present work with the aim of observing fatigue crack closure behaviour in 2024-type alloys. Two experiments were carried out, using two alloys; specifically 2024-T351 (1st experiment) and 2027-ReX(8) (2nd experiment), as described in Chapter 3. The specimen preparation work

was carried out at the University of Southampton, whilst the X-ray tomography experiment was carried out at the Beamline ID19 of European Synchrotron Radiation Facility (ESRF) in Grenoble, France.

To perform high resolution microtomographic imaging at the submicrometer level, the test sample was required to be approximately 1×1 mm^2 in cross-section. In order to obtain meaningful information in relation to real macroscopic cracks from such a small sample, a standard sized fatigue specimen was initially prepared using ordinary laboratory apparatus, and then carefully sectioned to the required dimensions.

5.2.1 Sample Preparation

Prior to the X-ray tomography experiment, conventional single edge notched (SEN) fatigue specimens (5 x 20 x 130 mm) were used in three point bending fatigue tests to grow a 'large' (macroscopic) fatigue crack. Figure 5.1 illustrates the specimen dimensions. A slit with an approximate tip radius of 0.15 mm was machined using electrical discharge machining (wire eroder), giving a ratio of nominal width (W) to initial crack length (a_o) at the onset of testing of 0.25.

Three point bending fatigue tests were carried out on an Instron 8501 servo hydraulic fatigue testing machine at room temperature in air with a load ratio, $R = P_{min} / P_{max}$, of 0.1, at a frequency of 20 Hz in the LT orientation. Four probe potential drop was used for crack monitoring. Specimens were pre-cracked at a constant ΔK of 10 MPa$\sqrt{m}$ for a crack extension of 1mm. Subsequently load shedding according to ASTM E647-95A [9] was employed to reduce the ΔK level to 6 MPa$\sqrt{m}$. Fatigue cracks were then allowed to grow under constant ΔK conditions at this level until a further 0.5 mm of growth had taken place at which point the tests were terminated. Another set of samples were prepared at the same time, however on completion of the process detailed above, a single 50% overload (i.e. to a maximum K of 10.0 MPa$\sqrt{m}$) was applied. The loading was then reverted to the constant ΔK = 6 MPa$\sqrt{m}$ baseline. Fatigue cracks in these samples were found to arrest almost immediately post overload (after ~ 50 μm of crack growth) and the tests were then terminated (see Chapter 6 for further consideration of overload behaviour of these materials).

In order to obtain high resolution imgaes in the X-ray tomography scan, a 'matchstick' like specimen was extracted at the crack-tip of the original SEN specimens with dimensions of approximately 1 x 1 mm^2 in cross-sectional area, and 25 mm in length, as illustrated in Figure 5.2. A low speed diamond saw was used to cut this matchstick specimen in order to preserve the crack profile with minimal cutting force or thermal input to the material. The matchstick specimen was extracted at the middle of the original SEN specimen: this was to avoid the surface layers that induce plane stress effects on the crack. Hence, the crack in the matchstick specimen was hoped to reasonably represent steady state plane strain growth in a large section sample. Figure 5.3 shows schematically the approximate specimen geometry and plastic zone dimensions associated with the applied loading; the crack length was hoped to be at a length of $W/2$ (i.e. ~500μm), with a maximum active plastic zone size ($R_{p.max}$) which was smaller than $W/20$, where W is the width of the sample (~1000μm). A certain length of elastic ligament is retained to provide constraint for crack closure to occur.

After the matchstick specimens were extracted from the original SEN specimens, each end was glued with pairs of brass 'T' shape tabs (using standard epoxy resin adhesive) as shown schematically in Figure 5.4. The function of the 'T' shape tab at each end of the specimen was to fit the specimen into the grip of the specially designed loading stage [10] when performing the X-ray tomography imaging. In the first ESRF experiment, the end tabs were glued to the matchstick by hand with optical checks of alignment. An alignment jig with greater alignment precision (to hold the sample and tabs in position) was design by the author for the second ESRF tomography experiments, as shown in Figure 5.5. The adjustment screws in the jig control the movement of the alignment blocks that ensure the position of the matchstick sample. A push block is applied carefully in the final stage to remove the whole sample from the jig without bending it.

5.2.2 In-situ Straining and Tomographic Imaging

After the specimen preparation was performed in the laboratory at Southampton, the matchstick specimens were taken to the ESRF. Figure 5.6 shows a schematic diagram of the tomography apparatus (Beamline ID-19). The experimental hall is shielded

with lead and concrete, and separated from the control room. The matchstick specimen with 'T' tabs in both ends was gripped in the high precision sample loading stage (previously designed by INSA-Lyon [11]), where it was placed approximately 145 m from the small beam source of the synchrotron. This particular large source to sample distance coupled with small source size provides a highly coherent beam with having either an extended wide homogeneous beam (up to 14 mm vertical x 40 mm horizontal) or a focus spot (down to 100 nm) when required. In the present case, the beam size is in the order of 1 mm^2. In order to obtain high quality 3D images, the incoming 'white' synchrotron radiation is monochromated to 20KeV using a multilayer filter. A high resolution cooled 2048×2048 pixel fast-readout (~ 0.06 s/frame), low-noise (FRELON) charge-coupled device (CCD) detector system was positioned 50 mm behind the sample, thereby making the imaging system edge sensitive via phase modulation in addition to absorption contrast [8]. The detector system consists of a fluorescence screen imaged microscopically, projecting onto a CCD camera. The camera then captured the 2D radiographic projection images of the specimen. All functional elements of the beamline, from the insertion device to the detection of the signal are computer controlled and adjusted on-line by the users in the control room. Projection images were taken by the detector behind the specimen for every 0.12 degree of rotation in a fixed rotation axis. Each view required 0.7 seconds to acquire the image: as such each tomographic scan required at least 17.5 minutes. The whole cross section of the specimen, to a height of ~ 300 μm, was captured on the CCD camera. In a complete scan, approximately 1500 projections were taken by the detector in 180 degrees of rotation. Each tomography reconstruction process then took two to three hours of CPU time on a SUN UNIX server [12]. Image slices were reconstructed using a conventional filtered backprojection algorithm [12]. Grey values in each dataset were calibrated so that variation between the most opaque and transparent voxels could be expressed within an 8 bit grey scale range (between 0 and 255). Isotropic voxels with a 0.7 μm edge are achieved in the reconstructed slices. The final data size of each 3D volume is about 500 Megabytes to 1 Gigabytes. Figure 5.7 shows a typical apparatus setting during the experiment at Beamline ID19, ESRF.

In-situ straining was performed in the specimen loading stage, which was essentially an X-ray transparent Perspex tube, with a stepper motor and load cell application and

sensing [10]. As illustrated in Figure 5.8, the specimen was held vertically between the grips of a high precision positioning stage. Before performing in-situ straining on the specimen, the actual crack lengths (a) of the samples were measured by taking projection radiographs on the sample. Stress intensity factors for the tip of a through-thickness, single edge crack of length a, under remote tensile loading were then based on the following equation:

$$K_I = \sigma\sqrt{a} f\left(\frac{a}{W}\right) \tag{5.1}$$

$$where\ f\left(\frac{a}{W}\right) = 1.99 - 0.41\frac{a}{W} + 18.7\left(\frac{a}{W}\right)^2 - 38.48\left(\frac{a}{W}\right)^3 + 53.85\left(\frac{a}{W}\right)^4$$

Where W is the specimen width and σ is the remote stress. Individual sample dimensions were carefully obtained from each sample imaged. The in-situ straining process was performed in 11 loading steps for each specimen; which is at successive ~ 20% increments/decrements of K_{max} applied in the original SEN test. The sequence is as shown in Figure 5.9. Although the load frame and the specimen were stabilized before every measurement, stress relaxation of the order of ~ 10 % of applied load was observed during some scans in first ESRF experiment. This is attributed to creep in the end tab adhesive. However, in the second experiment, the choice of adhesive has been modified to keep less stress relaxation down to the < 5% of applied load. For each loading step, a complete tomography scan was taken.

5.2.3 Grain Boundary Imaging

At present, only a few experimental techniques allow us to characterise the 3D grain structure in the bulk of a polycrystalline material such as aluminium. These include serial sectioning (e.g. mechanically or by focussed ion beam techniques) [13], and X-ray tracking [14, 15]. Sectioning methods have the clear disadvantage of being laborious and destructive. X-ray tracking is a non-destructive technique based on Laue diffraction, and can provide shape and crystallographic orientation of each individual grain within a bulk polycrystalline material, however, current spatial resolutions of X-ray tracking are of the order of 20 – 40 μm.

On the other hand, liquid Ga grain boundaries wetting technique have been recently applied in conjunction with X-ray microtomography to visualise the 3D grain structures of polycrystalline materials [8, 16, 17]. This technique is based on the rapid penetration (10^{-3} – 100 μm/s) of the liquid phase along the grain boundaries that takes place in a variety of metallic and ceramic systems. This process leads to the formation of a liquid film with a typical width of the order of 0.1 – 10 μm. The degree of liquid penetration depend on parameters such as temperature, composition of the involved materials, the detailed microstructural character of the grain boundaries, total amount of liquid metal, geometry of the sample, thermo-mechanical treatment of the base material (i.e. residual stress effects) and surrounding atmosphere. Only grain boundaries which fulfil the wetting condition $\nu_{gb} > 2\nu_{sl}$, where ν_{gb} and ν_{sl} denote the grain boundary and solid-liquid interface tensions respectively, may be prone to penetration.

In the present study, this technique was applied to fatigue cracked samples to visualise simultaneously 3D grain structures and fatigue crack topologies. Due to the fact that Ga has a considerably higher X-ray attenuation coefficient than Al, grain boundary Ga layers can be easily detected by absorption microtomography. Grain visualisation in the present Al-alloys sample was achieved by applying liquid Ga (T_m = 29.8°C) on the sample surface, which may then penetrate rapidly (~ 10 μm/s) [8] along the grain boundaries. To ensure intimate contact between the aluminium sample surface and the liquid Ga, the sample surface oxide was scratched during the application of the liquid Ga. Samples were then annealed at a temperature of 60°C for ~ 40 minutes before the acquisition of tomography data. Figure 5.10 shows a schematic diagram of the application of gallium wetting to the tomography samples. It should be noted that special grain boundaries (low $\sum$ value) and low angle boundaries which are known to have lower effective surface tensions and might not be detected by this technique [18]. Such Ga wetting of grain boundaryies may be identified with liquid metal embrittlement [19, 20], with the application of this technique to the samples leading to a profound loss of the mechanical integrity of the material (grain decohesion via the liquid metal layer): as such in-situ loading of samples is carried out before Ga charging, with considerable care being required for all subsequent sample handling.

Post-mortem EBSD analysis of grain orientations was also carried out on the Ga charged samples with a step size of 1.5 μm at an accelerating voltage of 15 kV and a specimen tilt of 55° in a Jeol 6500f FEG-SEM. Ga charged samples were cold resin mounted, mechanically polished (with distilled water) and electro-polished carefully at the through-thickness plane (L-S plane) for the subsequent EBSD scans to facilitate a crystallographic interpretation of the cracking process.

5.3 Analysis Techniques

A primary goal of this work was to explore the effectiveness of high-resolution X-ray tomography study of fatigue crack behaviour: as such several analysis methods were established to extract quantitative information from the tomography datasets. All analysis work was carried out using the commercial 3D image analysis package, VGStudio MAX (version 1.20) [21], using a Dell Precision Work Station with Dual Intel Xenon 3.0 GHz processors and 4 Gigabytes of memory (required for handling large 3D image dataset).

5.3.1 Volume Rendering

Crack volumes were extracted from the tomographically reconstructed volumes via a thresholding technique. Cracks were identified on two-dimensional reconstructed slices, and a three-dimensional 'seed' growth technique applied to 'fill' the volume of the whole crack. All voxels that are three-dimensionally connected to the manually set seed point and have a voxel grey value within a set tolerance range are thresholded and labelled as the crack volume. In order to threshold the crack volume accurately and consistently, the seed with the most applicable grey value has to be chosen (see Section 5.4.1). 3D visualisation of the Ga wetted grain boundaries and other microstructural features such as intermetallic particles and pores have also been implemented based on the same volume thresholding technique.

5.3.2 Microstructural Displacement Gauging

Pairs of approximately spherical microstructural features, such as intermetallic particles or micro-pores within the material, were identified and thresholded as gauge

marks on opposite crack faces, lying approximately parallel to the loading axis. Such pairs of microstructural features were again extracted from the reconstructed volume via the seed thresholding technique. Subsequently, by measuring changes in the separation of object pairs under loading, local compliance curves could be obtained to describe the micro-mechanical behaviour of the crack.

Although this procedure does not give absolute values of COD, there are several valuable features: such as (a) mode I, II and III displacement components can be assessed, and (b) robust automatic displacement mapping can potentially be constructed as a function of local crack topology.

5.3.3 Ray Casting Technique

With the extracted crack volume being obtained between two crack surfaces, the crack opening displacement (COD) can be measured on a scale of the order of one voxel size, using 2D representations of spatial distribution of opacity. Such measurements were produced by a direct ray casting technique [22] over whole crack surfaces. A notional ray of light is cast from a viewpoint perpendicular to the crack plane through each voxel of the segmented crack, projecting an overall opacity on to a plane perpendicular to the loading axis. The final grey-scale distribution for the resultant projected 2D image of the crack corresponds to accumulating opacity values along the rays to achieve crack opening measurement. All the voxels which belonged to the crack are set fully opaque before the projection using a simple boxcar transfer function [23] so that the total opacity along a given ray through the crack gives quantitative information on the local thickness of the thresholded volume. In terms of the accuracy of these measurements, the so-called partial volume effect [24] is crucial, which brings a transition area with a grey-value ramp over several voxels in width at an interface between radiographically dissimilar phases. Therefore, an appropriate tolerance value has to be applied when thresholding the crack volume in order to obtain useful results. As far as a specific choice of setting values (such as voxel thresholding tolerance) used, consistent sets of COD values can be sought using a consistent sequence of imaging operations. As part of this work, the ray casting

method was particularly assessed over small crack areas in relation to microstructural displacement gauging, described in Section 5.3.2.

5.4 Results and Discussion

Whilst an initial objective of the present study was to achieve a direct comparison of fatigue behaviour in overloaded and non-overloaded (normal) loaded samples, practical problems raised in the initial experiment, and also the nature of the materials have prevented the capture of a satisfactory set of comparable results between overload and normal loaded sample. This has been attributable to a combination of several factors which are discussed in Section 5.6. As a result, analysis in this chapter are particularly presented to demonstrate the feasibility and reproducibility of the application of X-ray tomography techniques in the investigation of fatigue crack closure where several analysis techniques have been developed, rather than comparing the significant fatigue behaviour differences between these two type of sample.

From the two ESRF beam sessions that were available, we managed to collect tomography data sets from five samples, out of a total 20 that were prepared. These data sets are discussed throughout this chapter based on their applicability to a particular analysis technique. Detailed information of these samples is listed in Table 5.1.

Sample No.	Loading Condition	Materials
O1	Overloaded	2024
N4	Normal loads	2027-ReX(8)
N5	Normal loads	2027-ReX(8)
O3	Overloaded	2027-ReX(8)
O9	Overloaded	2027-ReX(8)

Table 5.1 Tomography sample designation.

5.4.1 Object Thresholding

The general scale of the reconstructed volume obtained from each test piece is illustrated in Figure 5.11, which corresponds to approximately 1000 μm x 1000 μm x 300 μm. Figure 5.12 shows a typical 2D slice image of a reconstructed volume along the crack growth direction, captured from sample O1 under zero load. A complex crack morphology can be seen at the centre of the image, with relatively spherical micro-pores (black) [25] and complex intermetallic particle groups (white) in the surrounding matrix. The quality of the image may be seen to be comparable to that of a conventional optical microscope (i.e. resolution is of a similar order). In all cases, cracks were seen to be predominantly open, even at the zero loading condition, as shown in Figure 5.12. This may in itself be seen as evidence of a wedging action on the crack (i.e. closure), as an ideal elastic crack would of course be expected to be closed at zero load. Crack bifurcation and serrated crack paths are readily observable at points A and B respectively. In addition, a 'classical' crack closure contact between surface asperities can be identified at point C. It is worth noting that the 'wavy' features in the aluminium matrix which can be seen mostly in the area surrounding the crack are artefacts of the phase contrast imaging mode [1], see Figure 5.15. However, the main features of interest (such as overall crack shape) are still clearly evident in the corresponding figures. In Figure 5.13, curves (a) and (b), illustrate typical grey value profiles of the crack along transverse lines near the crack mouth and crack tip respectively. Distinct light and dark fringes at each crack edge can particularly be seen in Figure 5.13 due to phase contrast between the air and aluminium [26]. Average grey values at the minimum load of the aluminium and crack volumes were 190.4 and 95.1 respectively. The fringes generated by phase contrast at the crack edges were seen to exert a strong influence on the grey value of the crack region. The contrast value corresponding genuinely to X-ray absorption in air would in fact be close to that of the crack centre near the crack mouth (i.e. 130–150). As such the particular contrast of the micro-pores and the near-tip-crack volume (in Figure 5.13, curve (a)) is clearly enhanced by the dark fringes (associated with interface phase contrast) overlapping in such small objects.

Given the above contrast effects, a key issue in thresholding the crack in a reconstructed volume is the optimum threshold selection. Considering the partial

volume effect, it is interesting to adopt a mean value between the grey values of two neighbouring phases as a threshold value to determine the location of an associated interface. For example, such mean contrast values in sample O1 were identified as ~ 140 for the whole crack. However, due to the fact that voxel contrast values often slightly exceed these mean values near the crack centre (as illustrated in Figure 5.13), the thresholded volume of a crack would be significantly underestimated if such a mean value is applied for thresholding. This is illustrated in Figure 5.14 where approximately linear variations in the volume of a segmented crack are seen with thresholding tolerance values, t increasing between 120 and 160. As described in Section 5.3.1, an initial seed is chosen to growth with a pre-set t value; in this case the seed was 0 in grey value (i.e. black). From the linear increment of the crack volume it is inferred that the high-grey-value region at the crack centre becomes filled (i.e. becomes part of the thresholded volume) with increasing t. However, the crack volume started to increase drastically above t = 160, as the tolerance value exceeds the grey value of the crack and hence the seed starts to grow beyond the crack into the aluminium matrix, i.e. results in thresholding the crack together with the aluminium matrix, as illustrated in Figure 5.15, for different levels of crack thresholding (in yellow) at several t values. The 'over-thresholded' effect of the crack volume can be seen in the used of t above 160 (e.g. t = 180). Since the upper-bound grey value of the linear portion exceeded that of the internal high-grey-value region over almost all the crack, adopting the onset of nonlinearity of the upper part as a tolerance value in Figure 5.14 may be seen to give reasonable thresholding. This is evidenced in Figure 5.15 (c) where using t = 160 gives rather more representative volume segmentation compared to the used of mean value (i.e. t = 140). As different sample data sets exhibited different levels of image contrast, a similar threshold determination process was carried out for each sample to determine t values.

- ***General Features of 3D Rendered Image***

As a general illustration of the power of the tomographic imaging approach is presented in Figure 5.16, showing a typical section of a 3D rendered perspective view of a tomographic volume (200 x 300 x 200 voxels) from sample O1, encompasses a crack-tip and surrounding microstructural features. Within this volume the crack has

been visualised by removing the surrounding aluminium matrix from two-thirds of the volume (seen in grey at the 'back' of the image). Colour has been added to further the features to ease visualisation: micro-pores appear in yellow, whilst intermetallic particles appear in red, and the crack volume appears in green. These components were then rendered using front and side diffuse light sources to highlight their three-dimensional character [27]. The geometry of the crack's leading edge, and the surface topology of the crack are clearly complex. As can be seen in Figure 5.16 (b), showing a view of the crack in the direction of growth, bifurcated crack planes C_1 and C_2 are connected by a segment of the crack plane T which is sharply twisted about crack growth direction. Crack plane C_2 is located approximately 40 μm beneath C_1, with the two areas overlapping each other to some extent. There seems to be some crystallographic character to the bifurcation, implied by the relatively planar nature of the twisted section of the crack: more specific assessment of surface crystallography is presented in Section 5.4.4. The complex shape and scale of the intermetallic particles is clear from the 3D reconstruction, highlighting the limited impression obtained from 2D sections. The intermetallic particles seen in the immediate vicinity of the crack in this work remained intact, suggesting that any effect of the particles on crack propagation was limited, consistent with the low stress intensity load conditions under which the cracks were grown.

Figure 5.17 shows a plan view of two extracted crack volumes of sample O1 from different load levels. Figure 5.17 (a) shows the crack volume at zero load, whilst Figure 5.17 (b) shows the crack volume at maximum load. Areas where the background colour (black) can be seen through the crack imply the existence of crack closure or ligaments in the crack wake (i.e. the local absence of crack volume). Several large ridges are identified along the crack wake, running parallel to the crack growth direction. At zero load, a number of areas of contact were identified along the flanks ridges well behind the crack tip (e.g. such as that marked 'A'), along with many smaller contact areas scattered in the region near the crack tip. At maximum load, it is identified that some contacted areas disappeared (as marked 'C') or contracted to smaller areas (as marked 'B'). However, many small contacted areas still can be seen to remain in the region near the crack tip of this overloaded sample. It is significant to note that the only prior literature tomography results comparable to

those shown here [2] were unable to identify such fine detail of local contact areas given the order of magnitude voxel size that was used.

The apparent association of contact areas with ridges running parallel to the crack growth direction represents an interesting mechanistic insight into crack shielding processes, as the established literature on RICC processes has largely ignored the influences that crack twisting may have on associated surface contact mechanics. Whilst reduced to an extremely simplified, regular surface geometry, the 3D RICC modelling of Chapter 4 was stimulated by such tomographic imaging with a corresponding mechanistic interpretation and quantitative predictions being presented in that chapter.

- ***Crack Volume Analysis***

With the t value obtained specifically for each sample data set, crack volumes of each sample may be assessed at different loading levels. This was identified as preliminary observation of overall crack properties and opening behaviour. Figure 5.18 shows plan views of extracted crack volume of the 5 samples examined at maximum load level. The cracks clearly show quite different front shapes, with expected high levels of facture surface roughness at this ΔK level (~ 6MPam$^{1/2}$) in this material. Crack volumes are then plotted as a function of loading levels as illustrated in Figure 5.19. In the first instance it is interesting to see samples N4 and O3 exhibiting somewhat irrational crack volume changes as opposed to the simply increasing volume increments as a function of loading levels in the other samples. In terms of the N4 sample, detailed observation of the crack properties in 3D indicated that this crack exhibited a much higher degree of crack bifurcation compared to the other samples (covering up to ~ 60% of the crack front). For O3, as can be seen in Figure 5.18 (c), there is a somewhat irregular crack front, crack length varying dramatically across the sample. Whilst the exact origin of the unusual crack volume curves of N4 and O3 have not be quantified here, it is evident that displacements and crack opening in these samples may be subject to non-ideal influence, i.e. not representative of simple tensile opening of an independent single crack. Based on their reasonably rational, smooth crack opening behaviour O1, N5 and O9 have therefore been selected for further more detailed analysis in the following sections.

- ***Microstructural Displacement Gauging***

In terms of thresholding smaller objects like intermetallics or micro-pore which may then be used for microstructural displacement gauging, it is clearly valuable to study the accuracy and reliability of the thresholding technique being used to locate and measure particle positions. As such, typical pairs of spherical micro-pores (typically ~ 10 μm in diameter) were thresholded at different threshold tolerance values, where the effect of the threshold tolerance value on shifts in apparent centroid locations is shown in Figure 5.20 (apparent particles separation at t = 20 being used as a reference). The measured pore volumes were noted to increase with the increase in threshold tolerance values, however the centroid separation measurements were found to be reasonably consistent, i.e. variations in identification of the particle/matrix interfaces have a limited influence on centroid positions for approximately spherical bodies, as would have been hoped. From the analysis shown, changing the threshold tolerance value by 20 results in an absolute shift in the measured centroid of only 0.043 μm on average, and 0.139 μm at most, i.e. displacement *changes* appear measurable to sub-voxel accuracy independent of the image thresholding, to an accuracy of the order of 0.1 μm.

5.4.2 Displacement Mapping Results

As described earlier, there were two materials involved in the tomography experiments, specifically the 2024 and 2027-ReX(8) alloys. Unfortunately, the later material turned out to exhibit very few of the spherical micro-pores which were found to be desirable for microstructural COD mapping, and, as such, samples of this material were not considered suitable for this analysis. Local crack displacement measurements were then particularly focused on the 'O1' sample of 2024 with 9 different locations (labelled here as P1 - P9) being found over the crack wake for systematic assessment. Figure 5.21 illustrates the locations of the points, with each row of measurements back from the crack tip consisting of three locations. As noted earlier, a pair of spherical micro-pores (typically ~ 10 μm in diameter) within the material is sampled as gauge marks at each measurement location, where each micro-pore is located on opposite crack faces (with separation distances of ~ 100 – 150 μm), lying approximately parallel to the loading axis, as illustrated in Figure 5.22.

Centroid displacements of each pair of micro-pores were measured at the different loading levels. Variations in centroid spacings of the pairs were then be separated into three directions by orthogonal decomposition to assess local mode I, II and III effects. Figure 5.23 (a), (b) and (c) shows the variations of local mode I displacements with loading in Row 1, Row 2 and Row 3 respectively. Based on the accuracy in centroid measurements noted above (~ ±0.1μm), the mode I displacement curves observed in Figure 5.23 would appear to be reasonably consistent and meaningful (i.e. overall displacements are much greater than 0.1 μm). Bearing in mind the accuracy of the measurements there may be indications of local differences in compliance behaviour between individual points making up each row, particularly for Row 3, see Figure 5.23 (c). Row 3 results have the largest COD values as they are the locations at the greatest distance from the crack tip. Row 1 measurements, which are the closest to crack tip, have the smallest COD results (maximum of about 1.8 μm). From these local measurements, there is indeed evidence of low compliance at low loads, which can be seen most significantly in the Row 2 and 3 results. Such behaviour is of course consistent with some form of crack closure, although it must be noted that the increase in apparent compliance with increasing loads in Row 2 and 3 occurs at relatively low loads for the conditions tested (K_{cl}/K_{max} ~ 0.2 is suggested).

Figures 5.24 and 5.25 individually show variations of mode II, and mode III displacements of each of the pairs of micro-pores at locations P1 to P9 as a function of applied stress intensity. Relatively small mode II displacements were measured, corresponding to less than 0.3 μm in all cases. The generation of large mode III displacements was observed in comparison with the mode II displacements: the mode III displacements achieve values of about 1 μm at maximum load. Larger mode III displacements can particularly be observed when the crack is loaded > 2 MPa$\sqrt{m}$ with only subtle indications of a similar phenomenon occurring in the mode II results. The larger mode III displacements may be attributable to the features of crack surfaces shown in Figure 5.17, where the ridges and valleys run in the crack growth direction, presumably due to the texture of the samples and the incidence of crystallographic failure (discussed in Chapter 4). It may be noted that the directions of the mode II and

III displacements differ from point to point, implying that the observed mode II and III displacements are indeed attributable to the local topology of crack surfaces.

5.4.3 Ray Casting Results

Local COD across a crack wake was also measured using this ray casting algorithm. This method was explored as particularly valuable for samples which do not have spherical micro-pores to be used for microstructural COD mapping, (i.e. the 2027 samples in particular). In the first instance, to compare the reproducibility and accuracy of this technique to the microstructural centroid displacement gauging method, COD measurements were taken at the same locations of sample O1 as illustrated in Figure 5.21. Each local ray casting COD measurement was taken based on an average value of COD covering a small area of 60 x 60 pixel^2 (~ 42 x 42 μm^2) (i.e. local to the micropore displacements). Figure 5.26 shows mode I COD results obtained from the ray casting method compared well to microstructural centroid spacing displacement gauging method, especially in Row 1 and Row 2, providing a reasonable method of local crack compliance monitoring in the absence of clear microstructural gauge marks.

Similar COD measurements have been applied to samples O9 and N5 of the 2027 material. Four near crack tip locations (approximately ~ 100 μm behind the tip) were chosen for mode I COD measurement on each sample with Figure 5.27 (a) and (b) showing the mode I CODs of O9 and N5 respectively. As shown in Figure 5.27, it is interesting to note that the O9 shows distinct non-linearity in COD in contrast to the COD behaviour in N5, consistent with increased closure influence in the overloaded sample. In terms of a more quantitative analysis of the data however, the complexity and non-ideal nature of the crack shapes highlighted in samples N4 and O3 underlines a clear cause for caution in the present work. Not withstanding the presence of major crack bifurcation and non-linear crack fronts, local measurements of crack compliance may be expected to require consideration of local crack topography (placement in relation to particular crack kinks and/or twists). The potential influence of plasticity on local compliance during loading and unloading, and the elastic relaxation that must have occurred during the sectioning of large SEN bars into

tomography samples, would require further analysis, potentially via FE studies. In the first instance however, the present work may be seen to highlight the potential for such detailed in-situ crack monitoring, and issues associated in future experimental refinements, e.g. the choice of a test material with a more uniform crack front features, at least in relation to the scale of the tomography sample.

5.4.4 3D Crack and Grain Boundary Observation

Figure 5.28 illustrates 2D crack mouth images which are cross-sectional slices (in the L-S plane) of the tomographic dataset volume of sample N5. Figure 5.31 (a) shows the tomographic 2D image taken before the application of liquid Ga: an apparently faceted and deflected crack mouth opening profile (in black) can be seen across the middle of the image with intermetallic particles (in white) running parallel to the loading direction. Figure 5.28 (b) is taken after the application of liquid Ga, where lines of contrast can now be seen running parallel to the loading direction, consistent with the known grain structures of this rolled plate material. A clear visualisation of the apparent 3D grain boundary structure can be obtained by segmenting the boundaries from the aluminium matrix. As illustrated in Figure 5.29, a 3D rendered perspective view of the tomographic volume of sample N5 (500 x 1200 x 500 voxels) may be seen encompassing the crack, with and without grain boundaries. Within this volume the crack and grain boundary structures have been visualised by removing the surrounding aluminium matrix (seen in grey at the 'back' of the image) from of the volume. Colours have again been added to the features to ease visualisation, with the crack volume appearing in green and grain boundaries in yellow. To assess the 3D segmented grain boundary mapping quantitatively, it is compared directly with an EBSD grain map obtained after appropriate sectioning to the same location in Figure 5.30. A misorientation profile has been plotted across the *y-y* section showing the misorientation angles of grain boundaries. From the illustration, it can be seen that most of the high angle grain boundaries have indeed been picked up reasonably well by the segmentation of the liquid Ga wetted boundaries (i.e. matching with the EBSD orientation map), although several individual boundaries can be identified with little or no Ga effect. Specifically, the apparent high angle boundaries at points 'Z1' and 'Z2' in the misorientation profile, corresponding to misorientations of approximately 23 degrees, are essentially absent in the Ga images, whilst the boundaries at Z3 and

Z4 correspond to approximately 50 degrees misorientation and are relatively faint (the corresponding appearance of these boundaries in the unsegmented data is shown in Figure 5.28). Whilst a coincident site lattice assessment has not been made, such behaviour may indeed be seen as consistent with special boundary effects on surface tension and associated Ga charging behaviour [18, 28]. It may also be noted that as this material is ~ 90% un-recrystallised, it is clear that the Ga does not accumulate significantly at low angle boundaries of the associated sub-grain structure.

In terms of crack geometry and microstructure, it is clear that changes in crack path are closely linked to grain boundaries at various points in the region imaged (area circled in Figure 5.30 (a)), where those cracks appear to be deflected at high angle grain boundaries. With the available EBSD grain orientation data and the 3D tomography crack deflection information, it is possible to obtain detailed crystallographic information on the possible crack propagation mechanisms by measuring the angle of the crack kinks, θ (mode II deflection) and twists, ϕ (mode III deflection), as described in Section 4.4.4. Figure 5.31 illustrates a typical example of crystallographic indexing of an individual section of crack deflection, where the deflected section being analysed is labelled as X. By comparing the measured crack deflection angles (θ, ϕ) from Figure 5.31 (b) with the local pole figure, this particular section of deflection is identified as near-{111} as shown in Figure 5.31(c). Repeating this for individual deflections across the fracture plane is shown in Figure 5.32, highlighting crack plane indices, using a tolerance of $\pm 5^{\circ}$. From these observations, much of the surface orientation appears to be generated by a combination of {111} and {100} fracture, with little {110} failure, highlighting the importance of local imaging over the crystallographic observations in Chapter 4. {111} oriented failure is clearly consistent with slip band crack growth occurring (shear decohesion) whilst {110} and {100} failure in such a material is commonly attributed to environmental influences [29, 30]. Particularly sharp deflections (~ 60°) can be seen at section A and B where those predominant {111} failure arises (despite the presence of small sub-sections of {100} oriented fracture). It is worth noting that how the {111} oriented failure being high angle is of course consistent with slip band failure which requiring local shear/mode II deformation and/or opening along slip bands. In keeping with Chapter 4, the role of slip band formation and subsequent crack growth is confirmed

in generating the most deflected crack surface features which has thought to control closure in the materials. This is evident in Figure 5.33 where the high angle {111} failure deflection sections (A and B) as shown in Figure 5.32 are highlighted in a plan view to show the evidence of local closure behaviour. Significant closure area can be seen to be built up on the sides of the ridges when the crack is at minimum load, and either disappear completely or contract while the crack is loaded. Overall it may be seen that a uniquely detailed insight into crack trajectory, crystallography and micromechanics is achieved by the present synthesis of investigation methods.

5.5 Conclusions

1. High resolution synchrotron tomography has been explored in relation to the three dimensional visualisation and quantification of fatigue crack closure in 2024-type aluminium alloys.

2. Microstructural displacement gauging and ray casting are shown to yield useful micromechanical quantification of crack behaviour. Limitations in the present experiments were noted however, particularly in relation into the irregular scale of crack features at the scale of the tomography samples (constrained by image resolution requirements).

3. Evidence of mode III contributions to crack micromechanics and contact behaviour was noted, informing model development in Chapter 4.

4. The potential for highly 'information rich' crack micromechanics assessment is shown when experimental methods are synthesised: in particular the capability for grain-by-grain assessment of crack shape, displacement patterns, surface contract behaviour and crystallography is shown. The visualisation, interpretation and statistical validation of this level of information may in fact be seen as a significant challenge for the future of such work.

References

[1] J. Baruchel, J.-Y. Buffiere, E. Maire, P. Merle, and G. Peix, *X-Ray Tomography in Material Science*. 2000, Paris: Hermes Science Publications.

[2] A. Guvenilir and S.R. Stock, *Fatigue and Fracture Engineering Materials and Structures*, 1998. **21**: p. 439-450.

[3] A. Guvenilir, T.M. Breunig, J.H. Kinney, and S.R. Stock, *Acta Metallurgica*, 1997. **45**: p. 1977-1987.

[4] A. Guvenilir, T.M. Breunig, J.H. Kinney, and S.R. Stock, *Philosophy Transaction of The Royal Society Lond.*, 1999. **A 357**: p. 2755-2775.

[5] J.-Y. Buffiere, E. Maire, P. Cloetens, J. Baruchel, and R. Fougeres, *Alluminium Alloys, Proceeding of ICAA-6*, 1998. **1**: p. 529-534.

[6] P. Cloetens, M. Pateyron-Salome, J.-Y. Buffiere, G. Peix, J. Baruchel, F. Peyrin, and M. Schlenker, *Journal of Applied Physics*, 1997. **81**: p. 5878.

[7] J.-Y. Buffiere, E. Maire, P. Cloetens, G. Lormand, and R. Fougeres, *Acta Metallurgica*, 1999. **47**: p. 1613.

[8] W. Ludwig, *Development and applications of synchrotron radiation microtomography*. PhD Thesis, University of Munich. 2001.

[9] ASTM-E647-95a, *Annual Book of ASTM Standards*. 1996, Philadelphia, PA: ASTM International, p. 565-601.

[10] J.-Y. Buffiere, E. Maire, P. Cloetens, G. Lormand, and R. Fougeres, *Acta Metallurgica*, 1999. **47**: p. 1613-1625.

[11] J.-Y. Buffiere, *Private communication, INSA-Lyon (France)*, 2003.

[12] G.T. Herman, *The Fundamentals of Computerised Tomography*, 1980, New York: Academic Press.

[13] B.J. Inkson, M. Mullvihill, and G. Mobus, *Scripta Materialia*, 2001. **45**: p. 753-758.

[14] E.M. Lauridsen, S. Schmidt, R.M. Suter, and H.F. Poulsen, *Journal of Applied Crystallography*, 2001. **34**: p. 744-750.

[15] H.F. Poulsen, S.F. Nielsen, E.M. Lauridsen, S. Schmidt, R.M. Suter, U. Lienert, L. Margulies, T. Lorentzen, and D.J. Hensen, *Journal of Applied Crystallography*, 2001. **34**: p. 751-756.

[16] W. Ludwig and D. Bellet, *Materials Science and Engineering A*, 2000. **281**: p. 198-203.

[17] E. Pereiro-Lopez, W. Ludwig, D. Bellet, and J. Baruchel, *Nuclear Intrumetns and Methods in Physics Research B*, 2003. **200**: p. 333-338.

[18] W. Ludwig, J.-Y. Buffiere, S. Savelli, and P. Cloetens, *Acta Materialia*, 2003. **51**: p. 585-598.

[19] P.J.L. Fernandes and D.R.H. Jones, *International Materials Reviews*, 1997. **42**: p. 251.

[20] M.G. Nicholas and C.F. Old, *Journal of Materials Science*, 1979. **14**: p. 1-18.

[21] Volume Graphics GmbH, Germany (http://www.volumegraphics.com).

[22] S.D. Roth, *Computer graphics image processing*, 1982. **18**: p. 109.

[23] A.B. Jani, C.A. Pelizzari, G.T.Y. Chen, and R.P. Grzeszczuk, *Journal of Computer Assisted Tomography*, 1998. **22**: p. 459.

[24] C. Labbe, J.C. Froment, A. Kennedy, J. Ashburner, and L. Cinotti, *ESRF Newsletter*, 1996. **25**: p. 41.

[25] J.C. Ehrstrom, *Private communication, Pechiniey CRV (Voreppe, France)*, 2002.

[26] P. Cloetens, M. Pateyron-Salome, J.-Y. Buffiere, G. Peix, J. Baruchel, F. Peyrin, and M. Schlenker, *Journal of Applied Physics*, 1997. **81**: p. 5878-5886.

[27] K. Sassen, *Bulletin of the American Meteorological Society*, 1991. **72**(12): p. 1848-1866.

[28] W. Ludwig and D. Bellet, *Materials Science and Engineering A*, 2000. **281**: p. 198-203.

[29] R.P. Gangloff and R.S. Piascik, *Metallurgical Transactions*, 1993. **24A**: p. 2751-2762.

[30] R.P. Gangloff and R.S. Piascik, *Metallurgical Transactions*, 1993. **24A**: p. 2415-2428.

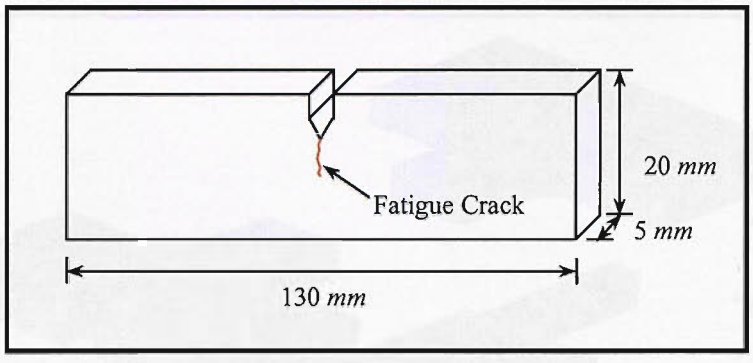

Figure 5.1 SEN specimen dimensions.

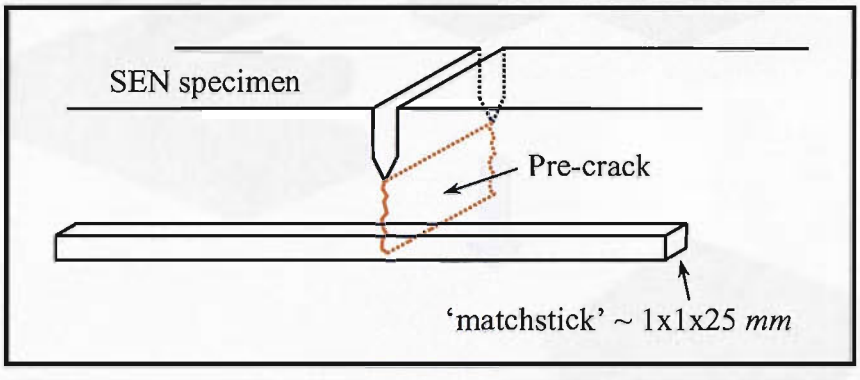

Figure 5.2 Schematic of 'matchstick' specimen preparation for tomography scanning.

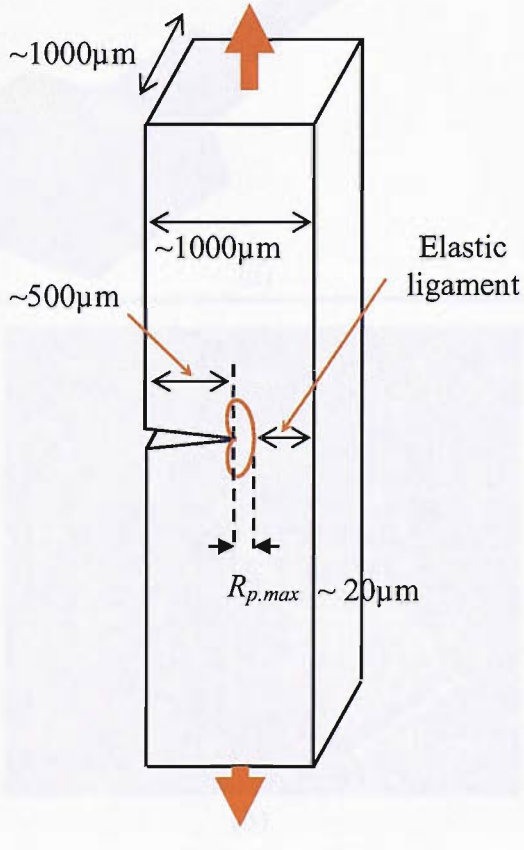

Figure 5.3 Schematic of matchstick sample design in terms of the plastic zone dimensions.

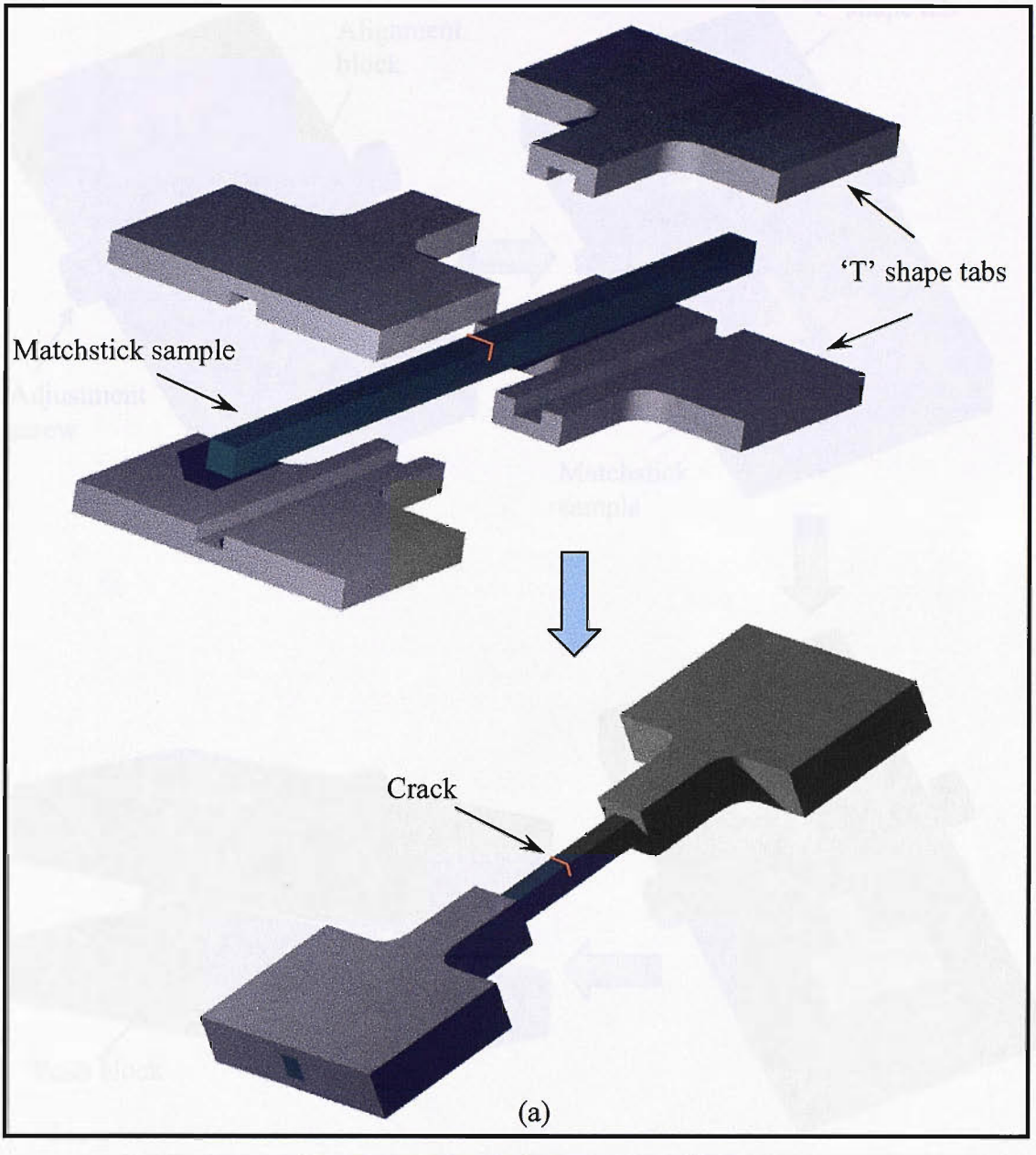

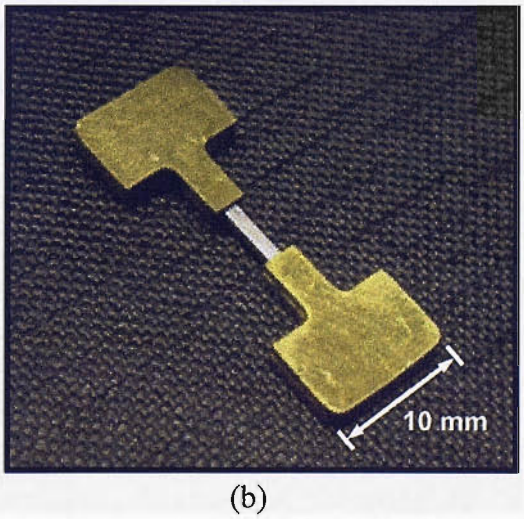

Figure 5.4 (a) Schematic diagrams showing the 'T' shape end tabs fixed to the matchstick sample, (b) typical finished sample.

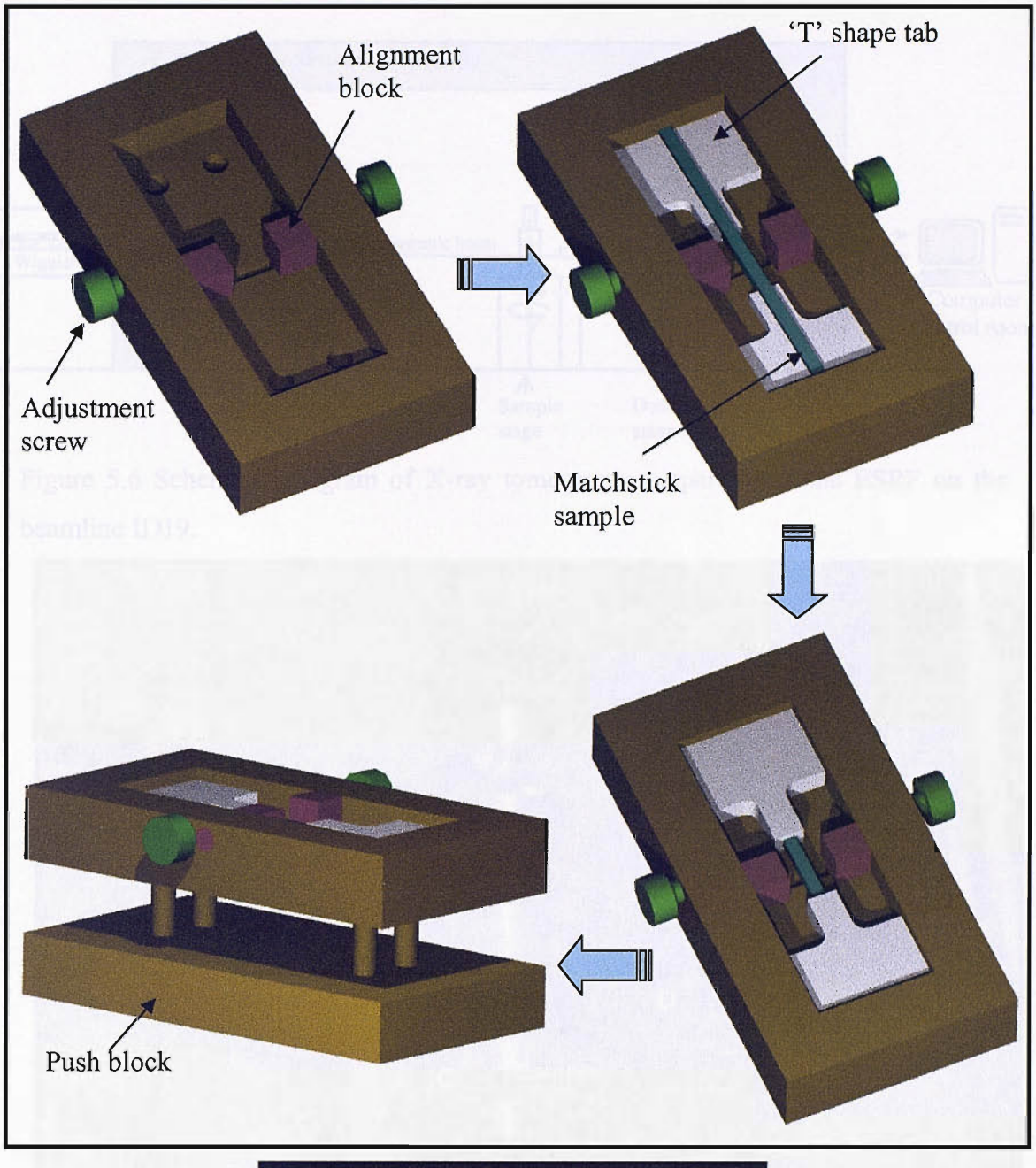

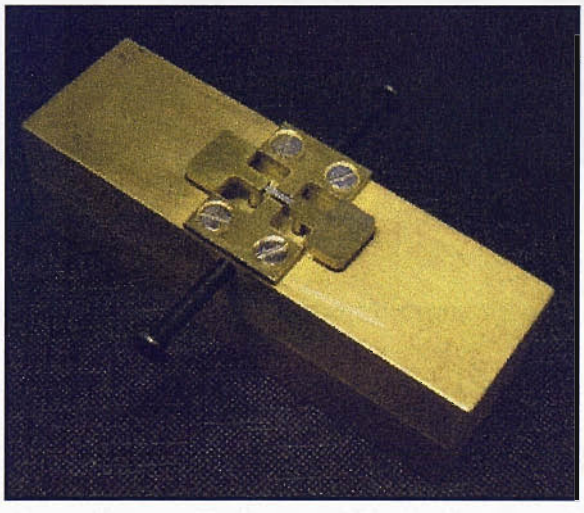

Figure 5.5 (a) Geometry and use of alignment jig for tomography sample assembly, and (b) typical assembly of sample and alignment jig.

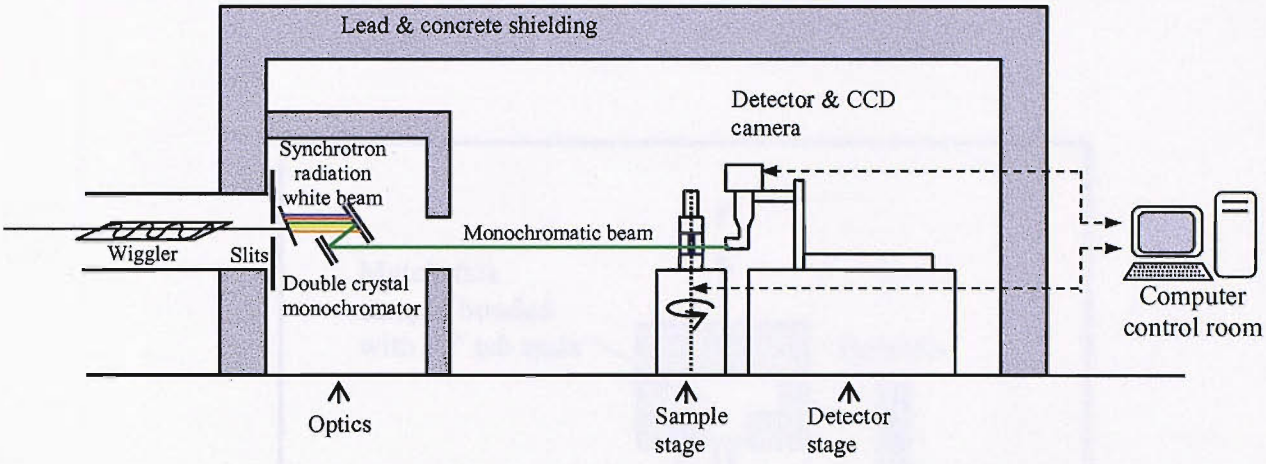

Figure 5.6 Schematic diagram of X-ray tomography apparatus at the ESRF on the beamline ID19.

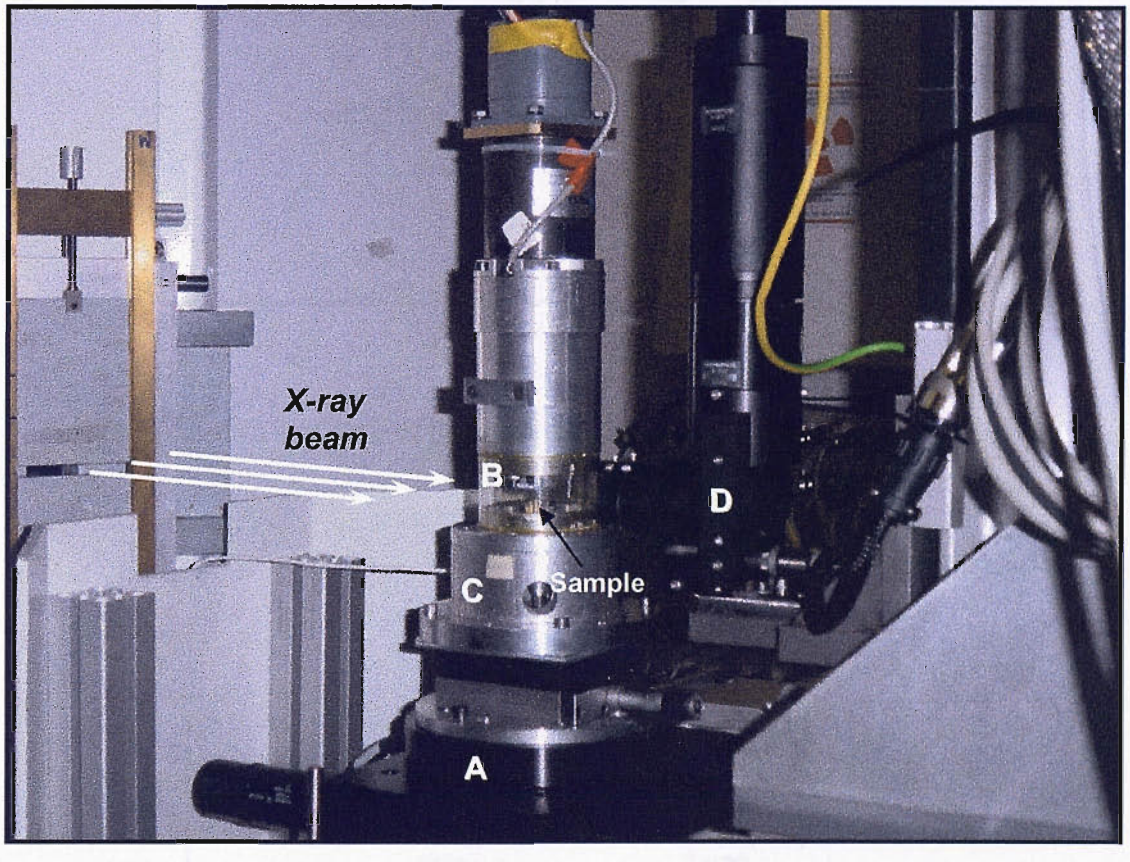

A – Rotating stage

B – Sample loading stage with X-ray transparent Perspex tube

C – Load cell

D – Scintillator and 2048 x 2048 pixels fast-readout, low noise (FRELON) CCD detector system

Figure 5.7 General arrangement of X-ray tomography experiment at the ESRF.

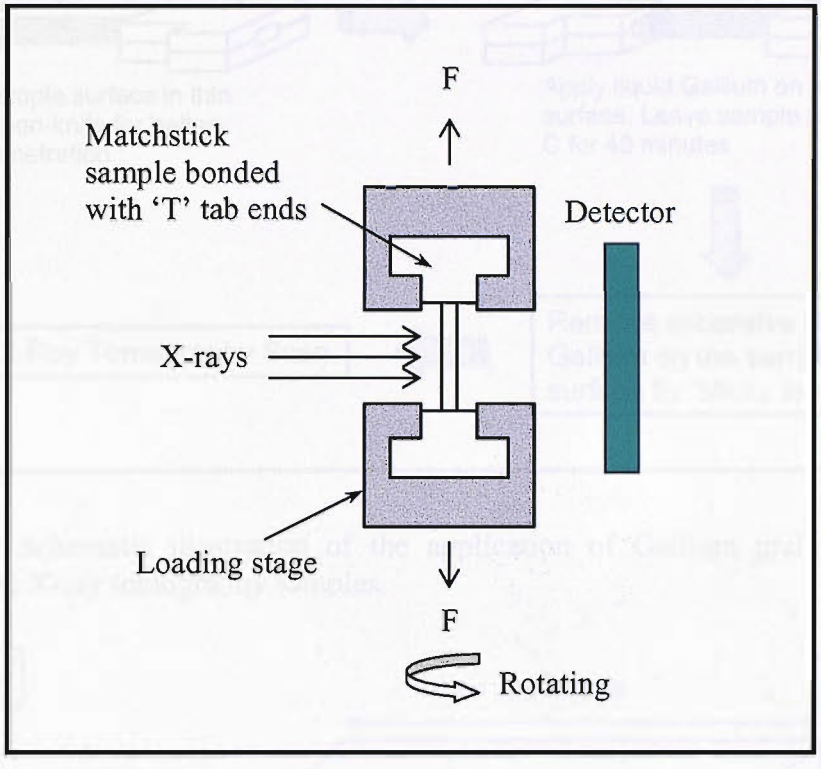

Figure 5.8 In-situ straining of the specimen in the high precision loading stage.

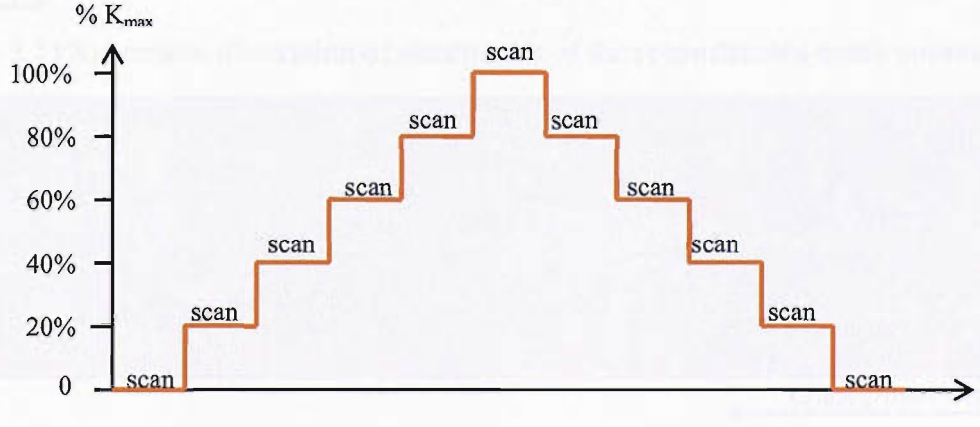

Figure 5.9 Scanning sequence of the tomography specimens in terms of loading steps.

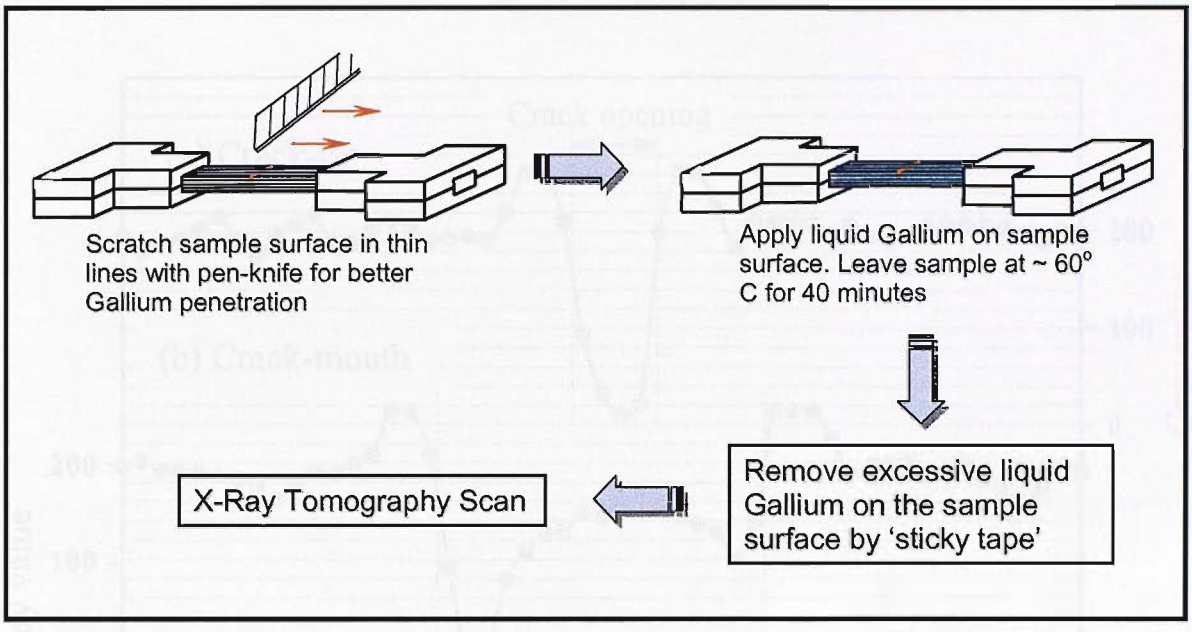

Figure 5.10 Schematic illustration of the application of Gallium grain boundary wetting to the X-ray tomography samples.

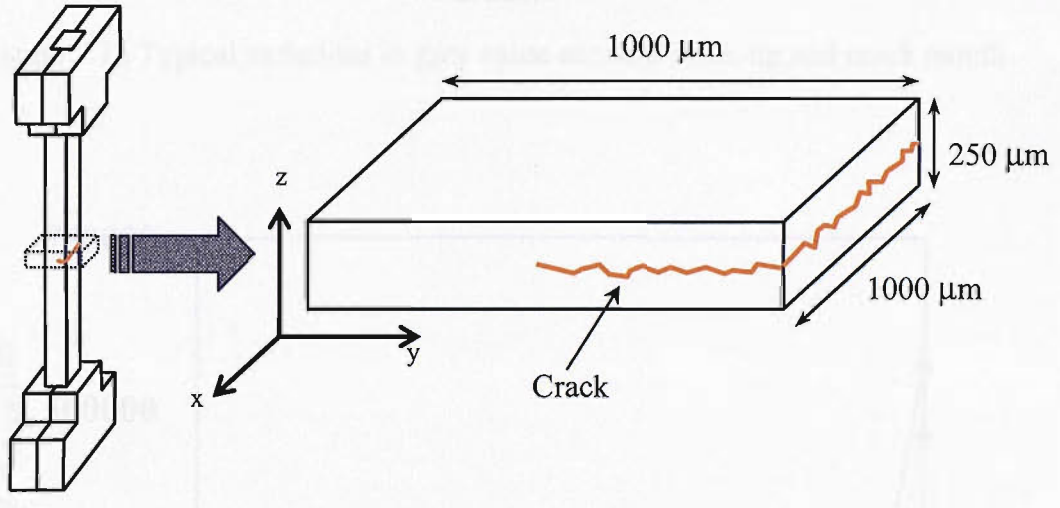

Figure 5.11 Schematic illustration of dimensions of the reconstructed crack volume.

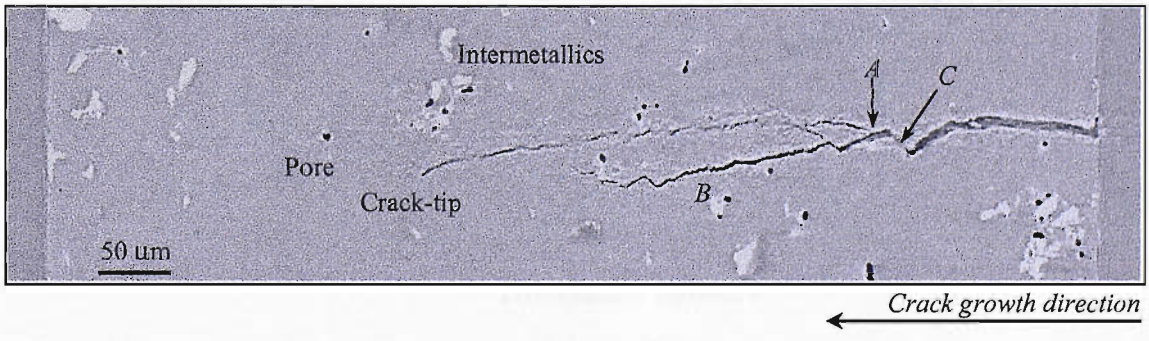

Figure 5.12 A typical two-dimensional slice of the reconstructed volume, captured from sample O1 at zero load.

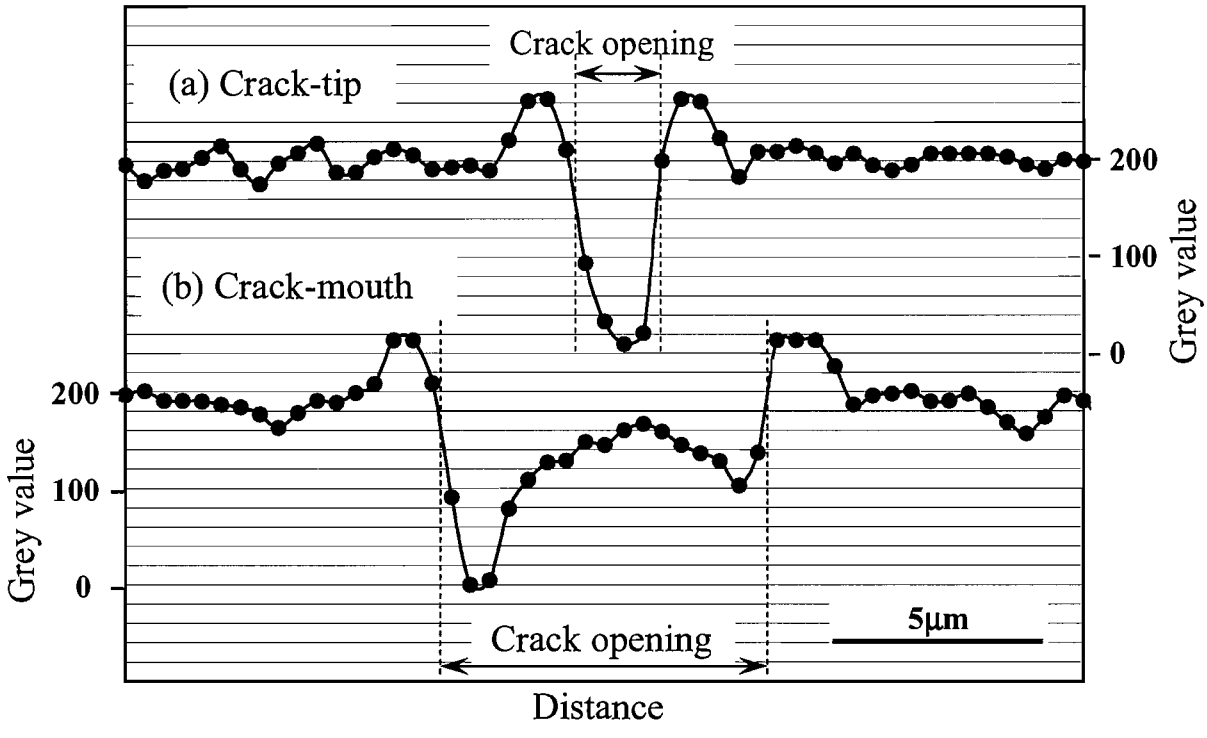

Figure 5.13 Typical variations in grey value across a crack-tip and crack mouth.

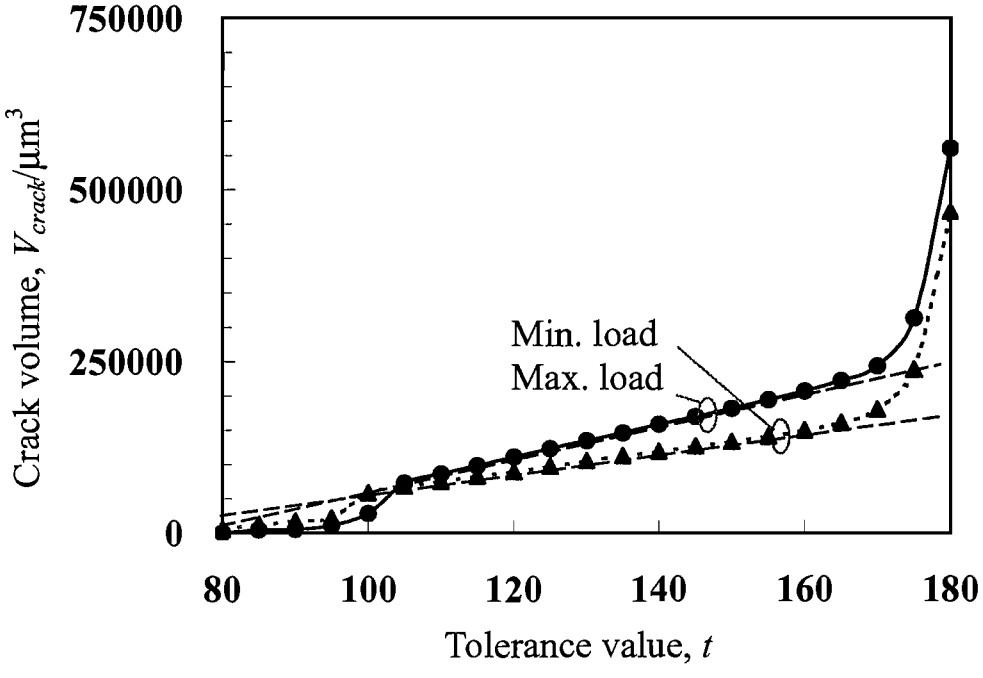

Figure 5.14 The results of preliminary investigations representing the effects of tolerance value used during crack segmenting in sample O1.

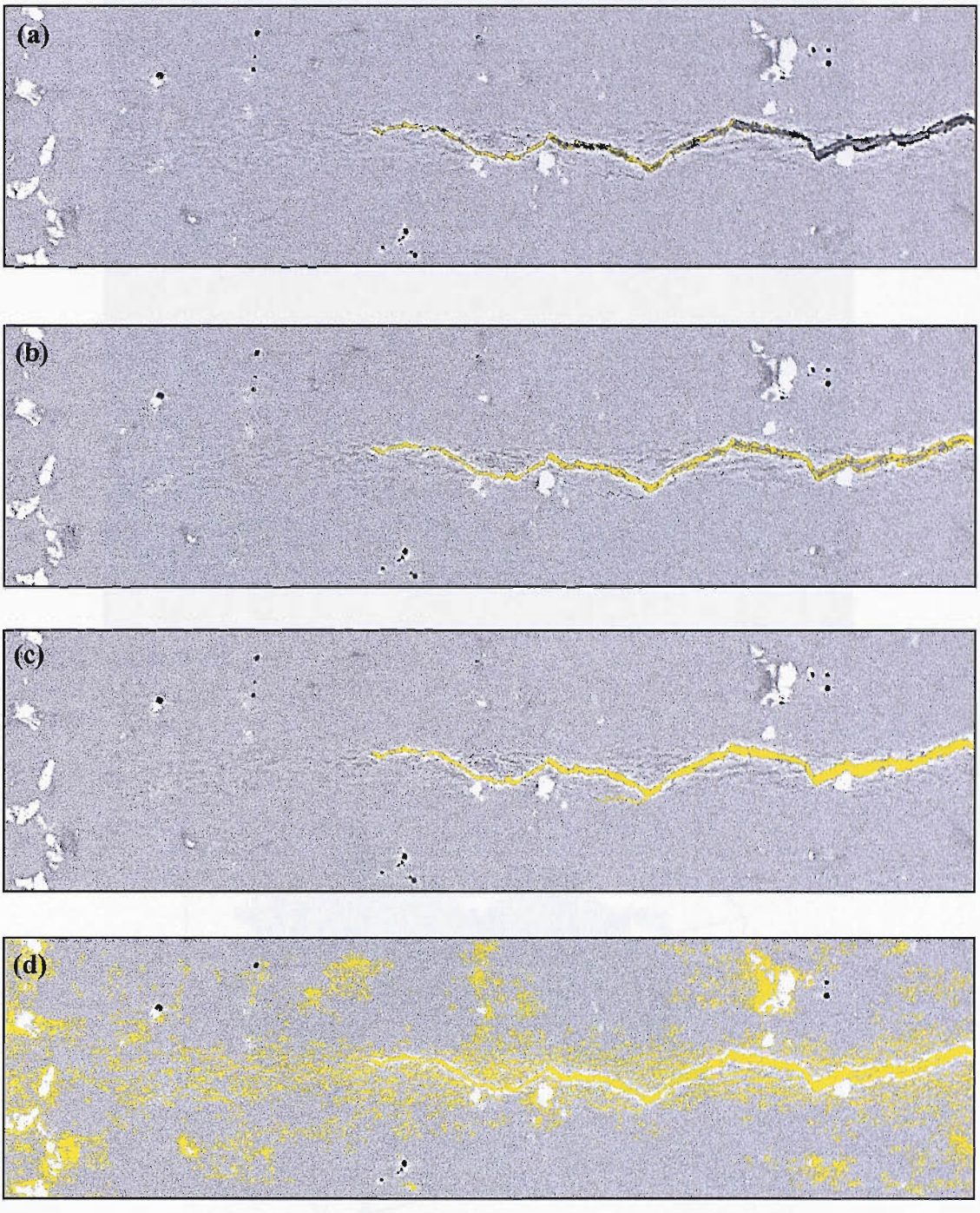

Figure 5.15 Typical crack volume segmentation stages of sample O1 corresponds to different levels of threshold tolerance value, t ; (a) t = 80, (b) t = 140, (c) t = 160 and (d) t = 180, where segmented part is in yellow.

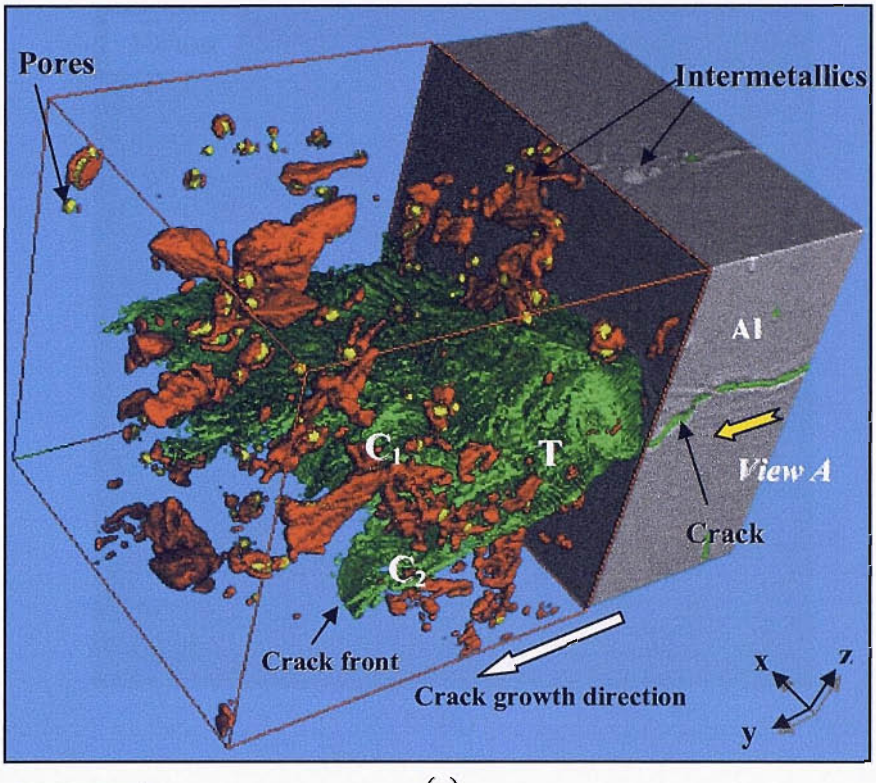

(a)

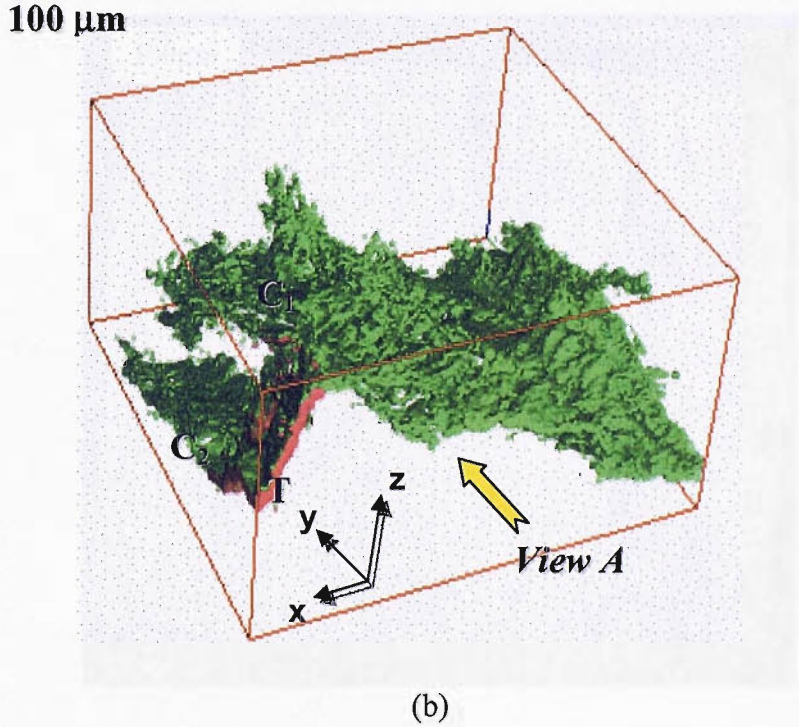

(b)

Figure 5.16 A 3D rendered perspective views of sample O1 tomographic dataset; (a) highlighting the crack volume and microstructural features, and (b) detail crack morphology observation of (a) viewed from direction *A*.

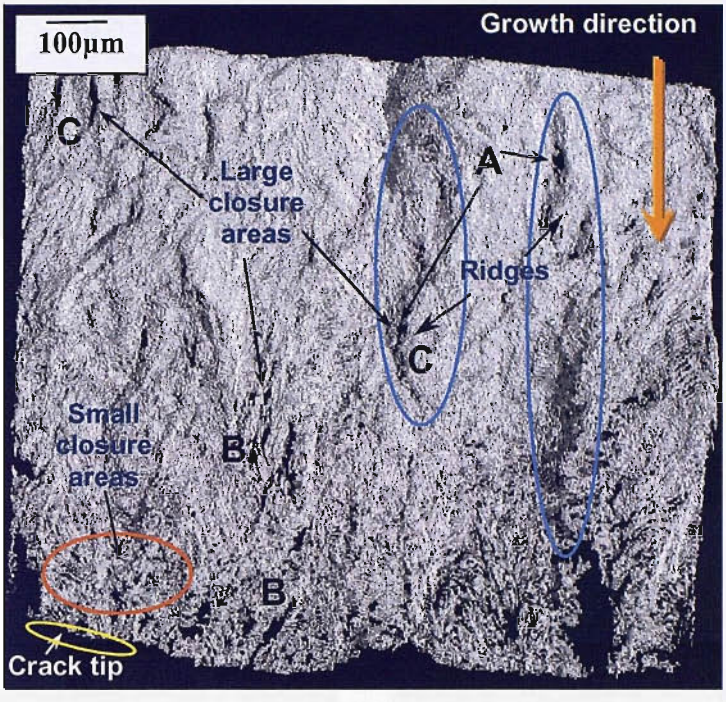

(a)

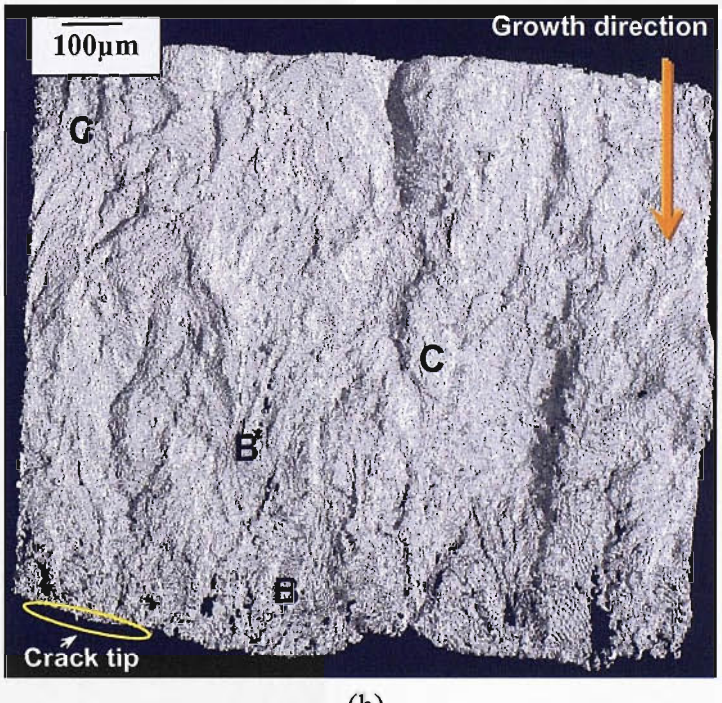

(b)

Figure 5.17 Extracted crack volume of sample O1 at; (a) zero load, and (b) maximum load condition.

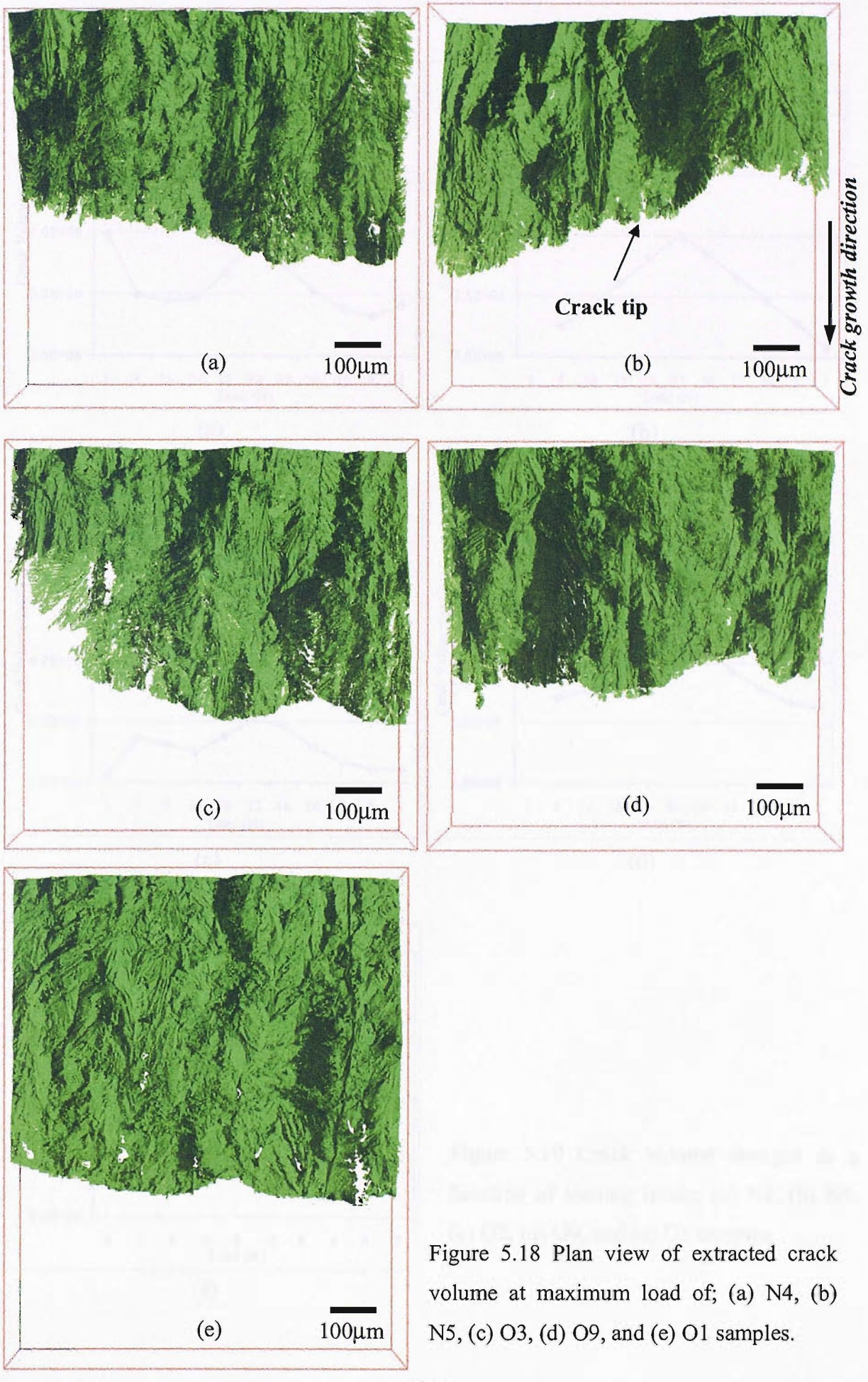

Figure 5.18 Plan view of extracted crack volume at maximum load of; (a) N4, (b) N5, (c) O3, (d) O9, and (e) O1 samples.

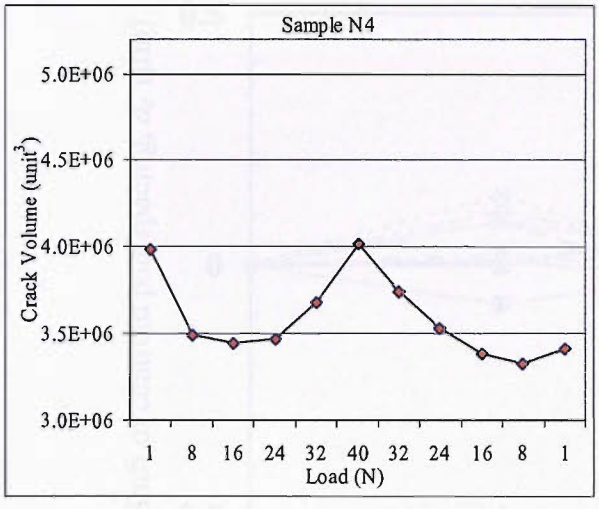

(a)

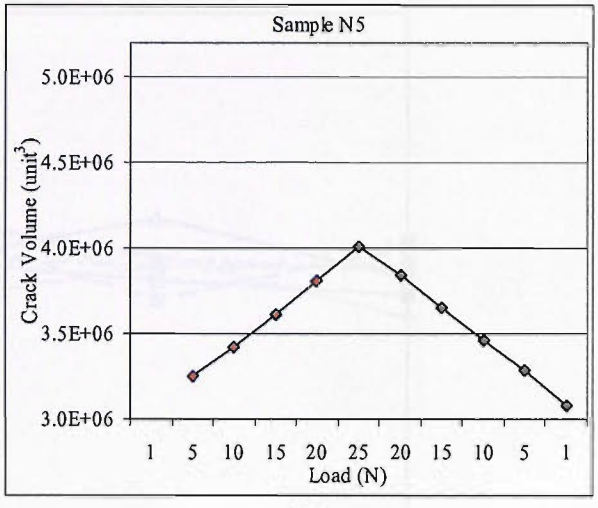

(b)

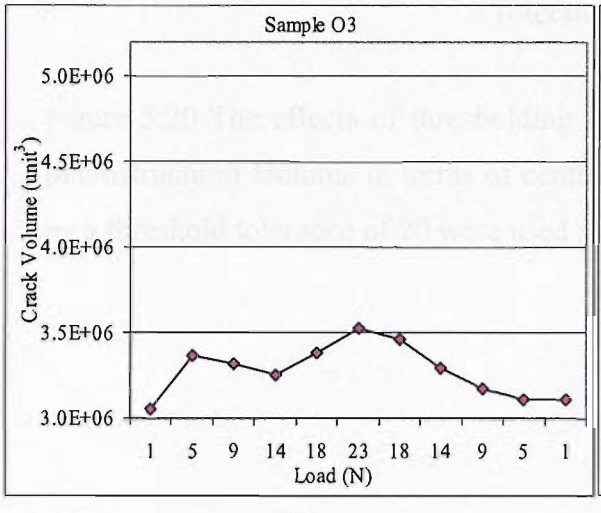

(c)

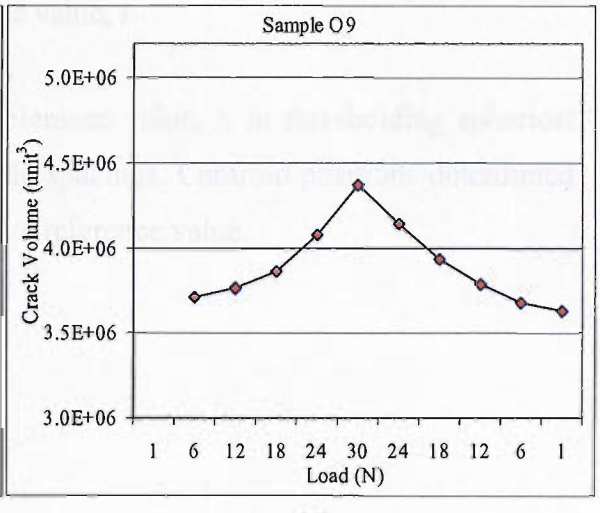

(d)

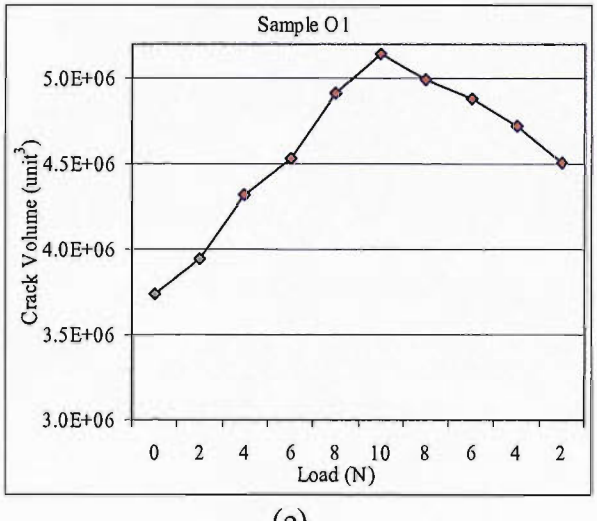

(e)

Figure 5.19 Crack volume changes as a function of loading levels; (a) N4, (b) N5, (c) O3, (d) O9, and (e) O1 samples.

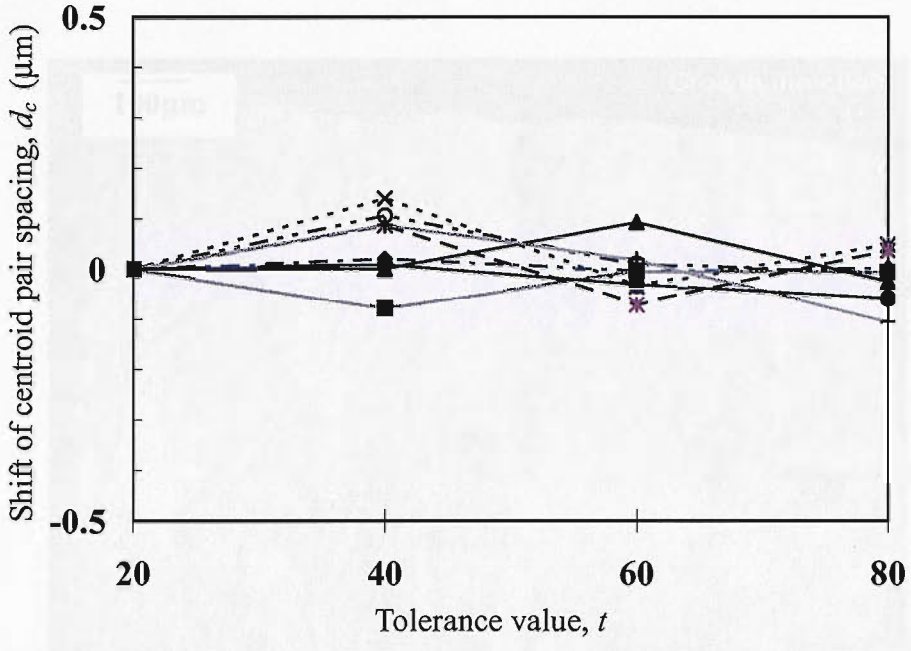

Figure 5.20 The effects of thresholding tolerance value, t, in thresholding spherical microstructural features in terms of centroid spacings. Centroid positions determined by a threshold tolerance of 20 were used as a reference value.

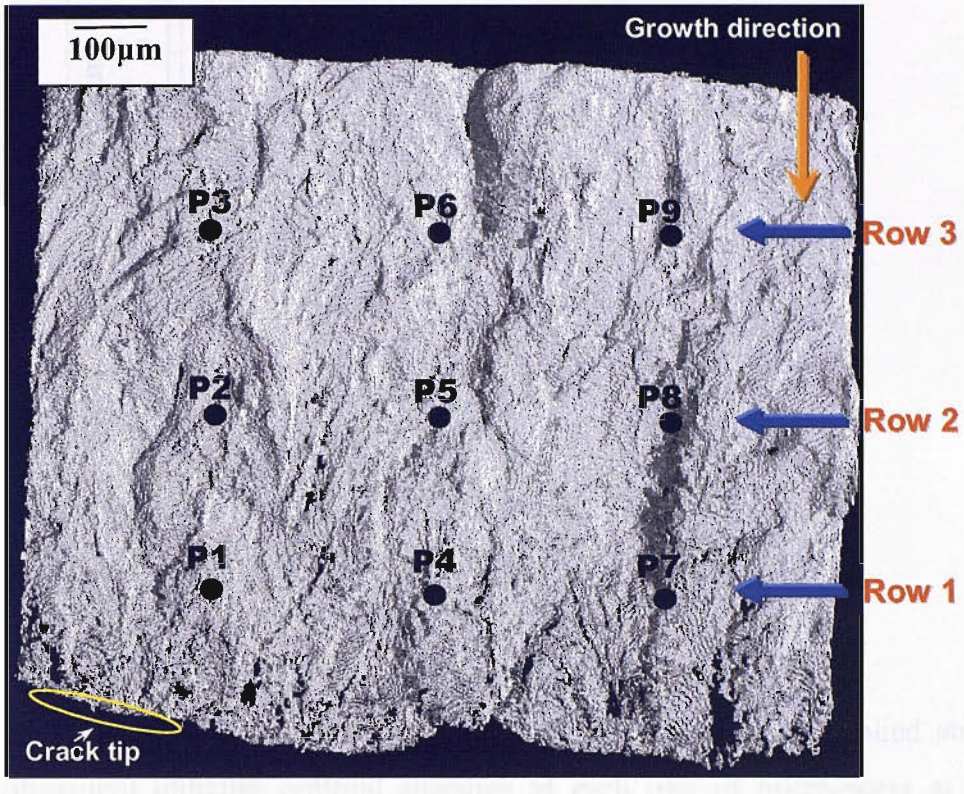

Figure 5.21 COD mapping across the crack wake of sample O1.

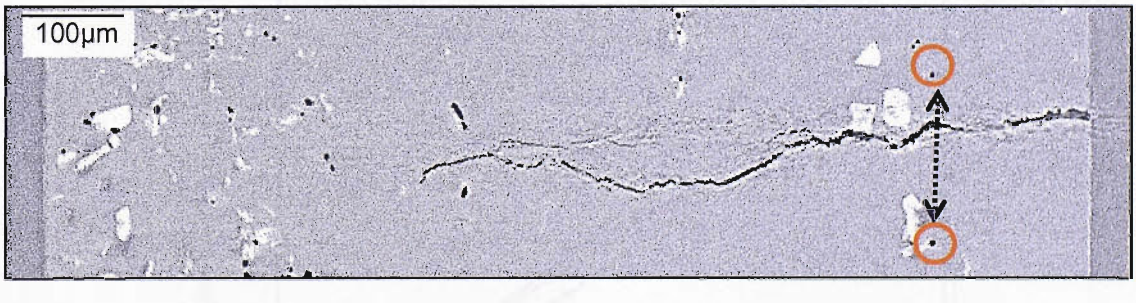

Figure 5.22 Typical micro-pore displacement measurement geometry.

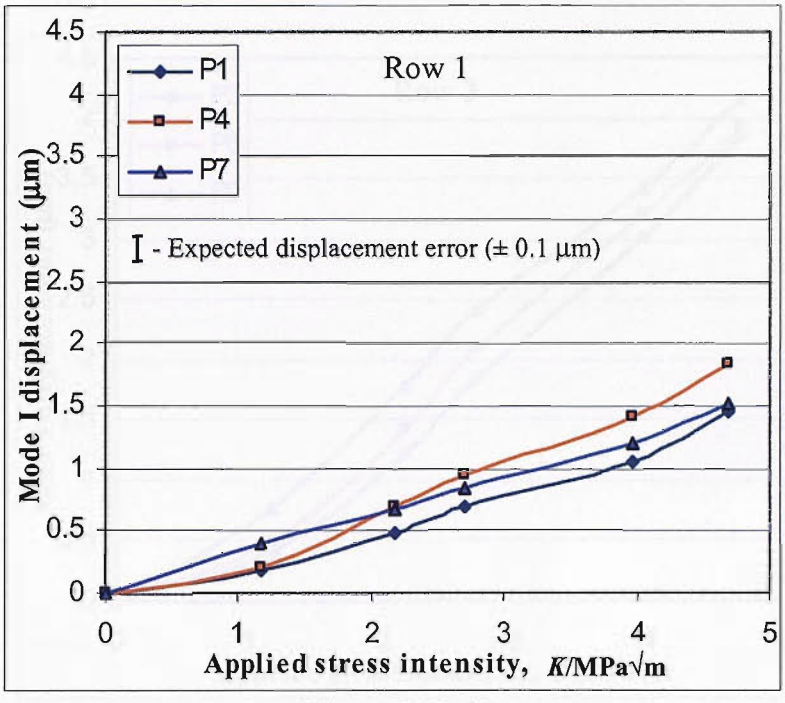

Figure 5.23 (a)

Figure 5.23 Variations of local mode I COD, δ_I, as a function of applied stress intensity measured utilizing centroid spacings of each pair of micro-pores at the locations of; (a) Row 1, (b) Row 2, and (c) Row 3 as illustrated in Figure 5.21.

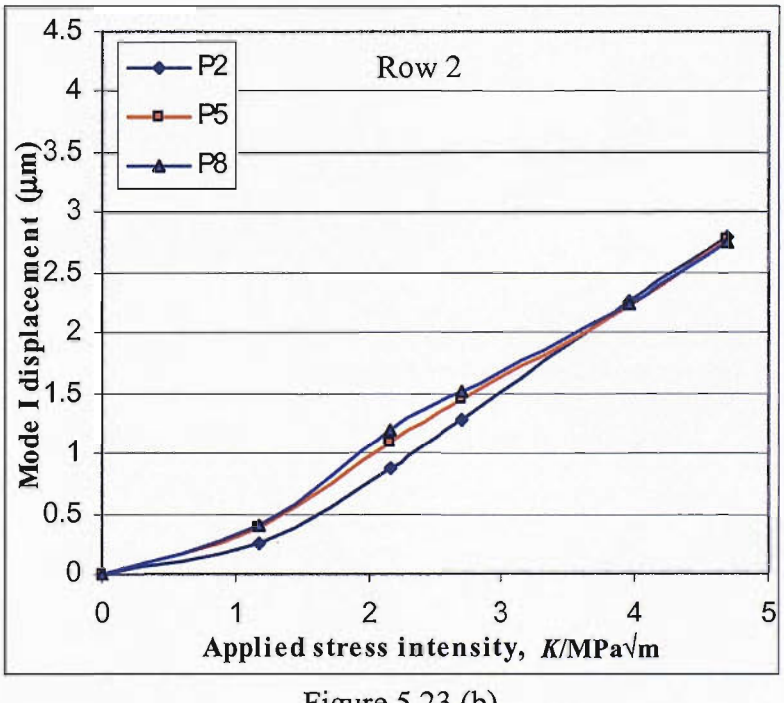

Figure 5.23 (b)

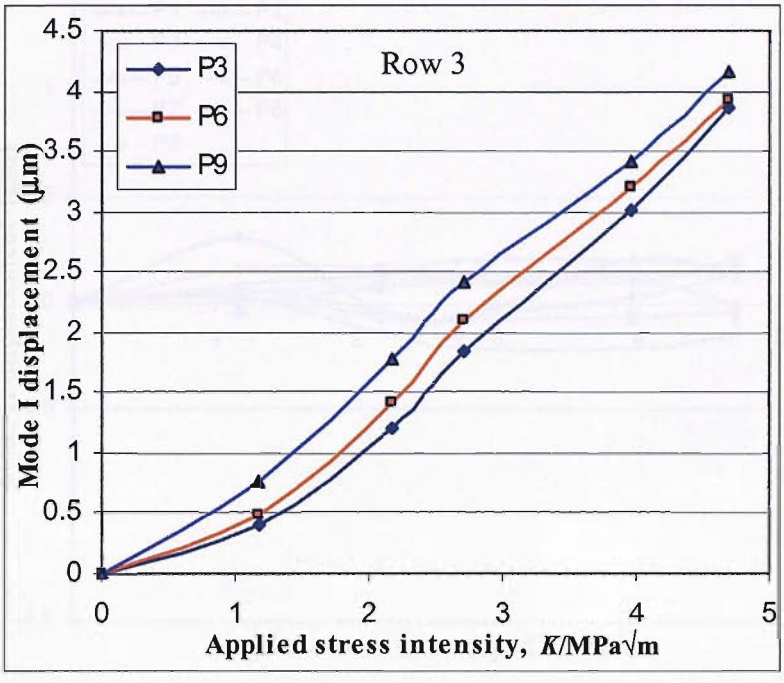
Row 3
P3
P6
P9
Mode I displacement (μm)
Applied stress intensity, K/MPa√m
0
0.5
1
1.5
2
2.5
3
3.5
4
4.5
0
1
2
3
4
5

Figure 5.23 (c)

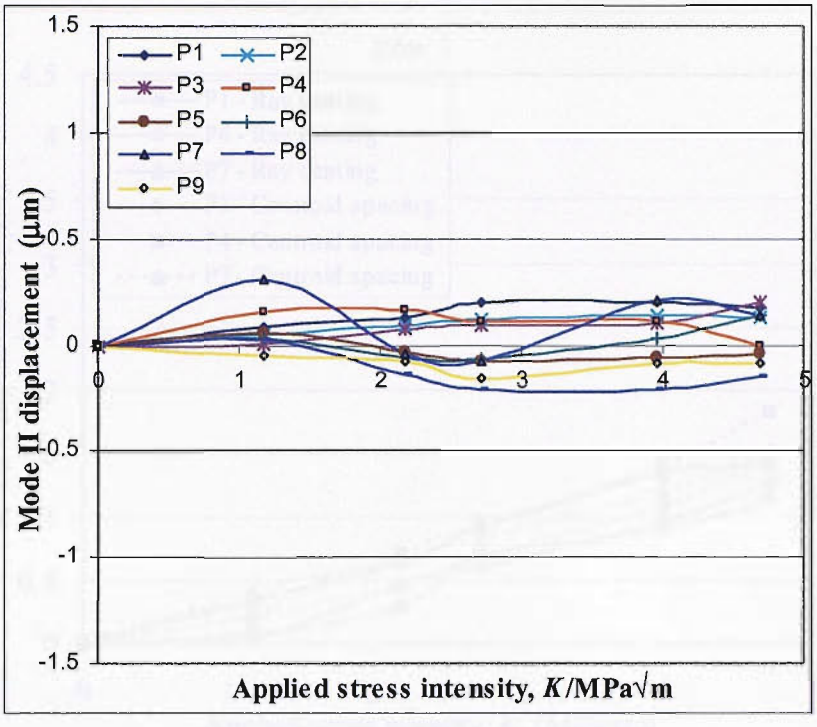

Figure 5.24 Variations in mode II displacement, δ_{II}, as a function of applied stress intensity, measured utilising centroid spacings of each pair of micro-pores from locations P1 to P9.

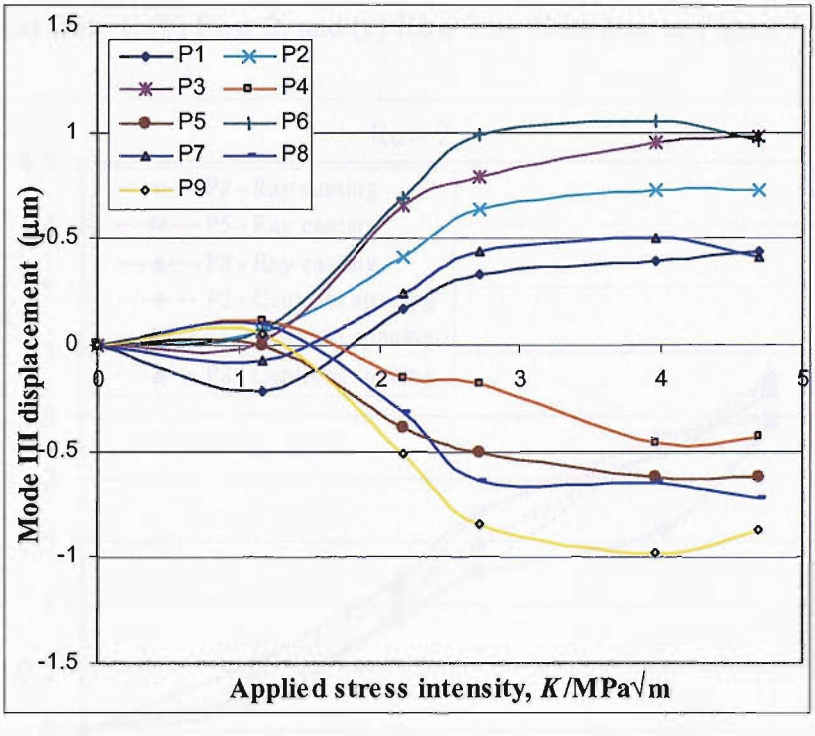

Figure 5.25 Variations in mode III displacements, δ_{III}, as a function of applied stress intensity, measured utilising centroid spacing of each pair of micro-pores from location P1 to P9.

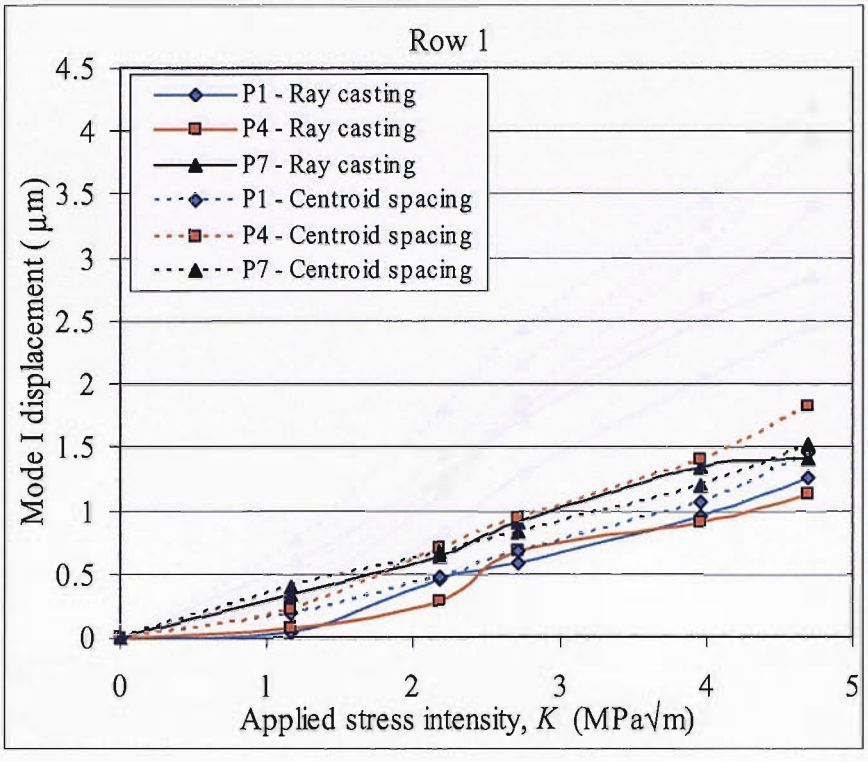

Figure 5.26 (a)

Figure 5.26 Comparison of sample O1 mode I COD measured using ray casting algorithm and microstructural centroid spacing displacement gauging method at the locations of; (a) Row 1, (b) Row 2, and (c) Row 3 as illustrated in Figure 5.21.

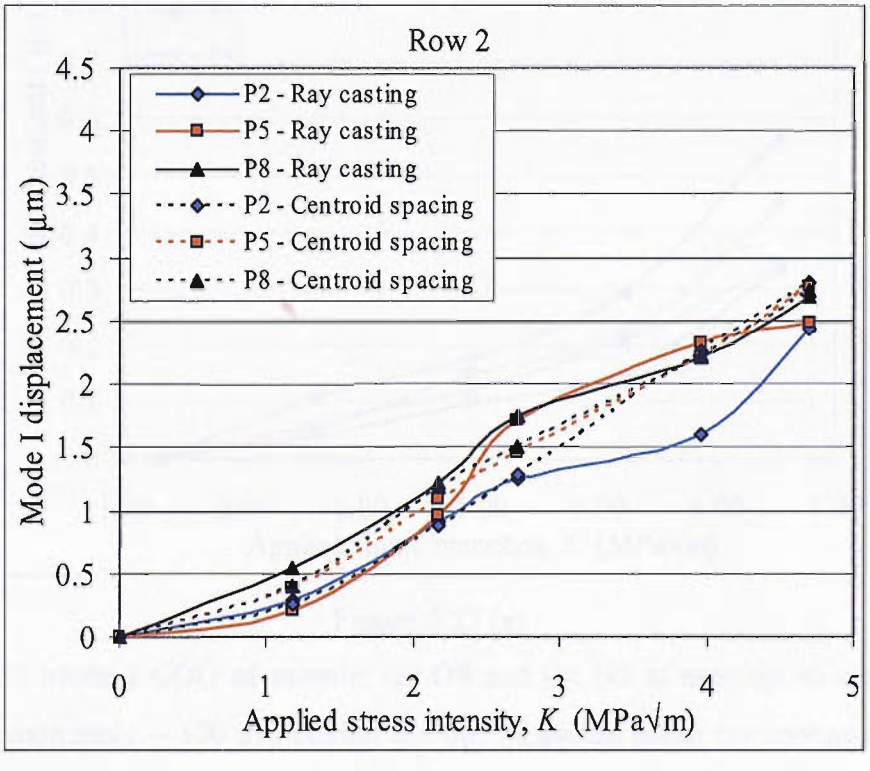

Figure 5.26 (b)

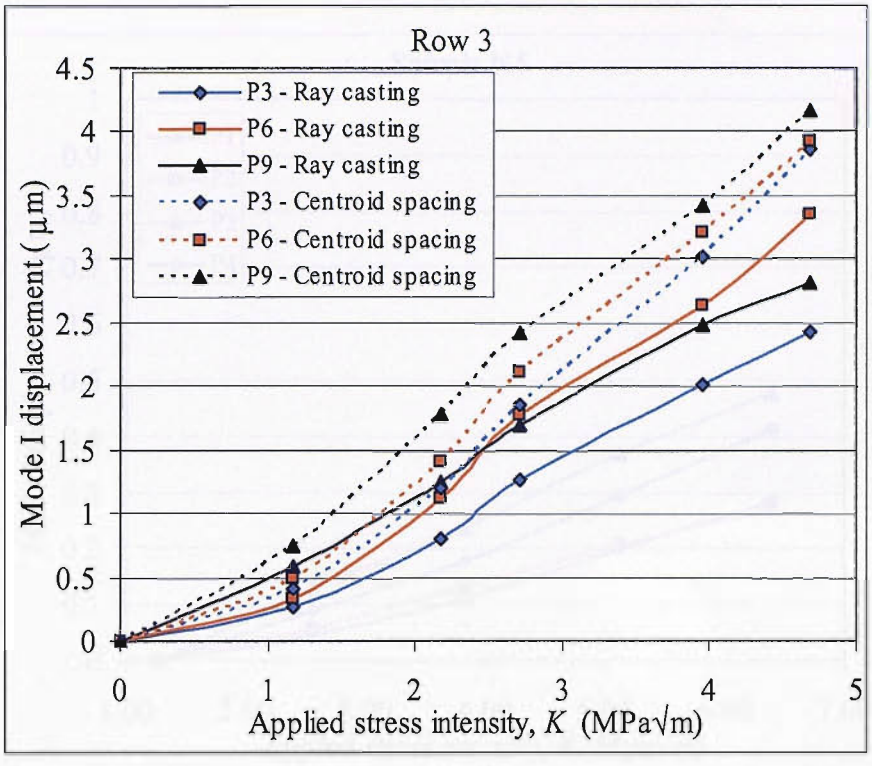

Figure 5.26 (c)

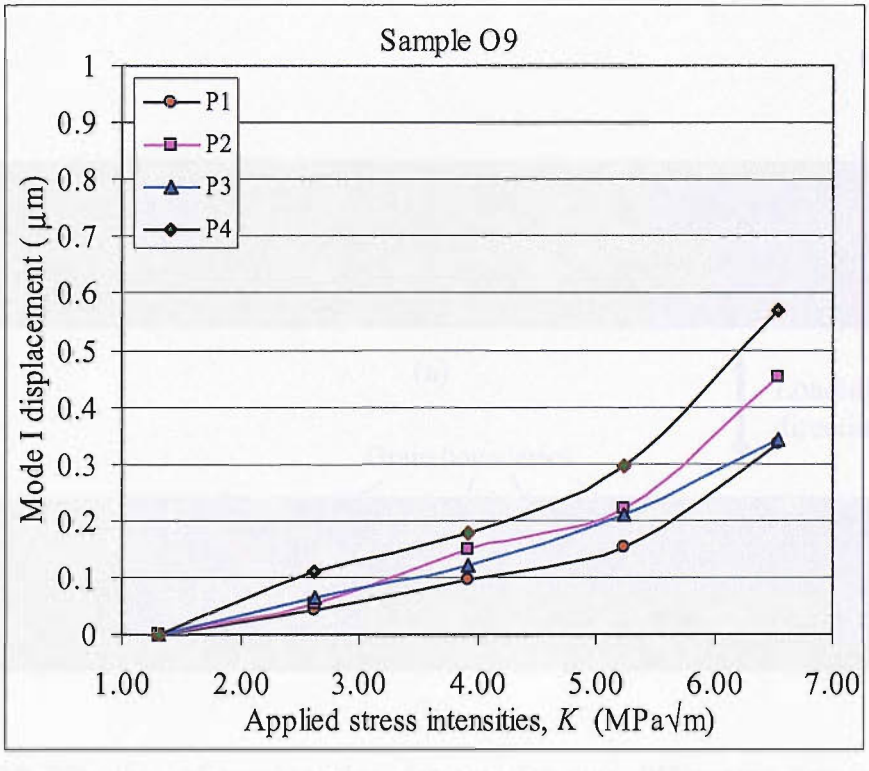

Figure 5.27 (a)

Figure 5.27 Mode I COD of sample; (a) O9 and (b) N5 at near tip locations (each point approximately ~ 100 µm behind the tip) measured using ray casting algorithm as a function of applied stress intensity.

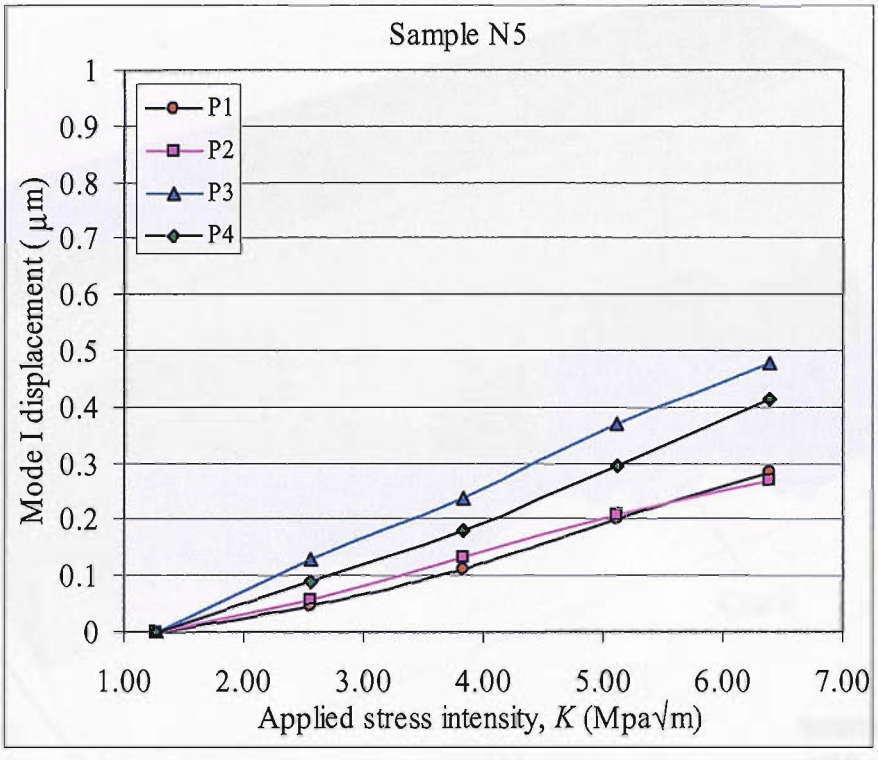

Figure 5.27 (b)

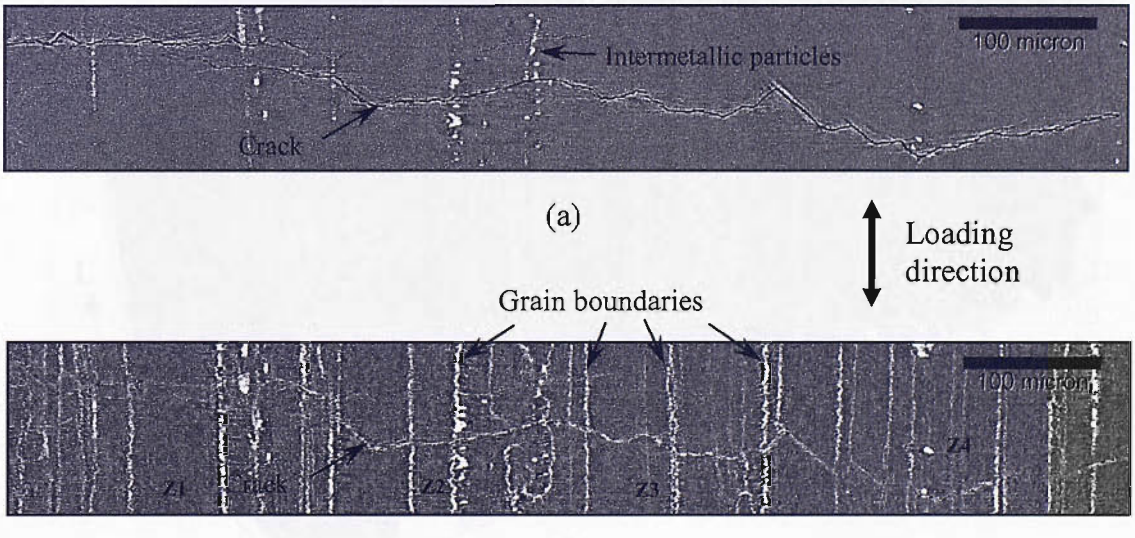

Figure 5.28 2D slice of tomographic dataset showing differences between cross-sectional view (L-S plane) of a crack mouth; (a) before application of liquid Ga, and (b) after application of liquid Ga.

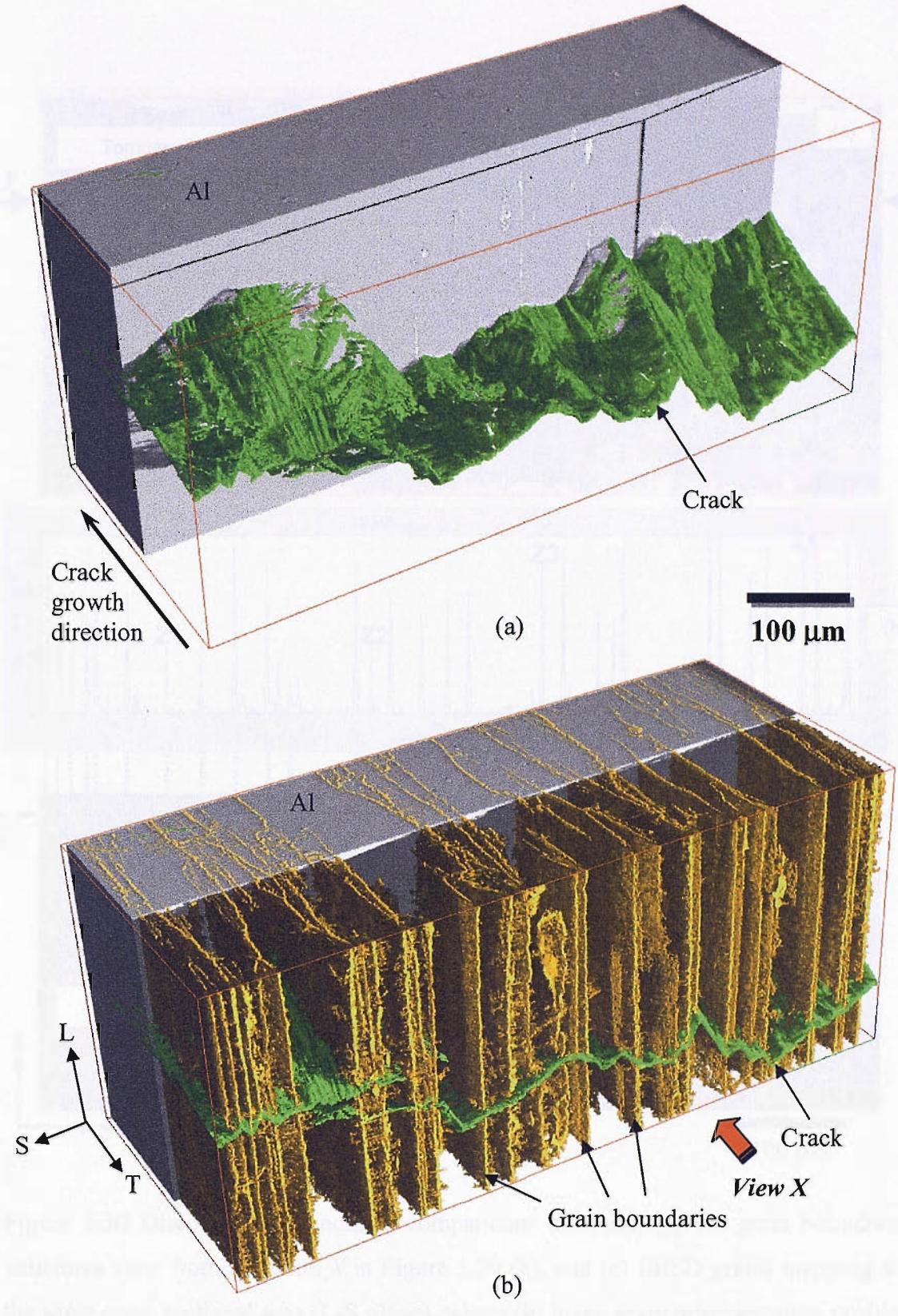

Figure 5.29 3D rendered perspective view of crack in a tomographic volume; (a) without, and (b) with highlighting 3D grain boundary structures.

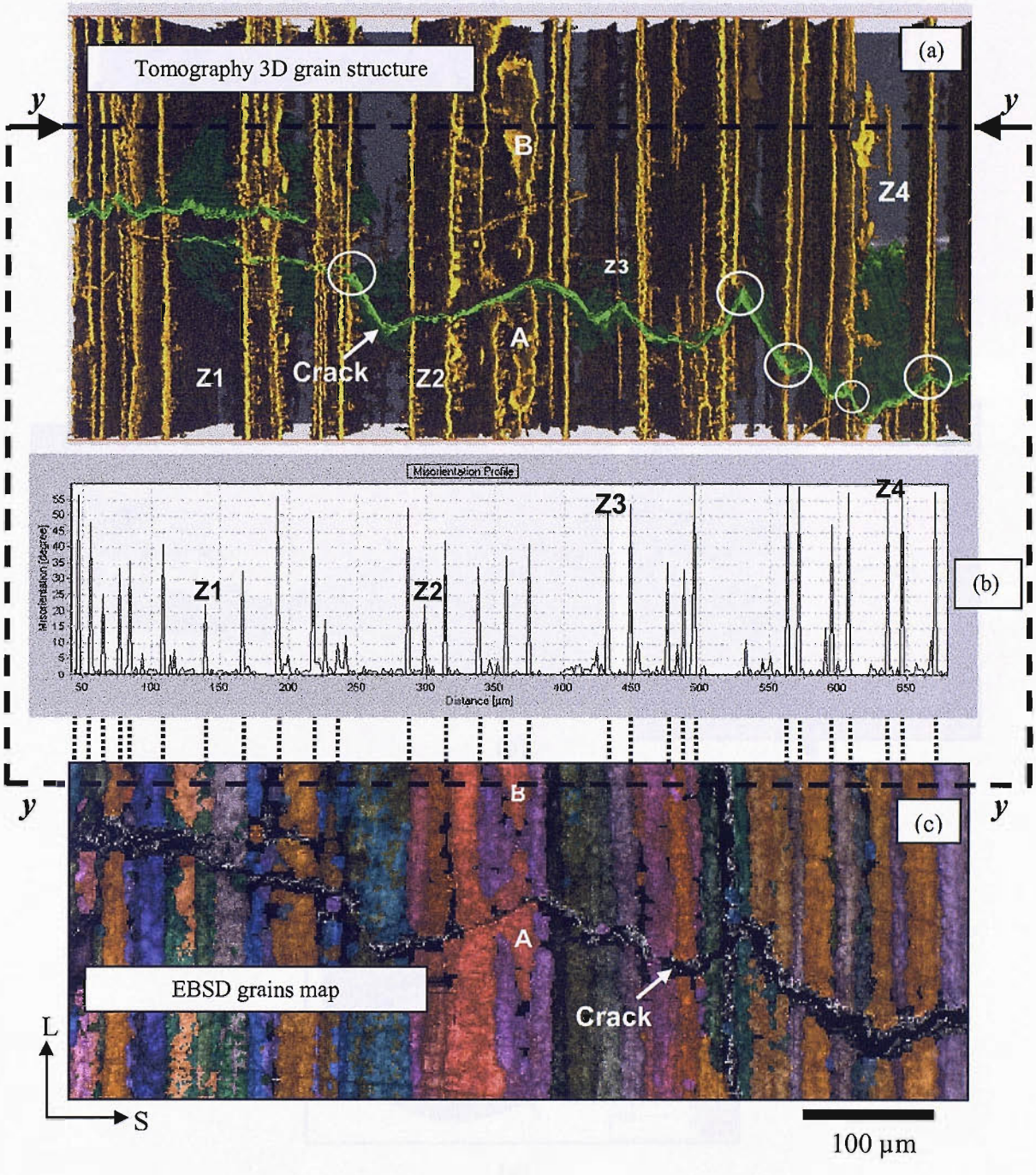

Figure 5.30 Direct grain boundaries comparisons between; (a) 3D grain boundary structures view from direction *X* in Figure 5.29 (b), and (c) EBSD grains mapping at the same cross sectional area (L-S plane), where (b) is the grain misorientation profile across the line *y-y*. Circled area shows the crack deflection turning points at grain boundary.

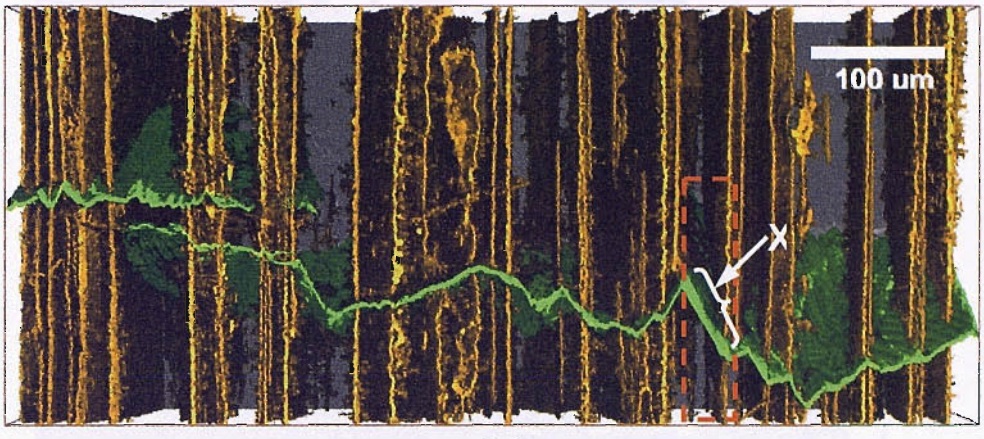

(a)

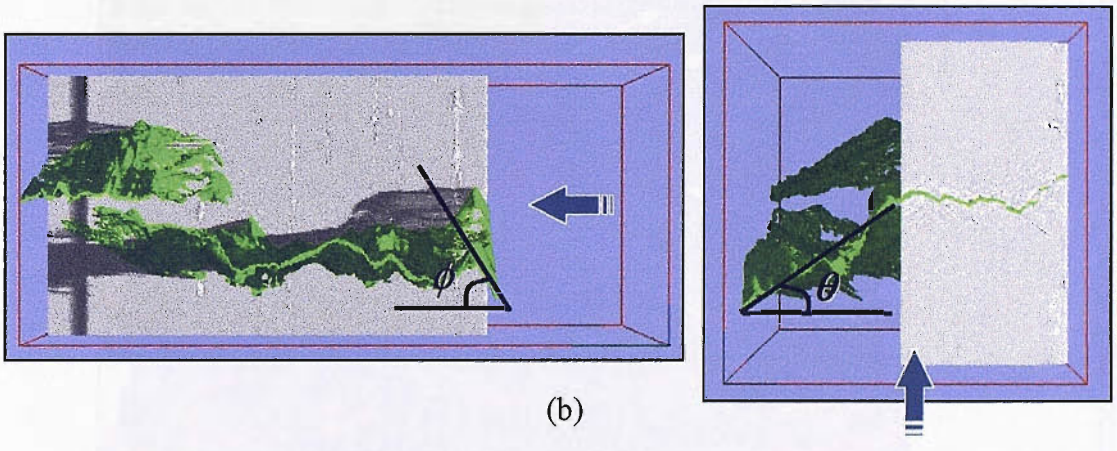

(b)

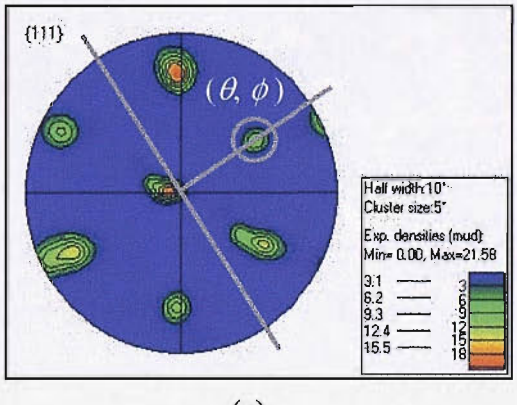

(c)

Figure 5.31 A typical example of crystallographic crack plane indexing of an individual section of crack deflection. (a) The corresponding section of deflected crack labelled as X. (b) Crack deflection angles (θ, ϕ) determination. (c) Peak determination at the sub-section {111} pole figure of the highlighted area in (a) by using measured (θ, ϕ) from (b).

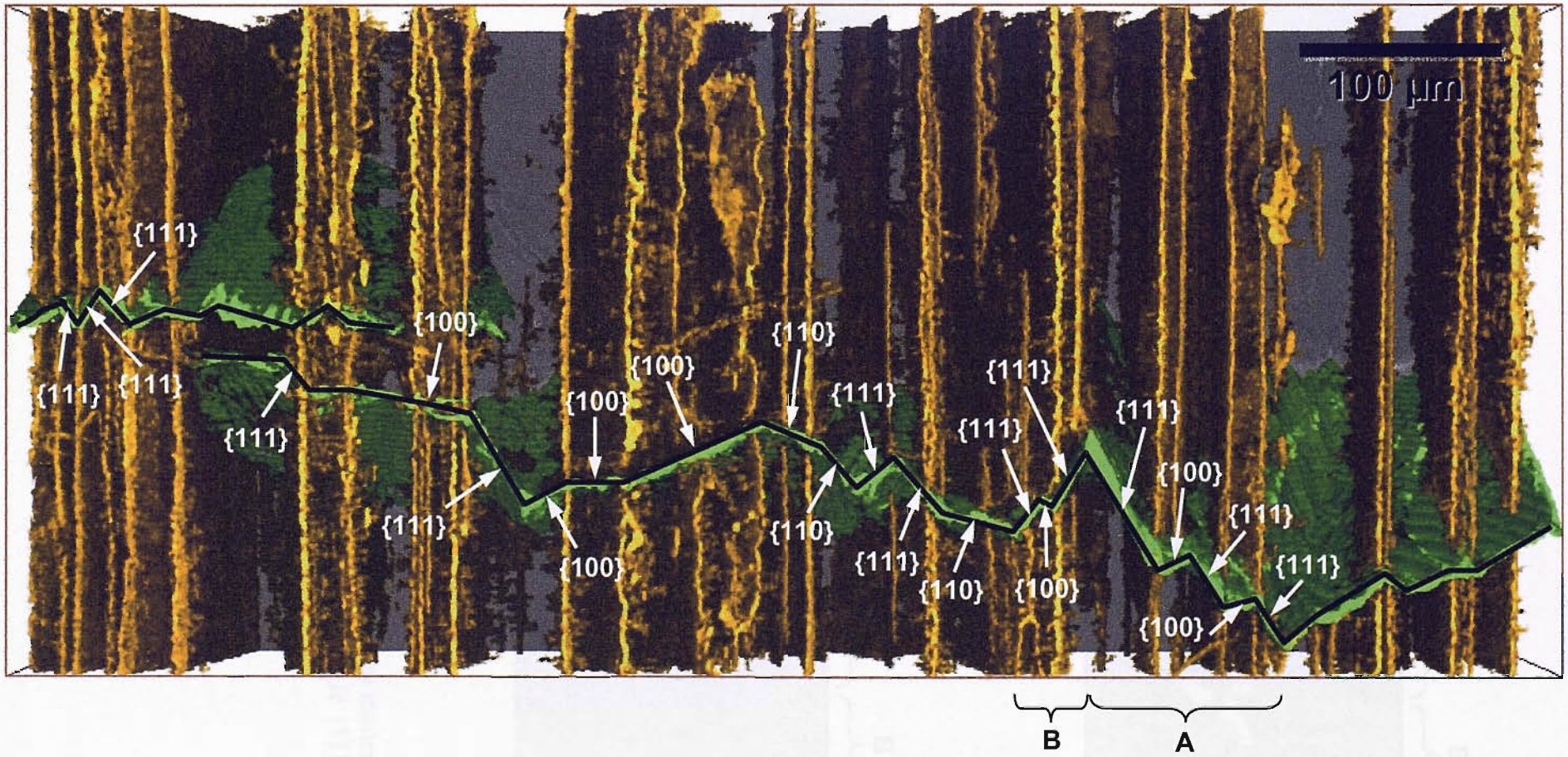

Figure 5.32 Measured closest fracture oriented crack plane for each sub-section of crack deflection.

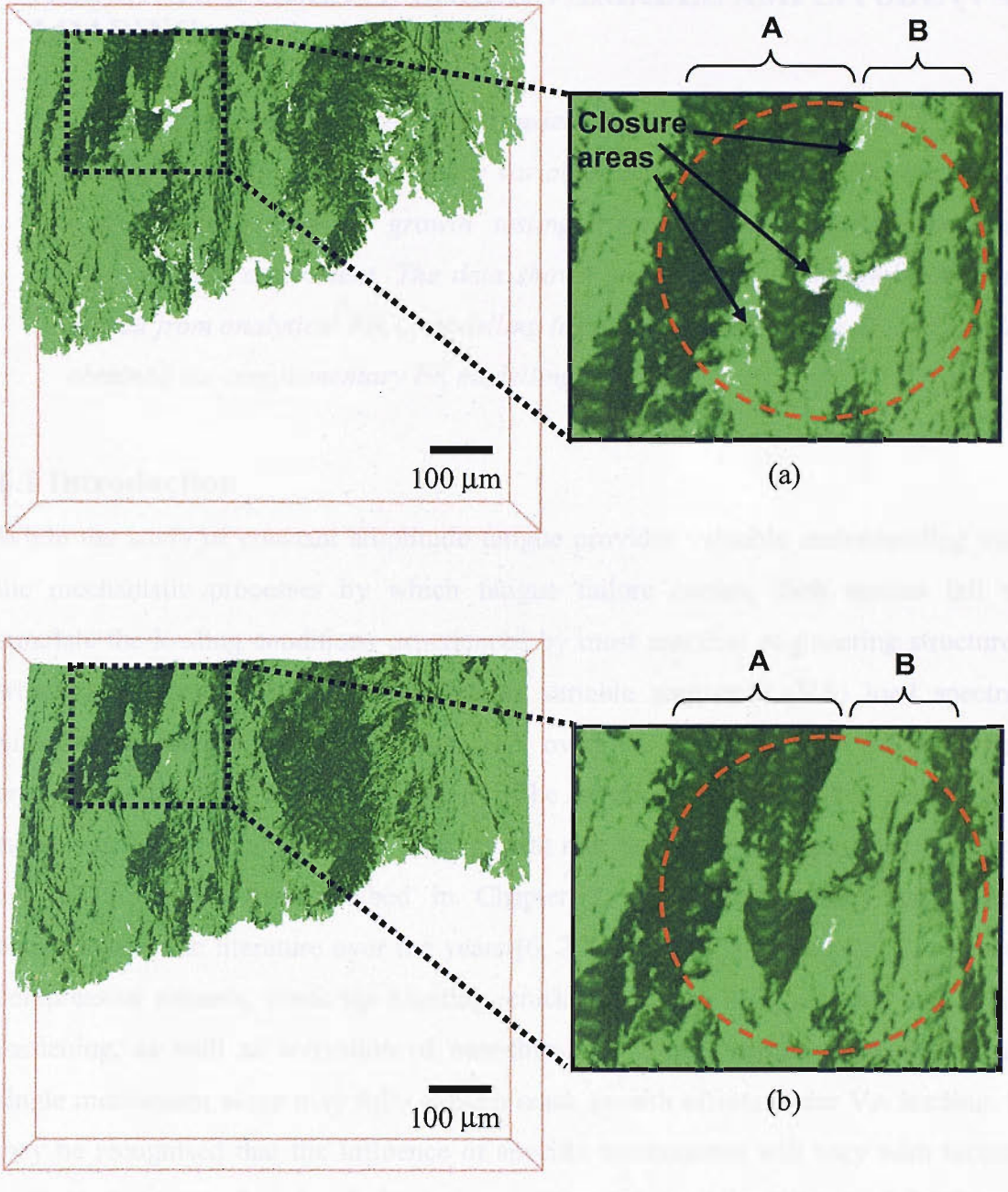

Figure 5.33 Plan view of extracted crack volume of N5 samples at; (a) minimum load, (b) maximum load, showing the changing of closure area at high angle {111} failure deflection sections (A and B) as highlighted in Figure 5.32.

6. TRANSIENT CRACK GROWTH BEHAVIOUR OF 2024-TYPE ALUMINIUM ALLOYS UNDER VARIABLE AMPLITUDE (VA) LOADING

This chapter presents a study of transient crack growth behaviour of several 2024-type aluminium alloys under variable amplitude (VA) loading via single overload fatigue crack growth testing, crack closure measurement and fractographic assessment. The data shown are linked with the understanding gained from analytical RICC modelling (as described in Chapter 4), and results obtained via complementary FE modelling [1].

6.1 Introduction

While the study of constant amplitude fatigue provides valuable understanding into the mechanistic processes by which fatigue failure occurs, such studies fail to simulate the loading conditions experienced by most practical engineering structures which are almost invariably subjected to variable amplitude (VA) load spectra. Simple peak transient load excursions (i.e. overloads) are known to affect fatigue crack growth rates dramatically [2-5]. The physical processes that have been suggested to influence such VA crack growth rate behaviour are somewhat complex and controversial. As described in Chapter 2, many explanations have been considered in the literature over the years [6, 7], including enhanced PICC, residual compressive stresses, crack tip blunting, crack deflection, RICC effects, and strain hardening, as well as activation of near-threshold growth mechanisms. Whilst no single mechanism alone may fully explain crack growth effects under VA loading, it may be recognised that the influence of specific mechanisms will vary with factors such as the type of material, loading condition (as such baseline load level and overload ratio) and environment conditions [8]. Among the various mechanisms that may operate, the crack closure concept (particularly plasticity-induced crack closure) has been widely recognised due to its ability to rationalise the three main stages of post-overload transient crack growth behaviour: (a) initial crack growth acceleration after application of overload (via reduced crack closure due to overload-induced plastic opening at the crack tip), (b) delayed growth retardation (due to the fact that a degree of crack growth is needed to pass into the overloaded plastic zone before the enhanced PICC effect it taken place), and (c) the recovery of pre-overload crack

growth behaviour (the crack grows beyond the affecting zone of the overload plasticity).

In keeping with the previous chapters of this work, influences of microstructural driven RICC processes are of interest here. Having outlined in Chapter 4 how RICC effects may contribute to CA crack growth in 2024-type materials, it is clearly valuable to consider how such efforts may or may not be carried over to VA load situations. As noted in Chapter 2, it has been suggested that the extreme fracture surface roughnesses achieved in Al-Li-based alloys may contribute to enhanced RICC (and hence crack growth retardation) following single peak overloads [8]. Similarly, the assertion of near-threshold mechanism influence of transient crack growth relates to RICC influences [9-11].

As the first step in understanding the influence of variable loading effects, simple single overload tests were carried out in this study. Although such tests do not give direct assessment of complex load spectrum performance as experienced by real structures, mechanistic insight may still be sought. Detailed closure measurements were taken during the experiments to monitor the possible closure contributions to transient crack growth behaviour. Fractographic features on overloaded fracture surface were assessed to gain better microstructural/micromechanical understanding of the transient mechanism, particularly in terms of possible RICC contributions to transient growth behaviour.

6.2 Materials and Experimental Details

6.2.1 Materials

Materials tested in this study are 2024A, 2027-ReX(8) and 2027-ReX(100), as detailed in Chapter 3. As described in Chapter 4, the 2024A and 2027 materials show the most significant differences in crack growth behaviour under CA loading, with distinct fracture surface roughness levels being linked to varying RICC effects: as such these two alloys were chosen to investigate possible RICC effects under simple single overload conditions.

6.2.2 Overload Fatigue Testing

All overload tests were carried out on same centre crack tension (CCT) panel geometry used in the CA fatigue tests (see Chapter 3 for details); i.e. 12mm thick plates with side grooves to minimise plane stress effects from the surface of the specimen and corresponding complications in closure measurement. A PD system was again used to monitor physical crack length increment during the tests. Multiple strain gauges were attached ~ 1 mm above the specimen side-grooves to record local closure compliance curves (see Figure 3.18 in Chapter 3), as described by Xu [12]. Such multiple gauging is used to ensure local compliance measurements are taken at a reasonably consistent distance of within 2 mm from the crack tip as propagation occurs.

All overload tests were performed with a 100% overload ratio, at a baseline ΔK level (ΔK_b) of 12 MPa$\sqrt{m}$, R = 0.1, at a frequency of 10Hz. Fractography assessment of post-overload fracture surfaces was carried out via FEG-SEM.

6.3 Results and Discussions

6.3.1 Post-Overload Crack Growth Rates

Figure 6.1 shows the transient crack growth behaviour after a 100% single overload at ΔK_b =12 MPa$\sqrt{m}$ for 2024A and the two 2027 materials, obtained from multiple tests of each case (at least 2) in Figure 6.1(a). The crack length increment, Δa, is normalised by the monotonic plane strain plastic zone size, r_{pOL}, at the maximum load of the overload cycle, and the transient crack growth rates, $(da/dN)_t$, are normalised by the baseline crack growth rate, $(da/dN)_b$, which takes into account differences in baseline crack growth rates at the same ΔK_b level. To validate the experimental data, results for 2024A were compared with Xu's [12] 2024A data which was carried under the same experimental conditions on the same alloy batch. It is illustrated in Figure 6.2 that good agreement with Xu's data is indeed obtained. In Figure 6.1, both 2027 materials appear to show similar overload transient crack growth behaviour to the 2024A material, at least within the resolution of the experiment. All materials show maximum retardation when the crack had propagated into the overload zone by about

~ 0.5 r_{pOL}, with growth rates being decreased by a factor about 30 times relative to the baseline. The normalised overload retardation distance is about ~ 4.0 – 5.0 r_{pOL} before recovery to pre-overload growth rates, although this distance is difficult to define accurately.

As such it may be seen that the material influence on the transient crack growth behaviour of these alloys can be well accounted for by the difference of the CA baseline crack growth behaviour, i.e. no marked difference in the transient crack growth behaviour was seen when data are potted in a normalised manner. Despite the differences of these alloys in terms of degree of recrystallisation and dispersoid content level, the similarity of post-overload transient behaviour suggests that these factors do not seem to play a key role in transient behaviour (at least under the studied overload ratio and ΔK_b level), consistent with the work from Xu [12] where similar post-overload transient behaviour was identified between 2024A and 2024 material in a single ReX condition.

6.3.2 Closure Measurements

As mentioned, it is widely suggested that the crack closure concept may provide a basis for rationalising post-overload crack growth behaviour. However, crack closure is only meaningful to explain this phenomenon when consistent measurement of closure point is available. To ensure the consistency and reliability of closure measurements, in keeping with the work discussed in Chapter 4, a non-subjective compliance curve fitting method has been used [12]. Local compliance curves from the near-tip strain gauges were used to define closure points in the current investigation: a conventional crack mouth clip gauge was not used as such measurements have been shown to be insensitive to very near tip contact process that may control transient behaviour [12, 13].

Figure 6.3(a) shows 10 compliance curves measured before and after the application of 100% single overload on 2024A materials at ΔK_b = 12 MPa$\sqrt{m}$. All curves in this case were measured from a strain gauge located behind the crack tip, where the tip is within 2 mm of the gauge position at all points (in the direction of crack growth).

Corresponding closure point detected by the curve fitting method are indicated by the red arrow on each curve. Figure 6.3(b) shows the corresponding measuring positions on a diagram presenting the (normalised) transient fatigue crack growth behaviour. It should be noted that, depending on the exact placement of the strain gauges relative to the crack tip, evidence of multiple curvature was seen in the near tip compliance data (more evident in Figure 6.4(a) for example). In keeping with the work of Xu [12] and Ward-Close and Ritchie [3], the present work has particularly examined the upper apparent closure points of the curves. Such multiple curvatures are identifiable with the action of near-tip contact processes (controlled by transient loading) and those occurring further in the crack wake ("far-field", essentially controlled by baseline load conditions) [12, 14]. In using the present curve fitting methods, such multiple compliance curve inflections are clearly problematic for the linear and quadratic formulation. In the first instance a degree of subjectivity has therefore been introduced into the measurements where the approximate location of the upper compliance inflection point is identified visually, and the quadratic fitting below this point is manually truncated to an interval of ~ 0.2 P_{max}. Clearly the non-subjective nature of the curve fitting is undermined by this process: visual inspection of the results does however suggest that detected closure points are reasonable in relation to the raw data, and it is still considered valuable that a consistent method has been applied.

Curve 1 in Figure 6.3(a) was measured before the application of the overload, with a transition point being detected by the usual curve fitting method. Curve 2 was taken immediately after the application of overload to the crack (i.e. before any cyclic crack growth), where the crack had apparently advanced into the overload plastic zone by ~ 0.05 r_{pOL}. A reduced closure level was measured by curve fitting. Curves 3 shows the compliance curve when the crack had propagated into the overload plastic by ~ 0.50 r_{pOL}. The highest closure level (~ 0.70) was detected from this curve, which agrees well with the position of the maximum crack growth retardation in Figure 6.3(b).

Curves 4 to 7 in Figure 6.3(a) were measured after the crack had propagated into the overload plastic zone by ~ 0.50 r_{pOL} to ~ 2.00 r_{pOL}. Decreasing closure levels can be seen with ongoing increasing crack growth rates. The closure results again appear to

be in good agreement with the length of crack growth transient after overload shown in Figure 6.3(b). Curves 9 and 10 are obtained when the crack had propagated into the overload plastic zone by~ 3.00 r_{pOL} and ~ 3.75 r_{pOL} respectively, with pre-overload closure levels being approximately recovered by this stage.

Similar observation were made for the other 100% single overload tests for 2027-ReX(8) and 2027-ReX(100) samples at ΔK_b = 12 MPa$\sqrt{}$m, as shown in Figure 6.4 and 6.5. All observations show the same pattern of changes in the shape of the compliance curves as a function of crack growth rates after overload.

Figure 6.6 shows the apparent closure levels in 2024A and both 2027 materials after 100% single overload at a baseline ΔK_b = 12 MPa$\sqrt{}$m. In keeping to the previous diagrams, the crack length increment is again normalised by the monotonic plastic zone size in plane strain at the maximum load of the overload cycle, r_{pOL}. Before the application of overload, baseline closure levels were measured for each material with the values consistent with closure levels obtained via CA crack growth at the same ΔK level (see Chapter 4). After the overload, all materials show similar basic patterns in the variation of crack closure. Closure level of each material appear to reach a maximum after the crack has propagated into the overload plastic zone by ~ 0.5 r_{pOL}, while pre-overload closure levels are eventually recovered with ongoing crack propagation. All materials seems to have similar magnitude of maximum retardation closure level at ~ 0.5 r_{pOL}, consistent with observed post-overload transient crack growth behaviour shown in Figure 6.1. The normalised overload affected distances in Figure 6.6 are perhaps slightly longer than those observed in Figure 6.1, although scatter in the data makes exact comparison difficult.

6.3.3 Correlation between Transients Crack Growth Behaviour and Measured Closure Levels

Whilst good qualitative agreement was observed between the transient crack growth behaviour and the measured post-overload closure levels, quantitative correlation between both results may of course be further assessed. Figure 6.7 shows '*predicted*' crack growth transients in the 2024A and 2027 materials based on the transient

closure measurements presented in this chapter, and the results in Figure 4.13 in Chapter 4, where ΔK_{eff} – *da/dN* data is derived from CA fatigue tests of the same side grooved sample geometry. Figure 6.7 shows equivalent predictions for all three materials where it may be seen that results are reasonably consistent with measured transient crack growth as shown in Figure 6.1. However, the predicted magnitude of the retardation is somewhat different to the measured crack growth results. For 2024A, the predicted transient severity (peak influence) is slightly under-estimated: is crack growth predicted to drop by about 14 times at the lowest levels, as opposed to ~ 30 times in Figure 6.1. On the other hand, for the 2027 materials, the predicted results overestimate with the crack growth being predicted to decrease by about 60 times at the lowest levels, about double the effect shown in Figure 6.1. The potential accuracy of growth rate estimates should be considered of course. Considering the closure results in the first instance, constant amplitude tests suggest a reproducibility in $\Delta K_{eff}/\Delta K_{app}$ measurements of the order of ± 0.025. As such, the assertion that closure transients for the three alloys in Figure 6.6 are equivalent may be considered reasonable. Considering the *da/dN* - ΔK_{eff} data of Chapter 4, it should then be noted that the ΔK_{eff} values relevant to the post-overload growth rate predictions (ΔK_{eff} from ~ 3 – 10 MPa$\sqrt{m}$) span the steepest part of the *da/dN* - ΔK_{eff} curves in Figure 4.13. As such, shifts of the order of ± 0.025 in $\Delta K_{eff}/\Delta K_{app}$ for the transient minima in Figure 6.6 will in fact produce changes in *da/dN* up to a factor of 3, which would be sufficient to account for the differences in predicted and measured transient behaviour.

6.3.4 Fractographic Assessments

Figure 6.8 shows macroscopic fracture surfaces of 2024A and 2027 samples after a 100% single overload at ΔK_b = 12MPa$\sqrt{m}$. A clear overload 'band' can be seen on the fracture surfaces with distinct black marking on the location of where overload was applied, consistent with the presence of post-overload oxide debris [11, 15], consistent with the role of crack closure in post-overload crack growth (i.e. local fretting effects). At this magnification level, 2024A can again be seen to have the largest scale of fracture surface features, followed by the 2027-ReX(100) and 2027-ReX(8) materials (consistent with observations in Chapter 4).

Figure 6.9, 6.11 and 6.13 show magnified FEG-SEM images of the highlighted area in Figure 6.8. To relate the fracture surfaces to the underlying microstructural scales, each figure has been presented together with a corresponding EBSD grains map of the same plane (S-T) as the fracture surface, scaled to the same magnification as the FEG-SEM images. In the first instance, fracture surface features appear to scale according to the respective grains dimensions with coarser surface features appearing in the coarser grained 2024A alloy. All materials show some evidence of a more crystallographic crack growth mode after the application of an overload, evident in 2027-ReX(8) in Figure 6.14 for example. Some interactions with intermetallic particles were observed in the vicinity of the overload line, which may therefore be expected to contribute to the brief crack growth acceleration at the application of the overload. Areas of excess oxide debris can be seen in an area within ~ 0.5 r_{pOL} after overloads as highlighted in Figure 6.9, 6.11 and 6.13: this 'band' is particularly clear in the 2027-ReX(8) images in Figure 6.13. Qualitatively it was found that the fracture mode transition distances were consistent with the crack growth results, where the baseline growth rates were recovered as the crack growth mode returned to 'normal', however accurate quantification from the FEG-SEM images was not considered feasible given the rather gradual changes and complexity of the surfaces features.

A more detailed assessment of the overload locations can be seen in Figure 6.10, 6.12 and 6.14 for each material. Typical oxide patches formed on post-overload fracture surfaces are highlighted in these figures. Looking at the post-overload fracture surfaces, it is interesting to note a distinct, nearly continuous oxide band immediately adjacent to the overload line in the 2027-ReX(8) material particularly (see Figure 6.13 and 6.14). The width of the oxide band is consistent with the distance where maximum retardation occurs as observed previously in Figure 6.1 (i.e. ~ 0.5 r_{pOL}). In 2024A the pattern of oxide formation is quite distinct, with no continuous oxide band arising: comparing Figure 6.10 (a) and 6.14 (a) directly, it may be seen that oxide debris in the 'rougher' 2024A fracture surfaces is focused at patches within the post-overload region, most obviously at ridges and asperities that are present.

6.3.5 Correlation between Experimental Observations and FE Modelling Results

As reported earlier, the 2024A and 2027 materials appear to show similar transient growth rate responses and closure behaviour under 100% single overloads at ΔK_b = 12MPa$\sqrt{m}$. In the current study, where samples were tested under plane strain conditions, it has been suggested that RICC is a key closure mechanism controlling fatigue crack growth rates for both materials under CA conditions. Whilst fractographic assessment of post-overload fracture surfaces shows an indication of changes in post-overload fracture surface contact patterns between the 2024A and 2027 materials (especially the 2027-ReX(8)), this does not appear to significantly affect transient crack growth.

To further understand this issue, the present experimental observations have been correlated to recent FE modelling efforts from Singh [1]. As reported earlier in Chapter 4, the ratio of asperity deflection length (L) to baseline plastic zone size (r_p) has been suggested to be critical to RICC effect (see Figure 4.38 in Chapter 4). In keeping with the observation on CA crack closure and the underlying L/r_p relationship that is implied, Singh's FE work [1] on varying fracture surface features (via asperity deflection length, L) was recently extended to overload conditions by considering both overload and baseline plasticity effects in relation to possible RICC-overload interactions. The schematic representation of overload and baseline loading influences on RICC obtained from FE modelling results is illustrated in Figure 6.15.

In the first instance, before considering the results in Figure 6.15(b), Figure 6.15(a) should be examined, showing a 2D description of load conditions in terms of asperity deflection size (L) and both baseline and overload plastic zone sizes. The black line shows the condition $L/r_{pOL} = L/r_p$, which represents 0% overload, and coloured parallel lines then represent different overload ratios with $L/r_{pOL} < L/r_p$. Moving upward along these lines may be equated to an increasing of L (for a fixed ΔK_b); moving downward may be equated with increasing of ΔK_b. Points plotted on Figure 6.15(a) represent those shown in the 3D plot of Figure 6.15(b) which includes an additional axis to represent the FE modelled influence of roughness on overload transient severity. For a given set of L/r_p and L/r_{pOL} conditions, transient closure levels were simulated using two different FE models: one with a fixed nominal 45° deflected

zig-zag crack, i.e. with the potential for RICC influences; while the other model is based on a simple straight crack which therefore only generates PICC. To capture differences between the deflected and straight crack models, Singh [1] defines the terms $[K_{cl}/K_{max}]_{\text{max-RICC}}$ and $[K_{cl}/K_{max}]_{\text{max-PICC}}$, referring to the peak closure levels occurring after overload for deflected and straight crack models respectively. Figure 6.15(b) then plots the ratio $[K_{cl}/K_{max}]_{\text{max-RICC}}$ / $[K_{cl}/K_{max}]_{\text{max-PICC}}$ as the z-axis, where a value of unity indicates that deflected and straight crack models show no difference in transient closure behaviour: PICC dominance of the closure transient behaviour is then is presumed. Values of $[K_{cl}/K_{max}]_{\text{max-RICC}}$ / $[K_{cl}/K_{max}]_{\text{max-PICC}}$ greater than unity then imply RICC influence/interaction with overload closure behaviour.

As the current study is concentrated on 100% single overloads, the red line in Figure 6.15(b) is clearly of interest. Looking at the low part of the 100% overload curve, it shows that for L/r_{pOL} smaller than ~ 0.5, the $[K_{cl}/K_{max}]_{\text{max-RICC}}$ / $[K_{cl}/K_{max}]_{\text{max-PICC}}$ ratio is close to unity: i.e. RICC effect are less important when the asperity deflection length is very much smaller than the overload plastic zone size. Under the current study overload condition at ΔK_b = 12MPa$\sqrt{\text{m}}$, it is then implied that L would be required to be larger than ~ 250 – 300 μm in order to have an effective RICC influence over PICC in the post-overload transient crack growth in these tests given the relevant plastic zone dimensions.

6.3.6 Discussion

In general terms, there are a number of points supporting predominant crack closure control of the overload transients investigated here. Particularly, the closure levels determined from the upper deflection points of the near-tip compliance curves show reasonable correlation with crack growth rate behaviour in terms of both the severity and duration of overload transients. The presence of distinct post-overload oxide bands is also consistent with closure and associated fracture surface fretting. The correlation between the width of fracture surface oxide bands and the distance over which crack growth reached the post-overload growth rate minimum is qualitatively consistent with closure influence, as initial growth across the excess oxide region would be equated to an increasing overload induced closure wake: growth beyond the

oxide band would then see a gradual return to baseline growth rates as the influence of load transfer at the overload-induced closure band diminishes at the crack tip.

In terms of the mechanism of crack closure and potential RICC influences in the alloys tested, the similarity in transient growth rate effects, overload distances, and measured post-overload closure levels all imply a limited micromechanical influence on overload behaviour. The consistency of overload transient lengths itself implies a detachment of microstructural scales from the overload process: a simple scaling of transient length with plastic zone size, and hence PICC influence, may then be implied from Figure 6.1, although scatter in the data prevents an explicit separation of yield strength influences between the materials. In terms of overload severity, it might be suggested alternatively that there are RICC-based micromechanical influences on transient behaviour, but the effect is equivalent for the materials/load condition combinations tested, i.e. any RICC effect is 'saturated' for the different materials and their associated range of fracture surfaces features. This observations may then be particularly related to the modelling of Singh [1], providing, to the best of the authors knowledge, the only relevant detailed treatment of RICC-overload interactions. Considering the red, 100% OL line of Figure 6.15(b), it is implied that for L/r_{pOL} values smaller than ~ 0.5, the presence of fracture surface asperities will have no significance of post-overload closure *cf.* a PICC-only controlled straight crack. Under the current study conditions of ΔK_b = 12MPa$\sqrt{m}$/100% overload ratio, L would then be required to be of the order of 250 – 300 μm to have an effective RICC influence over PICC. Referring to Table 4.2 in Chapter 4, effective asperity lengths determined from CA fracture surfaces are significantly less than 100 μm, even for the lower ΔK level measured. Whilst it is again noted that the L values of Table 4.2 are subject to a number of assumptions and procedures within the measurement approach, it may be seen that the values and their corresponding apparent accord with CA crack closure measurements is consistent with there being limited RICC effects in the overload tests of these materials. The observation of a relatively-uniform post overload oxide band in the finest scaled fracture surface tested here (i.e. the 2027-ReX(8)) would appear intuitively consistent with PICC controlled post-overload surface contact: the incidence of asperity controlled contact of the rougher 2024A fracture surface with no particular contribution of transient closure would then be

entirely consistent with the present overload test conditions lying at the low L/r_p end of the 100% overload line in Figure 6.15(b). An interesting deduction from the present results is that for a 100% overload and asperity sizes of the order of tens of micrometers, RICC contributions to overload behaviour might only be expected for baseline ΔK levels of the order of 3MPa$\sqrt{m}$ (assuming an r_{pOL} of 50 μm). For a 50% overload, the equivalent implied baseline ΔK level would be ~ 4.5MPa$\sqrt{m}$, with both values only affecting the lower range of load conditions commonly encountered in commercial airframe lifing [16].

The implications of these results can be extended to the results of Vankateshwara Rao and Ritchie [4], where post overload crack growth in the Al-Cu-Li alloy 2090-T8E41 are compared with 2124-T351 under plane strain conditions. In their work, enhanced overload transient retardation effects in the Li containing material are attributed to high levels of fracture surface roughness (as noted earlier). Individual crystallographic facets are indicated to run over distances of hundreds of micrometers in the 2090 material, very much greater than those in the 2124 alloy. For the tensile properties of the 2090 material and the conditions reported in [4], asperity sizes of the order of 250 μm would be sufficient for RICC contributions to transient behaviour according to the results of Singh [1], which may then be the possible. Profilometry of the Al-Li alloy, as set out in Chapter 4 would of course then be valuable to provide quantitative validation of the understanding outlined here.

6.4 Conclusions

1. Post-overload crack growth behaviour of 2024A and 2027 materials after 100% single overload at ΔK_b =12 MPa$\sqrt{m}$ are essentially similar, particularly when normalised retardation distances and crack growth rates are considered.

2. Post-overload closure measurements appear to describe overload transient crack growth well in these materials. Reasonable correlation between transient crack growth and measured closure variations has been observed when used in conjunction with '*intrinsic*' CA-derived crack growth data.

3. Crack growth mode transitions with classical activation of near-threshold mechanisms are observed in post-overload crack growth. Post-overload maximum retardation distances agree well with the observed width of clear oxide marking on fracture surfaces after overload.

4. Fractographic observations and FE modelling results suggest that PICC may be the predominant closure mechanism over RICC in controlling post-overload retardation effect in the studied materials for the conditions tested. This may be particularly linked to the proposed dependency of RICC effects on the ratio of fracture surface asperity sizes to plastic zone size. The intrinsically larger plastic zone sizes associated with overloads are seen to then limit RICC contributions to overload behaviour, except for relatively low baseline stress intensities, or materials with more extreme surface features than the present 2024-related alloys.

References

[1] K.D. Singh, *Modelling of combined roughness and plasticity induced closure effects in high strength Al-alloys*. PhD Thesis, University of Southampton. 2004.

[2] D.M. Corlby and P.F. Packman, *Engineering Fracture Mechanics*, 1973. **5**: p. 479-497.

[3] C.M. Ward-Close and R.O. Ritchie, *Mechanics of Fatigue Crack Closure, ASTM STP 982*, 1988, Philadelphia: ASTM, p. 93-111.

[4] K.T. Venkateshwara Rao and R.O. Ritchie, *Acta Metallurgica*, 1988. **36**: p. 2849-2862.

[5] E.F.J. Von Euw, R.W. Hertzberg, and R. Roberts, *Stress Analysis and Growth of Cracks, ASTM STP 513*, 1972, Philadelphia: ASTM, p. 230-259.

[6] K.T.V. Rao and R.O. Ritchie, *Acta Metallurgica*, 1988. **36**: p. 2849-2862.

[7] M. Skorupa, *Fatigue & Fracture of Engineering Materials & Structures*, 1998. **21**(8): p. 987-1006.

[8] K.T. Venkateshwara Rao and R.O. Ritchie, *International Materials Reviews*, 1992. **37**: p. 153-185.

[9] S. Suresh, *Engineering Fracture Mechanics*, 1983. **18**: p. 577-593.

[10] S. Suresh, *Scripta Materialia*, 1982. **16**(8): p. 995-999.

[11] S. Suresh, G.F. Zamiski, and R.O. Ritchie, *Metallurgical Transactions*, 1981. **12A**: p. 1435-1443.

[12] Y. Xu, *Closure assessment and overload transient behaviour in damage tolerant airframe materials*. Ph.D thesis, University of Southampton. 2001.

[13] E.P. Phillips, *NASA Technical Memorandum 101601*. 1989, Hampton, Virginia: Langley Research Centre.

[14] P.C. Paris and L. Hermann, *Fatigue Thresholds*, ed. J. Backlund. 1981, Wareley, UK: EMAS Publications, p. 11.

[15] R.J. Bucci, A.B. Thakker, T.H. Sanders, R.R. Sawtell, and J.T. Staley, *Effect of Load Spectrum Variables on Fatigue Crack Initiation and Propagation, ASTM STP 714*, eds. D.E. Bryan and J.H. Potter. 1980, Philadelphia: ASTM, p. 41-78.

[16] R.A. Collins, *Private communication, Fatigue Methods Group - Airbus (UK)*, 1998.

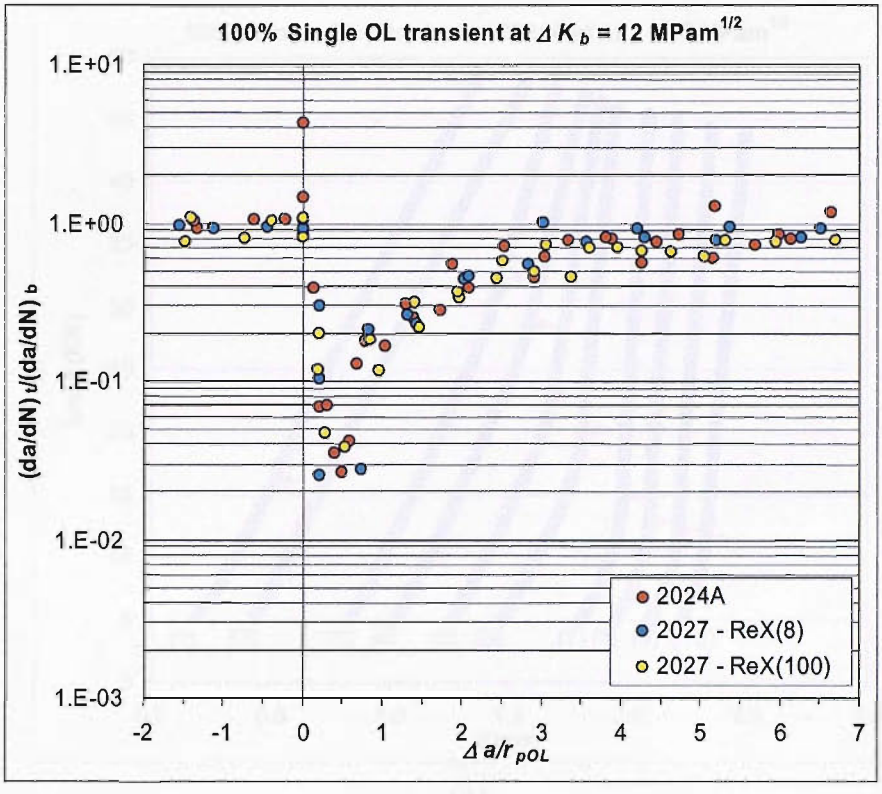

Figure 6.1 Transient crack growth behaviour of 2024A and 2027 materials after a 100% single overload at ΔK_b = 12 MPa$\sqrt{m}$.

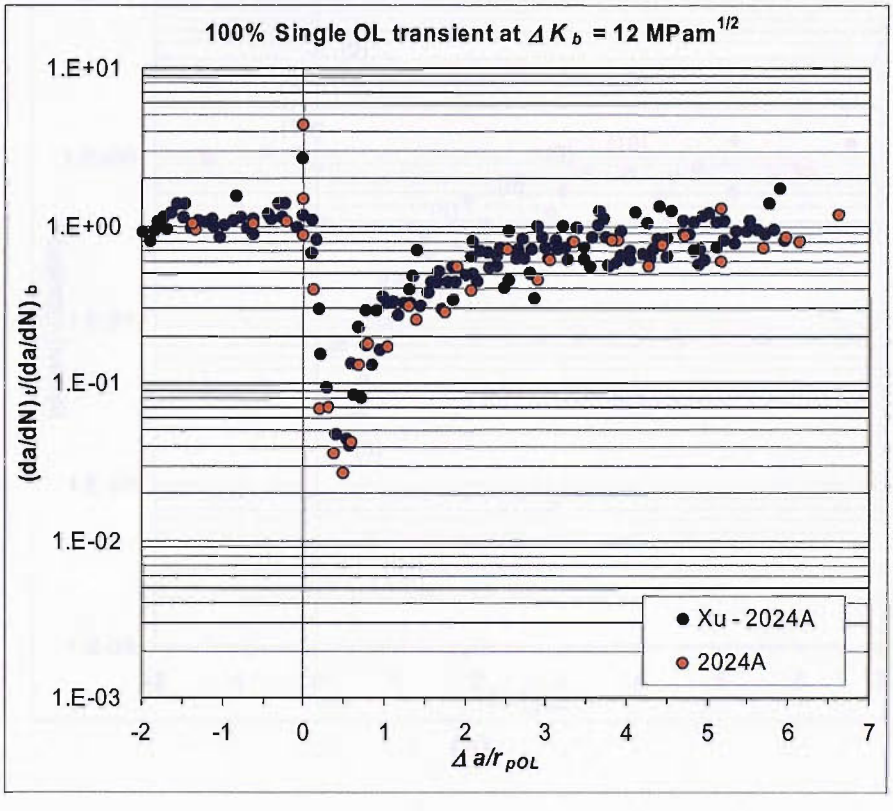

Figure 6.2 Comparison of 2024A materials transient crack growth behaviour with Xu's data at same testing condition.

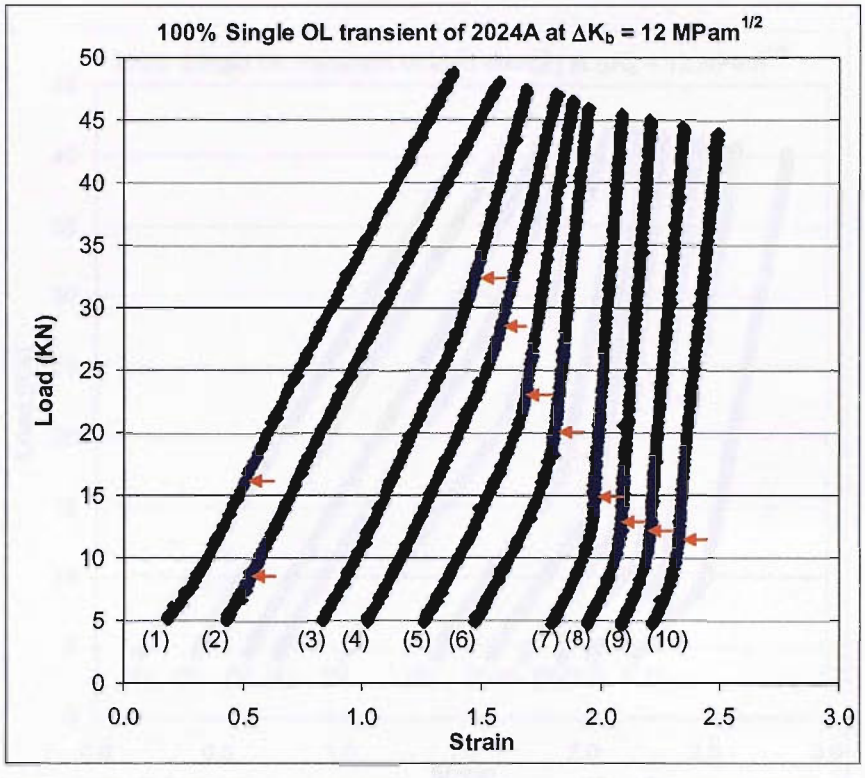

(a)

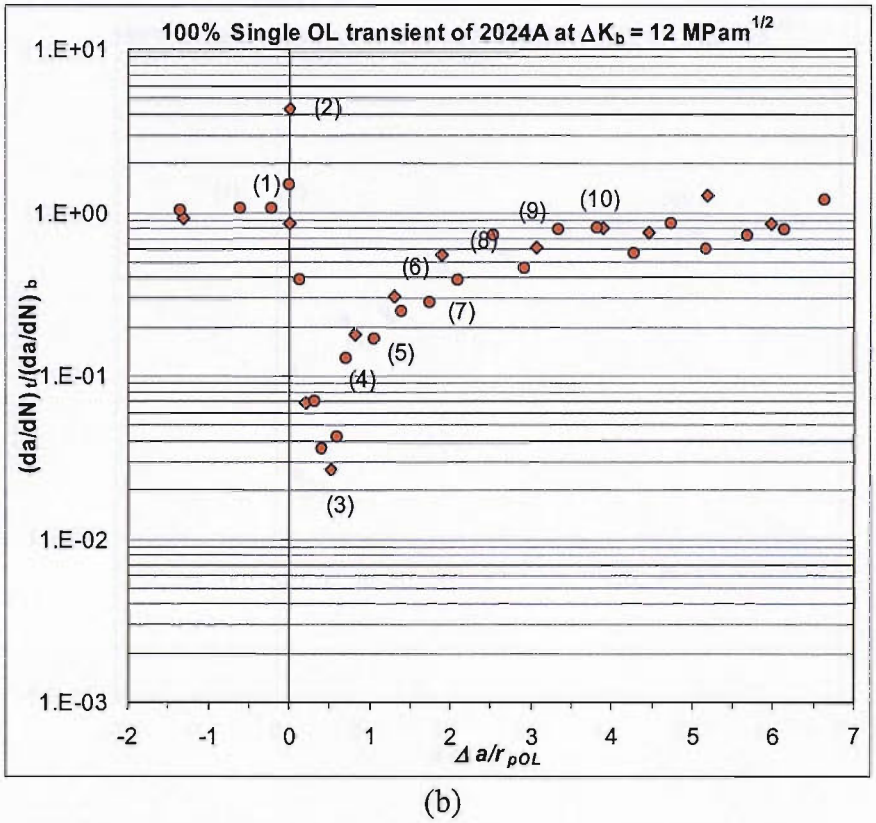

(b)

Figure 6.3 100% single overload of 2024A material at ΔK_b = 12 MPa$\sqrt{m}$. (a) Evolution of near-tip post-overload compliance curves, and (b) corresponding closure measuring positions in the transient crack growth process.

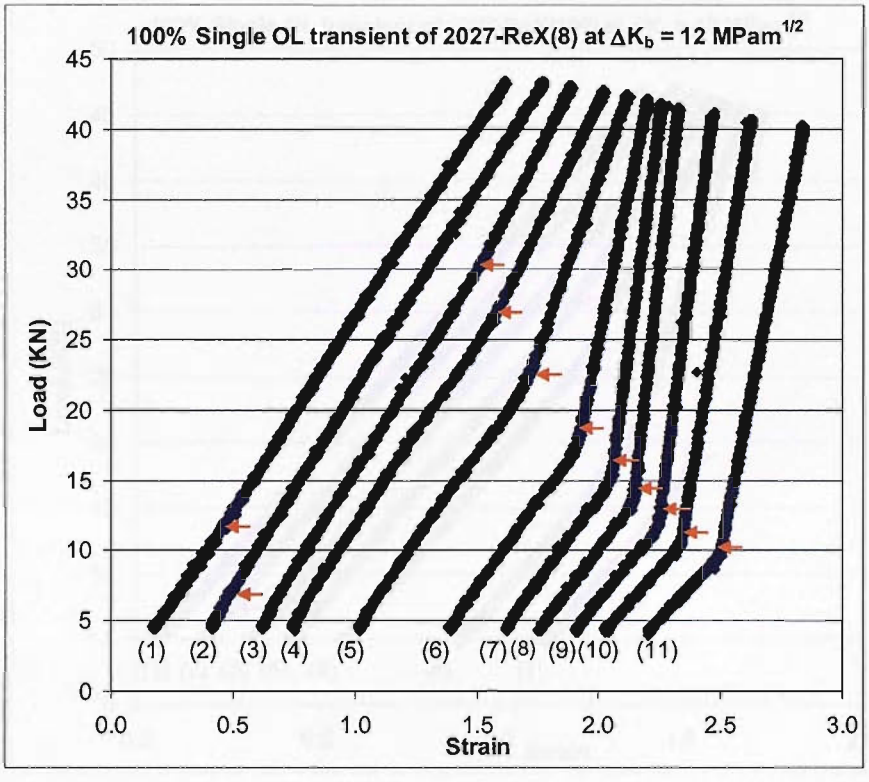

(a)

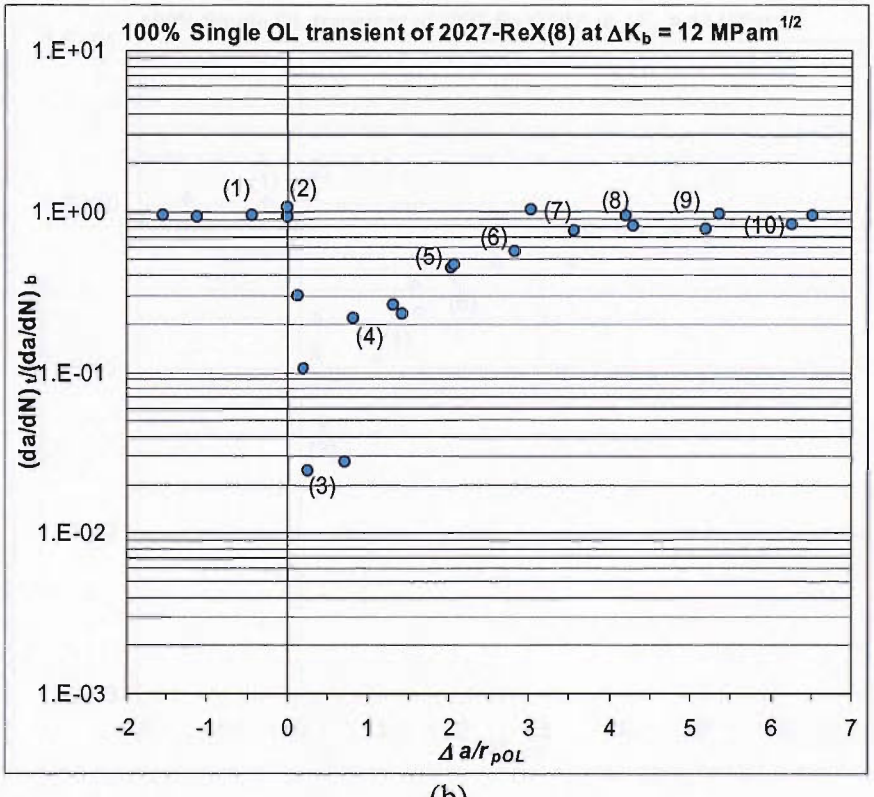

(b)

Figure 6.4 100% single overload of 2027-ReX(8) material at ΔK_b = 12 MPa√m. (a) Evolution of near-tip post-overload compliance curves, and (b) corresponding closure measuring positions in the transient crack growth process.

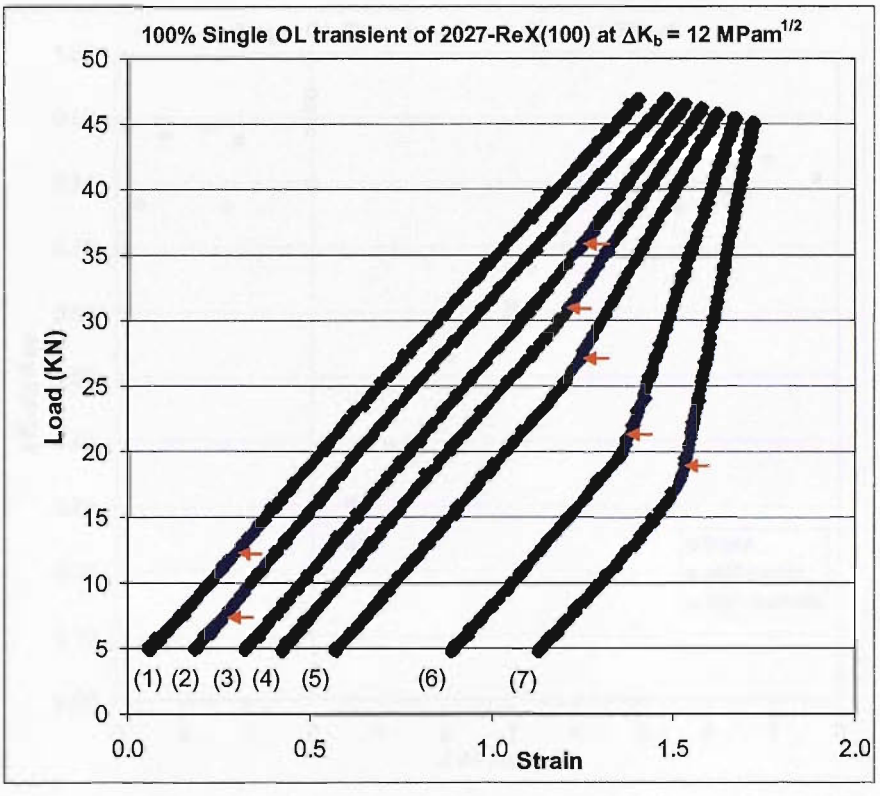

(a)

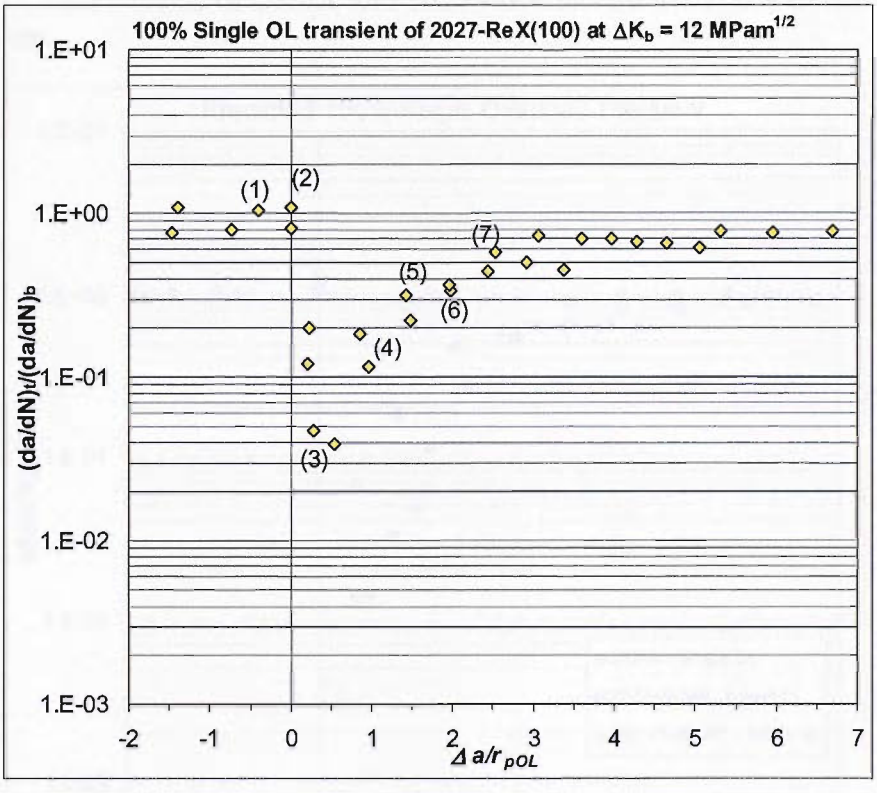

(b)

Figure 6.5 100% single overload of 2027-ReX(100) material at ΔK_b = 12 MPa√m. (a) Evolution of near-tip post-overload compliance curves, and (b) corresponding closure measuring positions in the transient crack growth process.

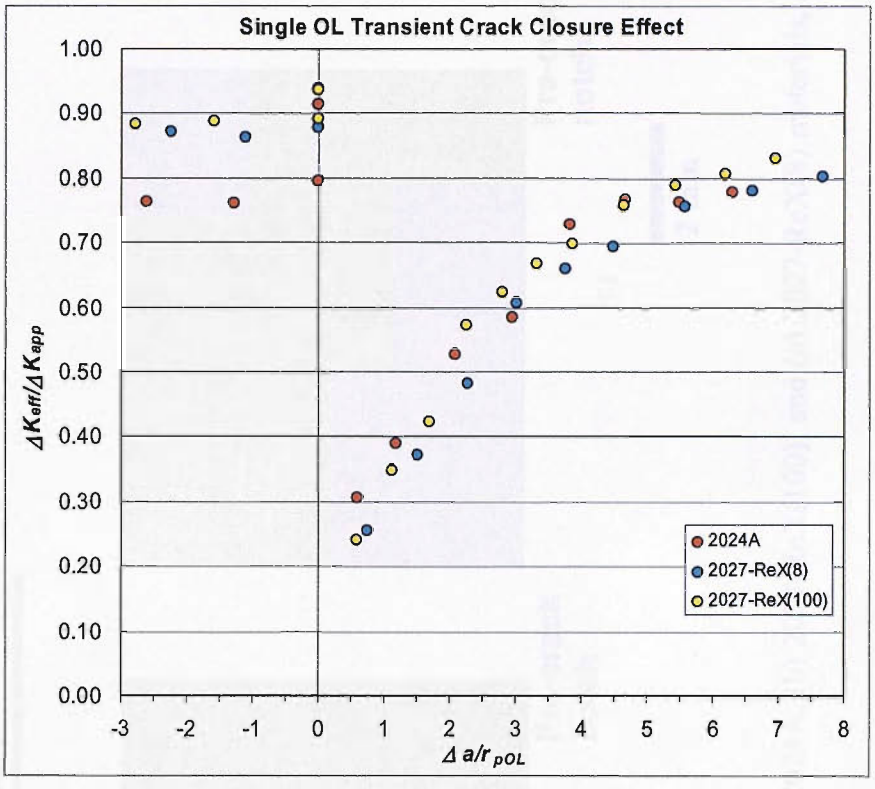

Figure 6.6 Closure levels of 2024A and 2027 materials after a 100% overload at ΔK_b = 12 MPa$\sqrt{m}$.

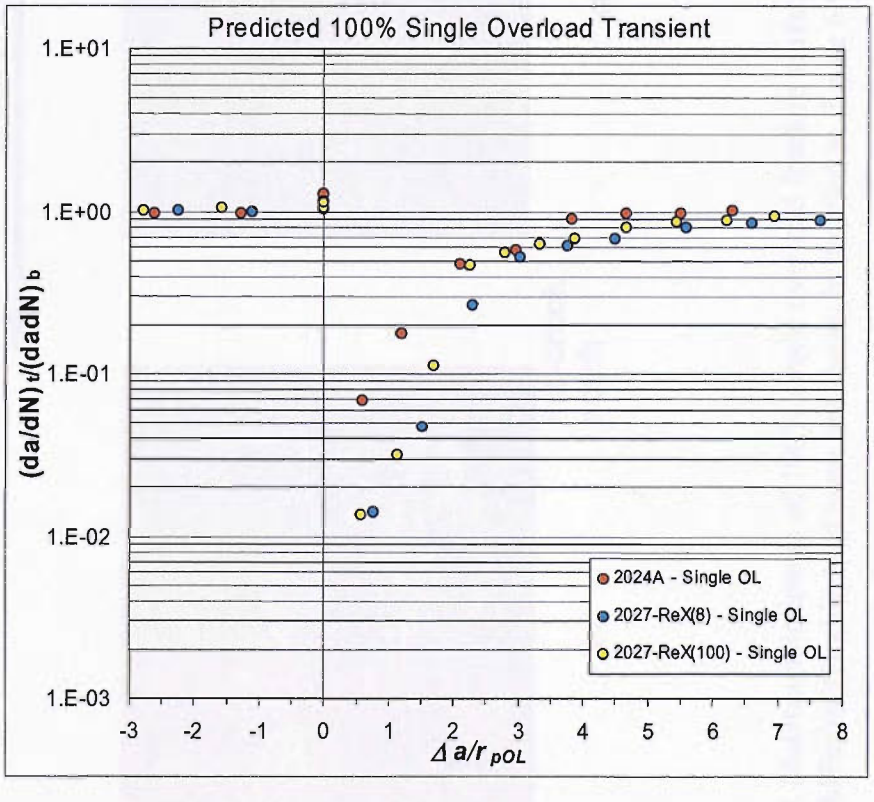

Figure 6.7 Transient crack growth of 2024A and 2027 materials *predicted* with closure results measured after a 100% overload at ΔK_b = 12 MPa$\sqrt{m}$.

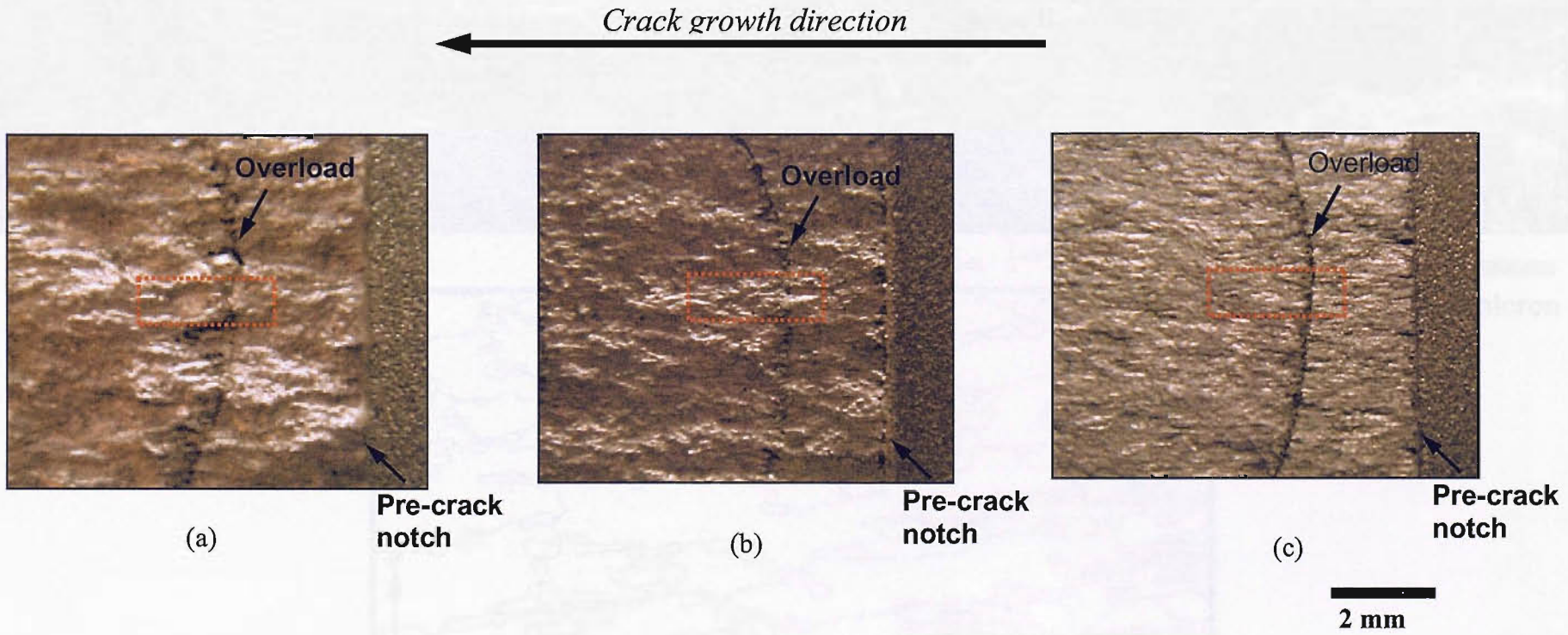

Figure 6.8 Macroscopic image of 100% single overload fracture surfaces of (a) 2024A, (b) 2027-ReX(100), and (c) 2027-ReX(8) materials, at ΔK_b = 12 MPa$\sqrt{m}$. (Highlighted areas are shown in detailed in Figure 6.9 – 6.14)

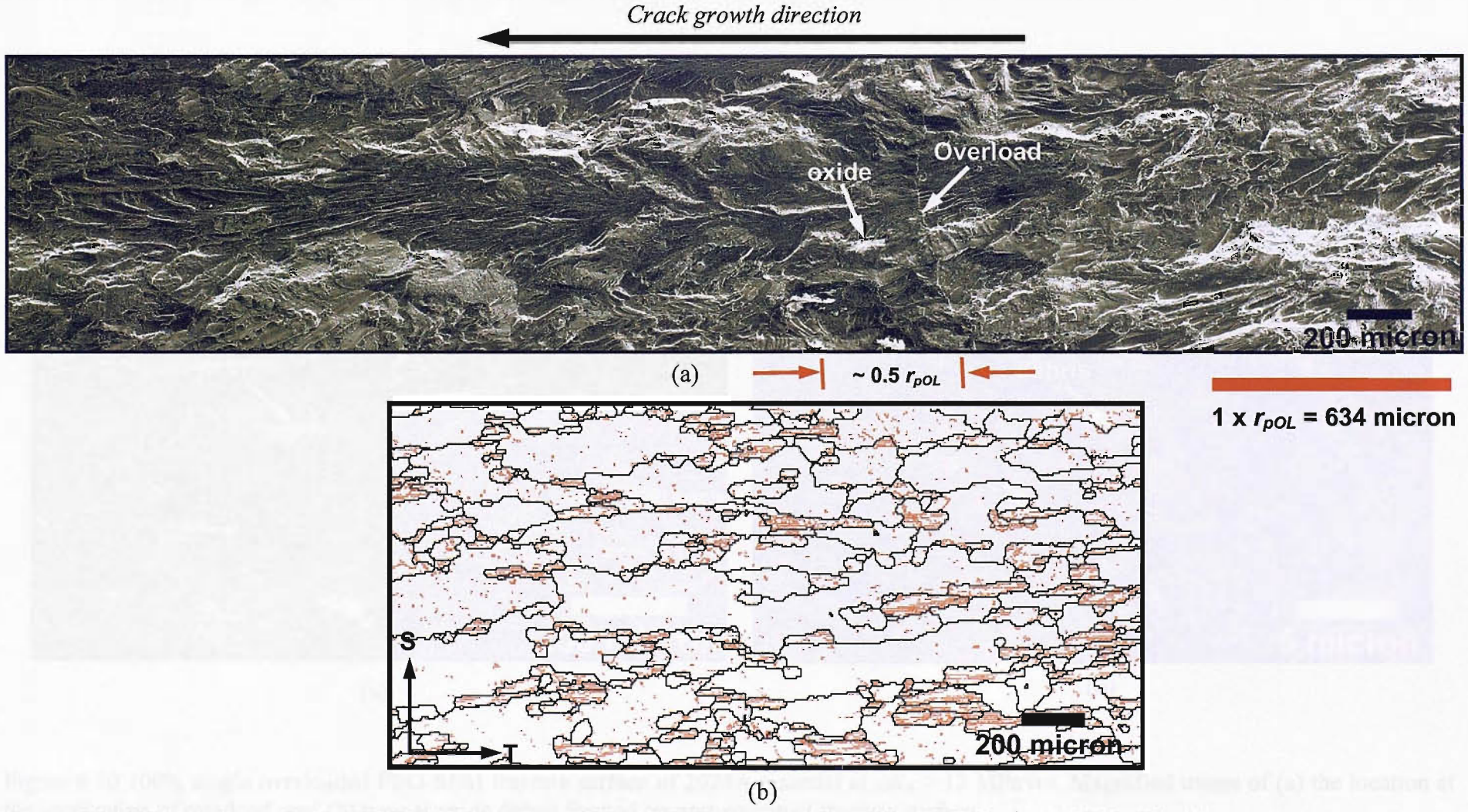

Figure 6.9 100% single overloaded FEG-SEM fracture surface of 2024A material at ΔK_b = 12 MPa√m. (a) Magnified image of highlighted area in Figure 6.8(a). (b) EBSD grains map which has been scaled to the same scale as (a) at the same plane as the fracture surface (S-T), black line is defined as high angle grain boundary with angle > 12°, while red line represents low angle grain boundary with angle between 2° and 12°. (**Note**: Red bar represents the size of ~ 1x r_{pOL} = 634 micron)

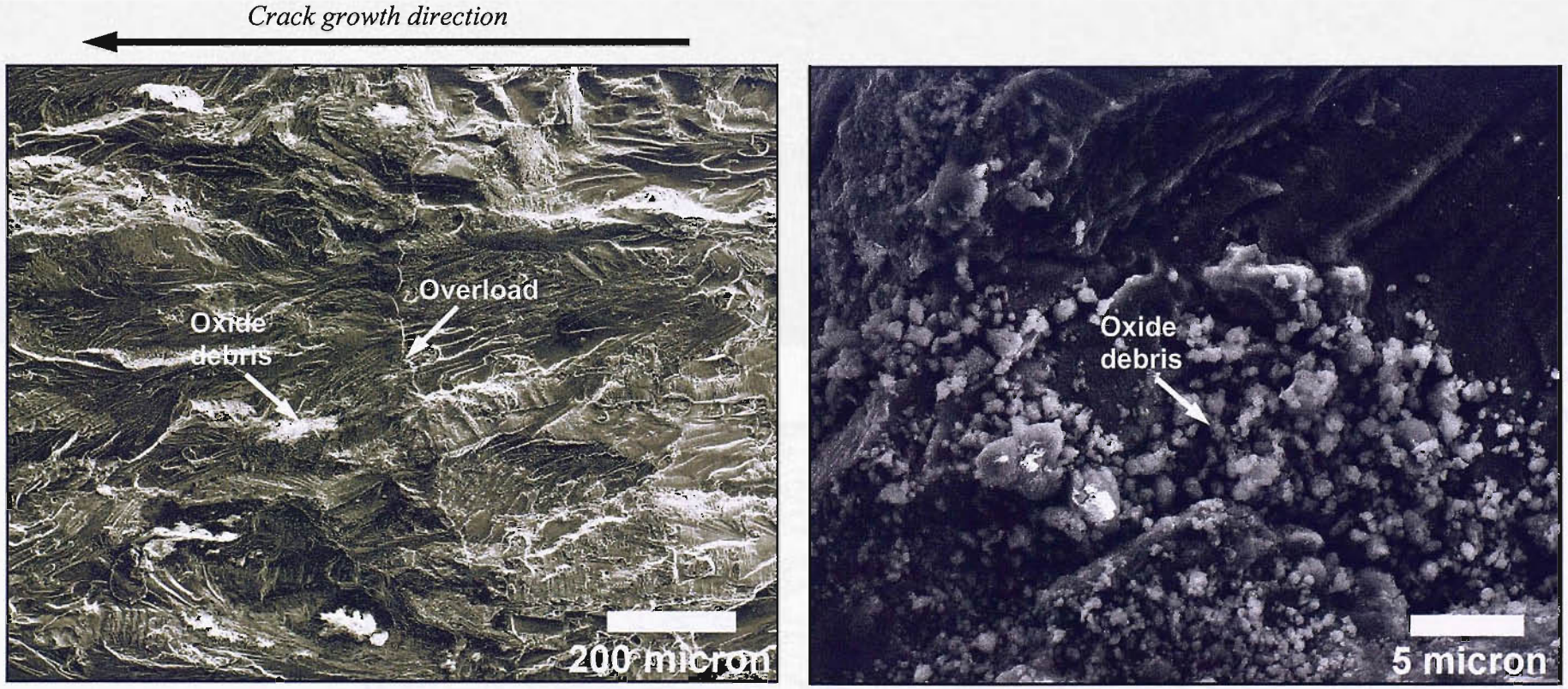

(a) (b)

Figure 6.10 100% single overloaded FEG-SEM fracture surface of 2024A material at ΔK_b = 12 MPa√m. Magnified image of (a) the location at the application of overload, and (b) typical oxide debris formed on post-overload fracture surface.

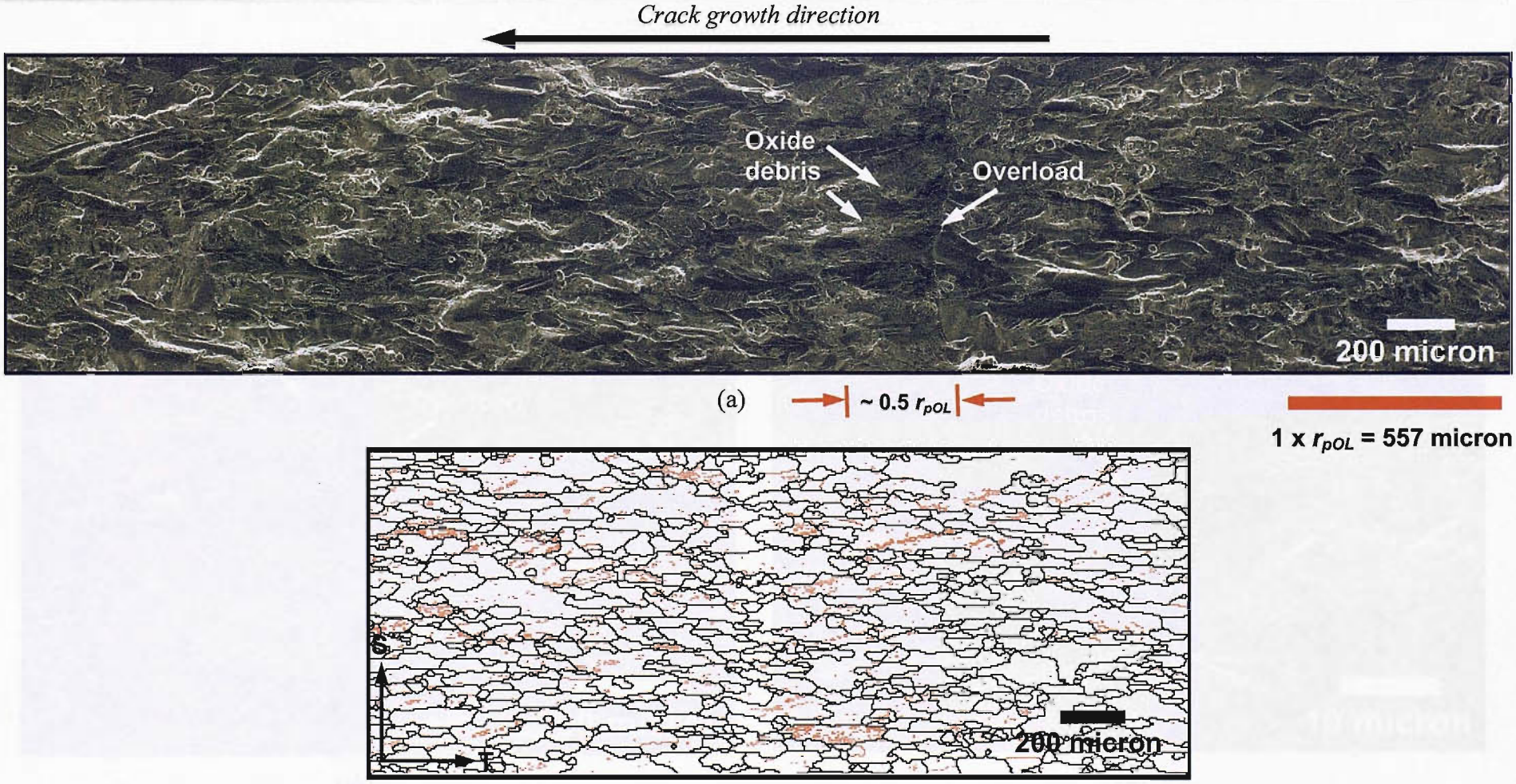

Figure 6.11 100% single overloaded FEG-SEM fracture surface of 2027-ReX(100) material at ΔK_b = 12 MPa$\sqrt{m}$. (a) Magnified image of highlighted area in Figure 6.8(b). (b) EBSD grains map which has been scaled to the same scale as (a) at the same plane as the fracture surface (S-T), black line is defined as high angle grain boundary with angle > 12°, while red line represents low angle grain boundary with angle between 2° and 12°. (**Note**: Red bar represents the size of ~ 1x r_{pOL} = 557 micron)

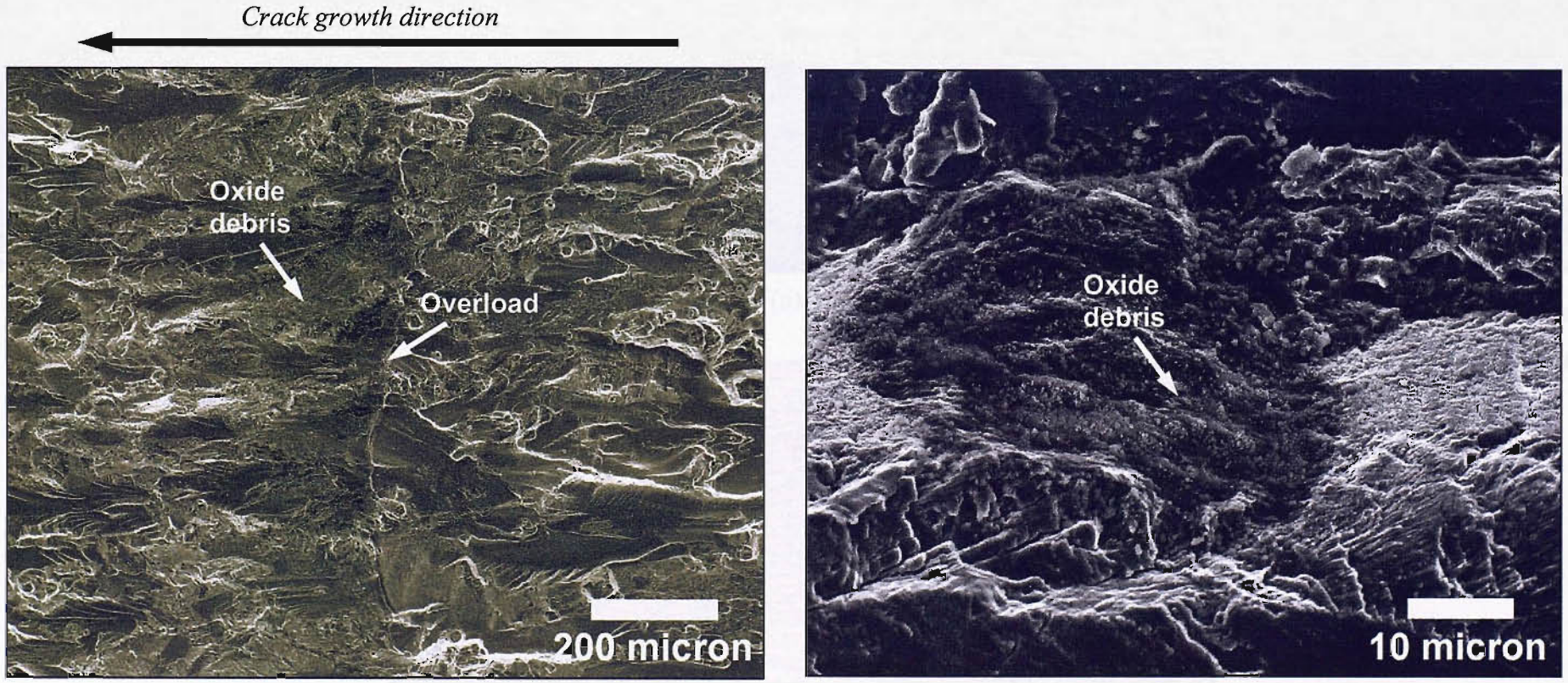

(a) (b)

Figure 6.12 100% single overloaded FEG-SEM fracture surface of 2027-ReX(100) material at ΔK_b = 12 MPa$\sqrt{m}$. Magnified image of (a) the location at the application of overload, and (b) typical oxide debris formed on post-overload fracture surface.

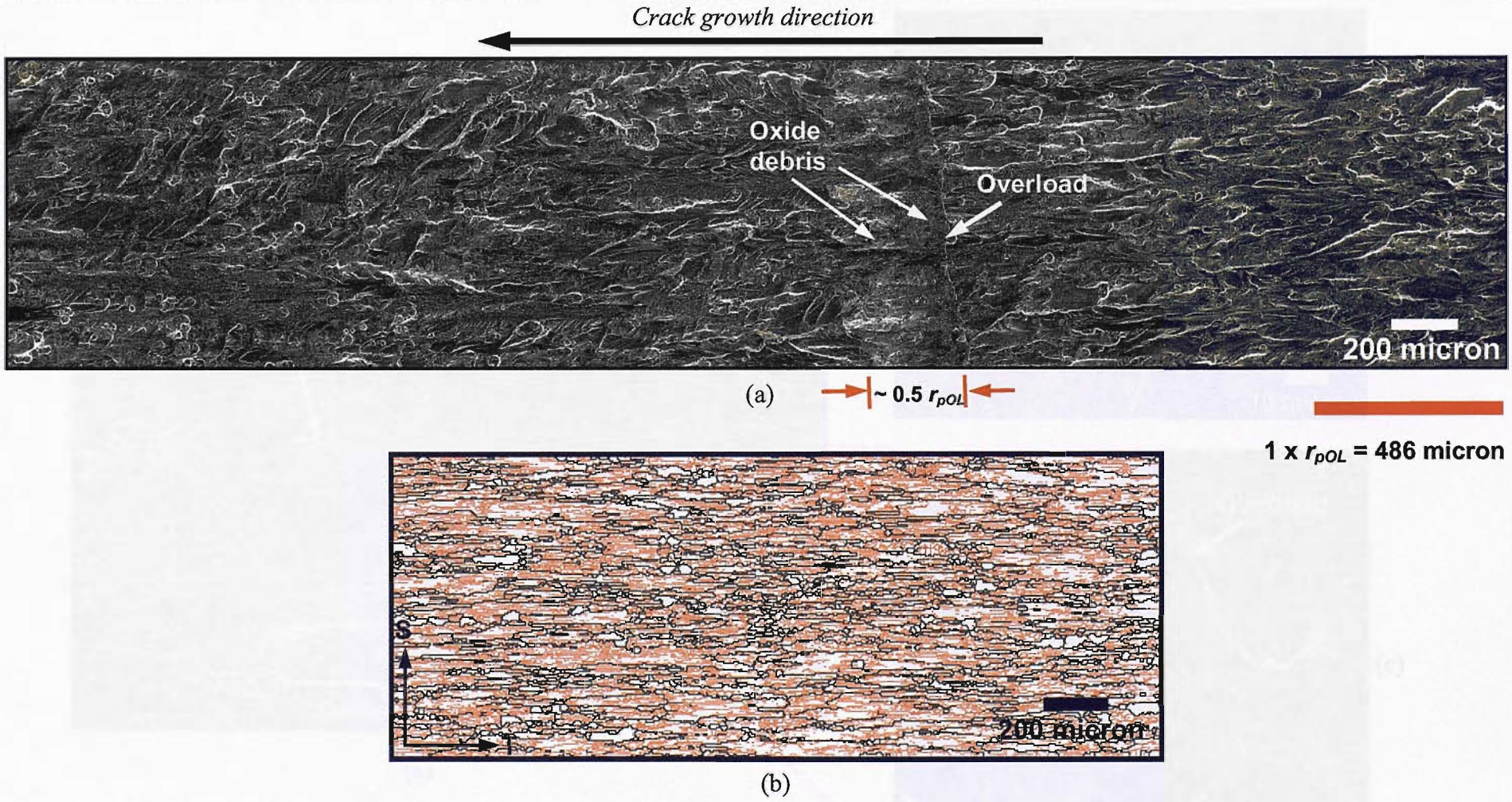

Figure 6.13 100% single overloaded FEG-SEM fracture surface of 2027-ReX(8) material at ΔK_b = 12 MPa√m. (a) Magnified image of highlighted area in Figure 6.8(b). (b) EBSD grains map which has been scaled to the same scale as (a) at the same plane as the fracture surface (S-T), black line is defined as high angle grain boundary with angle > 12°, while red line represents low angle grain boundary with angle between 2° and 12°. (**Note**: Red bar represents the size of ~ 1x r_{pOL} = 486 micron)

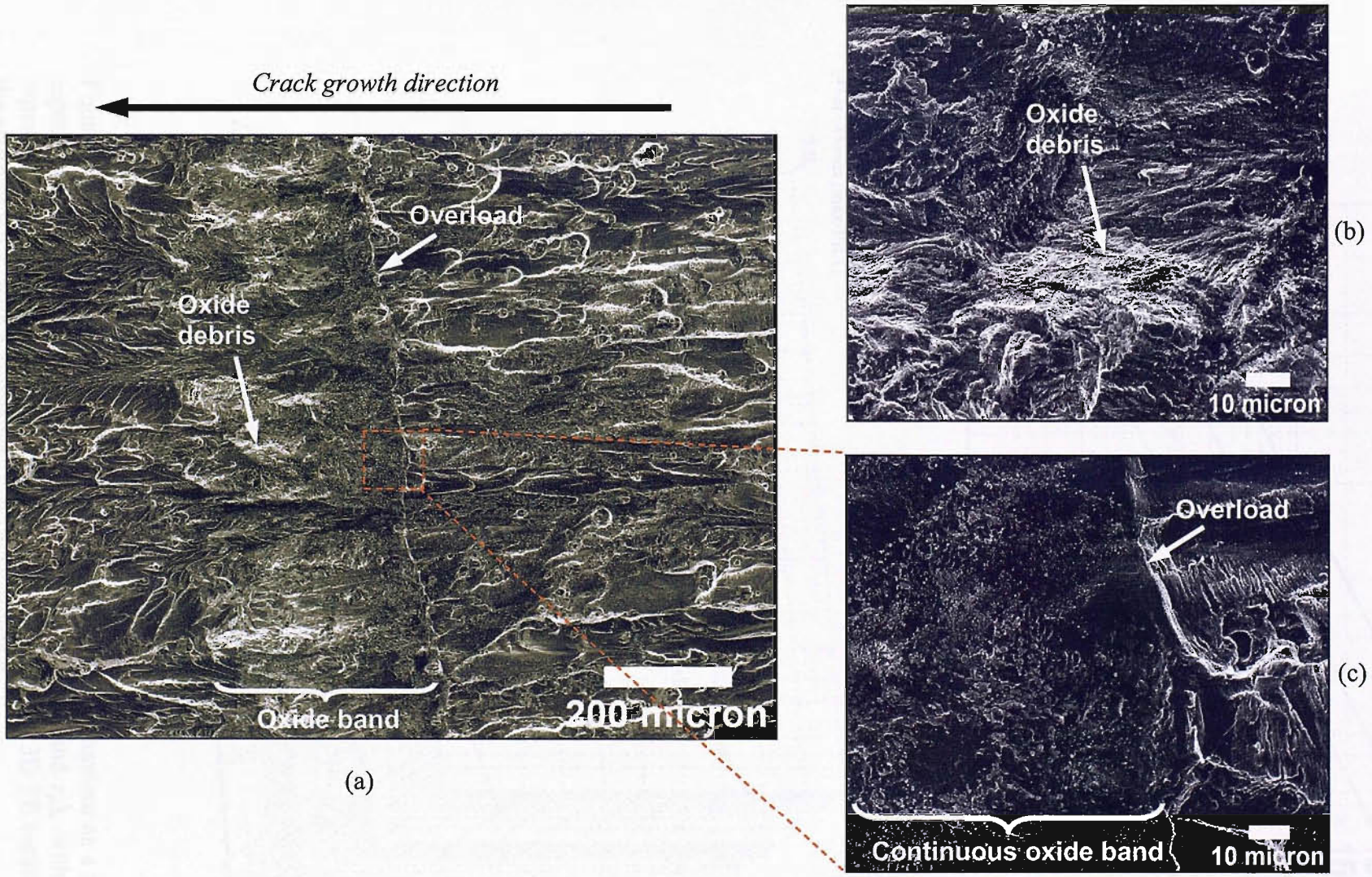

Figure 6.14 100% single overloaded FEG-SEM fracture surface of 2027-ReX(8) material at ΔK_b = 12 MPa√m. Magnified image of (a) the location at the application of overload, (b) typical oxide debris formed on post-overload fracture surface, and (c) distinct continuous oxide band formed at 'flat' area after overload.

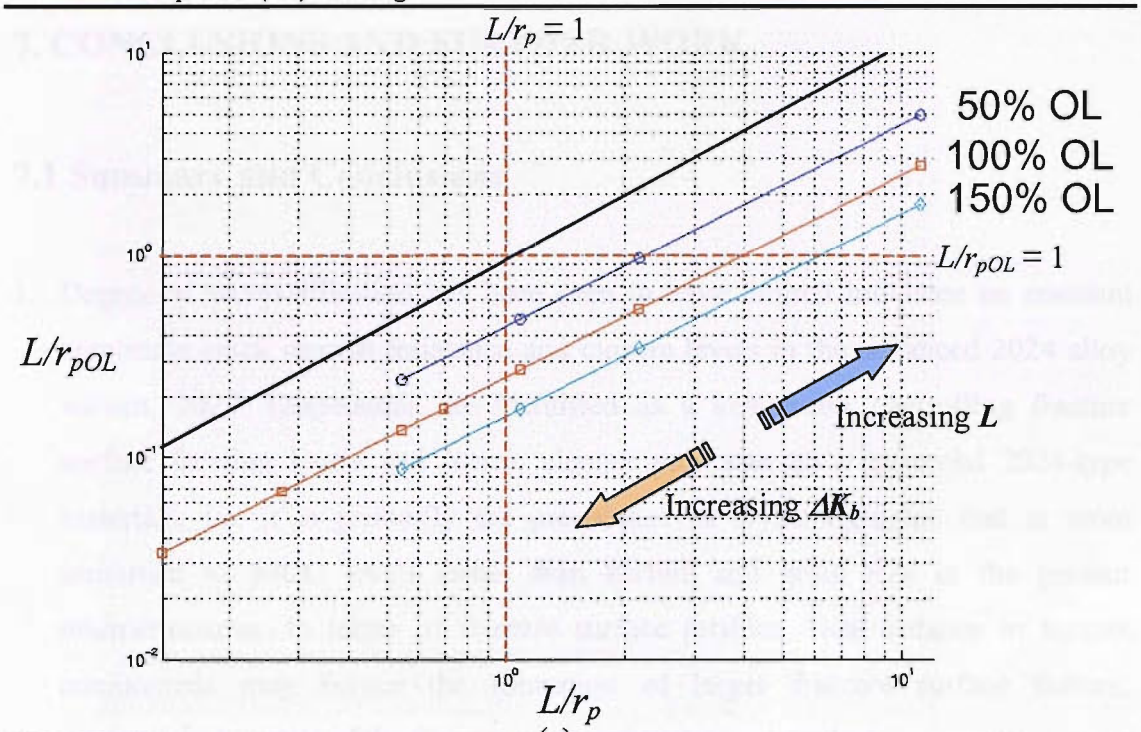

(a)

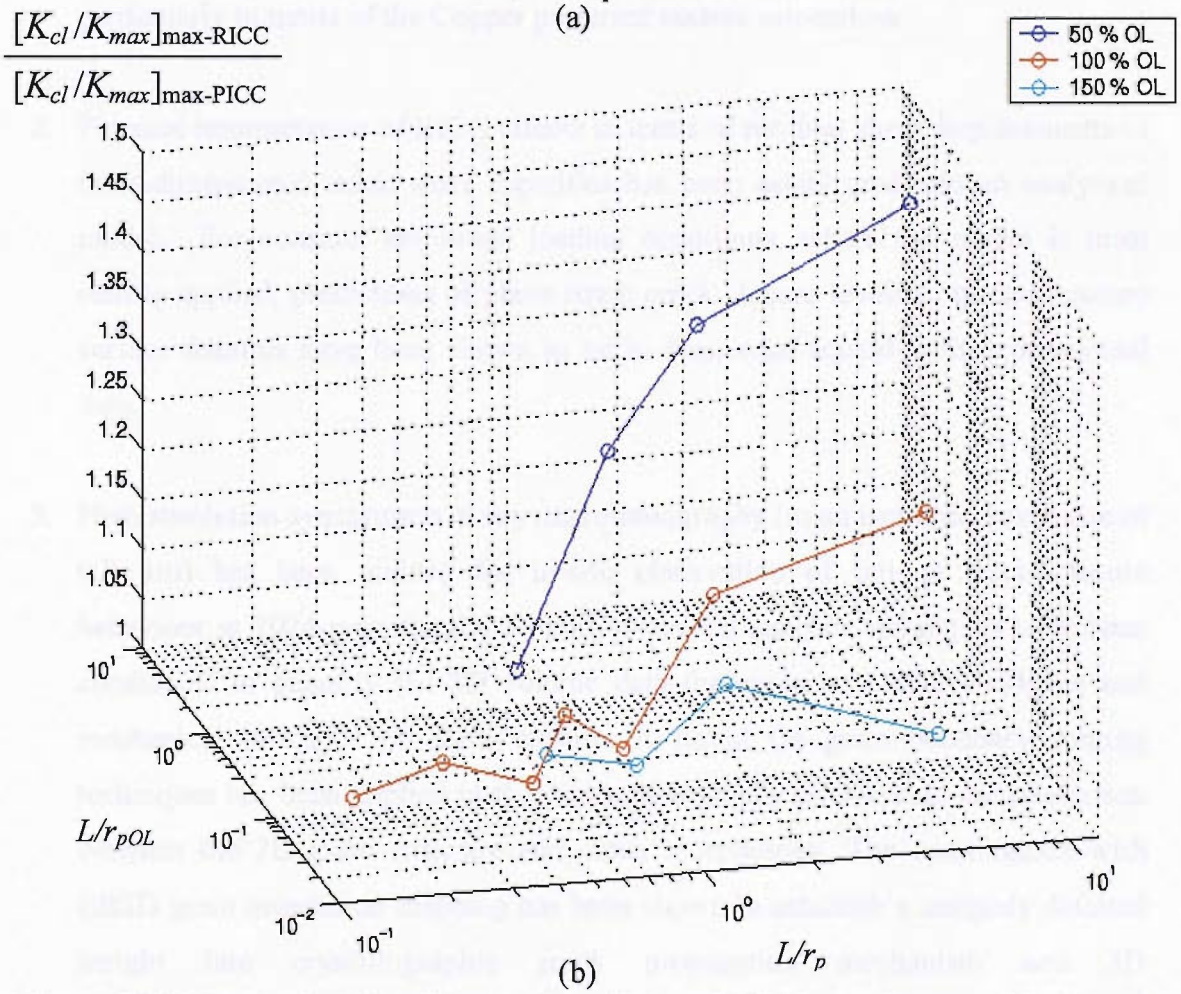

(b)

Figure 6.15 Overload and baseline loading effect on RICC behaviour as a function of asperities deflection size (L) and plastic zone sizes (r_{pOL} and r_p), with (a) a 2D representation of the FE results in terms of L and r_p, and (b) 3D FE results showing the effect of RICC with a normalised ratio closure effect.

7. CONCLUSIONS AND FURTHER WORK

7.1 Summary and Conclusions

1. Degree of recrystallisation has been seen to have limited influence on constant amplitude crack growth resistance and closure levels in the advanced 2024 alloy variant, 2027. Dispersoids are identified as a key factor controlling fracture surface faceting levels and hence, closure processes in commercial 2024-type materials, i.e. it is primarily the prevalence of crystallographic that is more important to RICC levels rather than texture and grain size in the present microstructures. In terms of fracture surface profiles, local balance in texture components may favour the formation of larger fracture surface feature, particularly in terms of the Copper preferred texture orientation.

2. Physical interpretation of RICC effects in terms of residual shear displacements in three-dimensional crack wake asperities has been established into an analytical model. For constant amplitude loading conditions, where the model is most readily applied, predictions of plane strain crack closure levels from real fracture surface features have been shown to be in functional accord with experimental data.

3. High resolution synchrotron X-ray microtomography (to an isotropic voxel size of 0.7 μm) has been utilized for in-situ observation of fatigue crack closure behaviour in 2024-type aluminium alloys. Several analysis techniques have been considered to quantify the 3D volume data for evidence of the incidence and mechanical influence of crack closure. A liquid Ga grain boundary wetting techniques has been applied in the X-ray tomography to illustrate the interaction between the 3D grain structure and crack morphology. The combination with EBSD grain orientation mapping has been shown to establish a uniquely detailed insight into crystallographic crack propagation mechanism and 3D micromechanical crack behaviour.

4. Post-overload crack growth behaviour of 2024A and 2027 materials (corresponding to low and high dispersoid alloys respectively) under single peak overloads has been studied. The alloys show essentially similar behaviour under the current studied conditions. Post-overload closure measurements appear to describe overload transient crack growth well. Crack growth mode transitions with classical activation of near-threshold mechanisms are observed in post-overload crack growth. Post-overload maximum retardation distances agree well with the observed width of clear oxide marking on fracture surfaces after overload.

5. Crack growth measurements, closure measurements, fractographic observations and FE modelling results are consistent with PICC being the predominant closure mechanism over RICC in controlling post-overload retardation effect in the studied materials and the conditions tested. This may be particularly linked to the proposed dependency of RICC effects on the ratio of fracture surface asperity sizes to plastic zone size. The intrinsically larger plastic zone sizes associated with overloads is then suggested to limit RICC contributions to overload behaviour, except for relatively low baseline stress intensities, or materials with more extreme surface features than the present 2024-related alloys.

7.2 Further Work

7.2.1 Modelling

Whilst the proposed physical interpretation of RICC effects in terms of residual shear displacements at three-dimensional crack wake asperities has been shown to provide a reasonable micromechanical description of plane strain crack closure phenomenon under constant amplitude loading conditions, it should be acknowledged that the proposed method to extract geometrical parameters from the fracture surfaces does not take into account complex surface topography concepts and the parameters obtained are not 'exact' representations of crack deflection angles and lengths, they are nevertheless a measure of fracture surface roughness levels directly related to the micromechanical origins of the present RICC modelling framework. Hence, further work in exploring the extraction of fracture surface parameters is valuable to refine the current model. Extension of the present RICC modelling and experimental validation effort over wider ranges of fracture surface scale and relative plastic zone size would also be of value in extending the present understanding of crack closure processes and the corresponding potential for microstructural control of material performance. On the other hand, a parallel high-computational-cost 3D FE modelling of rough fracture surfaces may be considered. Ultimately, even more computationally expensive 3D FE modelling of 'real' cracks imaged by the X-ray tomography could provide extremely exciting correlation of experimental and modelling effort.

7.2.2 Variable Amplitude Loading

Within the time frame of the present work, post-overload crack growth behaviour of the materials has only been studied under one load condition (i.e. 100% single overload at ΔK_b = 12MPa$\sqrt{m}$). Considering more loading conditions (i.e. different overload ratio, stress state and ΔK_b) would be of value to explore the validity of the current micro-mechanical interpretations. An alternative material with high fracture surface roughness (such as a highly textured Al-Li alloy) could be particularly ideal for validation of RICC and PICC influence regimes.

Practical engineering structural parts are often subjected to a wide spectrum of stresses over their lifetime, the current simple single peak overloading experiment is

somewhat insufficient to give detailed information of 'real' materials performance and fatigue lifting process. As such, additional consideration of phenomena such as multiple overload interaction, under-loads, block loading *etc.* should of course be examined.

7.2.3 X-Ray Tomography

The practicability of the application of high resolution synchrotron X-ray tomography to current study has been shown to be a successful technique. However, there are several problem which have limited the detailed interpretation of the data generated. As such the following may be considered:

1. 2024-type materials were shown to be non-ideal to investigate: the existence of large fractions of crack bifurcation (up to ~ 60% crack bifurcation in the samples imaged) and irregular crack fronts make the analysis process problematic and variable. Whilst the overlapping of crack volume caused by crack bifurcation limits the potential for COD measurement by ray casting, the absence of appreciate number of spherical micro-pores in the 2027 materials prohibited the use of microstructural displacement gauging technique to map CODs. Due to these problems, a more model material may be applied in future studies. An ultra fine grained material (grain size < 1 μm) which can produce a simple straight crack may be considered in the first instance in the assessment of PICC effects (e.g. during overloads). Materials with regular, intermediate scaled fracture surface roughness may also be valuable to examine the discern RICC effects (e.g. a moderate grain size Al-Li alloy).

2. Whilst relatively high imaging resolution have been achieved in the present work, further improvements would be valuable given the scales of crack opening and microstructures that may effect crack growth. Limitations of samples size must also be considered in parallel to ensure mechanical consistency with the phenomenon to be investigated.

3. Whilst tomography may be informative of the micromechanisms of materials failure, especially when used in conjunction with *in-situ* loading, the potential

to synthesise tomography measurement with high resolution lattice strain mapping and grain tracking in the synchrotron clearly represents an unprecedented level of failure microanalysis that may provide unique, direct information on a variety of fatigue and fracture processes. Such 'data rich' *in-situ* studies, in conjunction with detailed parallel modelling exercises may provide a fundamental step forward in materials mechanics, as physical understanding becomes less reliant on techniques such as *post-mortem* fractography, indirect signal measurements (e.g. acoustic emission), surface crack observation *etc.*.

APPENDIX A: MATERIALS CHARACTERISTICS AND FRACTURE MECHANICS

A.1 Material Characteristics

Commercial aluminium alloys are commonly considered in two classes: specifically wrought and cast products. Wrought alloys may be further subdivided into heat-treatable or non-heat-treatable materials, depending on whether or not they respond to precipitation hardening. Heat-treatable aluminium alloys then fall into three main groups: 2xxx-series (Al-Cu based), 6xxx-series (Al-Mg-Si based) and 7xxx-series (Al-Zn based). They contain appreciable amounts of the major alloying elements that are soluble at elevated temperatures; specifically copper, magnesium, silicon and zinc, in various combinations. 2xxx series alloys are commonly used in aircraft construction for damage-tolerant applications, such as lower wing skins, due to their good crack growth resistance, whereas 7xxx series alloys are commonly used in strength limited applications such as upper wing skins.

A.1.1 Heat-Treatable Aluminium Alloys

The medium to high strength aluminium alloys used for modern airframe construction almost exclusively rely upon precipitation hardening to achieve the required structural performance levels. As such, a proper understanding of precipitation hardened microstructure is required to understand their mechanical behaviour.

A.1.1.1 Precipitation Hardening (Age Hardening)

The strength of heat-treatable aluminium alloys is enhanced by appropriate heat treatments to form fine, dispersed precipitates of second phases within the parent matrix phase. Such heat treatment conventionally involves the following three stages:

i. Solution heat treatment:

   To obtain a complete solution by dissolving the alloying elements at a temperature within the single-phase region for the alloy concerned. Unnecessarily high temperatures and excessively long solutions times are to be avoided to prevent liquation (incipient melting) and the growth of coarse, recrystallised grains.

ii. Quenching:

Rapid cooling, commonly to room temperature, to obtain a supersaturated solid solution of the alloying elements and vacancies. Sufficient cooling rates are needed to avoid precipitation in the intermediate temperature range that may limit the response of the alloy to subsequent ageing.

iii. Ageing:

Controlled decomposition of the supersaturated solid solution to form a finely dispersed precipitate by ageing at room temperature (natural ageing), or intermediate temperatures (typically 100 – 200 °C), where this process is known as artificial ageing.

In certain alloys, additional strength can be obtained by imposing controlled amounts of cold work after quenching, particularly due to interactions between specific precipitation processes and enhanced dislocation densities [1].

Generally, three types of precipitates can be produced in aircraft aluminium alloys during the ageing treatment. They are; Zones, intermediate meta-stable precipitates, and equilibrium precipitates. Zones are traditionally identified as ordered, solute-rich clusters of atoms that may be only one or two lattice planes in thickness. They may be coherent and finely dispersed within the matrix with densities as high as 10^{17} to 10^{18} cm^{-3} [2]. The zones produce appreciable elastic strains and lattice distortion, both within the zones and extending into the matrix. The degree of disturbance to the regularity and periodicity of the lattice increases as the density or number of zones increases. Critical vacancy concentrations in the lattice are required for the nucleation of the zones, as influenced by the solution temperature and quenching rate [3, 4]. Recent studies via three dimensional atom probe methods (3DAP) reveal the complexity of the atom clustering process that may actually occur in commercial Al-Cu-Mg type materials [5] as discusses further in Section A.1.2.1.

Intermediate precipitates are typically semi-coherent with the parent matrix and may nucleate from prior structures such as zones, but may also nucleate heterogeneously at lattice defects such as dislocations and subgrain boundaries [1]: as such, intermediate

precipitates may particularly interact with cold working of a material, with improved mechanical properties in Al-Cu-Mg alloys containing S'/ S phase (Al_2CuMg), for example, being attributable to enhanced heterogeneous nucleation after cold work. Such precipitates may be identified with a definite composition and crystal structure which may only slightly differ from the equilibrium precipitate, particularly in relation to the S' and S phases. Equilibrium precipitates may be formed by transformation of intermediate precipitates, but are also commonly formed heterogeneously on high energy interfaces such as grain boundaries. Equilibrium precipitates are typically coarsely dispersed (contributing little strength), and are incoherent with the matrix.

A.1.1.2 Precipitate-free-zones

As in most age hardening systems, it is not uncommon to find precipitate-free-zones (PFZ) in high strength aluminium alloys, which are typically observed adjacent to gain boundaries. The PFZ may be caused by two phenomena: firstly, by depletion of solute to the boundary to form large equilibrium precipitates. Secondly, by depletion of vacancies (prior to ageing) to levels below those needed to assist with the nucleation of precipitates at a given ageing temperature. PFZs often have deleterious effects on the properties of aluminium alloys, where they form a softer, strain localising region in the material, i.e. the PFZs are relatively weak with respect to the age-hardened matrix and may deform preferentially leading to stress and strain concentrations (for example at grain triple points) which, in turn, may cause premature cracking [6]. Both types of PFZs may be minimised by lowering ageing temperatures [7], increasing the solute supersaturation and decreasing diffusion rates (which limits the nucleation and growth of the equilibrium precipitates).

A.1.1.3 Coarse Intermetallic Compounds and Dispersoids

In addition to the finely dispersed precipitates formed during age-hardening, coarse intermetallic compounds and dispersoids represent the other key second phase species exhibiting a strong influence on alloy performance.

Coarse intermetallic compounds are also commonly referred to as constituent particles: they form interdendritically by eutectic decomposition during ingot solidification. Generally they are classified into two major groups; soluble and insoluble constituents. Insoluble constituents normally contain impurity elements such as silicon and iron, such as $Al_6(Fe,Mn)$, Al_3Fe and Al_7Cu_2Fe. Soluble constituents consist of equilibrium intermetallic compounds of the major alloying elements; examples are Al_2Cu, Al_2CuMg and Mg_2Si. Both types of constituent form lacy networks surrounding the as-cast grains. Preheating or ingot homogenization is then usually carried out to dissolve the soluble constituents. The largest of the remaining particles usually fracture during subsequent fabrication of wrought products, reducing particle sizes to 0.5 - 10 μm, and causes them to become aligned as stringers in the direction of working. Intermetallic compounds have little useful function in high-strength wrought alloys and are tolerated to certain levels due to the costs of their effective 'removal' (particularly by the reduction of impurity concentration levels).

Dispersoids are typically smaller than the coarse intermetallic compounds, with a size range of the order of 50 – 500 nm [8]. They are formed during homogenisation of the ingots by solid state precipitation of compounds containing elements which have modest solubility and which diffuse slowly in solid aluminium, typically Mn, Cr or Zn. Typical phases are $Al_{20}Mn_3Cu_2$, Al_3Zr and $Al_{12}Mn_2Cr$. Dispersoids are introduced with the purpose of retarding recrystallisation and grain growth during processing and heat treatment. The effectiveness of a particular dispersoid in controlling grain structure depends on its size, spacing and coherency. Such small particles are known to retard recrystallisation by pinning grain and subgrain boundary migration (Zener pinning) [7].

A.1.2 Metallurgical Characteristics of 2xxx Series Aluminium Alloys

In the International Alloy Designation System (IADS), 2xxx series aluminium alloys are identified as wrought alloys having copper (Cu) as the main alloying element. The main materials involved in this research project are 2024-T351 type alloys. They are Al-Cu-Mg-Mn materials, where T3xx indicates that the materials are solution heated, cold worked, and naturally aged to a substantially stable condition. The last two digits (Tx51) indicate that the alloys have been stress relieved by stretching. 2024-T351 type alloys are often used in the fabrication of aerospace structures because of the good combination of strength, toughness and fatigue resistance, particularly under spectrum loading conditions. For example, on the Airbus A320, the fuselage skins and stringers, bottom wing skin and stringers, along with wing spars and slate are all fabricated from 2024-T351 type alloys. 2024-T351 is known to exhibit fatigue crack growth rates of the order of one third of those observed in 7xxx series alloys [9]. The nominal chemical composition of 2024-type alloys is listed in Table A.1 below [10].

Alloy	Cu	Mg	Zn	Mn	Cr	Si	Fe	Zr	Al
2024-T351	3.8-4.9	1.2-1.8	<0.25	0.3-0.9	<0.1	<0.5	<0.5	<0.25	Balance

Table A.1 Nominal compositions (wt %) of 2024-type aluminium alloys

A.1.2.1 Solid-State Precipitation Sequences

In simple binary Al-Cu aluminium alloys, the hardening observed during room temperature ageing is attributed to localised concentrations of copper atoms forming (Guinier-Preston) GPI zones. These have been reported to consist of two-dimensional copper rich disks, oriented parallel to {100} matrix planes [11, 12].

At temperatures of 100 °C and above, the GPI zones may disappear and may be replaced by fully coherent intermediate precipitates designated as GPII, which are considered to be three-dimensional and to have an ordered atom arrangement of a few atom layers in thickness. Some author used the term θ'' phase instead of GPII [13, 14]. The intermediate GPII precipitates may transform into another intermediate phase, designated as θ', which has the same composition as the equilibrium precipitates θ,

exhibiting partially coherency with the solid solution lattice. θ' will coexist with GPII over a range of time and temperature. The final stage in the precipitation sequence is the transformation of θ' into incoherent equilibrium phase precipitates θ ($CuAl_2$). The reaction sequence in aluminium-copper alloys may then be written as:

$$\text{Supersaturated solid solution } \alpha \rightarrow \text{GPI} \rightarrow \text{GPII} \rightarrow \theta' \rightarrow \theta\ (CuAl_2) \qquad (A.1)$$

When incoherent θ forms, the alloys are softened far beyond the maximum strength condition [15].

In Al-Cu-Mg alloys, the precipitation sequences maybe modified, dependent on the Cu/Mg ratio. For high Cu/Mg ratio alloys (Cu/Mg > 8), the precipitation sequence may be described as above for binary Al-Cu. For low Cu/Mg ratio alloys (1.5 < Cu/Mg < 4), the precipitation can be identified:

$$\text{Supersaturated solid solution } \alpha \rightarrow \text{GPB} \rightarrow S'\ (Al_2CuMg) \rightarrow S\ (Al_2CuMg) \qquad (A.2)$$

GPB zones are identified as Cu and Mg containing Guinier-Preston-Bagaryatsky zones. For alloys with a Cu/Mg ratio between 4 and 8 both sequences (Equation (A.1) and (A.2)) may occur.

Additions of magnesium to Al-Cu alloys typically accelerate and intensify natural age hardening. This may result from interaction between the solute elements and the vacancies. The GPB zones have been identified as thin rods on the {100} matrix plane [16]. Ageing at elevated temperatures produces the intermediate precipitate S' (Al_2CuMg), which has essentially the same composition and crystal structure as the equilibrium precipitate S, and is partially coherent with the matrix. S' precipitates normally nucleate at dislocations and grow as laths on {210} planes along <100> directions of the matrix. Overageing is associated with the formation of the equilibrium S phase (Al_2CuMg) and loss of coherency. The characteristics of the precipitates are summarised in Table A.2.

Alloys	Precipitates	Characteristics
Al-Cu (-Mg) (High Cu/Mg ratio)	GPI zone	Single layer of Cu atoms on $\{001\}_\alpha$
	GPII zone	Fully coherent, two or more layers of Cu atoms
	θ' ($CuAl_2$)	Tetragonal : a = 0.404 nm, c = 0.580 nm Semi-coherent plates nucleated at dislocations. Forms on $\{001\}_\alpha$
	θ ($CuAl_2$)	Tetragonal : a = 0.607 nm, c = 0.487 nm Incoherent equilibrium phase
Al-Cu-Mg (Low Cu/Mg ratio)	GPB zone	Ordered Cu- and Mg- rich zone as thin rods along $<100>_\alpha$ direction.
	S' (Al_2CuMg)	Orthorhombic, a = 0.404 nm, b = 0.925 nm, c = 0.718 nm Semi-coherent intermediate precipitate nucleated at dislocations. Forms as lath along $<100>_\alpha$ habit plane, only a slightly distorted version of S.
	S (Al_2CuMg)	Orthorhombic, a = 0.400 nm, b = 0.923 nm, c = 0.714 nm Incoherent equilibrium phase

Table A.2 Basic reported characteristics of precipitates age hardening in Al-Cu-Mg alloys [17]

The above descriptions of Al-Cu-(Mg) alloy decomposition should be recognised as a simple conventional representation of the processes that may be involved. It has been generally accepted that the origin of the first stage of hardening in such materials is related to the formation of so-called GPB zones, and the second stage is attributed to the precipitation of S' or S phase [16, 18]. It is noted that Ratchev *et al.* [19, 20] found a similar two-stage age hardening curve in an Al-4.7at%Mg-0.3at%Cu alloy. They claimed the first hardening stage is mainly attributable to heterogeneous formation of S' phase on dislocation helices. Ringer *et al.* [21] reported that in an Al-1.1at%Cu-1.7at%Mg alloy Cu/Mg sub-nanometer clusters have been observed after a short

ageing time (within 60s at 150°C) by means of atom probe field ion microscopy (APFIM) and suggested that the initial rapid hardening is due to these clusters. According to this work the second stage (the peak of hardness) is due to GPB zone formation. Zahra *et al.* [22] interpreted their differential scanning calorimetry (DSC) and high resolution TEM (HREM) results on an Al-0.87at%Cu-1.44at%Mg alloy in favour of the formation of GPB zones even for short ageing times at all temperature below 200°C, but they did not show direct microstructural evidence for the presence of zones or clusters at ageing treatments corresponding to the plateau of the hardness. Further work by Zahra and co-workers claimed that at a later stage (4h ageing at 200°C) partially ordered nanometer-sized Mg-rich clusters, ordered GPB zones of one monolayer thickness, as well as three further semi-coherence and incoherent phases were present [23]. Li *et al.* [24] showed that in commercial purity AA2024 (Al-Cu-Mg-Mn) alloy Mg-clusters formed after a T351 treatment (quench, stretch and naturally age) and that after a long natural aging, clusters become substantially enriched in Cu atoms.

As shown above, the interpretation and understanding of the mechanisms of early age hardening in Al-Cu-Mg alloys has been open to debate due to the lack of a high resolution nanoscale investigation of the real microstructural features. Since the mid 90's the introduction and use of the three-dimensional atom probe (3DAP) methods in APFIM has offered mapping of alloying elements in a three-dimensional space with near-atomic resolution [25]. This method is particular useful for the analysis of solute cluster and small precipitate particles. 3DAP has revealed early decomposition processes, identifying more complex clustering and zone formation processes than are conventionally considered to occur. Gao *et al.* [5] have shown a detailed microstructural investigation using DSC, TEM and 3DAP of Al-1.2at%Cu-0.5at%Mg and Al-1.2at%Cu-1.2at%Mg alloys in their hardening and microstructural evolution during ageing. They demonstrated that age hardening at 150°C is mostly dominated by the formation of solute clusters with varying composition, and plate-like zones rich in copper in the early stages of ageing ($t < 24h$) and by the formation of S'/S phase in the later stages of hardening; at higher temperature (190°C) no zones or clusters form and ageing is dominated by the formation of S'/S phase. However, the latest 3DAP work from this group [26] also shows formation of Cu clusters before the Mg atoms cluster after a short ageing time, it is claimed that the formation of Cu-Mg cluster on

room temperature ageing is responsible for the rapid hardness increase during natural ageing. It is noted that their results are at odds with other reports where it has been suggested that Mg-Mg clusters are the first type of clusters to appear, followed by Cu-Mg and Cu-Cu clusters [23]. However, Reich *et al.* [27] interpreted their 3DAP and TEM analysis data on an Al-1.7at%Mg-1.1at%Cu alloy and indicate that Cu-Mg co-clusters do not occur until close to the end of the hardness plateau and suggested that these evolve into GPB zones during the second stage of the age-hardening process. They suggested that a solute-dislocation interaction causes the first stage of strengthening. Whilst controversy exists in the data produced, the 3DAP technique has clearly provides an important advance in the microstructural analysis of these alloys.

A.1.2.2 Mechanical Behaviour

The principal microstructure features that control the mechanical properties of 2xxx series aluminium alloys are the coarse intermetallic compounds, dispersoid particles, fine precipitates, grain size and shape, dislocation substructure and crystallographic texture. In particular, tensile strength, fracture toughness and fatigue crack growth resistance are of most concern in the current project.

Tensile Strength

The finely dispersed precipitates formed in precipitation hardening have the dominant effect of raising the yield and tensile strength in high strength heat-treatable alloys. Strength is primarily controlled by size and spacing of the matrix precipitates, as well as the interaction of moving dislocations with precipitates. The internal strain around precipitates may be the primary obstacle to the motion of dislocation, i.e. as suggested for GP zones. Small precipitates like zones, clusters and/or intermediate precipitates which are formed in the early stages of ageing may be sheared by moving dislocations. Once precipitates are cut, it is generally recognised that dislocations may continue to pass through the material on the active slip planes due to the 'weakening' of the precipitates (localised work hardening) [28].

In general terms, strength due to such the particles can be described by the following equation:

$$\Delta\sigma_p \approx cf^m d_p{}^n \tag{A.3}$$

where $\Delta\sigma_p$ is the contribution of the particles to the yield strength of the alloy, c is an constant that depends on the properties of the particles and matrix, f is the volume fraction of particles, d_p is the particles diameter, and, m and n are positive exponents. From this equation, it may be seen that strength increases with increasing particle size and volume fraction. During the ageing process, small shearable particles grow and the overall strength increases, but only up to some certain point: when the precipitate particles become large and widely spaced, they will resist cutting and the deformation mode changes from precipitate shearing to a looping, or bypassing mechanism, where moving dislocations bow out between the particles, as proposed by Orowan [29]. The yield strength may then tend to drop with further ageing, but the rate of work-hardening is high, and plastic deformations tends to be spread more uniformly throughout the grains. This is the situation identified with overaging. The upper limit of this strengthening mechanism can be described by the modified Orowan equation:

$$\Delta\sigma_p \approx Gb\sqrt{f / d_p} \tag{A.4}$$

where G is the shear modulus and b is the Burgers vector of the matrix dislocations. From Equation (A.4), it may be seen that the strength decreases as the particles size grow, therefore a high volume fraction of very small strong particles is desired. The typical age-hardening behaviour in which strength increases and then decreases with ageing time may then be associated with a transition from shearing to bypassing of precipitates [30], as shown in Figure A.1. The critical radius, r_c, represents the maximum strength that can be developed in the alloys.

For 2024 alloys, considerable additional increases in strength can be obtained by imposing controlled amounts of cold work (strain hardening) after quenching, increasing dislocation density in natural aged materials, and by refining the size of S' produced during subsequent artificial ageing (T8 temper – solution, cold work & artificial ageing) [31].

Fracture Toughness

Large intermetallic particles are known to have a detrimental effect on the fracture toughness of aluminium alloys [32, 33]. Intermetallic particles participate in the fracture process through cracking and void formation at particle/matrix interfaces. Great improvements in fracture toughness in Al alloys can be obtained by reducing their volume fraction by minimizing impurity elements that form the particles, such as iron and silicon [34]. Speidel [35] showed that the plane strain fracture toughness in Al-Cu-Mg system alloys may be doubled by maintaining the combined levels of these elements (Fe and Si) below 0.5wt%, as compared with similar alloys in which this value exceeds 1.0wt% . Rice *et al.* [36] have for example proposed the following equation for the relationship between fracture toughness, K_{IC}, and intermetallic volume fraction, V_f, and mean diameter of intermetallic, D_i.

$$K_{IC} = \left[2\sigma_Y \cdot E\left(\frac{\pi}{6}\right)^{1/3} D_i \right]^{1/2} V_f^{-1/6} \qquad \text{(A.5)}$$

where σ_Y is the yield strength and E is Young's modulus. Equation (A.5) is however known to be an incomplete description of toughness, as increasing yield strength is not commonly identified with increasing K_{IC} level. An additional interaction between yield strength and work hardening influences on toughness is however considered to exist in age-hardening aluminium alloys [37].

Submicron dispersoids may have both positive and negative effects on fracture toughness. On the beneficial side, they suppress recrystallisation and limit grain growth. On the other hand, they may be detrimental in the fracture process as they may nucleate microvoids by decohesion or cracking. This may lead to the formation of sheets of fine voids between larger voids from constituent particles, facilitating void coalescence [38]. Alloys containing zirconium as the dispersoid forming element are considered more resistant to fracture compared to those which contain chromium and manganese for the same purpose [38]. This is particularly attributable to zirconium forming relatively small particles (of Al_3Zr), which may be coherent with the matrix.

Fine strengthening precipitates increase resistance to plastic deformation, which by itself, might be expected to increase resistance to ductile fracture. However, as noted

earlier, these fine particles are known to enhance localisation of strain (slip) during plastic deformation which leads to premature crack nucleation and low fracture toughness. Soft, solute-depleted PFZs also constitute regions that promote strain localisation. The toughness of many alloys is greatest in the underaged condition, and decreases as ageing proceeds to the maximum strength. When alloys are over-aged, toughness generally recovers but toughness typically compromised by the formation of large precipitate particles at grain boundaries and the presence of wide PFZs which may promote low-energy intergranular fracture [2].

A.2 Fracture Mechanics

With the particular interest of the current project in the growth of relatively long fatigue cracks, it is clear that an understanding of the related fracture mechanics is required.

A.2.1 Macroscopic Modes of Fracture

Any loading of a crack in a solid can be expressed as a sum of three different 'modes', as illustrated in Figure A.2. Normal stresses give rise to Mode I opening, in which the displacement of the crack surfaces are perpendicular to the plane of the crack. In-plane shear results in Mode II crack opening; the displacement of the crack surfaces is in the plane of the crack and perpendicular to the crack front. Mode III is the tearing or anti-plane shear mode, in which the crack surface displacements are in the plane of the crack and parallel to the of the crack front. Whilst all three modes of crack opening are commonly seen to influence failure processes at a microscopic scale, the majority of fracture studies focus on Mode I loading situations as these are found to be most critical in structural applications.

A.2.2 The Stress Intensity Factor

By using the analytical methods of Westergaard [39], Irwin [40] quantified the near-tip stress fields for linear elastic cracks in terms of the stress intensity factor, K. Consider a through thickness crack of arbitrary size, in a body of arbitrary size and shape, loaded in Mode I, as illustrated in Figure A.3. In the coordination system shown, the local stresses at the co-ordinates (r, θ) close to the crack tip are then approximated by,

$$\sigma_{xx} = \frac{K_I}{\sqrt{2\pi r}} \cos\left(\frac{\theta}{2}\right)\left[1 - \sin\left(\frac{\theta}{2}\right)\sin\left(\frac{3\theta}{2}\right)\right] \tag{A.6}$$

$$\sigma_{yy} = \frac{K_I}{\sqrt{2\pi r}} \cos\left(\frac{\theta}{2}\right)\left[1 + \sin\left(\frac{\theta}{2}\right)\sin\left(\frac{3\theta}{2}\right)\right] \tag{A.7}$$

$$\tau_{xy} = \frac{K_I}{\sqrt{2\pi r}} \cos\left(\frac{\theta}{2}\right)\sin\left(\frac{\theta}{2}\right)\cos\left(\frac{3\theta}{2}\right) \tag{A.8}$$

or, in general term; as,

$$\sigma_{ij} = \frac{K_I}{\sqrt{2\pi r}} f_{ij}(\theta) \tag{A.9}$$

where σ_{ij} represents the stresses acting on a material element *dxdy* at a distance r from the crack tip and an angle θ from the crack plane, and f_{ij} (θ) represents known functions of θ. K_I is then described as the stress intensity factor for Mode I. Similar solutions can be obtained for other modes of loading with stress intensity factors corresponding to K_{II} and K_{III}, but with different θ-functions. Each mode of loading of the crack produces a $1/r^{1/2}$ singularity at the crack tip. The stress intensity factor defines the amplitude of the crack tip singularity; that is, stresses near the crack tip increase in proportion to K. In general, K is a function of the applied stress, crack length, and the specimen geometry, according to:

$$K = Y\sigma\sqrt{\pi a} \tag{A.10}$$

where σ is the applied stress, a is the crack length and Y is a dimensionless parameter which depends on the geometries of the specimen and crack. The principle of similitude then allows cracks of different geometry to be compared in terms of stress intensity factors alone as K defines stress and strain conditions in the region critical to fatigue (i.e. near the crack tip).

Equations (A.6, A.7 and A.8) are only valid for a sharp crack within an elastic body. Due to the singular nature of the elastic stress fields, there is always a region of plastically deformed material at the crack tip in conventional structural metals. However, if the plastic zone is small compared to the area over which the Equation (A.6, A.7 and A.8) hold (the "K- dominated region"), then K is considered to be a valid description of the crack tip condition, even though the stress levels indicated by Equation (A.8) and (A.9) do not hold close to the tip. Such a situation is referred to as *small scale yielding*, forming the basis for the use of linear elastic fracture mechanics (LEFM) in a wide range of real-world engineering situations (i.e. involving structure metals where a degree of plasticity exists at any loaded crack tip).

A.2.3 Stress State and Plastic Zone Size/Shape

As described before, a stress singularity exists at the tip of an elastic crack. Metallic materials therefore commonly develop plastic strains as the yield strength is exceeded in the region near a crack tip. In a thin body, the stress through the thickness (σ_z)

cannot vary appreciably due to the presence of free surfaces ($\sigma_z = 0$), and a biaxial state of stress results. This is termed the *plane stress* condition. In a thick body, crack tip plastic deformation is constrained in the z direction due to the surrounding elastic material, so strain in the z direction equals zero ($\varepsilon_z = 0$). Through thickness stress (σ_z) is therefore developed in the z direction. This results in the *plane strain* condition. It may be seen [41] that if plane strain prevails in the interior of a cracked body, the stress σ_z gradually increases from zero (at the surfaces) to the plane strain value in the interior. The triaxiality of the stress state associates with a plane strain crack tip is then seen to limit the extent of plastic deformation (size of plastic zone), whilst greatly enhancing the peak stress levels that may be generated within the plastic zone close to the crack tip.

For static loading, when an elastic plastic material is subjected to a fixed far-field load P, the crack tip creates a *monotonic plastic zone*. According to Irwin's simple approximation (based on the elastic stress distribution) [42], the extent of the plastic zone r_p ahead of the crack tip ($\theta = 0$) is then proportional to the square of the stress intensity factor;

$$r_p = \frac{1}{\pi}\left(\frac{K_I}{\sigma_y}\right)^2 \qquad \text{for plane stress} \qquad \text{(A.11)}$$

$$r_p = \frac{1}{3\pi}\left(\frac{K_I}{\sigma_y}\right)^2 \qquad \text{for plane strain} \qquad \text{(A.12)}$$

where σ_y is the yield stress of the material. An effective multiplication of flow stress (by a factor of 3) is used to account for through-thickness constraint effects in Equation (A.11). Other methods to determine the monotonic plastic zone size include that of Dugdale [43]. In the Dugdale approach, under plane stress conditions, the plastic region is envisioned as a narrow strip (of near-zero height) which extends a distance r_p ahead of the crack tip, which is loaded by the traction $\sigma_{yy} = \sigma_y$ over the length r_p. Balance of remote applied forces against this traction leads to the plastic zone size estimate,

$$r_p = \frac{\pi}{8}\left(\frac{K_I}{\sigma_y}\right)^2 \qquad \text{(A.13)}$$

The results from Dugdale in Equation (A.13) compares well with the Irwin approximation in Equation (A.11). Over years a variety of more complex plastic zone analysis have been presented within the literature [40, 42, 43], leading to plastic zone size estimates of much the same order as those noted above.

In cyclic loading, when an elastic plastic material is subjected to a far-field load P, the crack tip creates a monotonic plastic zone as described above. If the material is unloaded by an amount of $-\Delta P$, a reversed plastic flow is produced [44-46]. Rice suggests that during the load change $-\Delta P$ from the peak load P, the effective reversed yield stress is given by twice the nominal tensile yield stress, due to the stress change required to take the crack tip from forward to reverse flow. Therefore Equations (A.11) and (A.12) can be modified for the *cyclic plastic zone size*, r_c,

$$r_c = \frac{1}{\pi}\left(\frac{K_I}{2\sigma_y}\right)^2 \quad \text{, for plane stress} \qquad \text{(A.14)}$$

$$r_c = \frac{1}{3\pi}\left(\frac{K_I}{2\sigma_y}\right)^2 \quad \text{, for plane strain} \qquad \text{(A.15)}$$

The development of cyclic plastic zone upon unloading is illustrated in Figure A.4.

A first order estimate of the shape of plastic zone may given by examining the yield condition, in conjunction with asymptotic K-field results, for all angles θ around crack tip by applying either the Von Mises or Tresca criterion. By using the Von Mises criterion, the extent of the plastic zone, in term of radius r_p as a function of θ, is given as;

$$r_p(\theta) = \frac{1}{4\pi}\left(\frac{K_I}{\sigma_y}\right)^2\left[1+\frac{3}{2}\sin^2\theta+\cos\theta\right] \qquad \text{(A.16)}$$

for plane stress, and;

$$r_p(\theta) = \frac{1}{4\pi}\left(\frac{K_I}{\sigma_y}\right)^2\left[\frac{3}{2}\sin^2\theta+(1-2\nu)^2(1+\cos\theta)\right] \qquad \text{(A.17)}$$

for plane strain.

Figure A.5 illustrates the corresponding Mode I plastic zone size and shape around the crack tip for plane stress and plane strain.

The ratio of plastic zone size to thickness is an important factor for the state of stress. If the size of the zone is of the order of the thickness of the cracked body, i.e. if r_p/B (B is the thickness) approaches unity, plane stress conditions can develop. The ratio must be appreciably less than unity for plane strain to exist through the greater part of the thickness, with the region of plane stress at the material surface then extending over a relatively small part of the thickness.

References

[1] H.Y. Hunsicker, *Aluminium - Properties, Physical Metallurgy and Phase Diagrams*, ed. K.R.V. Horn. 1968, 1, p. 109-162.

[2] I.J. Polmear, *Light Alloys*. 3rd ed, eds. R. Honeycombe and P. Hancock. 2000, Oxford: Butterworth-Heinemann.

[3] J.G. Embury and R.B. Nicholson, *Acta Metallurgica*, 1965. **13**: p. 403-417.

[4] D. Althenpohl, *Aluminium*. Vol. 37. 1961, p. 401-411.

[5] N. Gao, L. Davin, S. Wang, A. Cerezo, and M.J. Starink, *Materials Science Forum*, 2002. **396-402**: p. 923-928.

[6] G. Lutjering and A. Gysler, *Aluminium Transformation, Technology and Applications, American Society for Metals*. 1980, p. 171.

[7] E.A.J. Starke, *Treatise on Materials Science and Technology*. Vol. 31. 1989, p. 35-63.

[8] E.A.J. Starke and J.T. Staley, *Progress in Aerospace Sciences*, 1996, 32, p. 131-172.

[9] G.T. Hahn and R. Simon, *Engineering Fracture Mechanics*, 1973. **5**: p. 523.

[10] T.J. Warner, R.A. Shahani, P. Lassince, and G.M. Raynaud, *Research Report of Pechiney*, 1998.

[11] M. Karlik and B. Jouffrey, *Acta Materials*, 1997. **45**: p. 3251.

[12] T. Sato and T. Takahashi, *Scripta Metallurgical*, 1988. **22**: p. 941.

[13] V.A. Philips, *Acta Metallurgical*, 1973. **23**: p. 751.

[14] A. Guinier, *Journal of Physics Radium*, 1942. **8**: p. 124.

[15] J. Bradley and P. Jones, *Journal of the Institute of Metals*, 1933. **51**: p. 131.

[16] J.M. Silcock, *Journal of the Institute of Metals*, 1960-61. **89**: p. 203.

[17] P.J. Gregson, *Aluminium Alloys: Their Physical and Mechanical Properties (Materials Science Forum Series)*, eds. P.J. Gregson and S. Harris. 2002, Zurich-Uetikon: Trans Tech Publications, p. 49-84.

[18] J.T. Vietz and I.J. Polmear, *Journal of the Institute of Metals*, 1966. **94**: p. 410.

[19] P. Ratchev, B. Verlinden, P.D. Smet, and P.V. Houtte, *Acta Materialia*, 1998. **46**: p. 3523-3533.

[20] R.P. Ratchev, B. Verlinden, P.D. Smet, and P.V. Houtte, *Metallurgical Transactions*, 1999. **40**: p. 34.

[21] S.P. Ringer, T. Sakurai, and I.J. Palmear, *Acta Materialia*, 1997. **45**: p. 3731-3744.

[22] A.M. Zahra, C.Y. Zahra, C. Alfonso, and A. Charai, *Scripta Materialia*, 1998. **39**: p. 1553-1558.

[23] A. Charai, T. Walther, C. Alfonso, A.M. Zahra, and C.Y. Zahra, *Acta Materialia*, 2000. **48**: p. 2751-2764.

[24] D. Li, R.P. Gangloff, G.H. Bray, M.V. Galzov, and R.J. Rioja, *Proceeding of Materials Solutions Conference Indianapolis* 2001, p. 105

[25] K. Hono, *Acta Materialia*, 1999. **47**: p. 3127-3145.

[26] M.J. Starink, N. Gao, L. Davin, J. Yan, and A. Cerezo, *Proceedings of ICSMA13* 2003, Budapest, Hungary, p. 25-30

[27] L. Reich, S.P. Ringer, and K. Hono, *Philosophy Magazine*, 1999. **79**: p. 639.

[28] E. Hornbogen and K.H.Z. Gahr, *Acta Metallurgica*, 1976. **24**: p. 581-592.

[29] E. Orowan, *Symposium on Internal Stresses, Institute of Metals, London*, 1947: p. 451.

[30] R.B. Nicholson, *Strengthening Methods in Crystals*, eds. A. Kelly and R.B. Nicholson. 1971, Amsterdam: Elsevier, p. 535.

[31] W.G. Truckner, J.T. Staley, R.J. Bucci, and A.B. Thakker, *U. S. Airforce Material Laboratory Report AFML-TR-76-169*. 1976.

[32] W.E. Anderson and W.E. Quist, Aluminium Alloy, United States Patent Number 3, 1966, p. 284.

[33] R.K. Smith, *The quest for excellent, In: Milestones of Aviation*. 1991, p. 222.

[34] M.O. Speidel, *Metallurgical Transactions*, 1975. **6A**: p. 631.

[35] M.O. Speidel, *Proceedings of 6th International Conference on Light Metals* 1975, p. 125-136

[36] J.R. Rice and M.A. Johnson, *Inelastic Behaviour of Solid*, 1970, p. 641.

[37] N. Kamp, I. Sinclair, and M. Starink, *Metallurgy and Materials Science*, 2002. **33**(4): p. 1125-1136.

[38] R.H. Van Stone and J.A. Psioda, *Metallurgical Transactions*, 1975. **6A**: p. 668-670.

[39] H.M. Westergaard, *Journal of Applied Mechanics*, 1939. **61A**: p. 49-53.

[40] G.R. Irwin, *Journal of Applied Mechanics*, 1957. **24**: p. 361-364.

[41] J.R. Dixon, *International Journal of Fracture Mechanics*, 1965. **1**: p. 224-243.

[42] G.R. Irwin, *Proceedings of the Seventh Sagamore Ordance Materials Conference* 1960, p. 63-78

[43] D.S. Dugdale, *Journal of the Mechanics and Physics of Solids*, 1960. **8**: p. 100-108.

[44] P.C. Paris, *The growth of crack due to variations in loads, Ph.D thesis, Lehigh University*. 1960.

[45] F.A. McClintock, *Fracture of Solids*, 1963. **20**: p. 65-102.

[46] J.R. Rice, *Fatigue Crack Propagation, ASTM STP 415*, 1967, Philadelphia: ASTM, p. 247-309.

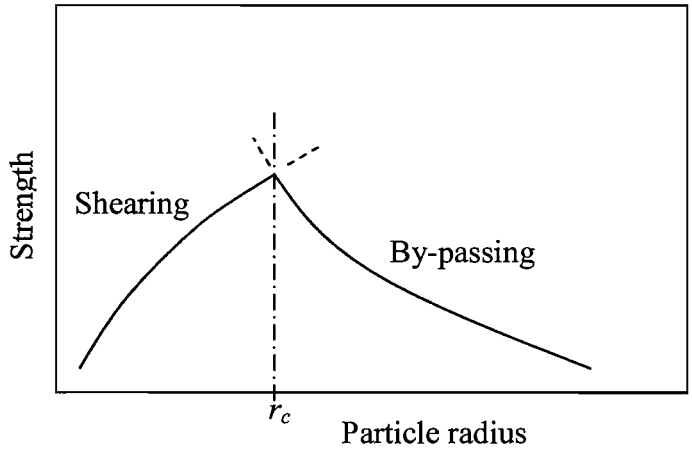

Figure A.1 Relationship between alloy strength and strengthening particle size for dislocation shearing and bypassing.

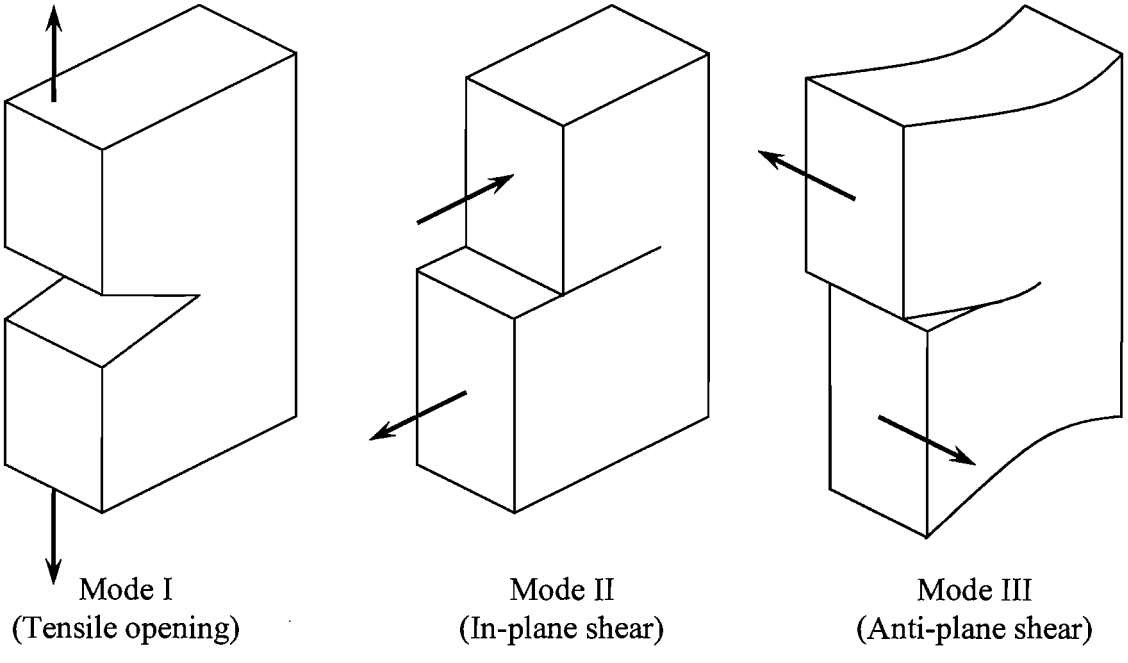

Figure A.2 The three basic modes of fracture.

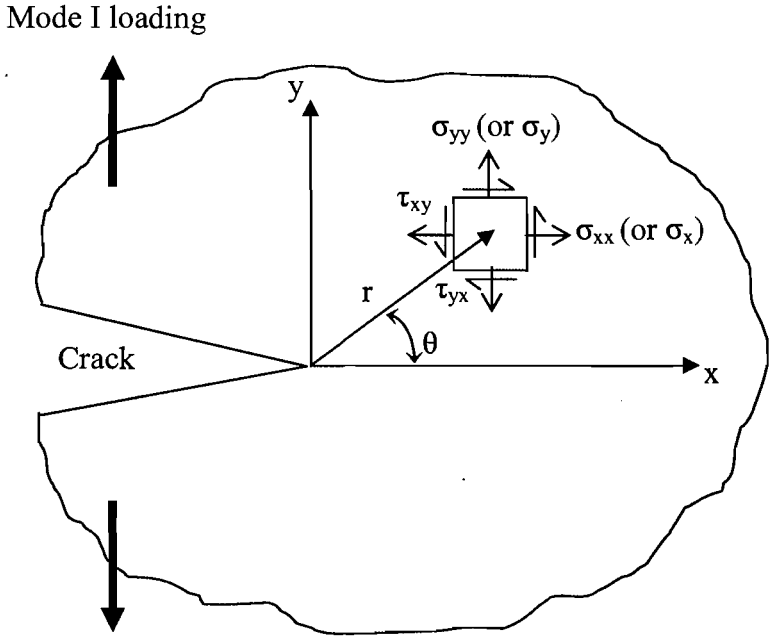

Figure A.3 Definition of the coordinate axis ahead of a crack tip.

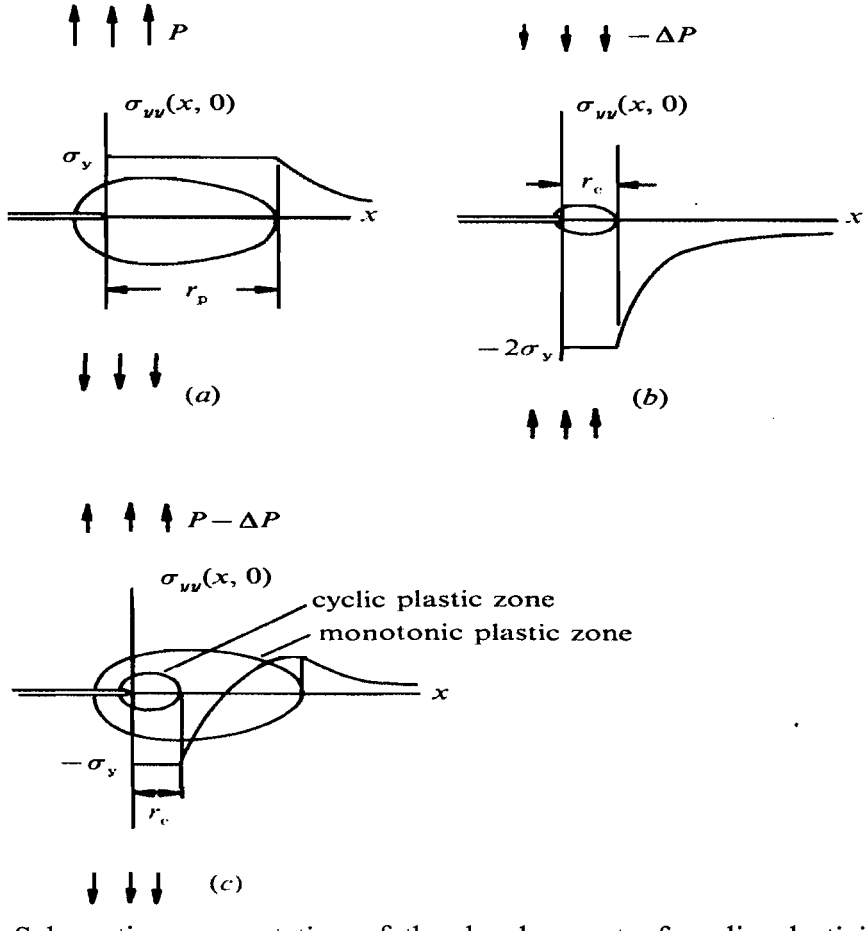

Figure A.4 Schematic representation of the development of cyclic plasticity upon unloading: (a) Monotonic plastic zone created by a far-field tensile load. (b) Nominal stress distribution due to the reduction of the load by ΔP, which, when superimposed with (a), gives the result in (c) [46].

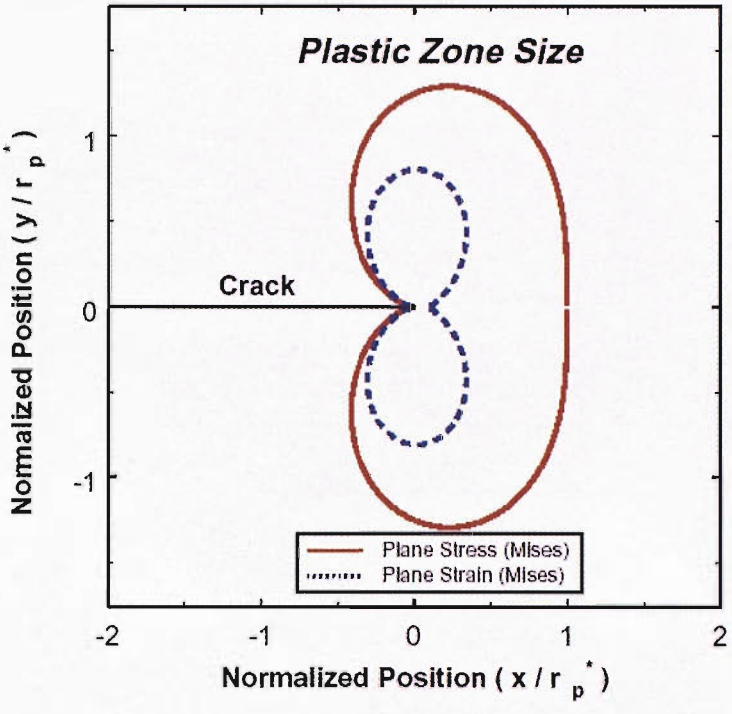

Figure A.5 Mode I plastic zone size and shape for plane stress and plane strain conditions using the Von Mises yield criterion, based on elastic crack tip stress fields.